

# Multi-Scale Analysis of Gas Hydrates Phase Transitions Focusing on Long-Term CO<sub>2</sub> Sequestration

Mojdeh Zarifi

Thesis for the degree of Philosophiae Doctor (PhD)  
University of Bergen, Norway  
2024

UNIVERSITY OF BERGEN



# Multi-Scale Analysis of Gas Hydrates Phase Transitions Focusing on Long-Term CO<sub>2</sub> Sequestration

Mojdeh Zarifi



Thesis for the degree of Philosophiae Doctor (PhD)  
at the University of Bergen

Date of defense: 27.06.2024

© Copyright Mojdeh Zarifi

The material in this publication is covered by the provisions of the Copyright Act.

Year: 2024

Title: Multi-Scale Analysis of Gas Hydrates Phase Transitions Focusing on Long-Term CO<sub>2</sub> Sequestration

Name: Mojdeh Zarifi

Print: Skipnes Kommunikasjon / University of Bergen

## Scientific environment

This scientific work was performed at the Department of Physics and Technology, Faculty of Mathematics and Natural Sciences, University of Bergen. The PhD thesis has started development under the supervision of Professor Bjørn Kvamme and co-supervision of Prof. Tatiana Kuznetsova, who subsequently became my main supervisor.

This research was financially supported by the Research Council of Norway and industrial partners through the following projects:

- CLIMIT, “Safe long term sealing of CO<sub>2</sub> in hydrate”, Research Council of Norway, project number: 224857.
- SSC-Ramore, “Subsurface storage of CO<sub>2</sub> - Risk assessment, monitoring and remediation”, project number: 178008/I30;
- PETROMAKS, “CO<sub>2</sub> injection for extra production,” Research Council of Norway project number 801445; PETROMAKS “CO<sub>2</sub> Injection for Stimulated Production of Natural Gas,” Research Council of Norway project numbers 175968 and 230083; and STATOIL, under contract 4502354080.

## **Dedication**

### **To my beloved parents, Mojgan and Keramat:**

This thesis stands as a testament to your enduring influence on my life and academic endeavors.

### **To my daughter Anita:**

As I embark on this academic milestone, I dedicate this thesis to you, may you always believe in the power of education, resilience, and dreams.

## Acknowledgements

Foremost, I would also like to extend my appreciation to the University of Bergen and staff of the physics and technology department for providing the resources, facilities, and friendly environment to pursue this research.

I would like to express my deepest gratitude to my first supervisor, Bjorn Kvamme, whose guidance, expertise, and support have been invaluable throughout this journey. Your insightful feedback, encouragement, and patience have played a pivotal role in shaping the direction and quality of this thesis.

I am also indebted to my co-supervisor, Tatiana Kuznetsova, for her valuable contributions, encouragement, and constructive criticism. Her expertise and guidance and dedication have enriched my research experience and contributed significantly to the success of this thesis. I am truly grateful as she has always been there to support me from the start of this PhD project.

I also use this opportunity to thank my parent Mojgan and Keramat, their sacrifices, guidance, boundless love and belief in me have shaped the person I am today. This thesis is a tribute to their enduring love and unwavering faith in my abilities. I am also grateful for my beloved brothers Mohammad and Masoud for their belief in me and their constant support and encouragement means more than a fortune.

I am grateful to my husband, Reza, for his understanding and patience throughout this journey. His encouragement, love, and support have been a constant source of strength and motivation. And I am grateful for my daughter Anita, the beauty of her simple attitude to life is my greatest joy and motivation. Her innocence, laughter, and presence have inspired me to persevere in the pursuit of knowledge.

Lastly, I am thankful to all my colleagues and friends, earned during this period, Kim, Gyula, Neda, Richard, Iman, Juri, and Solomon, who have offered their valuable insights throughout this journey. Your presence and contributions have enriched my academic experience and made this achievement possible.

## Abstract

The main goal of this thesis was to expand our understanding of gas hydrates transitions with a closer look at long-term CO<sub>2</sub> offshore storage. Hydrates are crystalline substances containing small non-polar or slightly polar molecules trapped in cavities made of water. The formation of these ice-like compounds during processing and transport of hydrocarbons has motivated substantial amounts of hydrate research in the past while another alternative putting gas hydrate on the high interest is that they are present in large quantities in arctic regions under the permafrost and in oceanic sediments along the continental margins around the world; these reserves are enough to fulfill the future energy demands, utilizing gas hydrate phenomena for transportation and storage purposes are other examples of today's interest in clathrate hydrates. Nevertheless, fully understanding the physics of gas hydrates requires multi-scale analysis with a coupling between different mechanisms involved in hydrate phase transitions. This PhD study also provides the relevant background necessary to understand methods used and correctly interpret thermodynamics and kinetics of hydrate phase transitions.

The first stage of the project involved a literature review of research done previously on theoretical and numeric development of the Phase Field Theory. Applying our PFT model has shown the inadequacy of hypotheses postulating relatively large-scale nature of local dynamics across hydrate-fluid interfaces. Our implementation of first-order-implicit free energy models for all co-existing phases makes it possible to compare the competing pathways of hydrate formation, dissociation, and reformation. Our results have led us to conclude that a complete overhaul of routines and algorithms would incur significant time investment, making the use of the legacy code worthwhile for running simplified theoretical studies.



During the second phase of the project, we focused on improving the prediction capabilities of our thermodynamic models with respect to the impact of impurities and water, with model consistency being the priority. The same methodology that involved following free energy gradients has proven to work well in several diverse scenarios while yielding significant physical insights and industrially relevant recommendations. Phase three of the project addressed successive stages of hydrate formation, with a focus on dynamic rate-limiting processes that can result in pockets of gas and liquid water being trapped inside the hydrate phase. In the context of this thesis, it was important to distinguish heat transport modeling from detailed modeling of well-defined experimental systems which can be monitored extensively and as such provide a very detailed distinction between various heat transport effects. We have recognized a need for a rigorous kinetic model that accounts for implicit coupling of mass and heat transport and the way this will affect the driving forces for hydrate formation and dissociation.

Finally, we were able to propose a simplified residual scheme which allowed us to construct a realistic representation of interfaces between hydrate and liquid phases. We have shown that in addition to being able to handle many alternative hydrate routes for hydrate formation and dissociation, our residual thermodynamics scheme enables one to calculate a variety of associated thermodynamic functions, with enthalpy being one of the most crucial properties. Description of our methodology is presented, together with a discussion of our implementations and results obtained from simulations performed within published papers.

## Sammendrag

Hovedmålet med denne avhandlingen var å utvide vår forståelse av gass hydrat faseoverganger med særlig fokus på langvarig CO<sub>2</sub>-lagring i sedimenter under havbunnen. Hydrater er krystallinske stoffer som inneholder små ikke-polare molekyler, eller svakt polare molekyler, fanget i hulrom laget av hydrogen-bundet vann. Dannelsen av disse is-lignende forbindelsene under prosessering og transport av hydrokarboner har vært motivasjonen som historisk sett har finansiert betydelige mengder hydratforskning på grunn av problemene som disse faste hydrate skapte. I senere tid har interessen for disse hydratene som kilde til energi økt betydelig. Naturgasshydrater er til stede i store mengder i arktiske regioner under permafrosten, og i havsedimenter langs kontinentalsoklene rundt om i verden. Disse reservene av naturgass på i innefrosset (hydrat) form er nok til å dekke fremtidige energibehov for mange tiår. Offisielle og optimistiske estimater fra US Geological Survey indikerer at energimengden i naturgasshydrater kan være mer enn to ganger så mye som alle kjente forekomster av konvensjonelle fossile energi-kilder på kloden, Hydrat som en termodynamisk fase har også vært undersøkt med sikte bruk i separasjon, transport av hydrokarboner og som en fase for lagring av hydrokarboner. Det er sågar foreslått klima-anlegg basert på bruk av hydrat som aktiv fase-overgang. Det er imidlertid behov for en dyp forståelse av fysikken til gasshydrater. Analyse og koblinger mellom ulike skala er sentralt. Fase-overganger er i seg selv prosesser på nano til meso skala. Dette nivået av dynamikk er imidlertid koblet til hydrodynamikk gjennom transport i rørstrømning eller strømninger i sedimenter. Kunnskap om koblinger mellom relevante og hastighets-styrende mekanismer på ulike skala er helt avgjørende.. Denne doktorgradsstudien gir også den relevante bakgrunnen som er nødvendig for å forstå de metodene som er anvendt, og den tilhørende tolkning av termodynamikk og kinetikk knyttet til hydrat faseoverganger..

Første fase av prosjektet innebar en litteraturgjennomgang av tidligere forskning på teoretisk og numerisk utvikling av fasefeltteorien («Phase Field Theory», PFT). Bruk av vår PFT-modell har vist at hypoteser som postulerer en relativ storskala natur av lokal dynamikk over hydrat-væskegrensesnittene er utilstrekkelige. Implementeringen av første-ordens-implisitte fri energimodeller for alle medvirkende faser gjør det mulig å sammenligne de konkurrerende veiene for hydrattdannelse, hydrat smelting og gjendannelse av hydrate.

Hovedfokus i andre fase a prosjektet var å forbedre prediksjonsevnen til de termodynamiske modellene som er anvendt in prosjektet. Viktig prioritet var effekten av urenheter og konsistens av modellen

En metodikk basert på å følge fri energigradienter har vist seg å fungere godt i flere ulike scenarier. Samtidig gir den betydelig fysisk innsikt og godt grunnlag for industrielt relevante anbefalinger.

Sentrale områder i fase tre av prosjektet er ulike stadier av hydrattdannelse, med fokus på ulike prosesser som kan være dynamisk begrensende for dannelsen av hydrat. Men også prosesser som kan bremse hydrat vekst og dermed resultere i at gass fanges inne i hulrom av hydrat-filmer og likeledes vanndråper fanget inne av hydrat filmer. I kontrollerte eksperimenter kan man observere og måle mange fenomener som for eksempel hvor raskt et hydrat film mellom vann og gass vokser. Transport av gass gjennom et hydrat film er veldig langsom og er karakterisert av ulike transportprosesser. En gass molekyl kan transporteres gjennom hydrat uten at det utveksles mye varme. Transport av vann gjennom hydrat film er mer komplisert og en implisitt dynamisk kobling mellom masse og varme transport. I denne avhandlingen var det viktig å skille varmetransportmodellering fra detaljert modellering av veldefinerte eksperimentelle systemer som kan overvåkes omfattende og dermed gi en

svært detaljert distinksjon mellom ulike varmetransporteffekter. Behovet for en grundig kinetisk modell som tar hensyn til den implisitte koblingen av masse og varmetransport, og hvordan dette vil påvirke drivkreftene for hydratdannelse og hydrat smelting er en viktig erkjennelse av denne avhandlingen.

---

## List of Publications and Contributions

### Publications in Peer-Review Journals

Gyula I. Tóth, Mojdeh Zarifi, and Bjørn Kvamme, Phase-field theory of multi-component incompressible Cahn-Hilliard liquids, *Phys. Rev. E* 93, 013126 – 2016. <https://doi.org/10.1103/PhysRevE.93.013126>

Bjørn Kvamme, Marthe Austrheim, Anette Knarvik, Mojdeh Zarifi Hydrate Formation During Transport of Natural Gas Containing Water And Impurities *International Journal of Engineering Research and Development (IJERD)*, Volume 13, Issue 5, 2017 PP.01-16

Bjorn Kvamme B., Eirik Iden , Jørgen Tveit, Veronica Veland, Mojdeh Zarifi., and Khadije Qorbani, Effect of H<sub>2</sub>S content on thermodynamic stability of hydrate formed from CO<sub>2</sub>/N<sub>2</sub> mixtures, *Journal of Chemical & Engineering Data*, 62, 1645–1658, 2017. <https://doi.org/10.1021/acs.jced.7b00027>

Mojdeh Zarifi, Bjørn Kvamme, Petter Gjerstad, Solomon Aforkoghene Aromada Dynamics of heat and mass transport during hydrate dissociation and reformation in sediments, *Proceeding of 14th International Conference on Heat Transfer, Fluid Mechanics and Thermodynamics, (HEFAT)*, Wicklow Ireland, 22-24 July 2019.

Bjorn Kvamme, Solomon Aforkoghene Aromada, Tatiana Kuznetsova, Petter Berge Gjerstad Pablo Charles Canong & Mojdeh Zarifi, Maximum tolerance for water content at various stages of a Natuna production *Journal of Heat and Mass Transfer*, -018-2490-4 <https://link.springer.com/article/10.1007/s00231-018-2490-4>

Mojdeh Zarifi, Bjørn Kvamme, Modelling heat transport in systems of hydrate filled sediments using residual thermodynamics and classical nucleation theory, *Appl. Sci.* 2021, 11, 4124. <https://doi.org/10.3390/app11094124>

Bjørn Kvamme, Richard B, Coffin<sup>1</sup>, Na Wei<sup>1</sup>, Shouwei Zhou, Jinzhou Zhao<sup>1</sup>, Qingping Li<sup>2</sup>, Navid Saeidi, Yu-Chien Chien, Derek Dunn-Rankin, Wantung Sun<sup>1</sup>, Mojdeh Zarifi, Stages in dynamics of hydrate formation and consequences for design of experiments for hydrate formation in sediments, *Energies* 2019, 12(17), 3399; <https://doi.org/10.3390/en12173399>

Bjørn Kvamme, Jinzhou Zhao , Na Wei , Wantung Sun , Mojdeh Zarifi, Navid Saeidi , Shouwei Zhou , Tatiana Kuznetsova and Qingping Li, Why Should We Use Residual Thermodynamics for Calculation of Hydrate Phase Transitions *Energies* 2020, 13(16), 4135; <https://doi.org/10.3390/en13164135>

Bjørn Kvamme, Jinzhou Zhao, Na Wei, Qingping Li, Navid Saeidi, Wantong Sun, Mojdeh Zarifi, Tatiana Kuznetsova, Thermodynamics of hydrate systems using a uniform reference state, *Asia-Pac J Chem Eng.* 2021; e2706 <https://doi.org/10.1002/apj.2706>

### **Reviews Conference Proceedings**

Mojdeh Zarifi, Bjørn Kvamme and Kuram Baig, Hydrate phase transition kinetics using phase field theory including mineral impact, 65th Canadian Chemical Engineering Conference, Calgary, Canada, October 4–7, 2015.

### **Conference Proceedings Without Review System**

Jordan Bauman, Bjørn Kvamme, Mojdeh Zarifi; Non-Equilibrium Aspects Of Hydrate and Driving Forces Phase Transition, 8th International Conference on Gas Hydrates (ICGH), Beijing, 28 July - 1 August, 2014, Beijing, China. Non-Equilibrium Aspects of Hydrate and Driving Forces Phase Transition.

### **International Presentations**

Jordan Bauman, Bjørn Kvamme, Mojdeh Zarifi; Non-Equilibrium Aspects Of Hydrate and Driving Forces Phase Transition, 8th International Conference on Gas Hydrates (ICGH), Beijing, 28 July - 1 August 2014,

M. Zarifi, B. Kvamme and K. Baig, Hydrate phase transition kinetics using phase field theory including mineral impact, 65th Canadian Chemical Engineering Conference, Calgary, Canada, October 4–7, 2015.

Bjørn Kvamme, Solomon Aforkoghene Aromada, Tatiana Kuznetsova, Petter Berge Gjerstad, Pablo Charles Canonge, Mojdeh Zarifi; M. Maximum limitations of adding N<sub>2</sub> to CO<sub>2</sub> during combined CO<sub>2</sub> storage and CH<sub>4</sub> production with examples from offshore Indonesia. Oral presentation at Fiery Ice 2017 in Corpus Christie, Texas, U.S.A., December 6 – 8, 2017.

Mojdeh Zarifi, Bjørn Kvamme, Petter Berge Gjerstad, Solomon Aforkoghene Aromada, Dynamics of heat and mass transport during hydrate dissociation and reformation in sediments, 14th International Conference on Heat Transfer, Fluid Mechanics and Thermodynamics, (HEFAT), Wicklow Ireland, 22-24 July 2019,

## Publications included in this thesis

- (1) Mojdeh Zarifi, Bjørn Kvamme, Jordan Bauman, “Non-Equilibrium Aspects of Hydrate and Driving Forces for Phase Transition”. Proceedings of the 8th International Conference on Gas Hydrates (ICGH8), July 28 – August 1, 2014, Beijing, China.
- (2) Gyula I. Tóth, Mojdeh Zarifi, and Bjørn Kvamme, “Phase-field theory of multi-component incompressible Cahn-Hilliard liquids”, *Phys. Rev. E* 93, 013126, 2016.
- (3) Bjørn Kvamme, Marthe Austrheim, Anette Knarvik, Mojdeh Zarifi, “Hydrate Formation During Transport of Natural Gas Containing Water and Impurities”, *International Journal of Engineering Research and Development (IJERD)*, 13, (5), 01-16, 2017
- (4) Bjørn Kvamme, Eirik Iden, Jørgen Tveit, Veronica Veland, Mojdeh Zarifi, and Khadije Qorbani, “Effect of H<sub>2</sub>S content on thermodynamic stability of hydrate formed from CO<sub>2</sub>/N<sub>2</sub> mixtures”, *Journal of Chemical & Engineering Data*, 62, 1645–1658, 2017.
- (5) Bjørn Kvamme, Solomon Aforkoghene Aromada, Tatiana Kuznetsova, Petter Berge Gjerstad, Pablo Charles Canong, “Mojdeh Zarifi, Maximum tolerance for water content at various stages of a Natuna production”, *Journal of Heat and Mass Transfer*, 55, 1059–1079, 2019
- (6) Mojdeh Zarifi, Bjørn Kvamme, Petter Gjerstad, Solomon Aforkoghene Aromada, “Dynamics of heat and mass transport during hydrate dissociation and reformation in sediments”, 14th International Conference on Heat Transfer, Fluid Mechanics, and Thermodynamics, (HEFAT), Wicklow Ireland, 22-24 July 2019.
- (7) Bjørn Kvamme, Richard B. Coffin, Na Wei, Shouwei Zhou, Jinzhou Zhao, Qingping Li, Navid Saedi, Yu-Chien Chien, Derek Dunn-Rankin, Wantung Sun, Mojdeh Zarifi, “Stages in dynamics of hydrate formation and consequences for design of experiments for hydrate formation in sediments”, *Energies* 12(17), 3399, 2019.

- (8) Mojdeh Zarifi, Bjørn Kvamme, “Modelling heat transport in systems of hydrate filled sediments using residual thermodynamics and classical nucleation theory”, *Appl. Sci.* 11, 4124, 2021
- (9) Bjørn Kvamme, Jinzhou Zhao, Na Wei, Wantong Sun, Mojdeh Zarifi, Navid Saeidi, Shouwei Zhou, Tatiana Kuznetsova and Qingping Li, “Why Should We Use Residual Thermodynamics for Calculation of Hydrate Phase Transitions”, *Energies* 2020, 13(16), 4135.
- (10) Bjørn Kvamme, Jinzhou Zhao, Na Wei, Qingping Li, Navid Saeidi, Wantong Sun, Mojdeh Zarifi, Tatiana Kuznetsova, “Thermodynamics of hydrate systems using a uniform reference state”, *Asia-Pac J Chem Eng.* 2021; e2706



---

## List of Figures

|   |    |
|---|----|
| FIGURE 1.1 TYPICAL STRUCTURE OF GAS HYDRATE TAKEN FROM MASLIN ET AL (M. MASLIN ET AL., 2010) .....  | 5  |
| FIGURE 1.2 OVERVIEW OF THREE MOST COMMON HYDRATE UNIT CRYSTAL STRUCTURES (KUMAR & LINGA, 2018) .....  | 9  |
| FIGURE 1.3 GAS HYDRATE FORMATION IN LIQUID-DOMINATED SYSTEM. REDRAWN FROM (SUM, KOH, & SLOAN, 2009) .....   | 13 |
| FIGURE 1.4 GAS HYDRATE FORMATION IN GAS-DOMINATED SYSTEM. REDRAWN FROM (MUSAKAEV, URAZOV, & SHAGAPOV, 2006).....  | 14 |
| FIGURE 1.5 MODEL OF HYDRATE FORMATION AND DECOMPOSITION IN OFFSHORE GAS RESERVOIR PRODUCTION PIPELINE (WEI ET AL., 2020).....   | 15 |
| FIGURE 1.6 POTENTIAL METHANE RELEASE IN THE EASTERN SIBERIAN ARCTIC SHELF ("METHANE RELEASES FROM ARCTIC SHELF MAY BE MUCH LARGER AND FASTER THAN ANTICIPATED," 2010; SHAKHOVA ET AL., 2010).....   | 17 |
| FIGURE 1.7 THE INTERACTION OF CLIMATE CHANGE AND METHANE HYDRATES: CLIMATE-HYDRATES INTERACTIONS (RUPPEL & KESSLER, 2017).....  | 18 |
| FIGURE 2.1 SCHEMATIC PHASE DIAGRAM FOR A WATER/HYDROCARBON/HYDRATE SYSTEM, THE SOLID CURVE IS THE THREE-PHASE-COEXISTENCE LINE.....   | 30 |
| FIGURE 2.2 THREE-PHASE (LIQUID WATER + HYDRATE + VAPOR) STABILITY CONDITIONS: (A) PERMAFROST AND (B) IN THE OCEAN (SLOAN ET.AL. 2010).....  | 32 |
| FIGURE 2.3 (A) FREE ENERGY BARRIER OF HYDRATE NUCLEATION AND CRITICAL NUCLEI SIZE AS A FUNCTION OF CLUSTER RADIUS; (B) ILLUSTRATIVE GRAPHS OF HYDRATE NUCLEATION (1), GROWTH (2), AND MASSIVE ACCUMULATION (3) PROCESSES. (KE ET AL. (2019) ..... | 36 |
| FIGURE 4.1 CATEGORIZED PHD RESEARCH IN A SNAPSHOT. ....   | 56 |

---

## List of Tables

|  |    |
|--|----|
| TABLE 1.1 DETAILS ABOUT EACH HYDRATE STRUCTURE (E. D. SLOAN & KOH, 2008).....                            | 10 |
| TABLE 2.1 SOME OF THE VARIOUS POSSIBLE ROUTES TO FORMATION AND DISSOCIATION OF NATURAL GAS HYDRATE ..... | 33 |
| TABLE 3.1 PARAMETERS FOR DIMENSIONLESS CHEMICAL POTENTIAL FUNCTIONS .....                                | 54 |

---

## Table of Contents

|   |          |
|---|----------|
| Scientific environment .....  | II       |
| Dedication .....  | III      |
| Acknowledgements.....   | IV       |
| Abstract .....  | VI       |
| Sammendrag.....   | VIII     |
| List of Publications and Contributions.....                             | XI       |
| Publications included in this thesis .....                              | XIII     |
| List of Figures .....   | XV       |
| List of Tables .....  | XVI      |
| <b>1. Background and Motivation .....</b>                               | <b>3</b> |
| 1.1. Introduction .....   | 3        |
| 1.2. What is Gas Hydrate? .....   | 4        |
| 1.3. Gas Hydrate Structure and Properties .....                         | 7        |
| 1.4. Gas Hydrate as a threat.....                                       | 12       |
| 1.4.1. Gas hydrate as a Flow Problem in industry .....                  | 12       |
| 1.4.2. Methane hydrate in nature as an emitter of CH <sub>4</sub> ..... | 15       |
| 1.4.3. The role of gas hydrate towards geohazards .....                 | 19       |
| 1.5. Gas hydrate as an opportunity .....                                | 20       |
| 1.5.1. Abundant and clean fossil fuel .....                             | 20       |
| 1.5.2. Potential for new innovative technologies.....                   | 21       |

|  |           |
|--|-----------|
| 1.5.3. CO <sub>2</sub> sequestration and methane hydrate recovery .....  | 22        |
| 1.6. <i>Motivation and purpose of this work</i> .....  | 24        |
| <b>2. Theoretical background</b> .....   | <b>26</b> |
| 2.1. <i>Equilibrium thermodynamics and the phase rule</i> .....  | 26        |
| 2.2. <i>Gibbs free energy</i> .....  | 28        |
| 2.3. <i>Kinetics of gas hydrate formation and dissociation</i> .....   | 34        |
| <b>3. Choice of Scientific Methods</b> .....   | <b>39</b> |
| 3.1. <i>Non-equilibrium thermodynamic approach</i> .....   | 39        |
| 3.2. <i>Phase Field Theory (PFT)</i> .....   | 41        |
| 3.2.1. <i>Phase Field Theory approach used in this study</i> .....   | 41        |
| 3.2.2. <i>The governing equation of the Phase Field Theory</i> .....   | 42        |
| 3.2.3. <i>High Performance computing</i> .....   | 48        |
| 3.3. <i>Heat transfer in hydrate systems</i> .....   | 49        |
| 3.4. <i>Advantages of using a uniform reference state method</i> .....   | 51        |
| 3.5. <i>Residual models for hydrate and aqueous phases</i> .....   | 52        |
| 3.5.1. <i>Residual thermodynamics for gas or liquid hydrate former phase and dissolved hydrate formers</i><br>.....                              | 54        |
| <b>4. Introduction to papers</b> .....   | <b>56</b> |
| 4.1. <i>Paper 1. Non-equilibrium aspects of hydrate and dynamic phase transition modeling</i> .....  | 59        |
| 4.2. <i>Paper 2. Phase-field theory of multi-component incompressible Cahn-Hilliard liquids</i> .....  | 60        |
| 4.3. <i>Paper 3. Impact of water and impurities on hydrate formation in natural gas pipeline</i> .....   | 60        |
| 4.4. <i>Paper 4. Effect of H<sub>2</sub>S content on thermodynamic stability of hydrate formed from CO<sub>2</sub>/N<sub>2</sub> mixtures</i> .. | 62        |
| 4.5. <i>Paper 5. Maximum tolerance for water content at various stages of a Natuna production</i> .....  | 63        |

4.6. Paper 6. Dynamics of heat and mass transport during hydrate dissociation and reformation in sediments..... 64

4.7. Paper 7. Stages in dynamics of hydrate formation and consequences for design of experiments for hydrate formation in sediments ..... 65

4.8. Paper 8. Modelling heat transport in systems of hydrate filled sediments using residual thermodynamics and classical nucleation theory..... 66

4.9. Paper 9. Why should we use residual thermodynamics for calculation of hydrate phase transitions?.. 67

4.10. Paper10. Thermodynamics of hydrate systems using a uniform reference state..... 68

**5. Conclusions ..... 70**

**6. Suggestions for further work..... 75**

6.1. Refine the physical underpinnings of the current phase field model ..... 75

6.2. Develop entirely new numerical framework: solver improvement ..... 75

6.3. Convert the standalone solver into a comprehensive PFT-based simulator ..... 76

6.4. Perform experimetns on real-life hydrate systems to validate theoretical results ..... 77

6.5. Extend thermodynamic model to other relevant hydrate formers systems ..... 77

6.6. Incorporate residual thermodynamic models into a reservoir simulator..... 77

**References ..... 78**

**7. Thesis Papers ..... 88**



# 1. Background and Motivation

## 1.1. Introduction

The main goal of this thesis was to expand our understanding of gas hydrates transitions with a closer look at long-term CO<sub>2</sub> offshore storage. This PhD study presents the results of a comprehensive multi-scale state-of-the-art modelling of hydrate systems supplemented by relevant background required to understand our methods and interpret the mechanisms involved in thermodynamics and kinetics of hydrate phase transitions under various realistic conditions.

One of the main goals of the project involved analysis of heat transport in systems that contained hydrate phases, while another part focused on the impact of parameters like gas-phase impurities and water tolerances. We have introduced and validated a generalized thermodynamic approach well suited for prediction of hydrate phase transition dynamics.

The motivation for the project which forms the background of all the studies, objectives and scope of the project and information about natural gas hydrate: history of hydrate, hydrate structures, and applications of gas hydrate are gathered in the background and motivation section that follows. Thermodynamics and kinetics of hydrate phase transitions and related theories are discussed in Chapter 2.

Chapter 3 provides a brief explanation of the scientific methods, including the Phase Field Theory for modelling of hydrate phase transition on the mesoscale, the application of rigorous thermodynamic approach to account for heat transfer during *in situ* hydrate conversion. Residual thermodynamics scheme, a physically consistent and theoretically rigorous approach, is introduced and extended in the case of multiphase

systems containing multiple hydrate phases, liquid water with dissolved hydrate formers, as well as solid phases.

The main part of this thesis is the attached publications, with the summary of the papers presented in Chapter 4, where we discuss both the evolution of the project and its goals as well as results disseminated in the publications. Chapter 5 outlines our conclusions, with suggestions for further works presented in Chapter 6.

## **1.2. What is Gas Hydrate?**

Clathrates or gas hydrates are crystalline structures resembling ice. However, they differ greatly from ice on the microscopic scale, the largest difference being that in addition to water as a host molecule, another component is needed to stabilize the water molecules, this is illustrated in Figure 1.1. These second components, often referred to as guest molecules, are completely encaged within the crystal structure of water (host). Guest molecules can be low molecular weight gases and volatile liquids. The guest molecules should not interfere with the hydrogen bonding of the lattice. In fact, they are stabilized inside the cages by van der Waals forces (Koh, et al., 2011). Examples of suitable components include methane, O<sub>2</sub>, N<sub>2</sub>, CO<sub>2</sub>, CH<sub>4</sub>, C<sub>2</sub>H<sub>6</sub>, HCl, SO<sub>2</sub>, and volatile liquids such as tetrahydrofuran and neohexane and even the noble gases Ar, Kr and Xe.



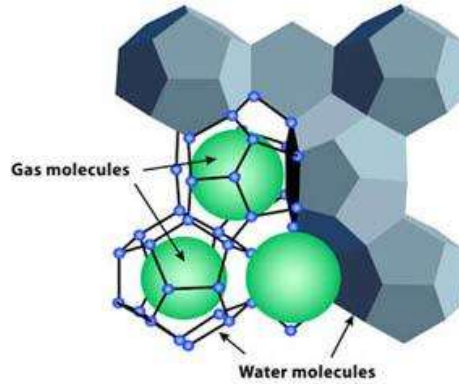


*Figure 1.1 Typical Structure of gas hydrate taken from Maslin et al (M. Maslin et al., 2010)*

Prominent scientists credited with the early discovery of gas hydrate included Sir Humphrey Davy (1810), Michel Faraday (1823), and Joseph Priestley (1778), (Makogon, 1997; Sloan & Koh, 2008). Afterwards, gas hydrate research remained mainly a scientific curiosity for more than a century. In the decades following the initial observation, gas hydrates were studied in more detail with a focus on identifying all compounds which form hydrates and describing the compounds quantitatively. If we divide the progress of gas hydrate research into three historical periods, Hammerschmidt's discovery of hydrate plugs in natural gas pipelines in 1934 marked the beginning of an industry-oriented second research period (Sloan & Koh, 2008). Since the goal was to avoid pipeline blockage, hydrate formation was of key interest in this phase.

Gas hydrates usually form at low temperatures, and since the hydrate lattice configuration of water molecules is more optimal in hydrates than ice, the melting point of a hydrate is generally higher. In addition, high pressures are generally a hydrate formation requirement as well. Thus, gas hydrates naturally occur in arctic regions,

permafrost regions, and deep-sea sediments. Given these specific thermodynamic conditions, they have been formed undesirably in the manmade environment and plugs the natural gas pipeline and are a major concern in natural gas flow assurance. Natural gas hydrates originated through two main natural phenomena. 99 % percent of the natural gas hydrates have a biogenic source and are typically dominated by methane that is formed through bio decomposition of the organic material and bacterial methanogenesis ( $\text{CH}_4$ -generating bacteria). These types of gas hydrate reservoirs can be found in 1km or upper depth of the sea, where there is more  $\text{O}_2$  access (E. D. Sloan & Koh, 2008) and (Yu F Makogon, Holditch, & Makogon, 2007), and the formed hydrates are usually structure I. Thermogenic natural gas hydrate are formed through thermal cracking of organic materials with fossil origins (very few of natural gas hydrate depositions have a thermogenic source). This process of hydrate formation would result in heavier gas components (e.g.,  $\text{C}_2$  and  $\text{C}_3 + \text{H}_2\text{S}$ ) forming the hydrate structures of I and II. The Caspian Sea and the Gulf of Mexico are examples of places with thermogenic hydrate occurrences.

More recently, the existence of natural gas hydrates as an energy resource (Yu F Makogon, Holditch, & Makogon, 2007) intensified worldwide hydrate research interest within the scientific community and energy industry. In the 1960s, Soviet scientists calculated that large quantities of methane-rich gas hydrates supposedly existed in arctic permafrost regions (Yuri F Makogon, 1965) as well as in marine sediments (Makogon et al., 1971). Following this, the first gas hydrate deposit in the Messoyakha field in Siberia was discovered by a group of geologists. Today, the only producing gas hydrate reservoir is the Messoyakha field, which confirms the possibility of economic production from gas hydrates (Collett & Ginsburg, 1998; Yu F Makogon et al., 2007). The discovery of gas hydrates was simultaneous with the energy crisis in 1970, which raised energy costs and, as a result, emphasized studies towards gas

production. Since then, large occurrences of methane hydrate have been established around the world and the possibility to produce methane from these sources has been the main driving force in hydrate research.

### **1.3. Gas Hydrate Structure and Properties**

Gas hydrates are non-stoichiometric compounds of water and gas that are mostly classified according to their lattice structure, which is dependent on local pressure and, temperature, as well as the type of gas molecule, and particularly, the diameter of the gas molecule. All hydrates are composed of repetitive crystal units composed of symmetric, spherical-like cages of hydrogen-bonded water molecules. Each cage typically contains at most one guest molecule. There are no strong chemical bonds between the guest and the host cage molecules, they are stabilized inside the cages by short-range van der Waals force or sometimes highly polar attraction dispersion forces (Sloan and Koh, 2008), and free to rotate and move within the void spaces of the lattice cage.

The bulk of hydrates commonly found in nature exist in three crystalline structures, Structure I, Structure II, and Structure H, typically referred to as sI, sII, and sH. More clathrate structure has also been identified or proposed; these other clathrate hydrates include new phases formed in laboratories at very high-pressure conditions (i.e., at pressures of around 1 GPa and higher at ambient temperature conditions) (Loveday and Nelmes, 2008; Sloan and Koh, 2008). SI and SII possess cubic symmetry, while SH structure is of hexagonal symmetry. Furthermore, SI and SII are made of two different cavity types, while SH, three types. Single crystals of these structures have been characterized using X-ray or neutron diffraction techniques.

The structure I (SI) hydrates is formed by gases with molecular diameter between 4.2 Å and 6 Å and may therefore have methane (4.36 Å), carbon dioxide (5.12), ethane (5.5 Å), and hydrogen sulfide (4.58 Å) as guests. As shown in Table 1, the SI unit cell is a cube comprising 46 water molecules and measuring 12.01 Å under the bulk of relevant conditions. SI structure is composed of six large tetradecahedron cavities and two small pentagonal dodecahedral cavities (Kvenvolden, 1993), with the large cavity made of 24 water molecules, and the small cavity, 20 molecules.

Structure II (sII) hydrates form from gases with molecules larger than ethane but smaller than n-butane (7.1 Å). It is worth noting that small molecules with a diameter less than 4.2 Å can form sII hydrates, a common example of these are hydrogen, nitrogen, Ar, and oxygen. A cubic cell of this hydrate structure will contain 136 water molecules, have the lattice constant of 17.0 Å, and be made of 16 small and 8 large cavities. The small cages in sII are similar to those found in sI ( $5^{12}$ ), while the large cages are made up of 12 pentagonal and four hexagonal faces, ( $5^{12}6^4$ ).

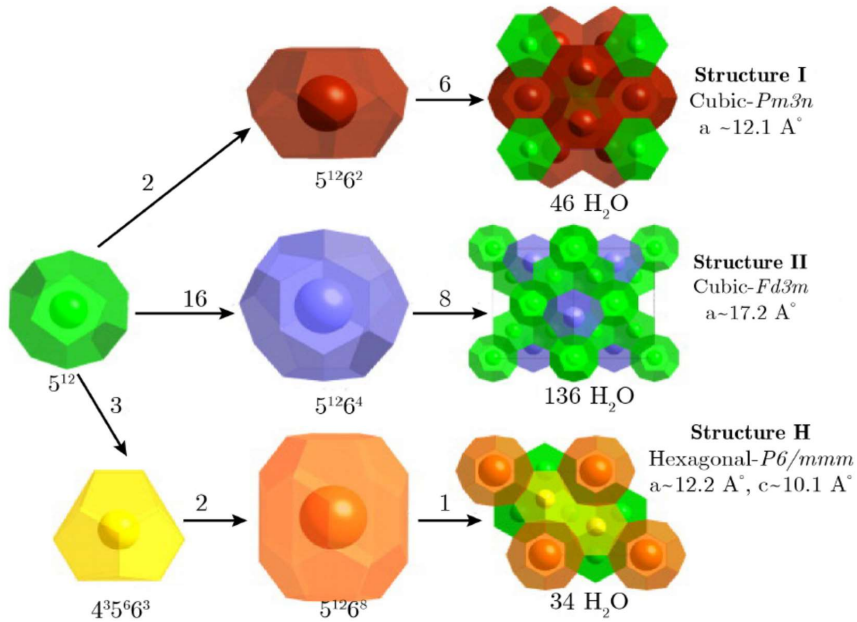


Figure 1.2 Overview of three most common hydrate unit crystal structures (Kumar & Linga, 2018)

The (sH) hydrate structure, which was not discovered until 1987 (E. D. Sloan & Koh, 2008), is able to incorporate larger hydrocarbon guest molecules with diameters between 7 Å to 9 Å in their large cavities while encaging smaller molecules in the small and medium cages. An example of this combination is methane and cyclopentane. Unlike structures I and II, the unit cell of structure sH is hexagonal. The small cages in sH are very much like their sI and sII counterparts,  $5^{12}$ ; the medium cavities are composed of three square, six pentagonal, and three hexagonal structures,  $4^35^66^3$ ; and the large cages are made up of 12 pentagonal and 8 hexagonal faces, ( $5^{12}6^8$ ).

Table 1.1 Details about each hydrate structure (E. D. Sloan & Koh, 2008)

| Hydrate structure             | SI              |                                | SII             |                                | SH              |  |                                |
|-------------------------------|-----------------|--------------------------------|-----------------|--------------------------------|-----------------|--|--------------------------------|
|                               | Small           | Large                          | Small           | Large                          | Small           | Medium                                       | Large                          |
| <b>Description</b>            | 5 <sup>12</sup> | 5 <sup>12</sup> 6 <sup>2</sup> | 5 <sup>12</sup> | 5 <sup>12</sup> 6 <sup>4</sup> | 5 <sup>12</sup> | 4 <sup>3</sup> 5 <sup>6</sup> 6 <sup>3</sup> | 5 <sup>12</sup> 6 <sup>8</sup> |
| <b>Cavities/unit cell</b>     | 2               | 6                              | 16              | 8                              | 3               | 2  | 1                              |
| <b>Cavity avg. radius</b>     | 3.95            | 4.33                           | 3.91            | 4.73                           | 3.94            | 4.04   | 5.79                           |
| <b>Radius variation (%)</b>   | 3.4             | 14.4                           | 5.5             | 1.73                           | 4.0             | 8.5  | 15.1                           |
| <b>Water molecules/cavity</b> | 20              | 24                             | 20              | 28                             | 20              | 20   | 36                             |

Eventually, it might be concluded that hydrate structure is dependent on the size of the guest molecules only. However, characteristics of things like shape and polarity and conditions of hydrate formers can have a significant impact on the hydrate stability. Normally guest molecules provide some attraction energy towards the water molecules and contribute to the stabilization of the lattice via the canonical partition functions for the different filled cavities in the hydrate structure. For most guest molecules, this is a limited short-range van der Waal type of interaction. However, for some guest molecules like H<sub>2</sub>S polarity and electrostatic interactions between water and H<sub>2</sub>S is making it a significantly better hydrate former than expected (Bjørn Kvamme &

Førrisdahl, 1993). There is, however, a limit to the degree of polarity of guest molecules it is logical that highly polar molecule will break the hydrate structure due to overly strong attraction to the water molecules, an example of such are ions and alcohols are not hydrate formers and instead are frequently used to prevent hydrate formation.

In some cases, once the second hydrate former is introduced a Complex guest size–structural relations and/or transitions may occur and affect the thermodynamic equilibrium between coexisting phases, for example, adding nitrogen to the mixture of methane and carbon dioxide hydrate ended up with structure I hydrate while Nitrogen is known to make SII.

Moreover, some hydrate formers can have more than one molecule in the same cage.as an example in nitrogen hydrates, N<sub>2</sub> stabilizes the small cavities of sII (size ratio of 0.82) and it also occupies in less degree the large (5<sup>12</sup>6<sup>4</sup>) sII cavities. At moderate pressures, in all three-hydrate structures, each cavity can contain at most one guest molecule (P. a. Y. T. N. Englezos, 1993). However, it is interesting to note that since nitrogen molecules are very small (~ 4 Å), more than one molecule can easily fit into the large cage at a pressure above 30 MPa, making multiple cage occupancy possible (Sloan & Koh, 2008).

Normally, in a fully filled hydrate of SI and SII, the mole percent of water would be about 85 %. Such a high water content would suggest similarities in the properties of hydrate and ice. However, hydrates are distinct from ice and liquid in properties like thermal conductivity, thermal expansion, and electrical conductivity, the dielectric constant of water is about 40 % higher than that of a hydrate. The latter have been used commercially as a supplement to seismic techniques for significantly with pressure due to the impact of guest molecules inside the Clathrate, the freezing point of gas hydrate is higher than that of water and critically dependent on the system pressure. This is the

reason that water following hydrocarbon flow has been a problem in the oil and gas industry, in which there are many situations of low temperatures and high pressures. The diffusion rate of hydrate is 75 times slower compared to water and hydrate are generally more elastic and stronger than the ice. Within the scope of work in this thesis, the focus is upon hydrate former methane, carbon dioxide, nitrogen, and Hydrogen Sulfide thus the main treatment will be upon structure I.

## **1.4. Gas Hydrate as a threat**

### **1.4.1. Gas hydrate as a Flow Problem in industry**

The scenario of pipeline plugging with gas hydrates will be highly system dependent. However, water is always produced alongside hydrocarbons. As in the petroleum industry where the pipeline is often filled with several liquid phases (Figure 1.3), hydrates can form on the interface between oil and aqueous phases, often on the surface of water droplets dispersed in the oil phase. As a result, they may build a solid shell around the droplet (Balakin, 2010) and since the diffusion of the gas molecule through the shell is very slow, the further conversions of water core are hindered significantly.



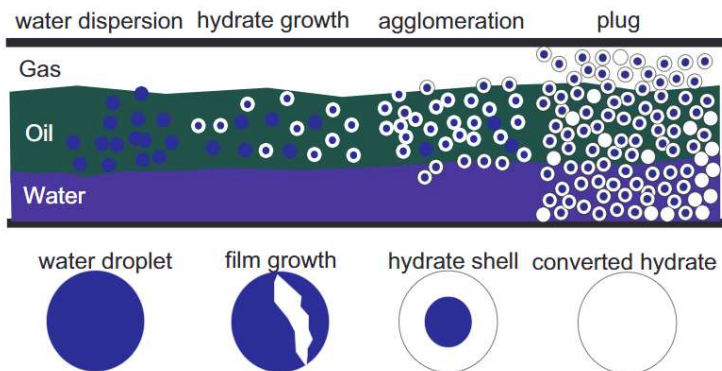


*Figure 1.3 Gas hydrate formation in liquid-dominated system. Redrawn from (Sum, Koh, & Sloan, 2009)*

While in a natural gas processing industry the hydrate-plugging scenario is different. During the processing of hydrocarbons, natural temperatures may be down to  $-22\text{ C}$  for dry gas with limited  $\text{C}_2^+$  of value and down to  $-70\text{ C}$  in plants in which the  $\text{C}_2^+$  and processing Pressure will be relatively high. Typical units of hydrate formations in such a plant are connecting pipelines, expanders, and separators. Transport of NG or  $\text{CO}_2$ -containing water through pipelines is typically at a pressure between 50 to 300 bars, and in most of these cases, water is usually in the vapor phase. During transport, the pipeline wall is often at a temperature lower than the equilibrium temperature for gas-water vapor flow. This leads to water condensation on the walls of the channel, forming a gas-liquid flow of the annular type. Hydrate formation may thus be induced on the pipeline walls. (Figure 1.4) Moreover, the formed hydrate obstruction is of a different character, as a monolith hydrate layer forms from the walls (Balakin, 2010), (Bilyushov, Bondarev, & Maron, 1988) Further water condensation on the hydrate layer makes it grow thicker, finally plugging the pipeline.

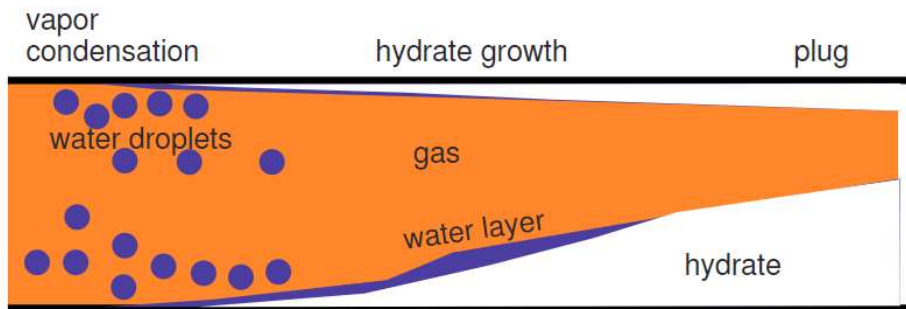


*Figure 1.4 Gas hydrate formation in gas-dominated system. Redrawn from (Musakaev, Urazov, & Shagapov, 2006).*

An additional pathway for hydrate formation in the pipeline is the presence of rust on the walls which provides water adsorption sites. Formed hydrate can partially or completely block pipelines. If the blockage is not removed quickly, then high pressure can build up inside the pipeline leading to its collapse, thus causing serious risk to the safety of operating personnel, equipment, and the surrounding environment. Besides production pipelines, (see Figure 1.5) the well and the platform are also susceptible portions of the system where hydrate plugs occur (D. Sloan, Creek, & Sum, 2011; Wei et al., 2020) It costs billions of dollars annually to the petroleum industry to prevent and inhibit hydrate formation.

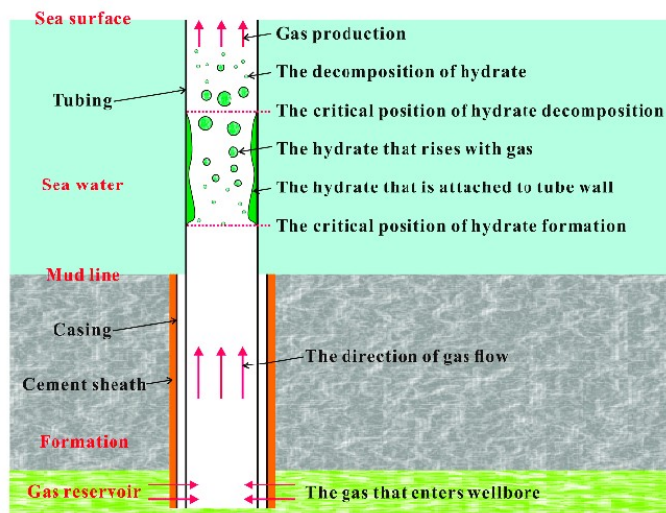


Figure 1.5 Model of hydrate formation and decomposition in offshore gas reservoir production pipeline (Wei et al., 2020)

#### 1.4.2. Methane hydrate in nature as an emitter of CH<sub>4</sub>

Methane hydrates are solid substances usually formed in nature during water and methane interaction at low temperatures of up to 15 °C and under moderate pressures of 3-12 MPa (Zhang, Wu, & Mu, 2017) and (Vysniauskas & Bishnoi, 1983). These conditions are present in sediments under the permafrost at depths between 500 and 1200 meters from the ground surface and in marine sediments directly under the seafloor (Ruppel & Kessler, 2017). However, in certain conditions, hydrates can form and remain stable at much shallower depths, even a few meters beneath the surface.

The concentration of CH<sub>4</sub>, as well as CO<sub>2</sub>, in the atmosphere, shows an increasing trend after the commencement of the industrial revolution in the period around 1750 (Ruppel & Kessler, 2017). It is difficult to figure out how much of the CH<sub>4</sub> in the atmosphere originated from human activities versus natural gas hydrate dissociation. Some researchers have estimated that, as of today, CH<sub>4</sub> from the dissociation of hydrate is

approximately 2% of the atmospheric CH<sub>4</sub> gas (Ruppel & Kessler, 2017). The Global Warming Potential (GWP) of CH<sub>4</sub> is estimated to be 21, which implies that over 100 years, one ton of released CH<sub>4</sub> to the atmosphere has 21 times more warming potential than one ton of CO<sub>2</sub> (Hope, 2006). However, the lifetime of methane in the atmosphere is significantly shorter than that of CO<sub>2</sub> because of the lower molecular weight and density of CH<sub>4</sub> (Solomon 2007), (Blasing, 2013). After a lifetime of twelve years (Anderson, 2010), CH<sub>4</sub> in the atmosphere has been transformed into CO<sub>2</sub>, which is the more commonly known greenhouse gas (Ruppel & Kessler, 2017).

According to some estimations, the amount of methane stored beneath the ocean could be in the range between 1600-2000 GtC (Archer, Buffett, & Brovkin, 2009), and the respective amount in the arctic permafrost regions could be in the range between 400 GtC (MacDonald, 1990), compared with just 760 GtC in the atmosphere. The "clathrate gun" is a hypothesis that has been proposed by several researchers due to the enormous amounts of stored gas within the gas hydrate reservoirs (M. Maslin et al., 2010), (Kvenvolden, 1993). Gas hydrates may potentially have a significant effect on future global warming (Leggett & Greenpeace, 1990). A mathematical model was used to investigate the effects of global warming on methane hydrate dissociation. According to this model, which was based on heat conduction in single and composite media, the critical required time for hydrate to start dissociation depends on the global warming scenario, the thermophysical properties of the earth, and the driving forces required for hydrate dissociation (Hatzikiriakos & Englezos, 1993). Both marine and permafrost gas hydrate deposits are sensitive to environmental changes, and they will be affected by global warming. According to IPCC (2007), by the year 2100, global mean surface temperature and global mean sea level could rise between 1.1°C and 6.4 °C and 28-79 cm or more, respectively. As stated by this prediction, warming includes both the oceans and the permafrost regions, which could end up melting a substantial amount

of gas hydrates and releasing unknown amounts of gas into the atmosphere (M. Maslin et al., 2010). Based on recent knowledge, shallow depth hydrates, which have poor reservoir qualities are more likely to be affected by the climate changes, rather than other hydrate reserves, which have the potential to be energy exploitation resources (Chong, Yang, Babu, Linga, & Li, 2016).

For example, investigations carried out in 2008 in the Siberian Arctic showed millions of tons of methane being released,(see Figure 1.6) apparently through perforations in the seabed permafrost,(Shakhova et al., 2010) This is what led to the original Clathrate gun hypothesis.

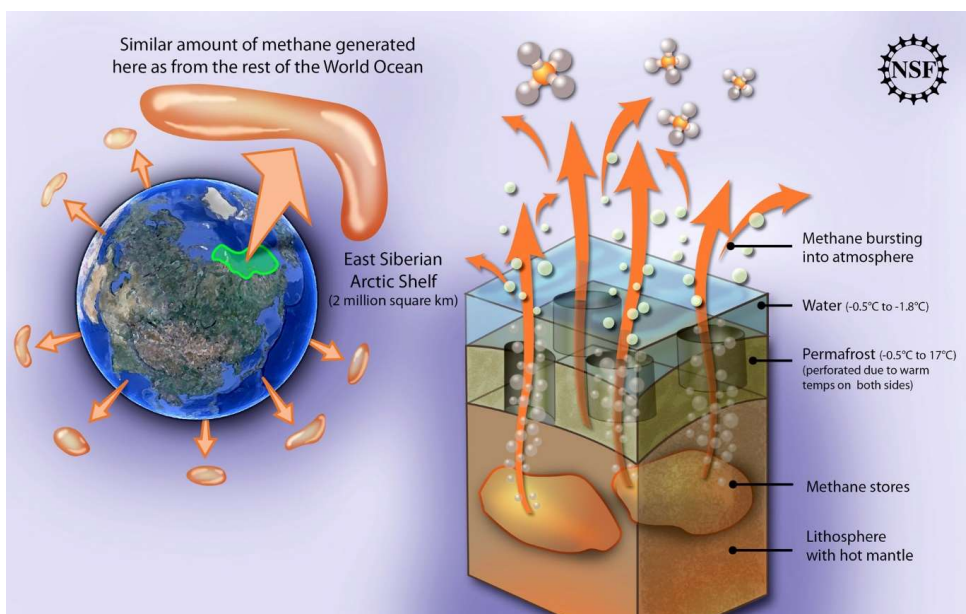


*Figure 1.6 Potential Methane release in the Eastern Siberian Arctic Shelf ("Methane Releases From Arctic Shelf May Be Much Larger and Faster Than Anticipated," 2010; Shakhova et al., 2010)*

Since hydrate stability depends on pressure and temperature, any changes which affect these two parameters will alter hydrate stability as well. Global warming, which also warms up the ocean's water, could jeopardize the stability of gas hydrates. Figure 1.7 illustrates methane hydrate stability and climate change interaction for better understanding.

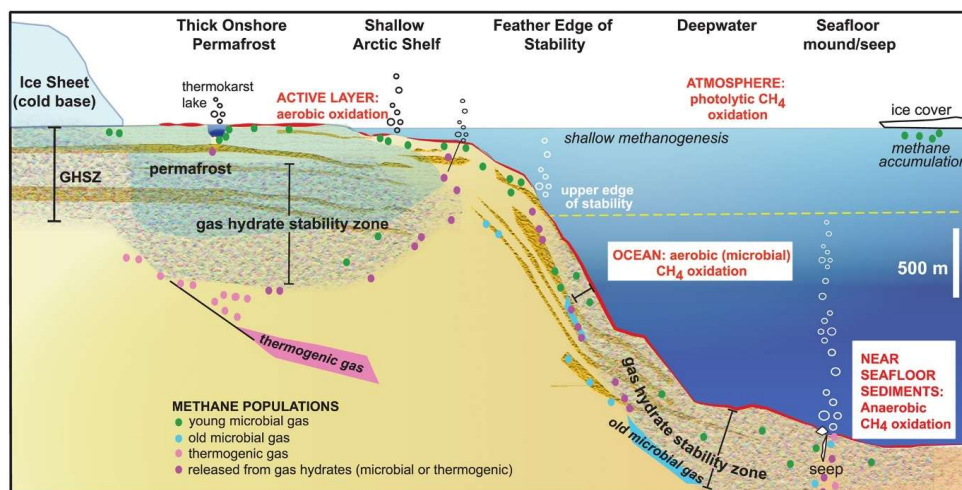


Figure 1.7 The interaction of climate change and methane hydrates: Climate-Hydrates Interactions (Ruppel & Kessler, 2017)

It has been claimed that the observed peaks in atmospheric methane in the ice core record at the end of the ice age could be related to the temperature increase, which leads to the destabilization of hydrates in the oceans. Hence, enormous amounts of gas were released into the atmosphere and caused climate change (M. A. Maslin & Thomas, 2003). Thus, Sea level rising increases hydrostatic pressure and assists the marine hydrate sediments to be more stable, while decreasing the sea level reduces hydrostatic pressure on the marine sediments, which in turn will push hydrates out of the stability conditions. Furthermore, when failure of marine sediment occurs, the weight on the underlying layers reduces. This rapid phenomenon reduces the pressure on the marine

gas hydrate sediments. Thus, hydrate can be destabilized and break down, releasing gas (M. Maslin et al., 2010). In permafrost areas, the stability of gas hydrate deposits may be affected by geographical temperature variation and sea level rising and flooding into the permafrost areas (M. Maslin et al., 2010).

Released methane gas from the seabed can dissolve in the water and change the water acidity. Corresponding methane gas release will also reduce the surrounding oxygen content, which may drastically change the marine ecology.

### **1.4.3. The role of gas hydrate towards geohazards**

It is essential to understand the geomechanical properties of hydrates in nature. McIver (McIver RD, 1978) was the first who suggested the possibility of a connection between gas hydrates and landslides. The sudden disappearance of massive hydrate deposits beneath the earth's surface can result in permafrost landslides. Gas hydrate dissociation may have contributed to submarine landslide at water depths of 1000 to 1300 m off the east coast of the United States and the Storegga slide off the east coast of Norway, as strongly suggested by (M. W. Lee & Collett, 2011) and Karstens (Karstens, Haflidason, Berndt, & Crutchley, 2023).

Hydrate presence within the pore space will affect the bulk properties of hydrate deposits. Gas hydrate formed in the porous media could act as a metastable cementing agent and help to stabilize the seabed (Kvenvolden, 1994) and (Grozic, 2010). On the other hand, the vast quantities of hydrates in marine sediments pose a geohazard and have been implicated in past climate change events Liping (Liu et al., 2019). The stability of gas hydrate is greatly dependent on the local temperature and pressure conditions but also concentrations of hydrate formers in the aqueous phases. Since gas solubility decreases with increase in temperature, global warming and temperature

change in the ocean surface water will enhance the risk of hydrate dissociation both onshore and offshore.

## **1.5. Gas hydrate as an opportunity**

### **1.5.1. Abundant and clean fossil fuel**

In addition to posing a clear environmental threat, the enormous deposits of methane gas in hydrates may be considered an unconventional future energy source and the world's largest carbon-based fuel reserve. After confirmation of the gas hydrate discovery around 1969, many attempts have been made to estimate the total amount of existing reserves of natural gas hydrates. The huge amounts of CH<sub>4</sub> that are preserved within the hydrate structures make these deposits appealing as a potential future energy source. However, there is no reliable way to predict the amount of fuel in gas hydrate deposits, (Milkov, 2004). The current amount of world hydrate reserves has been estimated to be in the range between  $2.5 \times 10^{15}$  and  $120 \times 10^{15}$  m<sup>3</sup>, which is a quite large uncertainty (Pinero, Marquardt, Hensen, Haeckel, & Wallmann, 2013), (Klauda & Sandler, 2005). But even the most conservative estimates indicate that the reserved potential energy in hydrate deposits exceeds that of all explored conventional coal, oil, and natural gas reserves (E. D. Sloan & Koh, 2008). However, these estimates are speculative since the bulk of studies into gas hydrates have focused on the number of gas reserves in place without considering if they are technically recoverable or economically feasible. Thus, there is little knowledge about the depth and location where gas hydrates can be found, as well as concerning the amount of recoverable gas. Most parts of the gas hydrate deposits are distributed offshore Bogoyavlensky (Bogoyavlensky, Kishankov, Yanchevskaya, & Bogoyavlensky, 2018), where the majority of hydrate-bearing sediments are very dispersed, with their saturation too low to be considered as a potential for gas production (Boswell & Collett, 2011; Milkov,



2004). None of the gas hydrate reserves was considered economical to recover and have been kept undocumented at present. However, it has been estimated that large in-place and highly concentrated "Chimney" gas hydrate deposits could exist. Their gas accumulation may even be higher than previous estimates, but as these reserves are usually found in mud-dominated sediment, no recovery method has ever been demonstrated (Boswell & Collett, 2011; C. Koh, Sum, & Sloan, 2012).

### **1.5.2. Potential for new innovative technologies**

Apart from using methane hydrate as a cleaner energy source, several other applications of gas hydrates are currently being investigated. The ability of gas hydrates to contain 150-180 volumes of gas per volume of hydrate (Taheri, Shabani, Nazari, & Mehdizahed, 2014) makes them be considered as a means for natural gas storage and transport. However, practical exploitation of this opportunity requires an ability to keep hydrates stable in a predictable and controllable manner (M. Yang, Zhao, Zheng, & Song, 2019). Gas storage and transportation based on hydrate technology have been a focus for many researchers (Gambelli, Rossi, & Cotana, 2022; Ge, Li, Zhong, & Lu, 2022; Masoudi & Tohidi, 2005; Wang, Sum, & Liu, 2021). Specifically, storing hydrogen molecules in semi-clathrate hydrates with an energy density comparable to that of current fossil fuel has become an opportunity for hydrogen-powered vehicles (Veluswamy, Kumar, & Linga, 2014) (Davoodabadi, Mahmoudi, & Ghasemi, 2021), (Saikia T, Patil S, & A., 2023).

Gas hydrates can also be used for flue gas separation. It was demonstrated that by exploiting the differing affinities of gases towards hydrate formation, one may achieve good separation efficiency by allowing gaseous mixtures to form hydrates. NO<sub>x</sub> gases, carbon dioxide, and hydrogen sulfide can thus be separated from methane through hydrate formation.

Freshwater scarcity is one of the world's major challenges. In many countries with low precipitation and limited or no water resources, seawater desalination is enormously important for freshwater generation (Khan, Lal, Mohamad Sabil, & Ahmed, 2020). At the same time, these countries often have oil and gas processing plants producing a large volume of wastewater ("produced water", PW) which is mostly higher in salinity compared to seawater and is considered the largest byproduct of the oil and gas industry (Lianna et al., 2016). Thus, gas hydrate-based desalination (HBD) method has received considerable attention since being proposed in the 1960s (Hong, Moon, Lee, Lee, & Park, 2019; H. Lee et al., 2016). Each volume of gas hydrate contains 0.8 volumes of freshwater. In addition, gas hydrate formation will exclude all solids, dissolved salts, and most organic components contaminating the aqueous solution; therefore, all the impurities can easily be separated and eliminated.

While the research conducted so far have mostly focused on carbon dioxide (CO<sub>2</sub>), cyclopentane, and refrigerant/Freon as a hydrate former in the hydrate-based desalination (Cha & Seol, 2013; H. Lee et al., 2016; Maniavi Falahieh, Bonyadi, & Lashanizadegan, 2021), there have been certain other equivalent methods based on CNG (Fakharian, Ganji, & Naderifar, 2017) which eventually melted to yield fresh water and methane gas. However, according to (Javanmardi & Moshfeghian, 2003) the operational economy of hydrate-based desalination technology is driven by numerous factors such as the presence of salt content, seawater temperature, the mobility of salt, and yield obtained. Finding the optimum methodology still requires considerably greater academic research and pilot studies.

### **1.5.3. CO<sub>2</sub> sequestration and methane hydrate recovery**

Carbon dioxide (CO<sub>2</sub>) contributes to approximately sixty-four percent (64%) of the greenhouse gas emission (Edvward Bryant, 1997), with anthropogenic activities

accounting for over 6 gigatons per year (Gt/yr) (Desideri & Paolucci, 1999). One of the key environmental challenges today is to mitigate CO<sub>2</sub> emissions into the atmosphere. Various techniques, such as chemical absorption in amines Meisen (Chakma, 1997; Hack, Maeda, & Meier, 2022; Meisen & Shuai, 1997), can capture CO<sub>2</sub> from different sources, followed by its sequestration in geological formations and oceans (Chatti, Delahaye, Fournaison, & Petitet, 2005), (Bachu, 2002; Hendriks & Blok, 1995).

CO<sub>2</sub> hydrates can form at depths of 500 to 900 meters in seawater rich in CO<sub>2</sub> (Kojima, Yamane, & Aya, 2003). Due to their higher density compared to seawater (Holder, Cugini, & Warzinski, 1995), CO<sub>2</sub> hydrates tend to sink to the bottom of the deep sea, where long-term stability can be achieved (Harrison, Wendlandt, & Dendy Sloan, 1995; S. Lee et al., 2003). However, subsea sequestration of CO<sub>2</sub> is still under experimentation (Chatti et al., 2005), highlighting the need for further research on CO<sub>2</sub> solubility (Kojima et al., 2003) kinetics of CO<sub>2</sub> hydrate formation (Circone et al., 2003; P. Englezos, 1992) , and the stability of CO<sub>2</sub> hydrates (Harrison et al., 1995; Kang & Lee, 2000).

The storage of CO<sub>2</sub> in natural gas hydrate reservoirs combined with release of methane trapped in the hydrate state could be considered a win-win scenario (Lee, Seo, Seo, Moudrakovski, & Ripmeester, 2003) This technique is discussed extensively in the rest of this thesis.

To summarize, by offering fuel for the future, means for transport and storage of natural gases, carbon dioxide and hydrogen, flue gas separation and desalination of seawater, gas hydrates present great opportunities as well as technological challenges.

## 1.6. Motivation and purpose of this work

The continuing growth of energy demands for industrial development needs, along with escalating human population, have resulted in anthropogenic carbon dioxide emissions. This alarming increase in carbon dioxide concentration from about 280 ppm (part per million) to over 450 ppm is believed to have caused significant climate change and global warming (Bierwirth, 2018; Kabir et al., 2023). As the world's need to use fossil fuel as the major energy source is foreseen for at least two more decades, Novel approaches should be developed to combat this environmental problem successfully. As discussed in the previous section, a significant number of gas hydrate deposits exist both onshore and offshore worldwide; their exploitation is rapidly becoming more and more appealing as an energy source since methane combustion results in lower CO<sub>2</sub> release than other fossil fuels.

Moreover, a strong focus on reducing CO<sub>2</sub> emissions during the latest two decades has also encouraged rapid development of various of putting CO<sub>2</sub> to use, like enhanced oil recovery. Given the overwhelming abundance of methane sequestered in gas hydrate deposits, the use of CO<sub>2</sub> to produce natural gas hydrate becomes yet another possibility. The exchange between CH<sub>4</sub> hydrate and CO<sub>2</sub> hydrate provides a win-win scenario of methane production combined with simultaneous safe CO<sub>2</sub> storage in the form of hydrate.

Another area where hydrate phase transition dynamics become relevant is the transport of CO<sub>2</sub> in pipelines, which is a routine process in offshore Norway and many places worldwide. Given the high pipeline pressures and low seafloor temperatures on the seafloor (typically below 6 °C), residual water present in the CO<sub>2</sub> stream may drop out via condensation in bulk or adsorption on rusty pipeline walls, subsequently form a hydrate.

The examples presented above present just a few practical scenarios that promote gas hydrate thermodynamics and kinetics studies. So far, both physics and mathematics used to model hydrate phase transitions have been oversimplified, and all based on the equilibrium approach. All available academic and commercial hydrate simulators consider independent thermodynamic variables (only temperature and pressure to evaluate energy processes, neglecting the phase transition dependencies on concentration. In comparison, concentration in all phases is one limitation expected to have varying implications over the lifetime of a hydrate and choosing a single route for hydrate phase transitions and ignoring any other possible options.

The objective of this work was to understand and model hydrate nonequilibrium systems at time scales varying from nano- to microseconds. We have used a novel thermodynamic approach capable of calculating free energies of the various co-existing phases and thus predicting the thermodynamic impact of specific essential phase transitions often omitted by other calculation schemes. Our approach combines Classical Nucleation Theory (CNT), Molecular Modeling, and Phase Field Theory to evaluate many different aspects of hydrate formation and stability. Besides providing these insights, thermodynamic and kinetic approaches shown and applied throughout this thesis can provide a deep theoretical understanding of hydrate phase transitions and kinetics and significant potential for further modification and applications.

## 2. Theoretical background

### 2.1. Equilibrium thermodynamics and the phase rule

The first law of thermodynamics is the principle of energy conservation applied to thermodynamic processes. This law deals with the quantity of energy of a system as a function of supplied and exported energy to/from the system in the form of heat or work. For a thermodynamic process in closed system without motion, differential form of the first law is often formulated as below (Smith, Van Ness, Abbot, & Swihart, 2005):

$$dU = dQ + dW \quad (2.1)$$

where  $U$  stands for internal energy,  $Q$  is heat, and  $W$  is work done by the system or on system. Equation (2.1) is the ultimate source of all properties relations that connect energy to measurable quantities. Note that the sign convention used here is recommended by International Union of Pure and Applied Chemistry, however the original choice of sign for work in the earlier edition of thermodynamics textbook was the opposite (Smith et al., 2005)

However, to guarantee that a process will occur, we need the second thermodynamic law to complete the first law. The second law of thermodynamics establishes the concept of entropy as a physical property of a thermodynamic system. The total entropy of an isolated system increases over time; entropy phenomena account for the irreversibility of the processes. Another interpretation would be that the second law puts constraints on the direction of changes and the degree of degradation of energy during a process. A thermodynamic process cannot occur unless it satisfies both the

---

first and the second laws of thermodynamics, thus the second law of thermodynamic states that in a closed system:

$$TdS \geq dQ \begin{cases} \Leftrightarrow \text{Reversible} \\ >\Leftrightarrow \text{Irreversible} \end{cases} \quad (2.2)$$

where T is temperature and S stands for entropy, The combined expression for the first and second laws of thermodynamics yield

$$dU - TdS - dW \leq 0$$

The above relation will also hold for non-reversible changes in a system of uniform temperature and pressure at constant composition (Prausnitz, Lichtenthaler, & De Azevedo, 1998) If our system of interest allows for matter transfer or have chemical reactions, the composition of the chemical components in an open system of consistent temperature and pressure can also change so that this fundamental thermodynamic relation can be generalized to:

$$dU \leq Tds - Pdv + \sum_i^n \mu_i dN_i \quad (2.3)$$

Where the chemical potential  $\mu_i$  of species i (atomic, molecular, or nuclear) is defined, as all intensive quantities are, expressed and held for both reversible and irreversible processes, the sum runs over all the components,  $i$ , in a specific phase, T is temperature, P is pressure, and  $N_i$  is the number of molecules.

## 2.2. Gibbs free energy

The Gibbs free energy of a system is a state function because it is defined in terms of thermodynamic properties that are state functions. So, to say it is used to predict whether a chemical process is spontaneous or non-spontaneous. (Prausnitz et al., 1998)

$$G(P, T) \equiv U + PV - TS \quad (2.4)$$

Following the second law of thermodynamics in a homogeneous open system, the total Gibbs free energy of a system will always strive toward minimum energy as function of temperature, pressure, and distribution of N components:

$$dG \leq 0 \quad (2.5)$$

$$dG \leq SdT - VdP + \sum_i^n \mu_i dN_i \quad (2.6)$$

This equation shows that for a system that is not in equilibrium, the Gibbs energy will continuously decrease, and when it is in equilibrium (i.e., no longer changing), the infinitesimal change  $dG$  will be zero. This will be true even if the system is experiencing any number of internal chemical reactions or experiences matter transfer on its path toward equilibrium.

There is a general natural tendency to achieve a minimum of the Gibbs free energy.



Eventually, a system always strives toward the lowest Gibbs free energy, and it is not possible to reach equilibrium each time. **phase rule** provides the theoretical foundation, based on thermodynamics, for characterizing the state of a system and predicting the equilibrium relations of the phases (solids, liquids, vapors) and given by:

$$F = n - \pi + 2 \quad (2.7)$$

$F$  is the number of variables needed to define system (degree of freedom),  $n$  is the number of components and  $\pi$ , the number of phases. This means that a simple composite system, without any chemical reactions, will possess  $n + 2$  independent variable intensive properties, which are referred to as degrees of freedom.

As an example, hydrate can form in a homogenous system in a laboratory containing gas molecules dissolved in water in this case  $n=2$  (guest and water),  $\pi = 2$  (hydrate phase and aqueous phase) so we will have 2 degrees of freedom, literally in industrial applications pressure and temperature are usually specified and controlled so the system can reach equilibrium.

However, this rarely happens outside of the laboratory for example, for a most straightforward hydrate system containing guest molecules and water in the gas phase, aqueous phase, and hydrate phase, having three phases, which leaves us one degree of freedom and as temperature and pressure are given the system will be overdetermined and will never reach equilibrium. However, the system still tries to reach the lowest energy possible, and this will lead to hydrate reorganization while large and thick regions compete with more thin regions in a stability limit. (B Kvamme, Graue, Buanes, Kuznetsova, & Ersland, 2007).

Hydrates are not stable at all ranges of pressure and temperature; while other driving forces of hydrate phase transitions will be presented later, we can start with the pressure and temperature projection of the general phase diagram. Hydrate stability is usually illustrated by analyzing the phase diagram of water, hydrate, and gas (hydrocarbon) mixtures, qualitatively presented in Figure 2.1.

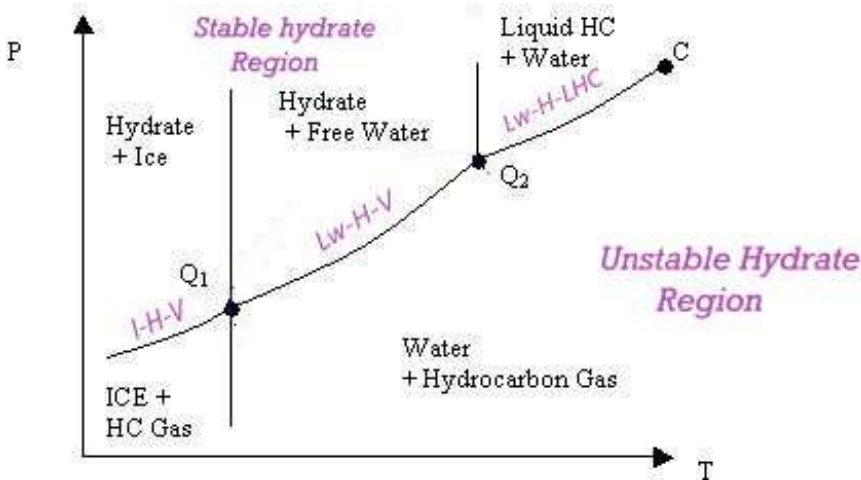


Figure 2.1 Schematic phase diagram for a water/hydrocarbon/hydrate system, the solid curve is the three-phase-coexistence line

Thus, any T and P combinations to the left of the three-phase-coexistence line can be considered as a stable hydrate region, so if we move toward the right side region by lowering pressure or increasing temperature, the hydrate will be unstable and dissociate eventually.

Using the phase diagram makes it possible to predict where hydrates can form below the deep-sea sediment and permafrost regions (see Figure 2.2). The possibility of hydrate occurrence will be determined by the temperature and pressure conditions of

specific regions. Pressure in hydrates is expected to change depending on the load from the earth crust layers above them. This provides a limited depth range suitable for hydrate formation according to the hydrate stability curve. However, the existence of different geothermal gradient illustrated in Figure 2.2 is likely to have a far more significant effect on hydrate stability.

A somewhat different scenario will occur in the case of marine hydrates. The hydrothermal gradient in the oceanic water has a negative slope (i.e. temperature decreases with the sea depth), while turning positive in the sediments below. This will result in a large region above the sea floor where temperature and pressure conditions formally allow for hydrate existence. Typical seawater methane concentration is significantly lower than the solubility limit, making chemical potential of dissolved  $\text{CH}_4$  close to its infinite dilution value, which is typically substantially lower than the chemical potential of  $\text{CH}_4$  guest in hydrate. As a result, any hydrate that may start to form above the sea floor will dissociate almost immediately.

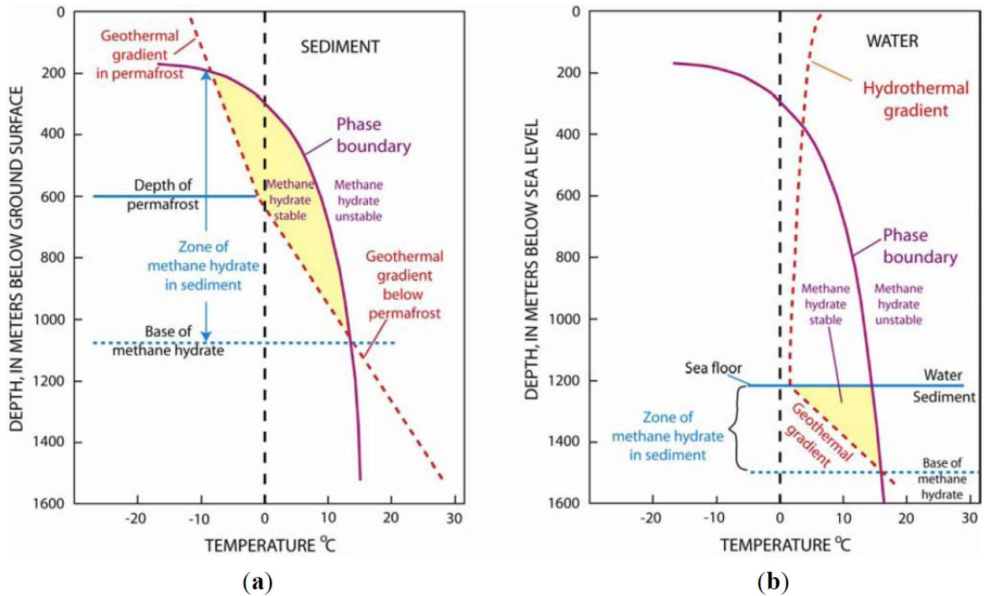


Figure 2.2 Three-phase (liquid water + hydrate + vapor) stability conditions: (a) permafrost and (b) in the ocean (Sloan et al. 2010)

As mentioned earlier, temperature and pressure are not the only driving forces for hydrate formation and dissociation. For example, another parameter, which is less discussed in the literature, is the concentration of hydrate formers in the media. The concentration of hydrate formers should also be sufficient to allow hydrate formation. In the analysis of hydrate systems, it is usually assumed that hydrate formers are available in abundance, and concentration requirement is assumed to be satisfied. Hydrate formation and dissociation can be reached via following various pathways; for example, hydrate can form from liquid water or ice while hydrate formers are in the gas phase. In other conditions, hydrate formers dissolved in the water can promote hydrate formation as well as hydrate former absorbed on mineral surfaces. Table 2.1 presents a summary of the alternative routes to hydrate formation and re-dissociation relevant for hydrate in sediment and pipeline transport of natural gas.

*Table 2.1 Some of the various possible routes to formation and dissociation of natural gas hydrate*

| $\delta$ | Initial phase(s) |                     | Driving force   | Final phase(s)      |
|----------|------------------|---------------------|---|---------------------|
| 1        | -1               | Hydrate             | Outside stability in terms of local P and/or T  | Gas, Liquid water   |
| 2        | -1               | Hydrate             | Sublimation (gas under saturated with water)  | Gas                 |
| 3        | -1               | Hydrate             | Outside liquid water undersaturated with respect to methane and/or other enclathrated impurities originating from the methane phase           | Liquid water, (Gas) |
| 4        | -1               | Hydrate             | Hydrate gets in contact with solid walls at which adsorbed water have lower chemical potential than hydrate water                             | Liquid water, Gas   |
| 5        | +1               | Gas/fluid           | Hydrate more stable than water and hydrate formers in the fluid phase   | Hydrate             |
| 6        | +1               | Gas + Liquid water  | Hydrate more stable than condensed water and hydrate formers from gas/fluid   | Hydrate             |
| 7        | +1               | Surface reformation | Non-uniform hydrate rearranges due to mass limitations (lower free energy hydrate particles consume mass from hydrates of higher free energy) | Hydrate             |
| 8        | +1               | Aqueous phase       | Liquid water super saturated with methane and/or other hydrate formers, with reference to hydrate free energy                                 | Hydrate             |
| 9        | +1               | Adsorbed            | Adsorbed water on rust forms hydrate with adsorbed hydrate formers  | Hydrate             |
| 10       | +1               | Adsorbed + fluid    | Water and hydrate formers from gas/fluid forms hydrate  | Hydrate             |

$\delta$  is the sign of free energy change involved in hydrate phase transition, in which value 1 indicates favorable formation and -1 dissociation.  $i$  is just a phase transition index.

### **2.3. Kinetics of gas hydrate formation and dissociation**

As it was indicated in the previous section above, gas hydrates in industrial applications and in nature are unable to reach thermodynamic equilibrium due to the Gibbs phase rule and dynamic nature of the environment. Hydrate formation and dissociation present a multi-phase puzzle with the Gibbs free energy changes determining phase distribution under certain mass and heat transport constraints. Since pressure and temperature provide only a two-dimensional projection of all independent thermodynamic variables, concentrations of hydrate formers and water in all the co-existing phases will become additional independent thermodynamic variables that must be accounted. Every section of a hydrate-filled reservoir is unique and exists in a steady-state balance governed by many factors. Fluxes of hydrocarbons coming from below will encourage the formation of new hydrates, while the inflow of seawater through the fractures will lead to hydrate dissociation. Mineral/fluid/hydrate interactions and geochemistry are among the many other factors determining the local hydrate saturation inside reservoir pores. Even when an actual sediment sample obtained from reservoir coring is analyzed in a laboratory, it would still be impossible to reproduce all reservoir conditions.

Many factors govern the formation and dissociation of hydrate; however, free energy can be considered as the most critical one; in general, the phase with lower Gibbs free energy is more stable this means if Gibbs free energy of hydrate phase is lower than the parent phase (water and hydrate former) hydrate will forms. These processes are very complex and require a more profound understanding.

Since hydrate is a crystal structure, we can use theories of crystal growth as the basic; based on this theory, the formation of crystal is generally a three-step process involving (1) nucleation, (2) growth (unstable and stable growth phase), followed by (3)

---

induction. Nucleation is a random microscopic phenomenon in which small clusters of water and hydrate former make a new phase that can have irreversible growth to large macroscopic size. However, two main competing processes are involved: first, the benefits of the stable crystalline phase, and second, the work penalty associated with pushing the surroundings out to get some space. After Nucleation, the crystal will enter in the process of unstable growth until the critical cluster size is reached; note that this phase transition only occurs because Gibbs free energy is lower in the new-formed phase. In order to illustrate this mechanism, we can use classical nucleation theory (CNT), thus the associated free energy change ( $\Delta G$ ) will be given by:

$$\begin{aligned}\Delta G &= \Delta G_s + \Delta G_v \\ &= \gamma_{interface} A^H + \Delta G^{Phase\ Trans} \rho_N V^H\end{aligned}\tag{2.8}$$

Where terms  $\Delta G_s$  and  $\Delta G_v$  correspond to the surface free energy and volume free energy, respectively;  $\gamma_{interface}$  is the interface free energy,  $\rho_N$  is molar density, and  $V^H$  is the molar volume of hydrate. the interface free energy ( $\Delta G_s$ ) is the minimum work required to create the interface,  $A^H$  is the cross-sectional contact area between hydrate and parent phases. The term  $\gamma_{interface} A^H$  can be called the penalty, which is the energy used to push away parent phases (water and hydrate formers). While  $\Delta G^{Phase\ Trans} \rho_N V^H$  is the benefit of the phase transition. If the benefit of the phase transition overcomes the penalty of expansion, the critical size and shape of the core will transition over to stable growth.

Schematics of hydrate growth nucleation and post-nucleation are illustrated in (Figure 2.3b) It is difficult to set a precise boundary between nucleation and initial growth, since both take place at the molecular level. On the other hand, it may be

straightforward to detect macroscopically the point of hydrate onset and observe the subsequent massive hydrate formation.

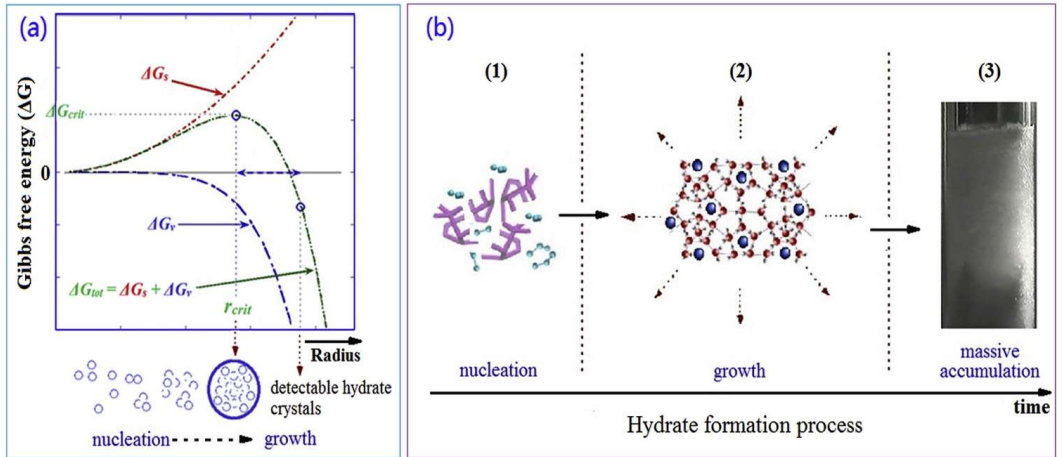


Figure 2.3 (a) Free energy barrier of hydrate nucleation and critical nuclei size as a function of cluster radius; (b) Illustrative graphs of hydrate nucleation (1), growth (2), and massive accumulation (3) processes. (Ke et al. (2019))

The time needed to overcome the balance between penalty and the gain term, the time is taken for crystal nuclei to form, is called nucleation time and often is too difficult to observe experimentally. Sloan (C. A. Koh, Sloan, Sum, & Wu, 2011)

Critical size is a turning point to stable growth process assuming a simple geometry (e.g., ellipse or sphere) for hydrate core, and the critical radius can be easily found through differentiation of equation below with respect to the radius of the sphere,

$$\Delta G = \gamma_{interface} 4\pi r^2 + \Delta G^{Phase Trans} \rho_N \frac{4}{3} \pi r^3 \quad (2.9)$$

the critical size of a sphere will be:



$$r^{crit} = \frac{-2\gamma_{interface}}{\Delta G^{Phas\ Trans} \rho_N} \quad (2.10)$$

As shown in Figure. 2.3a, the sum ( $\Delta G_{tot}$ ) of surface excess free energy ( $\Delta G_s$ ) and volume excess free energy ( $\Delta G_v$ ) is a function of cluster radius ( $r$ ) and will reach a peak at point 1. At this peak and point 1 the derivative of  $\Delta G_{tot}$  as a function of nuclei radius equals zero ( $\frac{\delta \Delta G_{tot}}{\delta r} = 0$ ). The energy level at this peak is considered to be the energy barrier for hydrate nucleation ( $\Delta G_{crit}$ )

There exist two types of nucleation, homogenous and heterogenous; homogeneous nucleation happens when all the hydrate components are extracted from a single uniform phase, for instance, hydrate forming from an aqueous phase and gas dissolved in the water. On the other hand, heterogeneous formation occurs at the interface between two phases, heterogenous nucleation can also occur on solid surfaces from adsorbed water and adsorbed hydrate former. In a non-laboratory environment in industry and nature, homogenous nucleation seldom occurs; however, it will give us good insight into the concept.

The stable growth or massive growth phase of hydrate is considered as induction, and the time it takes for the first detectable onset of massive growth is called induction time. This stage is not a physically well-defined process since actual induction time is system-dependent and depends on what method is used for detecting that point (pressure change, laser, and visual) (Sloan & Koh, 2008). Many empirical and semi-empirical industrial models have been developed to predicate the induction time and massive growth rate) that still need to be improved profoundly to provide more actual results.



### 3. Choice of Scientific Methods

This chapter presents both the fundamental concepts of statistical thermodynamics as well as arguments in favor of our chosen thermodynamic approaches and schemes presented in the papers, with the emphasis on:

- Non-equilibrium thermodynamics as the only physically valid approach to evaluation of hydrate phase transitions
- Details on phase field theory and model application relevance in the context of High-Performance Computing
- The importance of including heat transfer for analysis of processes governing phase transitions in gas hydrate systems
- Residual systems thermodynamics as our method of choice for calculation of vapor-liquid equilibria

#### 3.1. Non-equilibrium thermodynamic approach

As discussed in the previous chapter, hydrates in nature can form in gaseous, aqueous, and adsorbed phases. The specific phase that the hydrate originates from will determine its filling fractions, chemical potentials, and density, giving rise to distinct hydrate phases. Due to too many phases involved, the Gibbs phase rule will prohibit the hydrate system from ever reaching equilibrium, thus keeping it in a non-equilibrium state. In this situation, assessing the behavior of complex hydrate systems can be done efficiently through the Gibbs free energy minimization scheme (Tóth, Pusztai, & Gránásy, 2015) With pressure and temperature fixed, a system will strive towards the minimum of Gibbs free energy (Callen, 1985). Furthermore, as illustrated in Table (3-1), the second law of thermodynamics will decide the direction of phase transitions.

Under local constraints of access to mass and heat transport, the most stable hydrates will form first, with the local concentrations in the existing phases readjusting themselves to yield the lowest possible free energy. This process will result in the competition between various hydrate formers, and a sequence of formation, dissociation, and reformation of different hydrate phases, including a non-equilibrium process of hydrate dissociation when in contact with aqueous phases undersaturated with respect to hydrate guests.

Non-equilibrium systems can be effectively analyzed using more advanced theoretical approaches like the Multicomponent Diffuse Interface Theory (MDIT) (Bjørn Kvamme, 2002a, 2003) , where the estimation of kinetic rates is based on changes in structure, or the Phase Field Theory (PFT) (Tegze et al., 2006) where both variations in structure and Helmholtz free energy are taken into account. Still, there are advantages to using a simple technique like the classical nucleation theory (CNT), since it presents a more intuitive and straightforward distinction between the competing factors, the importance of coupled mass transport and thermodynamic control of kinetics, while emphasizing the fact that hydrate nucleation is indeed a nano-scale phenomenon. CNT makes it easier to understand the multitude of hydrates that can form in a real system, in addition to presenting a better insight into critical nuclei sizes and nucleation times (Tegze et al., 2006).

The CNT equations are simple enough to implement directly into hydrate risk evaluation software and reservoir simulators, our in-house simulator being a good example of the latter. Moreover, previous hydrate kinetics research performed in this group have successfully used MDIT (Bjørn Kvamme, 2002b) and PFT (K Baig, 2009; B Kvamme, Baig, Qasim, & Bauman, 2013; Bjørn Kvamme, Qasim, Baig, Kivelä, & Bauman, 2014; M Qasim, Baig, Kvamme, & Bauman, 2012; M Qasim, Kvamme, & Baig, 2011; Svandal et al., 2006) thus providing the groundwork for our own analysis.

## **3.2. Phase Field Theory (PFT)**

### **3.2.1. Phase Field Theory approach used in this study.**

Phase transitions between solid, liquid, and gaseous phases are a complex phenomenon involving a multitude of factors, with heat and mass exchanges across different interfaces playing a crucial role. Understanding the key processes governing the evolution of these systems will require isolating and investigating their mechanisms on temporal and spatial scales spanning from nano to micro levels. It is widely recognized that predicting the changes in relevant local parameters such as super and under saturation in response to the variation of independent thermodynamic variables (temperature and pressure) requires a multi-scale dynamic model. (Ishii & Hibiki, 2010)

Density functional theory (DFT) (Mathews, Daghash, Rey, & Servio, 2022; Politzer & Seminario, 1995) states that phase transition kinetics will be proportional to the changes in structures over the phase transition boundaries. Since structure is directly linked to free energy, it might be more convenient to use changes in free energy directly. This is the basis for Phase Field theory (PFT) (Provatas & Elder, 2011). Molecular dynamics simulations and other theoretical methods can link these two theories even tighter through the shape of the interface and corresponding concentration profiles of the interface, as well as through estimates of interface free energies. Phase Field theory (PFT) can be considered as free energy minimization under the constraints of mass and heat transport dynamics. Molecular structures are uniquely linked to corresponding free energies via statistical mechanics (for details see (Huang, 2008; Provatas & Elder, 2011; C. N. Yang, 1988).

---

PFT uses free energy change directly as the driving force for the evolution of phase change transition therefore it is required to use appropriate description of non-equilibrium thermodynamics.

### 3.2.2. The governing equation of the Phase Field Theory

We will follow (Wheeler, Boettinger, & McFadden, 1992) and various PhD theses from this group (Muhammad Qasim, 2012; Svandal, 2006; Svandal et al., 2006) (Khuram Baig, 2017) (Bauman., 2015) to outline the phase field theory approach as applied to binary mixtures. Consider an isothermal solution of two different components A and B which may exist in two different phases contained in a fixed region. In the case of hydrates, component A is water, and component B is a guest molecule. Within the scope of this work B could then be CO<sub>2</sub> or CH<sub>4</sub> in either gas, liquid, or fluid state. The solid state is represented by the hydrate and an aqueous solution represents the liquid phase. The solidification of the new solid phase is described in terms of the scalar phase field  $\phi(x, t)$  and the local solute concentration of component B denoted by  $c(x, t)$ . The field  $\phi$  is a structural order parameter assuming the values  $\phi = 0$  in the solid and  $\phi = 1$  in the liquid. Also note that this concentration formulation does not distinguish between densities of the liquid water phase and the hydrate phase. Given that the water density difference between hydrate and liquid water is roughly 10%, the difference was considered not be critical in the cases When hydrate dissociation is slow enough for the hydrate former to dissolve directly into surrounding water. Intermediate values of  $\phi$  correspond to the diffuse interface between the two phases. The starting point of the model is a free energy functional,  $F$ , given in qualitative terms by:

$$F = \int d^3r [\{f_{thermal\ fluctuation}\} + \{f_{components}\} + \{f_{bulk}\}] \quad (3.1)$$

where the free energy density integration is performed over the system volume.  $f_{thermal\ fluctuation}$  is the fluctuation of thermal energy at the interface,  $f_{components}$  is the change of free energy related to capillary waves of components across the interface, and  $f_{bulk}$  represents the density of the bulk phase as a function of phase and concentration, yielding the following

$$F = \int d^3r \left( \frac{\varepsilon_\phi^2 T}{2} |\nabla\phi|^2 + \frac{\varepsilon_c^2 T}{2} |\nabla|^2 + f(\phi, c) \right) \quad (3.2)$$

where  $\varepsilon_\phi$  is proportional to interface thickness, and the gradient term correction  $\nabla\phi$  ensures higher free energy at the diffuse crystal – liquid interface between the phases.

Rather than treating the phases as ideal solutions (as is the norm for binary alloys), the hydrate system thermodynamics is handled more rigorously following (Bjorn Kvamme & Tanaka, 1995) (see references wherein for exact free energy equations). Since the solution of the subsequent differential equations following from eq. (3.2) eventually requires minimization of free energy under constraint of mass transport, it is desirable for all thermodynamic properties to have a consistent reference state like ideal gas.

The normal expression for free energy of bulk  $f(\phi, c)$  can be safely approximated by

$$f(\phi, c) = WTg(\phi) + (1 - p(\phi))g_s + p(\phi)g_L \quad (3.3)$$

Where  $g_s$  and  $g_L$  are free energy of the solid and liquid phase respectively, phase field switches on and off the solid and liquid contributions through the probability function which is related to the shape of interfacial energy profile and has been found by

---

molecular dynamic simulation for hydrate to be  $p(\phi) = \phi^3(10 - 15\phi + 6\phi^2)$ , where  $p(0) = 0$  and  $p(1) = 1$ .

The quadratic function  $g(\phi) = \phi^2(1 - \phi)^2 / 4$  ensures a double well form for the  $f(\phi, c)$  function, and  $W$  provides a free energy scale  $W = (1 - c)W_A + cW_B$ , where  $g(0) = g(1) = 0$ . While concentration  $c$  most often used in the phase field literature is expressed in the mass units, our approach was to use the mole fraction of component  $B$ ,  $c = n_B / (n_A + n_B)$ . Under the assumption of constant molar volume, mole fraction,  $c$ , and molarity,  $c_v$ , are related by  $c = c_v v_m$ , where  $v_m$  is the average molar volume. In order to derive a kinetic model, we assume that time evolution of our system will involve monotonic decline in its total free energy. Since the phase field is not a conserved quantity, the simplest form for the evolution that ensures a minimization of the free energy will be given by

$$\dot{\phi} = -M_\phi \frac{\delta F}{\delta \phi} \quad (3.4)$$

where  $M_\phi$  represents the always positive phase field mobility whose composition dependence could be approximated as linear superposition of individual component mobilities  $M_\phi = 1 - cM^A + cM^B$

where

$$M^A = [1 - p(\phi)]M_{solid}^A + p(\phi)M_{fluid}^A \quad (3.5)$$

$$M^B = [1 - p(\phi)]M_{solid}^B + p(\phi)M_{fluid}^B \quad (3.6)$$

Classical linear irreversible thermodynamics generalizes Fick's 1<sup>st</sup> law of diffusion to assume that flux will be proportional to the generalized driving force close to



---

equilibrium (Philibert, 2006). Following the notations in (Muhammad Qasim, 2012) (Svandal, 2006) , we can then write the following:

$$J_c = -M_c \nabla \frac{\delta F}{\delta c} \quad (3.7)$$

Fick's 2<sup>nd</sup> law of diffusion states that time rate of change of concentration is negatively proportional to the flux gradient:

$$\dot{c} = -\nabla \cdot J_c \quad (3.8)$$

Inserting Eq.(3.7) into (3.8) yields the following equation

$$\dot{c} = \nabla \cdot M_c \nabla \frac{\delta F}{\delta c} \quad (3.9)$$

where  $M_c = c(1 - c)(v_m/RT)D$  and  $D$  is diffusion coefficient interpolated between its solid and liquid values using the same phase field expression introduced in Eq. (3.3),

$$D = D_S + p(\phi)(D_L - D_S) \quad (3.10)$$

The form of  $M_c$  in the above equations has been chosen to reproduce Fick's law of diffusion in the bulk phase. Combining them with the free energy expression of Eqs. (3.2) and (3.4) yields the following governing equations for the phase field:

---


$$\dot{\phi} = M_{\phi}(\varepsilon_{\phi}^2 T \nabla^2 \phi - W T g'(\phi) - P'(\phi)(g_L - g_S)) \quad (3.11)$$

and concentration

$$\dot{c} = \nabla \left[ \frac{v_m}{RT} D_c (1 - c) \nabla \left[ (W_A - W_B) T g(\phi) + (1 - p(\phi)) \frac{\partial g_S}{\partial c} p(\phi) \frac{\partial g_L}{\partial c} \right] \right] \quad (3.12)$$

The model parameters  $\varepsilon_{\phi}$ ,  $W^A$ ,  $W^B$ ,  $M^A$ , and  $M^B$  can be estimated basing on measurable quantities. As an example, interface thickness,  $\delta_{A,B}$ , interfacial free energy,  $\sigma_{A,B}$ , temperature of melting  $T_{A,B}$ , are two properties that can be used to fit parameters due to their relationship to free energy changes across the interface. Both  $M_c$  and the phase field mobility  $M_{\phi}$  are expected to be related to diffusivity. However, the dependencies are quite complex and may also reflect the dynamics of aqueous phase restructuring. Molecular dynamics simulations, generally considered a valuable tool for studying diffusion phenomena, might be able to provide good estimates for mobility values, but at this stage, concentration mobility value was used.

To include the flow of heat in the simulation, an energy or thermal field is introduced. Example of this is given in the work by (Conti, 1997, 2000) the energy field is a conserved quantity, and the time derivative can be derived by associating a flux to the flow of energy and a driving force as in equations below:

$$\dot{e} = -\nabla \cdot J_c \quad (3.13)$$

$$\dot{e} = \nabla \cdot M_e \nabla \frac{\delta F}{\delta e} \quad (3.14)$$

---

### Three-Component PFT

The extension of PFT to three components is needed to study more complex scenarios like the CH<sub>4</sub> to CO<sub>2</sub> hydrate exchange. The phase field theory for three components is a straightforward extension of the basic theoretical model, especially in the case of only two phases and three components. Hydrodynamical effects and variable density were incorporated into the three components phase field theory through implicit integration of Navier stokes equation following the approach of (M Qasim et al., 2011). Eq. (3.2) can then be generalized into the following free energy functional.

$$F = \int d\mathbf{r} \left( \frac{\varepsilon^2 \phi}{2} |\nabla \phi|^2 + \sum_{i,j=1}^3 \frac{\varepsilon_{ij} T}{4} (c_i \nabla c_j - c_j \nabla c_i) + f_{bulk}(\phi, c_1, c_2, c_3) \right) \quad (3.15)$$

The integration is over the system volume with the subscripts i and j running over the components, and bulk free energy density described by

$$f_{bulk} = WTg(\phi) + (1 - p(\phi))g_s(c_1, c_2, c_3) + p(\phi)g_L(c_1, c_2, c_3) \quad (3.16)$$

However, the first generation of the PFT model has proven to be very computationally expensive, requiring a large number of CPUs. It was therefore important that the numerical routines are optimized for the best performance. Moreover, the challenge has been to find a systematic way to utilize mass concentration as a variable while still retaining physical and mathematical consistency.

These missing elements have acted as a strong incentive to find a more solid and physically valid assumption to build up a model for gas–liquid and hydrate equilibria. A new numeric approach to developing the phase field model was proposed in Paper 2, where we have targeted simplified cases like the binary liquid phase. This direction

enabled us to find a framework that can further extended to the hydrate phase transition.

### **3.2.3. High Performance computing**

The most efficient theoretical tool describing chemical and structural pattern formation on multiple length and time scales efficiently is the above-discussed Phase-Field Theory (PFT), a continuum description relying on the combination of the fundamental equations of continuum mechanics and the thermodynamic description of diffuse interfaces.

Although analytic solutions of the model exist for simple scenarios, addressing pattern formation in multiphase and/or multicomponent mixtures of complex thermodynamics ultimately means the numerical solution of highly nonlinear, coupled partial differential equations (PDEs). Since the simulations cover multiple length and time scales, efficient real-time realization of the task necessitates the utilization of computationally efficient High-Performance Computing (HPC) facilities.

Besides traditional CPU-based clusters, the development of Graphical Processing Units (GPU) opened the possibility of building a highly cost and energy efficient "personal laboratory" using only a single PC. From the computational point of view, the basic concept of the GPU (associated with its primary purpose, i.e. producing high resolution graphics) also catalyzed the development of novel parallel algorithms.

The practice started with a brief a review on diffuse interface modeling of pattern formation phenomena, and by re-evaluating the basic concepts of massively parallel HPC algorithms, these basis was used to develop a general GPU-based solver for extending the phase field simulation

### 3.3. Heat transfer in hydrate systems

Heat transport associated with formation and dissociation of hydrate will be dominated by heat conduction and heat convection mechanisms. When hydrate is formed during the flow of hydrocarbons containing water, a variety of scenarios may occur. Most flow lines in the oil and gas industry, including pipelines inside hydrocarbon processing plants and pipelines transporting gas and oil to onshore customers, are made of rusty pipes. Hydrate can nucleate towards pipeline walls due to favorable adsorption of water (Aromada & Kvamme, 2019). The heat convection mechanism will transport heat between different phases (gas, liquid water, hydrate) at different temperatures, while the heat conduction will distribute heat within the same phase. Hydrate nucleation on the interface between liquid water and gas leads to heat transport from gas/water interface towards bulk water.

For hydrates in subsea sediments or hydrates under the permafrost, the heat transport situation is quite complex, with very limited experimental data currently available, and laboratory reproduction of those conditions being quite challenging. For this reason, it is very common to lump together heat conduction and heat convection into an “effective” heat conduction model employing apparent conductivity:(Chérif & Sifaoui, 2004)

A typical sediment example will involve aquifer storage of CO<sub>2</sub> in reservoirs that contain regions favorable for hydrate formation. Liquid water is available in the sediments, and a continuous inflow of CO<sub>2</sub> will lead to the formation of hydrate films that will reduce vertical CO<sub>2</sub> migration. In addition to the presence of natural sealing (clay, shale), these hydrate films reduce risk of CO<sub>2</sub> leakage to the surroundings above the storage site. These two practical examples alone illustrate the importance of having a model that assumes that the original “bulk” phases of the water and hydrate former

phase will not be totally consumed and disappear. There are numerous other relevant examples.

A typical simplified heat transport model in this scenario will involve heat conduction through the water across the growing film. The most straightforward approach would entail a sum of two different uniform heat fluxes due to heat conduction from below the growing hydrate and through the hydrate film towards the CO<sub>2</sub> phase. At the same time, the latent heat of crystallization will accumulate on the interface due to poor CO<sub>2</sub> conductivity and contribute to temperature increase. When the temperature on the hydrate surface reaches the hydrate melting point, hydrate dissociation dynamics will enter the mass and energy balances. Additionally, mineral bedrock may also affect the overall energy balance, and it is entirely feasible to incorporate the associated heat transport into the simplified model.

When water dissolved in the carbon dioxide has been depleted in the CO<sub>2</sub> to the level of quasi-equilibrium with the CO<sub>2</sub> hydrate, a new hydrate will only be able to form either through CO<sub>2</sub> transport through the hydrate film and into the liquid water side of the hydrate film or water transport through the hydrate film and into the CO<sub>2</sub> side of the hydrate film.

The diffusion of CO<sub>2</sub> through hydrate will be very slow and most probably limited by the existence of empty large cavities; this process will trigger local destabilization of the hydrate lattice and induce counter diffusion of water molecules.

In the absence of “fresh” building blocks, the combination of the first and the second laws of thermodynamics will result in a dynamic process where the least stable hydrates (those with highest free energy) will melt to support the growth of hydrate regions with lower free energy (B Kvamme et al., 2007). Even by themselves, these processes can generate mass fluxes across the hydrate membrane film. Ultimately, these local free energy-governed processes can even lead to the creation of holes in the hydrate membrane, allowing for supply of new building blocks.

### **3.4. Advantages of using a uniform reference state method**

Evaluating the risk of hydrate formation typically focused solely on pressure and temperature stability limits, i.e. just one projection of the whole multidimensional phase diagram. Since hydrate stability regime also includes concentrations in all co-existing phases, the conventional approach is thus unable to predict the free energy changes needed to create hydrate. Moreover, this approach cannot describe how the heat of hydrate formation and dissociation will be transported away from the formed hydrate into the surrounding phases. This indicated the need to develop a systematic framework enabling analysis of hydrate formation and hydrate dynamics based on free energy variation in response to evolution of temperature, pressure, and concentrations. Phase distributions established in an ongoing phase transition will be implicitly coupled to mass and heat transport, pressure, and temperature dynamics as discussed in the previous sections. We will also require a consistent route for calculations of enthalpies, as the first law-governed response to independent variables like temperature, pressures, and concentrations.

In other words, we aimed to develop a new thermodynamic toolbox capable of estimating all the hydrate phase transitions of significance for sediments and pipeline transport of hydrate formers. The bulk of available thermodynamic packages for calculating pressure and temperature stability limits are based on old calculation routines from the seventies. On top of their many drawbacks related to the outdated approaches, the fundamental limitation they have in common is the use of empirically fitted thermodynamic properties (chemical potential in particular). Basically, these packages only calculate hydrate formation from a separate hydrate former phase and liquid water or ice.

---

As shown below, using ideal gas reference state for all components in all the phases (aka residual thermodynamics scheme) provides a comprehensive and consistent thermodynamic model allowing to calculate, among other things, hydrate stability limits in various projections. However, it is reasonably straightforward to reformulate routines based on other reference states into residual-thermodynamics based models.

### 3.5. Residual models for hydrate and aqueous phases

A thermodynamic model consists of a reference state, a way to describe the entropy effects of ideal mixing, and finally a model estimating the differences between the real system and its ideal mixing counterpart. Classical Molecular Dynamics is based on orthonormal splitting of the canonical partition function into the momentum space (ideal gas) and the configurational space (the effects of molecule interactions).

(Bjorn Kvamme & Tanaka, 1995) utilized a harmonic oscillator to calculate chemical potentials for ice and water in empty hydrate structures I and II. The properties for ice were extrapolated to liquid water using experimental enthalpy of latent heat of crystallization at 273.15 K and specific heat capacity for liquid water for temperatures above 273.15 K, yielding a residual thermodynamic model system for the water phases. The statistical mechanical model for hydrate in (Bjorn Kvamme & Tanaka, 1995) was similar to the one proposed by van der Waals & Platteeuw (Waals & Platteeuw, 1958) but more general since it could also account for effects of flexible water lattice and associated destabilization effect of large guest molecules.

The residual thermodynamic model for water in hydrate is given by:

$$\mu_{H_2O}^H = \mu_{H_2O}^{O,H} - \sum_{k=1,2} RT v_k \ln \left( 1 + \sum_j h_{kj} \right) \quad (3.18)$$

where  $\mu_{H_2O}^{O,H}$  is the chemical potential for water in an empty clathrate lattice for the given hydrate structure. This chemical potential has been derived from Molecular Dynamics



simulations using the harmonic oscillator approach  $k$  runs over cavity types, and  $j$  is an index for guest molecules in different cavities.  $v$  is the stoichiometric ratio of guest versus water molecules, with subscripts  $k$  for large and small cavities respectively. For structure I, which is the focus here,  $v_{\text{large}}=3/24$  and  $v_{\text{small}}=1/24$ . For structure II the corresponding ratios are  $v_{\text{large}}=1/17$  and  $v_{\text{small}}=2/17$ .  $R$  is the universal gas constant,  $T$  is temperature.  $h_{kj}$  is the canonical partition function for guest molecule of type  $j$  in cavity type  $k$  given by (Bjorn Kvamme & Tanaka, 1995):

$$h_{kj} = e^{\beta[\mu_{kj}^H(T,P,\vec{x}^H) - \Delta g_{kj}(T)]} \quad (3.19)$$

where  $\beta$  is the inverse of the universal gas constant times temperature.  $\Delta g_{kj}(T)$  is the free energy change on including molecule  $j$  in cavity  $k$  (Bjorn Kvamme, 2019a, 2020, 2021).

The residual thermodynamic based approach applied to the aqueous phase will yield the following for chemical potential of water:

$$\mu_{\text{H}_2\text{O}}^{\text{water}}(T, P, \vec{x}^{\text{water}}) = \mu_{\text{H}_2\text{O}}^{\text{pure, H}_2\text{O}}(T, P) + RT \ln[x_{\text{H}_2\text{O}}^{\text{water}} \gamma_{\text{H}_2\text{O}}^{\text{water}}(T, P, \vec{x}^{\text{water}})] \quad (3.20)$$

The first term on the right-hand side is the chemical potential of pure liquid water, available from Kvamme (Bjorn Kvamme & Tanaka, 1995) as an analytical expression. Superscript “water” denotes the liquid aqueous phase, while subscript “H<sub>2</sub>O” indicates water as component. The first term in the brackets is the ideal liquid mixing contribution, while  $\gamma_{\text{H}_2\text{O}}^{\text{water}}$  is the deviation from ideal liquid mixture and approaches unity when mole fraction water approach 1.0.

Correlated chemical potentials for water in ice, liquid water, and empty structures I and II with ideal gas as reference are given in table 1 below. These are values estimated at

1 bar, and thus must be corrected for actual pressures by means of trivial Poynting correction using the molar volume for water for the phases listed in table 1.

Table 3.1 Parameters for dimensionless chemical potential functions

| Water phase, m              | $a_0$   | $a_1$   |
|-----------------------------|---------|---------|
| Empty structure I           | -21.333 | -18.246 |
| Empty structure II          | -21.374 | -18.186 |
| Ice (T < 273.15 K)          | -21.690 | -19.051 |
| Liquid water (T > 273.15 K) | -21.690 | -16.080 |

$$\frac{\mu_{H_2O}^m}{RT} = a_0^m + a_1^m \left[ \left( \frac{273.15}{T} \right) - 1 \right]$$

### 3.5.1. Residual thermodynamics for gas or liquid hydrate former phase and dissolved hydrate formers

When applied to the gaseous phase, residual thermodynamic scheme results in the following equation for chemical potential of components:

$$\mu_j^{gas}(T, P, \vec{x}) = \mu_j^{ideal\ gas, pure}(T, P) + RT \ln[x_j \phi_j^{gas}(T, P, \vec{x})] \quad (3.21)$$

where  $x_j$  is mole fraction of component  $j$  in the gas mixture.  $\vec{x}$  with the arrow is the mole-fraction vector for the gas mixture.  $P$  is pressure. Ideal gas chemical potential (first term on right hand side) is trivially given by statistical mechanics from molecular mass and moments of inertia of molecule  $j$ .  $\phi_j^{gas}$  is fugacity coefficient for component  $j$  in the gas mixture at the actual  $T$  and  $P$ . It is equal to unity for ideal gas and can generally be derived from Helmholtz free energy for the given equation of state (the Soave Redlich Kwong equation of state (Soave, 1972) used in this work).

Calculation of chemical potential at infinite dilution via atomistic-level simulations can be performed by several well-established techniques. Asymmetric-excess models for CH<sub>4</sub> and CO<sub>2</sub> based on molecular modeling are also available, see: (Bjørn Kvamme, 2019b; Bjørn Kvamme, Aromada, Saeidi, Hustache-Marmou, & Gjerstad, 2020) and references wherein for details.

## 4. Introduction to papers

The focus of this project was to improve thermodynamic schemes formulated earlier by our research group and apply them to the analysis of gas hydrate thermodynamics, kinetics, and phase transitions occurring both in situ and industrial systems, with a specific focus on the simultaneous production of CH<sub>4</sub> from in-situ hydrate and CO<sub>2</sub> long-term storage in the form of hydrates. An illustrative flow chart with categorized Ph.D. research is shown below:

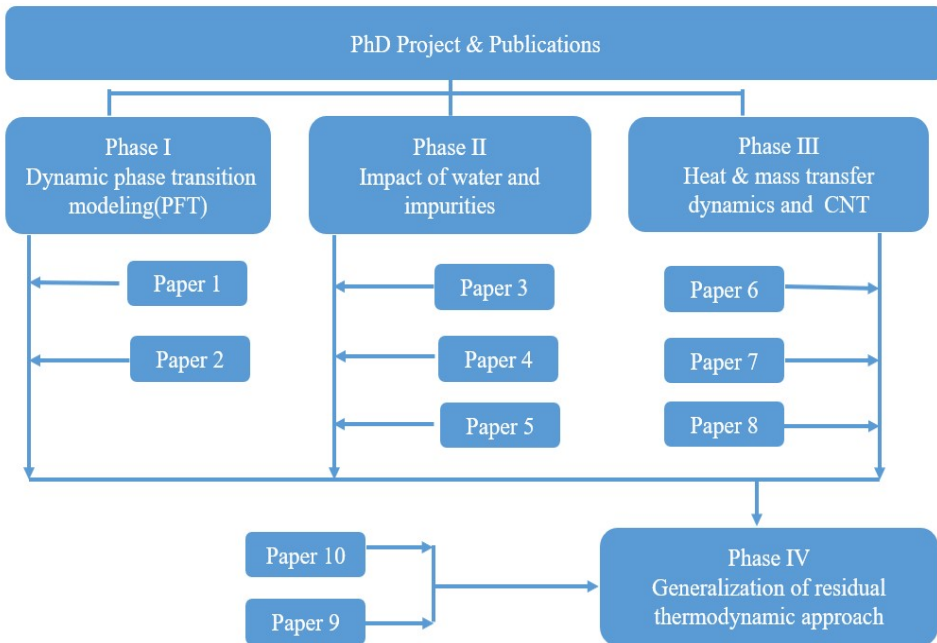


Figure 4.1 Categorized PhD Research in a snapshot.

### **Dynamic phase transition modeling applied to non-equilibrium hydrate phenomena (Paper 1 and 2)**

The first phase of these studies started with an overview of the earlier developed model based on the Phase Field Theory (PFT). This model has the advantage of implementing consistent absolute thermodynamics approach and thus enabling detailed investigation into complex phase transition mechanisms and corresponding mapping of rate-limiting processes such as mass transport, heat transport, and phase transition kinetics.

However, the first generation of the PFT model has proven to be very computationally intensive, requiring substantial optimization of numerical algorithms. Moreover, there remained inconsistencies related to physical factors and numeric algorithms.

These shortcomings have acted as a strong true incentive to find a more solid and physically valid assumption to build up a model for gas–liquid and hydrate equilibria. Eventually, a new framework and approach to developing the phase field model were proposed (paper 2) where we focused on simpler cases like binary liquid mixtures. This direction enabled us to find the modeling framework that can further extended to hydrate phase transitions.

### **Impact of water and impurities on hydrate phase transitions under pipeline and reservoir conditions (Papers 3, 4, and 5)**

The reality of hydrate phase transitions under reservoir conditions and pipeline transport involves multiple diverse scenarios, with water content, various impurities, and presence of competing hydrate former species like  $N_2$  and  $H_2S$  potentially playing a significant part.

Thus, finding a practical way to introduce them to the model gives us a benefit of derisking unwanted hydrate formation while promoting the hydrate formation/

dissociation process in other systems. Studies under constraint of paper 3-4 and 5 has been carried out to meet these targets.

### **Heat & Mass transfer Dynamics and application of CNT (Papers 6, 7, and 8)**

In the third group of research papers, we analyze the various stages in hydrate formation based on residual thermodynamics and classical nucleation theory (CNT). While we present a new approach for calculating the heat of hydrate formation and dissociation based on residual thermodynamics of all phases, including the hydrate phase. Our goal here is to update and improve the heat transfer schemes within the thermodynamic models while highlighting the current lack of reliable enthalpy data in current literature. Owing to the limitations associated with current methods, we propose a solution by using residual thermodynamics for the evaluation of enthalpy changes of hydrate phase transitions in

### **Generalization of residual thermodynamic approach for analysis of hydrate phase transitions (paper 9 & 10)**

The last two papers form a decisive conclusion to the thesis work, harmonizing and presenting all our previous efforts under a generalized thermodynamic approach, which could be used as a reference basis for hydrate phase transition studies within various systems. More details are provided in the next section which contains a summary of individual papers.

## **4.1. Paper 1. Non-equilibrium aspects of hydrate and dynamic phase transition modeling**

In this paper, we present a literature review of all development done for the Phase Field model (PFT), developed in our research group. We aimed to provide general guidelines for using the PFT approach to formulate simplified kinetic models suitable for industrial applications, with hydrates in porous media being the focus. Since the theory provides very detailed information on the possible impacts of different kinetic contributions to the overall kinetics of hydrate formation and dissociation in non-equilibrium systems

However, the first generation of the modeling software had proven to be very computationally expensive, moreover, there was a need to revisit and reassess certain physical assumptions underlying the numerical scheme. A proper implementation of hydrodynamic phenomena is also essential since one needs to incorporate variations in viscosity, density, and interfacial tension through which local forces of collisions are analyzed with respect to either bubble merging or bubble deformation. Another vital element missing in this model accounting for the impact of convective heat transport. Our previous hypothesis postulating a relative large-scale nature of local dynamics across hydrate-fluid interfaces has proven to be inadequate, thus replacing the uniform grid with a dynamically adaptive one may facilitate a more accurate representation. We conclude that complete overhaul of routines and algorithms as well as improving the existing code would incur significant time investment, making the use of the legacy code worthwhile running simplified theoretical studies.

## **4.2. Paper 2. Phase-field theory of multi-component incompressible Cahn-Hilliard liquids**

This paper aimed to generalize the Cahn-Hilliard theory for liquid phase separation in case of an arbitrary number of components and this practice is considered as the first step required to build a reliable model for gas-liquid and clathrate hydrate equilibria, and thus advance continuum theory of multi-component liquids. A consistent, entropy-producing advection-diffusion dynamics was set up, and then the Cahn-Hilliard free energy functional was expanded to include several components.

Our controlled pattern formation is of increasing importance in several practical applications. For instance, one crucial field is carbon emission reduction: a controlled emulsion-emulsion transition in the CO<sub>2</sub>/water/heavy crude oil system has a potential to result in an efficient and environmentally sound combination of CO<sub>2</sub> storage and Enhanced Oil Recovery.

We have shown that a simple triplet energy term can be used to stabilize the binary planar interfaces, and the equilibrium contact angles are in near-perfect agreement with theoretical values. We have also demonstrated that the system will undergo spinodal decomposition when starting from a high-energy non-equilibrium state. Asymmetric ternary and quaternary systems will tend to progress towards the equilibrium by developing a bulk-interface-trijunction topology in two dimensions.

## **4.3. Paper 3. Impact of water and impurities on hydrate formation in natural gas pipeline**

Paper 3 started the second phase of the project, where we focused on improving the prediction capabilities of our models when it comes to the effect of impurities and water. Thermodynamic consistency has been a high priority throughout this work. It



was not our intention to adjust any parameters to fit experimental data. In this paper, we present a robust thermodynamic scheme able to calculate chemical potential of water in all phases, including the empty hydrate lattice, the adsorbed phase, and aqueous solutions. The scheme utilizes classical thermodynamic relationships with parameters derived from molecular dynamics simulations. The free energy of inclusion was estimated following (Bjorn Kvamme & Tanaka, 1995).

The typical industrial way to evaluate the risk of hydrate formation in an upstream natural gas pipeline is via calculation of water dropping out and subsequent evaluation of formation kinetics involving condensed water and hydrate formers present in the gas stream. Carbon steel transport pipelines tend to be rusty, opening the possibility of additional routes to hydrate formation starting with water absorbing onto rust. To be on the safe side, the industry tends to be very conservative when it comes to the water tolerances, going as far as tightening their estimates based on water dew-point calculations by a large degree instead of applying analysis techniques based on water dropping out due to adsorption on hematite.

For pure methane, water tolerance tends to decrease with increasing pressures from 50 to 250 bars in the temperature range between minus one and plus six Celsius. Since typical natural gas mixtures are dominated by methane, their behavior will be largely like that of pure methane (with some variations due to differing water drop-outs).

In a possible revision of current best practices for hydrate prevention, we therefore recommended reducing water level in the methane-rich phase to below that triggering adsorption-dominated drop-out.

#### **4.4. Paper 4. Effect of H<sub>2</sub>S content on thermodynamic stability of hydrate formed from CO<sub>2</sub>/N<sub>2</sub> mixtures**

Paper 4 focuses on combined carbon dioxide storage and methane production by means of methane hydrate conversion. Our scenario envisaged CO<sub>2</sub> being injected into a reservoir and triggering methane hydrate conversion into CO<sub>2</sub>-dominated hydrate. Though thermodynamically favored, this process has proven to pose challenges due to kinetic factors, with nitrogen admixture often administered to lower the driving force towards hydrate formation and thus improve carbon dioxide penetration into the reservoir. However, increasing the nitrogen fraction faces a thermodynamic limit because formation of new hydrates becomes impossible, this is why we investigated the feasibility of adding a potent hydrogen former, hydrogen sulfide, to carbon dioxide/nitrogen mixtures.

Hydrogen sulfide is both abundant in thermogenic hydrocarbon reservoirs and often follows carbon dioxide during sour gas removal. Four case studies were investigated, the Bjørnøya gas hydrate basin, the Nankai field in Japan, the Hikurangi Margin in New Zealand, and a gas hydrate basin in South-Western Taiwan.

The same methodology as in Paper 3 was applied to follow the free energy gradients until the binary CO<sub>2</sub>/N<sub>2</sub> phase has been depleted of the most aggressive hydrate former, carbon dioxide for temperatures between 273.16 and 280 K.

It was shown that even a small mole fraction of H<sub>2</sub>S (1%) added to the CO<sub>2</sub>/N<sub>2</sub> mixture was enough to significantly raise the driving force for new hydrate formation.

#### **4.5. Paper 5. Maximum tolerance for water content at various stages of a Natuna production**

Paper 5 aimed to assess the risk of hydrate formation during transport of gas produced at the Natuna gas field, an enormous gas reservoir containing over 70% CO<sub>2</sub>, which both makes the scenarios very different to the Norwegian shelf and brings in a higher risk of hydrate formation.

Two different approaches for estimating the maximum water tolerances were evaluated: the traditional industrial technique based on water dewpoint versus our approach that accounts for alternative routes of hydrate formation.

The industrial case under investigation involved the separation of original produced gas into two streams: a methane-rich and a CO<sub>2</sub>-rich one, with our thermodynamic analysis suggesting that pipeline transport conditions expected for all three streams listed above will fall inside the hydrate formation regions. We have concluded that the conventional water dewpoint-based method will overestimate the safe limit of water in all the gas streams. The low chemical potential of water adsorbed on hematite will result in substantially lower tolerance limits for the water content of transported gas; when the water dewpoint is used as the criteria, the permitted water content is eighteen times higher than based on water adsorption on rust.

The paper also includes a feasibility study for reinjecting the carbon dioxide stream from Natuna into the North Makassar Basin hydrate field at offshore Indonesia to achieve simultaneous safe long-term storage of CO<sub>2</sub> and release of methane. We found that the minimum level of CO<sub>2</sub> required to create new hydrates while retaining fast exchange rate will be reasonably low (even CO<sub>2</sub> fraction as low as 2 mol% in CO<sub>2</sub>/N<sub>2</sub> mixture will allow the new hydrate to form).

#### **4.6. Paper 6. Dynamics of heat and mass transport during hydrate dissociation and reformation in sediments**

Peper 6 presented our first foray in the third phase of the PhD project devoted to more detailed analysis of kinetics of heat and mass transfer and their relative significance. Most of the previously proposed models found in the literature for the kinetics of heterogeneous hydrate film formation and growth are frequently incomplete and lack true physical underpinnings. Moreover, a number of kinetic models attempting to describe the creation of hydrate films are based on heat transport alone. Given that heat transport is orders of magnitudes faster than the mass transport through the films, it is the kinetic limitations of mass transport that control the rate of hydrate phase transitions. There is a need for a realistic kinetic model that accounts for actual coupled processes of mass and heat transport to driving forces for hydrate formation, and dissociation, in a more general way that includes all independent thermodynamic variables.

Paper 6 put forward a physically sound approach to generate rigorous theoretical models accounting for implicit thermodynamic coupling between mass and heat transport that ultimately governs the phase transition. We also show that all thermodynamic properties for all phases, including hydrate, can be calculated by means of residual thermodynamics scheme, i.e. using the same reference state, ideal gas. This also includes a scheme for calculation enthalpies of hydrate formation and dissociation. Being applicable to all hydrate phase transitions, this approach is both more straightforward and significantly more general. When we applied this new approach to evaluating the stability of methane and carbon dioxide hydrates; our findings indicated that mass transport through established hydrate films may be the most important reason for the delay in observable hydrate films between water and hydrate former phases.

#### **4.7. Paper 7. Stages in dynamics of hydrate formation and consequences for design of experiments for hydrate formation in sediments**

Research performed in paper 7 aimed to extend and generalize techniques and conclusions reached in paper 6. The primary goal was to shed light on how to design better experimental studies for hydrate formation between water and CH<sub>4</sub> or CO<sub>2</sub> in sediments. We have utilized classical nucleation theory (CNT) and residual thermodynamics to examine the dynamics of hydrate formation.

Heterogeneous hydrate nucleation on an interface between liquid water and hydrate-former phase will rapidly result in formation of mass transport-limiting films of hydrate. These hydrate films may delay the onset of massive, visible, hydrate growth by several hours.

We have isolated and analyzed the stages of hydrate formation, with the focus on dynamic rate-limiting phenomena which frequently result in pockets of gas and liquid water trapped inside hydrate. This is used as the basis for considering various ways to break hydrate films and increase formation rate. Reducing trapped gas pockets and trapped liquid water to a minimum will be an important step towards creating hydrates in sediments that in important ways can be compared to natural gas hydrates in nature.

Lack of heat transport analysis is also a limitation of this work. Since the heat transfer kinetics in systems of liquid water and solid hydrate are orders of magnitude faster than that of mass transport, the approach used in this paper ignored its impact, limiting the scope of the work. Any simulation model without real phase transition analysis in terms of free energy-based functions is inherently limited as well.

#### **4.8. Paper 8. Modelling heat transport in systems of hydrate filled sediments using residual thermodynamics and classical nucleation theory**

This paper completes the research initiated in paper 6. The focus of this work is to review some of the more recent and popular models applied to study hydrate phase transition dynamics in terms of actual kinetic rate limiting factors. Our secondary objective was to shed more light on the connection between nanoscale transition dynamics and hydrodynamic flow (which happens across a thin interface of 1–1.5 nm). Our third objective is related to the need for thermodynamic consistency. Many models describing enthalpy changes related to hydrate phase transitions are disconnected from the formal thermodynamic coupling between phase transition thermodynamics (Gibbs free energy changes) and the enthalpy changes related to heat transport requirements.

To achieve this aim, a fairly straightforward kinetic model, the classical nucleation theory (CNT), was modified to incorporate new models for mass transport across water/hydrate interfaces. A novel and consistent model suitable for the calculation of enthalpies is also discussed and appropriate calculations for pure components and relevant mixtures of carbon dioxide, methane, and nitrogen are demonstrated. The kinetic model for hydrate phase transitions that we have demonstrated in this work (CNT) contains a newly developed mass transport term based on modern theoretical concepts and results from molecular dynamics simulations. The implicit heat transport model is also numerically straightforward and has the advantage of couplings to a new model for enthalpy calculations which are completely consistent with the free energies in hydrate and all co-existing phases.

#### **4.9. Paper 9. Why should we use residual thermodynamics for calculation of hydrate phase transitions?**

This paper presents the advantages of using residual thermodynamics scheme for all the phases, including hydrates. Finding alternatives to conventionally used excess thermodynamics scheme for treatment of formally overdetermined hydrate systems was an important focus for this work. In addition to being able to handle many alternative hydrate routes for hydrate formation or dissociation, residual thermodynamics also opens a way to calculate a variety of associated thermodynamic properties (for instance enthalpies of pure components and mixtures) in a straightforward and rigorous way. A Clapeyron-based scheme for calculation of enthalpies associated with hydrate phase transitions is proposed.

The most common method used for assessment of hydrate phase transitions found in literature involves fitting empiric parameters to calculate the free energy difference between liquid water and empty hydrate lattice. To the best of our knowledge, all commercial and academic codes following this approach can only hydrate formation from free gas and liquid water. Specifically, one might argue that there is a need for a more comprehensive definition of hydrate stability which accounts not only for temperature and pressure limits but concentration of guest components in the aqueous phase. Another benefit of our approach is that it makes it possible to handle all potential hydrate stability limits and formation/dissociation routes within the same framework.

This approach was illustrated through analyses of several hydrate phase transitions, examples of free energy evaluation of phase stability, and calculation of enthalpies of hydrate formation, with the enthalpies compared to both experimental data and results derived from the Clapeyron equation. Mechanisms for conversions of in situ CH<sub>4</sub> hydrate to facilitate safe CO<sub>2</sub> storage are discussed while considering hydrate stability limits in additional projections describing guest saturation of the liquid phase. Both

formation of hydrates from dissolved hydrate formers, as well as their dissociation when in contact with undersaturated water is often considered in the P-T projection of the phase diagram only, while the significant impact of CO<sub>2</sub> supercritical transition is frequently overlooked.

#### **4.10. Paper10. Thermodynamics of hydrate systems using a uniform reference state**

The objective of this paper was to extend and generalize the use of ideal gas as a uniform reference state, which has the advantages of both physical existence (unlike the ideal solution) and having properties that are straightforward to calculate.

We believe that this approach (commonly referred to as residual thermodynamic or  $\phi$ - $\phi$  scheme) presented and illustrated in this paper is superior to the more conventional excess reference technique (also known as the  $\phi$ - $\gamma$  scheme). While a distinct advantage of residual thermodynamics lies in it providing a consistent scheme for calculating properties needed to evaluate a wide range natural and industrial hydrate applications, it is not at all restricted to those scenarios.

This reference state also provides a direct bridge between molecular dynamics simulations of model systems since ideal gas is sampled in momentum space and residual contributions are samples in configurational space. This opens for modeling of hydrate nucleation in many phases. Another benefit of our approach is that it makes it possible to handle the variety of stability limits and routes of hydrate formation and dissociation within the same framework.

Paper 9 emphasized a need for more complete hydrate stability description including the hydrate former concentration in the surrounding aqueous phase. This paper describes the further development of our residual thermodynamic schemes and presents



case application studies for various hydrate formation/dissociation routes and phase transition stages for the following scenarios:

- Residual models for aqueous systems
- Heterogeneous and homogeneous hydrate formation
- Hydrate nucleation and growth
- CO<sub>2</sub>/CH<sub>4</sub> hydrate conversion for combined safe CO<sub>2</sub> storage and energy production.

While mainly presented in the context of hydrate thermodynamic properties, including enthalpy calculations, all the equations and schemes can be parameterized using water chemical potentials derived from molecular modeling of other relevant systems and thus easily generalized in other scenarios.

## 5. Conclusions

The first stage of the project involved a literature review of research done previously on theoretical and numeric development of the Phase Field Theory model has shown the inadequacy of hypotheses postulating relatively large-scale nature of local dynamics across hydrate-fluid interfaces. Our implementation of first-order-implicit free energy models for all co-existing phases makes it possible to compare the competing pathways of hydrate formation, dissociation, and reformation.

But while formally enabling a wide range of theoretical studies, these model improvements were hampered by the numerical code. Addressing pattern formation in multiphase and/or multicomponent mixtures of complex thermodynamics ultimately means the numerical solution of highly nonlinear, coupled partial differential equations (PDEs).

We have concluded that complete overhaul of routines and algorithms as well improving the existing code would incur significant time investment, making the use of the legacy code worthwhile running simplified theoretical studies. Our preliminary testing of in-house code has proven that the state-of-the-art Graphical Processing Units (GPU) open the possibility of building a highly cost and energy efficient "personal laboratory" using only a single PC.

The attempt to generalize the Cahn-Hilliard theory for liquid phase separation and an arbitrary number of components has shown that a simple triplet energy term can be used to stabilize the binary planar interfaces, with the equilibrium contact angles remaining in near-perfect agreement with theoretical values. We have also demonstrated that the system will undergo spinodal decomposition when starting from a high-energy non-equilibrium state.

Our results contribute to the continuum theory of multi-component liquids since controlled pattern formation in these systems is of increasing importance in several practical applications. This approach itself may be extended further to serve as the basis for description of vapor-liquid-solid phase transition within the gas hydrate transitions in different natural and industrial systems.

During the second phase of the project, we focused on improving the prediction capabilities of our thermodynamic models when it came to the impact of impurities and water, with model consistency being the most important priority. The same methodology that involved following free energy gradients has proven to work well in several diverse scenarios while yielding significant physical insights and industrially relevant recommendations.

In case of pipeline methane transport, we recommended a revision of current best hydrate prevention practices would be to reduce water concentration in the methane-rich phase to avoid triggering adsorption-dominated drop-out rather than unnecessarily tightening the dewpoint-based tolerances.

In the scenario where methane hydrate conversion is used to combine carbon dioxide storage and methane production, we have shown that even a small mole fraction of hydrogen sulfide added to the CO<sub>2</sub>/N<sub>2</sub> mixture might be enough to significantly raise the driving force for new hydrate formation. The general trend was that the deeper is the hydrate reservoir, the smaller the amount of CO<sub>2</sub> in the N<sub>2</sub> will be needed to form a new hydrate and thus facilitate fast release of *in situ* CH<sub>4</sub> hydrate.

While assessing the risks of hydrate formation during transport of gas produced at the Natuna field, a gas reservoir containing over 70% of carbon dioxide, we have concluded that the conventional water dewpoint-based method will significantly overestimate the safe limit of water in all the gas streams. When combined with our

previous analysis of nitrogen impact, insights obtained above emphasized even further the risks posed by even a small admixture of hydrogen sulfide.

Our feasibility study focused on reinjection of carbon dioxide stream from Natuna into the nearby North Makassar Basin hydrate field to achieve simultaneous long-term storage of CO<sub>2</sub> and release of methane. We have found that even CO<sub>2</sub> fraction as low as 2 mol% in CO<sub>2</sub>/N<sub>2</sub> mixture will allow new hydrate to form.

Phase three of the project addressed successive stages of hydrate formation, with a focus on dynamic rate-limiting processes that can result in pockets of gas and liquid water being trapped inside the hydrate phase. The bulk of existing kinetic models describing the creation of hydrate films are based on heat transport alone. Given that heat transport is orders of magnitudes faster than the mass transport through the films, we have recognized a need for a rigorous kinetic model that accounts for implicit coupling of mass and heat transport and the way this will affect the driving forces for hydrate formation and dissociation.

Mineral/fluid/hydrate interaction and geochemistry are among many relevant factors determining the local hydrate saturation in reservoir pores. Even using real sediments cores does not allow one to reproduce a natural gas hydrate reservoir that has developed over geological time scales in the laboratory, thus necessitating theoretical and numerical thermodynamic analysis of the many diverse scenarios.

The proposed simplified residual scheme has allowed us to construct a realistic representation of interfaces between hydrate and liquid phases. Our analysis emphasized the important distinction between nucleation rate and induction time (ie the onset of massive growth) frequently confused in the literature. Our results based on the classical nucleation theory indicate that nucleation will always occur on the nanoscale, both in terms of time and critical radius dimensions (which agreed with

estimates based on more advanced approaches). On the other hand, the diffusion of hydrate formers across the newly formed hydrate film will be a very slow process responsible for the very long interval before hydrates are observed on the macroscopic scale.

This type of information is essential for efficient design of experimental setups. For example, when applied to evaluating the stability of methane and carbon dioxide hydrates, our findings indicated that mass transport through hydrate films may be the most important factor delaying observable hydrate growth on the interface between water and hydrate former phases.

As utilized in this work, models based on both classical nucleation theory and multicomponent diffusive interface theory have proven fast enough to be implemented into large-scale reservoir simulations.

We have shown that in addition to being able to handle many alternative hydrate routes for hydrate formation and dissociation, our residual thermodynamics scheme enables one to calculate a variety of associated thermodynamic functions, with enthalpy being one of the most crucial properties. Thus, this knowledge allowed us to formulate a Clapeyron-based scheme for general analysis of hydrate phase transitions. The residual thermodynamic model proposed for hydrate has proven to be consistent with the free energy model for hydrate, ensuring that our revised CNT model is thermodynamically harmonious.

We have also concluded that while frequently overlooked, the impact of CO<sub>2</sub> transitioning into the supercritical state will have a large impact on both formation of hydrates from dissolved hydrate formers and their dissociation when in contact with water undersaturated with carbon dioxide.

Detailed case studies utilizing residual thermodynamics have been performed for several phenomena and mechanisms relevant for hydrate formation, dissociation, and conversion:

- Dissolution of hydrate formers from gas and liquid phases into liquid water systems
- Heterogeneous and homogeneous hydrate formation analyzed by means of internally consistent Gibbs free energy and enthalpy values
- Hydrate nucleation and growth in dynamic systems in contact with seawater (conventional hydrate seeps included)
- CO<sub>2</sub>/CH<sub>4</sub> hydrate conversion in a reservoir with focus on feasibility

We have come to believe that this approach (commonly also referred to as the  $\phi$ - $\phi$  scheme) is significantly superior to more conventional excess reference technique (aka the  $\phi$ - $\gamma$  scheme). And while residual thermodynamics has the distinct advantage of providing a consistent scheme for evaluating a wide range natural and industrial hydrate applications, it can easily be generalized and is not restricted to those scenarios.

## 6. Suggestions for further work

### 6.1. Refine the physical underpinnings of the current phase field model

- Since mole fraction is not a conserved property per se, it would be beneficial to derive a systematic way to utilize mass concentration as a variable while still retaining physical and mathematical consistency.
- Another vital element missing in this model is accounting for the impact of convective heat transport. It is an important mechanism that transfers heat between different phases (gas, liquid water, hydrate) at different temperatures while the heat conduction distributes heat within a specific phase.
- When more than one species of guest molecules is present, the most stable hydrate will form first, consuming thermodynamically favorable hydrate formers, with the less stable hydrate phases becoming feasible after depletion of the best formers. The PFT model must be extended to treat these multiple hydrates as different phases.
- While numerous experimental data is available for mixed nitrogen-methane and nitrogen-carbon dioxide hydrate systems highly relevant for *in situ* conversion of methane hydrates, almost no theoretical investigation has been done far. The current PFT thermodynamic model is unable to handle multiple occupancies, but the required extension can be accomplished following the work by Kvamme (2016) and Bauman (2015) via extending the free energy functional to four components.
- The presence of salt ions in the aqueous phase will result in reduction of water chemical potentials decreasing the thermodynamic driving force for hydrate formation and the stability of hydrates, as well as affecting guest solubility.

### 6.2. Develop entirely new numerical framework: solver improvement

- Phase Field Theory simulations are incredibly computationally expensive. Any optimization in routines and algorithms would yield large benefits. The simplest

way to realize this would involve improving the gravity code via implicit implementation of the extended thermodynamics in the current PFT model.

- Implementation of adaptive grid technique is yet another option to improve the efficiency of the code. The current solver uses a uniform grid which has severely limits any chances of efficiently capturing the local regions. Since the most important phenomena occur at the interface, fewer grid points can be used by making the spatial resolution larger inside and in the vicinity of the bulk regions.
- In the current implementation of the PFT, a new state is accepted only if it is of lower Gibbs free energy. In Monte Carlo simulations, convergence is sped up by accepting unfavorable states occasionally. The unfavorable state must still be within the bounds of the physical possibilities of the system. This approach might also prove beneficial for the PFT code and so is worth investigating.

### **6.3. Convert the standalone solver into a comprehensive PFT-based simulator**

- Develop a graphical preprocessor. Case studies probing the effect of different parameters would be much easier to set up with the aid of a graphical interface where the system initial configuration, including geometry (interfaces and boundaries) and component distribution, can be specified directly and then preprocessed for use as input to PFT solver.
- Visual inspection has proven to be an invaluable tool when it comes to analysis of numeric results. Developing a graphical postprocessor will be extremely useful, for example, when it comes to monitoring of time evolution of hydrate growth, conversion, and dissociation, as well as following the concentration gradients in the aqueous phase.
- Couple the PFT solver with gas hydrate reservoir simulator, for example RetrasoCodeBright (RCB), this will allow one to determine the effect of hydrate sealing and could be useful for study of long-term storage of CO<sub>2</sub> in aquifers.



#### **6.4. Perform experiments on real-life hydrate systems to validate theoretical results**

- The focus of this thesis was on developing a physically consistent model accounting for all the mechanisms and effects relevant for hydrate-related processes on the lab and reservoir scale (phase field model and generalized thermodynamic approaches). While a very powerful tool yielding reliable results, experimental data will undoubtedly provide the best foundation to validate the models and improve them further.
- Especially, experimental studies probing methane-to-CO<sub>2</sub> hydrate exchange in porous media mimicking reservoir conditions can provide observation that will serve as valuable input parameters for our models and prove the feasibility of this technique of carbon mitigation in the long run.

#### **6.5. Extend thermodynamic model to other relevant hydrate formers systems**

- Extend the residual thermodynamic scheme by adding hydrogen as a possible hydrate former to enable studying hydrogen hydrate formation and transport for the purposes of middle-stage or seasonal storage of hydrogen.

#### **6.6. Incorporate residual thermodynamic models into a reservoir simulator**

- Implement residual thermodynamic models developed in this study into a reservoir simulator to improve the accuracy of mass and energy balance calculations.
- Use the improved simulator to perform a follow up study to shed light on the macroscopic consequences of hydrogen sulfide presence (e.g. possible local blockages due to mixed hydrate formation).
- Evaluate the extent of proper nitrogen admixture to promote safe CO<sub>2</sub> storage and methane hydrate dissociation by retaining the driving force for mixed CO<sub>2</sub>-N<sub>2</sub> hydrate formation while ensuring blockage-free flow.

## References

- Anderson, B., Bartlett, K., Frolking, S., Hayhoe, K., Jenkins, J. and Salas, . (2010). *Methane and Nitrous Oxide Emissions from Natural Sources*. Retrieved from Office of Atmospheric Programs, US EPA, EPA 430-R-10-001, Washington DC.
- Archer, D., Buffett, B., & Brovkin, V. (2009). Ocean methane hydrates as a slow tipping point in the global carbon cycle. *Proceedings of the National Academy of Sciences*, 106(49), 20596-20601. doi:10.1073/pnas.0800885105
- Aromada, S. A., & Kvamme, B. (2019). New approach for evaluating the risk of hydrate formation during transport of hydrocarbon hydrate formers of sI and sII. *AIChE Journal*, 65(3), 1097-1110.
- Bachu, S. (2002). Sequestration of CO<sub>2</sub> in geological media in response to climate change: road map for site selection using the transform of the geological space into the CO<sub>2</sub> phase space. *Energy Conversion and Management*, 43(1), 87-102. doi:[https://doi.org/10.1016/S0196-8904\(01\)00009-7](https://doi.org/10.1016/S0196-8904(01)00009-7)
- Baig, K. (2009). *Phase field theory modeling of CH<sub>4</sub> and CO<sub>2</sub> fluxes from exposed natural gas hydrates reservoir*. master thesis, University of Bergen, Norway,
- Baig, K. (2017). Nano to Micro Scale Modeling of Hydrate Phase Transition Kinetics.
- Balakin, B. V. (2010). *Experimental and theoretical study of the flow, aggregation and deposition of gas hydrate particles*. (PhD). University of Bergen, University of Bergen.
- Bauman., J. M. (2015). *Kinetic Modeling of Hydrate Phase formation dissociation and reformation* (PhDs). University of Bergen, , Bergen, Norway.
- Bierwirth, P. (2018). Carbon dioxide toxicity and climate change: a major unapprehended risk for human health. *Web Published: ResearchGate*, 10.
- Bilyushov, V. M., Bondarev, É. A., & Maron, V. I. (1988). Hydrate formation process with consideration of heat and mass exchange. *Journal of engineering physics*, 55(2), 870-874. doi:10.1007/BF00870733
- Blasing, T. J. (2013). *Recent Greenhouse Gas Concentrations* [Report Number: cdia:doi:10.3334/CDIAC/atg.032; osti:1389528; doi:10.3334/CDIAC/ATG.032]. Retrieved from: <https://www.osti.gov/biblio/1394398>
- Bogoyavlensky, V., Kishankov, A., Yanchevskaya, A., & Bogoyavlensky, I. (2018). Forecast of Gas Hydrates Distribution Zones in the Arctic Ocean and Adjacent Offshore Areas. *Geosciences*, 8(12). doi:10.3390/geosciences8120453

- 
- Boswell, R., & Collett, T. S. (2011). Current perspectives on gas hydrate resources. *Energy & Environmental Science*, 4(4), 1206-1215. doi:10.1039/C0EE00203H
- Callen, H. B. (1985). *Thermodynamics an introduction to thermostatics* (2. ed ed.). N.Y.: John Wiley & Sons.
- Cha, J.-H., & Seol, Y. (2013). Increasing gas hydrate formation temperature for desalination of high salinity produced water with secondary guests. *ACS Sustainable Chemistry & Engineering*, 1(10), 1218-1224.
- Chakma, A. (1997). CO<sub>2</sub> capture processes — Opportunities for improved energy efficiencies. *Energy Conversion and Management*, 38, S51-S56. doi:[https://doi.org/10.1016/S0196-8904\(96\)00245-2](https://doi.org/10.1016/S0196-8904(96)00245-2)
- Chatti, I., Delahaye, A., Fournaison, L., & Petitet, J.-P. (2005). Benefits and drawbacks of clathrate hydrates: a review of their areas of interest. *Energy Conversion and Management*, 46(9), 1333-1343. doi:<https://doi.org/10.1016/j.enconman.2004.06.032>
- Chérif, B., & Sifaoui, M. S. (2004). Theoretical study of heat transfer by radiation conduction and convection in a semi-transparent porous medium in a cylindrical enclosure. *Journal of Quantitative Spectroscopy and Radiative Transfer*, 83(3), 519-527. doi:[https://doi.org/10.1016/S0022-4073\(03\)00103-1](https://doi.org/10.1016/S0022-4073(03)00103-1)
- Chong, Z. R., Yang, S. H. B., Babu, P., Linga, P., & Li, X.-S. (2016). Review of natural gas hydrates as an energy resource: Prospects and challenges. *Applied energy*, 162, 1633-1652.
- Circone, S., Stern, L. A., Kirby, S. H., Durham, W. B., Chakoumakos, B. C., Rawn, C. J., . . . Ishii, Y. (2003). CO<sub>2</sub> hydrate: Synthesis, composition, structure, dissociation behavior, and a comparison to structure I CH<sub>4</sub> hydrate. *Journal of Physical Chemistry B*, 107(23), 5529-5539. doi:10.1021/jp027391j
- Collett, T. S., & Ginsburg, G. D. (1998). Gas hydrates in the Messoyakha gas field of the West Siberian Basin - A re-examination of the geologic evidence. *International Journal of Offshore and Polar Engineering*, 8(1), 22-29. Retrieved from <https://pubs.usgs.gov/publication/70020726>
- Conti, M. (1997). Solidification of binary alloys: Thermal effects studied with the phase-field model. *Physical Review E*, 55(1), 765.
- Conti, M. (2000). Thermal and chemical diffusion in the rapid solidification of binary alloys. *Physical Review E*, 61(1), 642.

- 
- Davoodabadi, A., Mahmoudi, A., & Ghasemi, H. (2021). The potential of hydrogen hydrate as a future hydrogen storage medium. *iScience*, *24*(1), 101907. doi:10.1016/j.isci.2020.101907
- Desideri, U., & Paolucci, A. (1999). Performance modelling of a carbon dioxide removal system for power plants. *Energy Conversion and Management*, *40*, 1899-1915.
- Edward Bryant. (1997). *Climate process and change. 1997*. Cambridge Cambridge University Press.
- Englezos, P. (1992). Computation of the incipient equilibrium carbon dioxide hydrate formation conditions in aqueous electrolyte solutions. *Industrial & Engineering Chemistry Research*, *31*(9), 2232-2237. doi:10.1021/ie00009a021
- Englezos, P. a. Y. T. N. (1993). Incipient equilibrium data for propane hydrate formation in aqueous solutions of sodium chloride, potassium chloride and calcium chloride. *Journal of Chemical and Engineering Data*, *38*(2), 250-253.
- Fakharian, H., Ganji, H., & Naderifar, A. (2017). Desalination of high salinity produced water using natural gas hydrate. *Journal of the Taiwan Institute of Chemical Engineers*, *72*, 157-162. doi:<https://doi.org/10.1016/j.jtice.2017.01.025>
- Gambelli, A. M., Rossi, F., & Cotana, F. (2022). Gas Hydrates as High-Efficiency Storage System: Perspectives and Potentialities. *Energies*, *15*(22). doi:10.3390/en15228728
- Ge, B.-B., Li, X.-Y., Zhong, D.-L., & Lu, Y.-Y. (2022). Investigation of natural gas storage and transportation by gas hydrate formation in the presence of bio-surfactant sulfonated lignin. *Energy*, *244*, 122665. doi:<https://doi.org/10.1016/j.energy.2021.122665>
- Grozic, J. L. H. (2010). Interplay Between Gas Hydrates and Submarine Slope Failure. In D. C. Mosher, R. C. Shipp, L. Moscardelli, J. D. Chaytor, C. D. P. Baxter, H. J. Lee, & R. Urgeles (Eds.), *Submarine Mass Movements and Their Consequences* (pp. 11-30). Dordrecht: Springer Netherlands.
- Hack, J., Maeda, N., & Meier, D. M. (2022). Review on CO<sub>2</sub> Capture Using Amine-Functionalized Materials. *ACS Omega*, *7*(44), 39520-39530. doi:10.1021/acsomega.2c03385
- Harrison, W. J., Wendlandt, R. F., & Dendy Sloan, E. (1995). Geochemical interactions resulting from carbon dioxide disposal on the seafloor. *Applied Geochemistry*, *10*(4), 461-475. doi:[https://doi.org/10.1016/0883-2927\(95\)00018-F](https://doi.org/10.1016/0883-2927(95)00018-F)

- 
- Hatzikiriakos, S. G., & Englezos, P. (1993). The relationship between global warming and methane gas hydrates in the earth. *Chemical Engineering Science*, 48(23), 3963-3969. doi:[https://doi.org/10.1016/0009-2509\(93\)80375-Z](https://doi.org/10.1016/0009-2509(93)80375-Z)
- Hendriks, C. A., & Blok, K. (1995). Underground storage of carbon dioxide. *Energy Conversion and Management*, 36(6), 539-542. doi:[https://doi.org/10.1016/0196-8904\(95\)00062-1](https://doi.org/10.1016/0196-8904(95)00062-1)
- Holder, G. D., Cugini, A. V., & Warzinski, R. P. (1995). Modeling Clathrate Hydrate Formation during Carbon Dioxide Injection into the Ocean. *Environmental Science & Technology*, 29(1), 276-278. doi:10.1021/es00001a037
- Hong, S., Moon, S., Lee, Y., Lee, S., & Park, Y. (2019). Investigation of thermodynamic and kinetic effects of cyclopentane derivatives on CO<sub>2</sub> hydrates for potential application to seawater desalination. *Chemical Engineering Journal*, 363, 99-106. doi:<https://doi.org/10.1016/j.cej.2019.01.108>
- Hope, C. W. (2006). The marginal impacts of CO<sub>2</sub>, CH<sub>4</sub> and SF<sub>6</sub> emissions. *Climate Policy*, 6(5), 537-544. doi:10.1080/14693062.2006.9685619
- Huang, K. (2008). *Statistical mechanics*: John Wiley & Sons.
- Ishii, M., & Hibiki, T. (2010). *Thermo-fluid dynamics of two-phase flow*: Springer Science & Business Media.
- Javanmardi, J., & Moshfeghian, M. (2003). Energy consumption and economic evaluation of water desalination by hydrate phenomenon. *Applied thermal engineering*, 23(7), 845-857.
- Kabir, M., Habiba, U. E., Khan, W., Shah, A., Rahim, S., Farooqi, Z. U. R., . . . Shafiq, M. (2023). Climate change due to increasing concentration of carbon dioxide and its impacts on environment in 21st century; a mini review. *Journal of King Saud University-Science*, 102693.
- Kang, S.-P., & Lee, H. (2000). Recovery of CO<sub>2</sub> from Flue Gas Using Gas Hydrate: Thermodynamic Verification through Phase Equilibrium Measurements. *Environmental Science & Technology*, 34(20), 4397-4400. doi:10.1021/es001148l
- Karstens, J., Haflidason, H., Berndt, C., & Crutchley, G. J. (2023). Revised Storegga Slide reconstruction reveals two major submarine landslides 12,000 years apart. *Communications Earth & Environment*, 4(1), 55. doi:10.1038/s43247-023-00710-y
- Khan, M. S., Lal, B., Mohamad Sabil, K., & Ahmed, I. (2020). Desalination of Seawater through Gas Hydrate Process: An Overview. *Journal of Advanced Research in Fluid*

---

*Mechanics and Thermal Sciences*, 55(1), 65-73. Retrieved from <https://www.akademiabaru.com/submit/index.php/arfmts/article/view/2458>

- Klauda, J. B., & Sandler, S. I. (2005). Global Distribution of Methane Hydrate in Ocean Sediment. *Energy & Fuels*, 19(2), 459-470. doi:10.1021/ef049798o
- Koh, C., Sum, A., & Sloan, E. (2012). State of the art: Natural gas hydrates as a natural resource. *Journal of Natural Gas Science and Engineering*, 8, 132-138. doi:10.1016/j.jngse.2012.01.005
- Koh, C. A., Sloan, E. D., Sum, A. K., & Wu, D. T. (2011). Fundamentals and Applications of Gas Hydrates. . *Annual Review of Chemical and Biomolecular Engineering*, 2, pp. 237-257.
- Kojima, R., Yamane, K., & Aya, I. (2003). - Dual Nature of CO<sub>2</sub> Solubility in Hydrate Forming Region. In J. Gale & Y. Kaya (Eds.), *Greenhouse Gas Control Technologies - 6th International Conference* (pp. 825-830). Oxford: Pergamon.
- Kumar, R., & Linga, P. (2018). Gas Hydrates. In W. M. White (Ed.), *Encyclopedia of Geochemistry: A Comprehensive Reference Source on the Chemistry of the Earth* (pp. 535-541). Cham: Springer International Publishing.
- Kvamme, B. (2002a). Initiation and growth of hydrate from nucleation theory. *International Journal of Offshore and Polar Engineering*, 12(4), 256-262.
- Kvamme, B. (2002b). Kinetics of hydrate formation from nucleation theory. *International Journal of Offshore and Polar Engineering*, 12(04).
- Kvamme, B. (2003). Droplets of dry ice and cold liquid CO<sub>2</sub> for self-transport of CO<sub>2</sub> to large depths. *International Journal of Offshore and Polar Engineering*, 13(02).
- Kvamme, B. (2019a). Enthalpies of hydrate formation from hydrate formers dissolved in water. *Energies*, 12(6), 1039.
- Kvamme, B. (2019b). Environmentally friendly production of methane from natural gas hydrate using carbon dioxide. *Sustainability*, 11(7), 1964.
- Kvamme, B. (2020). Consistent thermodynamic calculations for hydrate properties and hydrate phase transitions. *Journal of Chemical & Engineering Data*, 65(5), 2872-2893.
- Kvamme, B. (2021). Kinetics of hydrate formation, dissociation and reformation. *Chemical Thermodynamics and Thermal Analysis*, 1-2, 100004. doi:<https://doi.org/10.1016/j.ctta.2021.100004>

- 
- Kvamme, B., Aromada, S. A., Saeidi, N., Hustache-Marmou, T., & Gjerstad, P. (2020). Hydrate nucleation, growth, and induction. *ACS Omega*, 5(6), 2603-2619.
- Kvamme, B., Baig, K., Qasim, M., & Bauman, J. (2013). Thermodynamic and kinetic modeling of CH<sub>4</sub>/CO<sub>2</sub> hydrates phase transitions. *Nano to Micro Scale Modeling of Hydrate Phase Transition Kinetics*.
- Kvamme, B., & Førrisdahl, O. K. (1993). Polar guest-molecules in natural gas hydrates. Effects of polarity and guest-guest-interactions on the Langmuir-constants. *Fluid phase equilibria*, 83, 427-435. doi:[https://doi.org/10.1016/0378-3812\(93\)87047-5](https://doi.org/10.1016/0378-3812(93)87047-5)
- Kvamme, B., Graue, A., Buanes, T., Kuznetsova, T., & Ersland, G. (2007). Storage of CO<sub>2</sub> in natural gas hydrate reservoirs and the effect of hydrate as an extra sealing in cold aquifers. *International Journal of Greenhouse Gas Control*, 1(2), 236-246.
- Kvamme, B., Qasim, M., Baig, K., Kivelä, P.-H., & Bauman, J. (2014). Hydrate phase transition kinetics from Phase Field Theory with implicit hydrodynamics and heat transport. *International Journal of Greenhouse Gas Control*, 29, 263-278.
- Kvamme, B., & Tanaka, H. (1995). Thermodynamic stability of hydrates for ethane, ethylene, and carbon dioxide. *The Journal of Physical Chemistry*, 99(18), 7114-7119.
- Kvenvolden, K. A. (1993). Gas hydrates—geological perspective and global change. *Reviews of Geophysics*, 1,114. doi:<https://doi.org/10.1029/93RG00268Citations>
- Kvenvolden, K. A. (1994). Natural Gas Hydrate Occurrence and Issues. *Annals of the New York Academy of Sciences*, 715(1), 232-246. doi:<https://doi.org/10.1111/j.1749-6632.1994.tb38838.x>
- Lee, Seo, Y., Seo, Y. T., Moudrakovski, I. L., & Ripmeester, J. A. (2003). Recovering methane from solid methane hydrate with carbon dioxide. *Angew Chem Int Ed Engl*, 42(41), 5048-5051. doi:10.1002/anie.200351489
- Lee, H., Ryu, H., Lim, J.-H., Kim, J.-O., Dong Lee, J., & Kim, S. (2016). An optimal design approach of gas hydrate and reverse osmosis hybrid system for seawater desalination. *Desalination and Water Treatment*, 57(19), 9009-9017.
- Lee, M. W., & Collett, T. S. (2011). In-situ gas hydrate hydrate saturation estimated from various well logs at the Mount Elbert Gas Hydrate Stratigraphic Test Well, Alaska North Slope. *Marine and Petroleum Geology*, 28(2), 439-449. doi:<https://doi.org/10.1016/j.marpetgeo.2009.06.007>
- Lee, S., Liang, L., Riestenberg, D., West, O. R., Tsouris, C., & Adams, E. (2003). CO<sub>2</sub> Hydrate Composite for Ocean Carbon Sequestration. *Environmental Science & Technology*, 37(16), 3701-3708. doi:10.1021/es0263011

- 
- Leggett, J. K., & Greenpeace, U. (1990). *Global Warming: The Greenpeace Report*: Oxford University Press.
- Lianna, J., Kim, A. R., Jeong, G., Lee, J.-K., Lee, T. Y., Lim, J.-H., & Won, Y. S. (2016). Salinity Effect on the Equilibria and Kinetics of the Formation of CO<sub>2</sub> and R-134a Gas Hydrates in Seawater. *Korean Journal of Materials Research*, 26(7), 382-387. doi:10.3740/MRSK.2016.26.7.382
- Liu, L., Ryu, B., Sun, Z., Wu, N., Cao, H., Geng, W., . . . Wang, L. (2019). Monitoring and research on environmental impacts related to marine natural gas hydrates: Review and future perspective. *Journal of Natural Gas Science and Engineering*, 65, 82-107. doi:<https://doi.org/10.1016/j.jngse.2019.02.007>
- MacDonald, G. J. (1990). Role of methane clathrates in past and future climates. *Climatic Change*, 16(3), 247-281. doi:10.1007/BF00144504
- Makogon, Y. F. (1965). A gas hydrate formation in the gas saturated layers under low temperature. *Gas Industry*, 5, 14-15.
- Makogon, Y. F., Holditch, S., & Makogon, T. Y. (2007). Natural gas-hydrates—A potential energy source for the 21st Century. *Journal of petroleum science and engineering*, 56(1-3), 14-31.
- Maniavi Falahieh, M., Bonyadi, M., & Lashanizadegan, A. (2021). A new hybrid desalination method based on the CO<sub>2</sub> gas hydrate and capacitive deionization processes. *Desalination*, 502, 114932. doi:<https://doi.org/10.1016/j.desal.2021.114932>
- Maslin, M., Owen, M., Betts, R., Day, S., Dunkley Jones, T., & Ridgwell, A. (2010). Gas hydrates: past and future geohazard? *Philosophical Transactions of the Royal Society A: Mathematical, Physical and Engineering Sciences*, 368(1919), 2369-2393.
- Maslin, M. A., & Thomas, E. (2003). Balancing the deglacial global carbon budget: the hydrate factor. *Quaternary Science Reviews*, 22(15), 1729-1736. doi:[https://doi.org/10.1016/S0277-3791\(03\)00135-5](https://doi.org/10.1016/S0277-3791(03)00135-5)
- Masoudi, R., & Tohidi, B. (2005). *Gas Hydrate Production Technology for Natural Gas Storage and Transportation and CO<sub>2</sub> Sequestration*. Paper presented at the SPE Middle East Oil and Gas Show and Conference. <https://doi.org/10.2118/93492-MS>
- Mathews, S., Daghash, S., Rey, A., & Servio, P. (2022). Recent advances in density functional theory and molecular dynamics simulation of mechanical, interfacial, and thermal properties of natural gas hydrates in Canada. *The Canadian Journal of Chemical Engineering*, 100(9), 2557-2571.



- 
- McIver RD. (1978). Hydrates of Natural Gas—Important Agent in Geologic Processes, . *Houston Geological Society Bulletin*, 20, 3.
- Meisen, A., & Shuai, X. (1997). Research and development issues in CO<sub>2</sub> capture. *Energy Conversion and Management*, 38, S37-S42. doi:[https://doi.org/10.1016/S0196-8904\(96\)00242-7](https://doi.org/10.1016/S0196-8904(96)00242-7)
- Methane Releases From Arctic Shelf May Be Much Larger and Faster Than Anticipated. (2010). *NSF*.
- Milkov, A. V. (2004). Global estimates of hydrate-bound gas in marine sediments: how much is really out there? *Earth-Science Reviews*, 66(3), 183-197. doi:<https://doi.org/10.1016/j.earscirev.2003.11.002>
- Musakaev, N. G., Urazov, R. R., & Shagapov, V. S. (2006). Hydrate formation kinetics in piped natural-gas flows. *Thermophysics and Aeromechanics*, 13(2), 275-281. doi:10.1134/S0869864306020090
- Philibert, J. (2006). One and a half century of diffusion: Fick, Einstein before and beyond.
- Pinero, E., Marquardt, M., Hensen, C., Haeckel, M., & Wallmann, K. (2013). Estimation of the global inventory of methane hydrates in marine sediments using transfer functions. *Biogeosciences*, 10(2), 959-975.
- Politzer, P., & Seminario, J. M. (1995). *Modern density functional theory: a tool for chemistry*: Elsevier.
- Prausnitz, J. M., Lichtenthaler, R. N., & De Azevedo, E. G. (1998). *Molecular thermodynamics of fluid-phase equilibria*: Pearson Education.
- Provatas, N., & Elder, K. (2011). *Phase-field methods in materials science and engineering*: John Wiley & Sons.
- Qasim, M. (2012). *Microscale modeling of natural gas hydrates in reservoirs*. University of Bergen Bergen, Norway,
- Qasim, M., Baig, K., Kvamme, B., & Bauman, J. (2012). Mix Hydrate formation by CH<sub>4</sub>-CO<sub>2</sub> exchange using Phase Field Theory with implicit Thermodynamics. *Nano to Micro Scale Modeling of Hydrate Phase Transition Kinetics*.
- Qasim, M., Kvamme, B., & Baig, K. (2011). Phase field theory modeling of CH<sub>4</sub>/CO<sub>2</sub> gas hydrates in gravity fields. *Nano to Micro Scale Modeling of Hydrate Phase Transition Kinetics*.

- 
- Ruppel, C. D., & Kessler, J. D. (2017). The interaction of climate change and methane hydrates. *Reviews of Geophysics*, 55(1), 126-168. doi:10.1002/2016RG000534
- Saikia T, Patil S, & A., S. (2023). Hydrogen Hydrate Promoters for Gas Storage—A Review. *Energies*. 16(6), 2667. doi: <https://doi.org/10.3390/en16062667>
- Shakhova, N., Semiletov, I. P., Salyuk, A., Yusupov, V. I., Kosmach, D., & Gustafsson, Ö. (2010). Extensive Methane Venting to the Atmosphere from Sediments of the East Siberian Arctic Shelf. *Science*, 327, 1246 - 1250.
- Sloan, D., Creek, J., & Sum, A. K. (2011). Chapter Two - Where and How Are Hydrate Plugs Formed? In D. Sloan, C. Koh, A. K. Sum, A. L. Ballard, J. Creek, M. Eaton, J. Lachance, N. McMullen, T. Palermo, G. Shoup, & L. Talley (Eds.), *Natural Gas Hydrates in Flow Assurance* (pp. 13-36). Boston: Gulf Professional Publishing.
- Sloan, E. D., & Koh, C. A. (2008). Clathrate hydrates of natural gases third edition. *CHEMICAL INDUSTRIES-NEW YORK THEN BOCA RATON-MARCEL DEKKER THEN CRC PRESS*, 119.
- Smith, M., Van Ness, H., Abbot, M., & Swihart, M. (2005). Introduction to Chemical Engineers Thermodynamics. *Chemical Engineering Series, McGraw-Hill*.
- Soave, G. (1972). Equilibrium constants from a modified Redlich-Kwong equation of state. *Chemical Engineering Science*, 27(6), 1197-1203.
- Solomon, D. Q., Manning, Z. Chen, M. Marquis, K. Averyt, M. Tignor. (2007). *The Physical Science Basis., Tech. rep., (2007)*. Retrieved from
- Sum, A. K., Koh, C. A., & Sloan, E. D. (2009). Clathrate Hydrates: From Laboratory Science to Engineering Practice. *Industrial & Engineering Chemistry Research*, 48(16), 7457-7465. doi:10.1021/ie900679m
- Svandal, A. (2006). *Modeling hydrate phase transitions using mean-field approaches*. (PhD). University Of Bergen Bergen, norway.
- Svandal, A., Kvamme, B., Gránàsy, L., Pusztai, T., Buanes, T., & Hove, J. (2006). The phase-field theory applied to CO<sub>2</sub> and CH<sub>4</sub> hydrate. *Journal of crystal growth*, 287(2), 486-490.
- Taheri, Z., Shabani, M. R., Nazari, K., & Mehdizahed, A. (2014). Natural gas transportation and storage by hydrate technology: Iran case study. *Journal of Natural Gas Science and Engineering*, 21, 846-849. doi:<https://doi.org/10.1016/j.jngse.2014.09.026>
- Tegze, G., Pusztai, T., Tóth, G., Gránàsy, L., Svandal, A., Buanes, T., . . . Kvamme, B. (2006). Multiscale approach to CO<sub>2</sub> hydrate formation in aqueous solution: Phase field theory

- 
- and molecular dynamics. Nucleation and growth. *The Journal of chemical physics*, 124(23).
- Tóth, G. I., Pusztai, T., & Gránásy, L. (2015). Consistent multiphase-field theory for interface driven multidomain dynamics. *Physical Review B*, 92(18), 184105. doi:10.1103/PhysRevB.92.184105
- Veluswamy, H. P., Kumar, R., & Linga, P. (2014). Hydrogen storage in clathrate hydrates: Current state of the art and future directions. *Applied energy*, 122, 112-132.
- Vysniauskas, A., & Bishnoi, P. R. (1983). A kinetic study of methane hydrate formation. *Chemical Engineering Science*, 38(7), 1061-1072. doi:[https://doi.org/10.1016/0009-2509\(83\)80027-X](https://doi.org/10.1016/0009-2509(83)80027-X)
- Wang, F., Sum, A. K., & Liu, B. (2021). Editorial: Recent Advances in Promoters for Gas Hydrate Formation. *Front Chem*, 9, 708269. doi:10.3389/fchem.2021.708269
- Wei, N., Sun, W., Meng, Y., Zhao, J., Kvamme, B., Zhou, S., . . . Pei, J. (2020). Hydrate Formation and Decomposition Regularities in Offshore Gas Reservoir Production Pipelines. *Energies*, 13(1). doi:10.3390/en13010248
- Wheeler, A. A., Boettinger, W. J., & McFadden, G. B. (1992). Phase-field model for isothermal phase transitions in binary alloys. *Physical Review A*, 45(10), 7424.
- Waals, J. v. d., & Platteeuw, J. (1958). Clathrate solutions. *Advances in chemical physics*, 1-57.
- Yang, C. N. (1988). Journey through statistical mechanics. *International Journal of Modern Physics B*, 2(06), 1325-1329.
- Yang, M., Zhao, J., Zheng, J.-n., & Song, Y. (2019). Hydrate reformation characteristics in natural gas hydrate dissociation process: A review. *Applied energy*, 256, 113878. doi:<https://doi.org/10.1016/j.apenergy.2019.113878>
- Zhang, P., Wu, Q., & Mu, C. (2017). Influence of temperature on methane hydrate formation. *Scientific Reports*, 7(1), 7904. doi:10.1038/s41598-017-08430-y

## **7. Thesis Papers**



---

## **PAPER II**

### **PHASE-FIELD THEORY OF MULTI-COMPONENT INCOMPRESSIBLE CAHN-HILLIARD LIQUIDS**



# Phase-field theory of multi-component incompressible Cahn-Hilliard liquids

Gyula I. Tóth

*Department of Physics and Technology, University of Bergen,  
Allégaten 55, N-5007 Bergen, Norway and  
Wigner Research Centre for Physics,  
P.O. Box 49, H-1525 Budapest, Hungary\**

Mojdeh Zarifi and Bjørn Kvamme

*Department of Physics and Technology, University of Bergen,  
Allégaten 55, N-5007 Bergen, Norway*

(Dated: December 11, 2015)

In this paper a generalization of the Cahn-Hilliard theory of binary liquids is presented for multi-component incompressible liquid mixtures. First, a thermodynamically consistent convection-diffusion type dynamics is derived on the basis of the Lagrange multiplier formalism. Next, a generalization of the binary Cahn-Hilliard free energy functional is presented for arbitrary number of components, offering the utilization of independent pairwise equilibrium interfacial properties. We show that the equilibrium two-component interfaces minimize the functional, and demonstrate, that the energy penalization for multi-component states increases strictly monotonously as a function of the number of components being present. We validate the model via equilibrium contact angle calculations in ternary and quaternary (4-component) systems. Simulations addressing liquid flow assisted spinodal decomposition in these systems are also presented.

## I. INTRODUCTION

Multi-component liquid mixtures are of continuously increasing scientific and industrial importance. For instance, it has recently been discovered, that controlled pattern formation in ternary colloidal emulsions / polymer mixtures could be used in producing advanced pharmaceuticals, biochemical assays, or templating microporous materials [1, 2]. Multi-component emulsions might also play important role in developing a new, efficient, and environmentally sound enhanced crude oil recovery technique [3–6]. Although numerous theoretical studies addressing binary liquid flows are available, significantly less is known about ternary flows, and desperately less about 4 and more component systems. The continuum descriptions of binary systems undergoing phase separation originate from Cahn and Hilliard [7], and was further improved by Cook [8] and Langer [9, 10]. The binary theory was successfully extended also for ternary systems by de Fontaine [11, 12], Morral and Cahn [13], Hoyt [14, 15], and Maier-Paape et al [16] (for many components), although the latter was applied exclusively for ternary systems. Coupling liquid flow to the Cahn-Hilliard theory is also possible on the basis of the Korteweg stress tensor [17, 18] (also interpreted as the least action principle in statistical physics [19]), and has been done for binary systems by several authors [20–22], thus resulting in a reasonable picture of binary liquids [23], while a liquid-flow coupled generalization of the Cahn-Hilliard model for arbitrary number of components was developed by Kim and Lowengrub [24], and later by Kim [25]. The Kim-Lowengrub model was tested mainly for the ternary

case, while quite limited calculations are available for 4-component systems. Furthermore, as it will be demonstrated in this paper, the construction of neither the free energy functional nor the diffusion equations used by Kim and Lowengrub satisfy all conditions of physical and mathematical consistency, or if so, the constraints on the model parameters strongly limit the applicability of the theory. Therefore, the problem needs further investigation.

The main difficulty in describing many-component flows is finding appropriate extensions of both the thermodynamic functions and the dynamic properties for high-order multiple junctions. This is far from being trivial, mostly due to the lack of microscopic data. Nevertheless, one can extrapolate from the binary interfaces, while keeping physical and mathematical consistency. In case of spinodal decomposition, for example, physical consistency means, that the multi-component states of the material should be energetically less and less favorable with increasing number of components. Consequently, the system should converge to equilibrium configurations showing a single component – binary interface – trijunction topology. The conditions of mathematical consistency can be summarized as the *condition of formal reducibility*, i.e. writing up the model for  $N$  components, then setting the  $N^{\text{th}}$  component to zero should result in the  $N - 1$  component model on the level of *both* the free energy functional and the dynamic equations.

In this work, we formulate such a consistent generalization of the binary Cahn-Hilliard theory for arbitrary number of components, for which (i) the bulk states are absolute minima of the free energy functional, (ii) the two-component equilibrium interfaces represent stable equilibrium, and (iii) the energy of multiple junctions increases as a function of the number of compo-

---

\* Gyula.Toth@ift.uib.no



nents. In addition, the free energy density landscape has no multi-component local minima, therefore, the system cannot get trapped into a multi-component homogeneous state during spinodal decomposition. Furthermore, a convection-diffusion dynamics is also developed, which (i) does not label the variables in principle, and (ii) extends / reduces naturally, when a component is added to / removed from the model.

The paper is structured as follows. In Section II, we define first the relevant variables describing a multi-component liquid flow, together with introducing a general free energy functional formalism. Next, we study equilibrium via the Euler-Lagrange equations, and construct a general convection-diffusion dynamics. The application of the general framework for multi-component spinodal decomposition follows then in Section III. We construct a consistent extension of the binary Cahn-Hilliard free energy functional for arbitrary number of components, and demonstrate both the physical and mathematical consistency of our approach. After presenting the numerical methods in Section IV, the validation of the model follows in Section V, including equilibrium contact angle measurements and modeling spinodal decomposition in both ternary and quaternary systems. The conclusions are summarized in Section VI.

## II. THEORETICAL FRAMEWORK

### A. Energy functional formalism

Consider a system of  $N$  incompressible liquids of unique mass density  $\rho$ . In a mixture of the liquids, the *mass fraction* of component  $i$  reads  $c_i = m_i/m$ , where  $m_i$  is the mass of component  $i$  and  $m = \sum_{i=1}^N m_i$  is the total mass in a control volume  $V$ . The mass fractions then sum up to 1 by definition, i.e.  $\sum_{i=1}^N c_i = 1$ . Taking the limit  $V \rightarrow 0$ , all quantities become local, therefore, the (local and temporal), *conserved* composition fields  $c_i \rightarrow c_i(\mathbf{r}, t)$  characterizing an inhomogeneous system can be introduced. The relation  $\sum_{i=1}^N c_i = 1$  transforms then into the following *local* constraint:

$$\sum_{i=1}^N c_i(\mathbf{r}, t) = 1. \quad (1)$$

Assume that the Helmholtz free energy of the inhomogeneous non-equilibrium system can be expressed as a *functional* of the fields:

$$F = \int dV \{f[c_i(\mathbf{r}, t), \nabla c_i(\mathbf{r}, t)]\}, \quad (2)$$

where the integrand is a function of the fields and their gradients. This type of energy functional is called square gradient theory. In the literature the local constraint is often handled by eliminating one of the components already at the level of the free energy functional, thus

resulting in an unconditional system. In contrast, Eq. (1) is taken into account here by using a Lagrange multiplier as:

$$\tilde{F} := F - \int dV \left\{ \lambda(\mathbf{r}, t) \left[ \sum_{i=1}^N c_i(\mathbf{r}, t) - 1 \right] \right\}, \quad (3)$$

where  $\tilde{F}$  is the *conditional* free energy functional and  $\lambda(\mathbf{r}, t)$  the Lagrange multiplier. In our derivations, we will use this general formalism to derive consistent dynamic equations for the system.

### B. Equilibrium

Equilibrium solutions represent extrema (minimum, maximum or saddle) of the free energy functional, therefore, they can be determined by solving the following Euler-Lagrange equations:

$$\frac{\delta \tilde{F}}{\delta c_i} = \frac{\delta F}{\delta c_i} - \lambda(\mathbf{r}) = \tilde{\mu}_i^0, \quad (4)$$

where  $\delta F/\delta c_i$  is the functional derivative of  $F$  with respect to  $c_i(\mathbf{r})$  ( $i = 1 \dots N$ ), whereas  $\tilde{\mu}_i^0 = [(\delta F/\delta c_i) - \Lambda(\mathbf{r})]_{c_0}$  is a diffusion potential belonging to a homogeneous reference state  $\mathbf{c}_0 = (c_1^0, c_2^0, \dots, c_N^0)$ . Since the variables are conserved, the Lagrange multiplier cannot be expressed directly from Eq. (4). Nevertheless, one can take the gradient of Eq. (4) to eliminate the constant  $\tilde{\mu}_i^0$  [also containing the background value of  $\lambda(\mathbf{r})$ ], yielding

$$\nabla \frac{\delta F}{\delta c_i} = \nabla \lambda(\mathbf{r}), \quad (5)$$

or, equivalently

$$\nabla \left( \frac{\delta F}{\delta c_i} - \frac{\delta F}{\delta c_j} \right) = 0 \quad (6)$$

for any  $(i, j)$  pairs. In general,  $\nabla \lambda(\mathbf{r})$  can be eliminated from Eq. (5) as follows. Multiplying the equations by arbitrary weights  $A_i \neq 0$ , then summing them for  $i = 1 \dots N$  results in:

$$\nabla \lambda(\mathbf{r}) = \sum_{i=1}^N a_i \nabla \frac{\delta F}{\delta c_i}, \quad (7)$$

where  $a_i = A_i / \sum_{k=1}^N A_k \neq 0$  is a normalized coefficient, i.e.  $\sum_{i=1}^N a_i = 1$ . Substituting Eq. (7) into Eq. (5), then re-writing the equations in a matrix form results in

$$(\mathbb{I} - \mathbf{e} \otimes \mathbf{a}) \cdot \nabla \frac{\delta F}{\delta \mathbf{c}} = 0, \quad (8)$$

where  $\mathbb{I}$  is the  $N \times N$  identity matrix,  $\mathbf{e} = (1, 1, \dots, 1)^T$  is a column, while  $\mathbf{a} = (a_1, a_2, \dots, a_N)$  a row vector,  $\otimes$  denotes the dyadic (tensor or direct) product and  $\delta F/\delta \mathbf{c} = (\delta F/\delta c_1, \delta F/\delta c_2, \dots, \delta F/\delta c_N)^T$  is the column

vector of the functional derivatives. Note that the matrix  $\mathbb{A} = \mathbb{I} - \mathbf{e} \otimes \mathbf{a}$  has a *single* eigenvalue  $s = 0$  with eigenvector  $\mathbf{e}$ , thus prescribing equal functional derivative gradients in equilibrium, independently from the weights  $\mathbf{a}$ . (In other words,  $\mathbf{e}$  is the algebraic representation of equilibrium.) Consequently, the solution of Eq. (5) coincides with the solution of Eq. (6) for arbitrary positive  $\{\mathcal{A}_i\}$  weights.

## C. Dynamic equations

### 1. Diffusion equations

The incompressible multi-component flow is governed by a *convection-diffusion* type dynamics. We start the derivation of the kinetic equations following Kim and Lowengrub [24]. The diffusion equations follow from the mass balance for the individual components, thus resulting in [24]:

$$\rho \dot{c}_i = \nabla \cdot \mathbf{J}_i, \quad (9)$$

where  $\dot{c}_i = \partial c_i / \partial t + \mathbf{v} \cdot \nabla c_i$  is the material derivative,  $\mathbf{v} = \sum_{i=1}^N c_i \mathbf{v}_i$  is the mixture velocity, where  $\mathbf{v}_i$  is the individual velocity field of the  $i^{\text{th}}$  component. Furthermore,  $\sum_i \mathbf{J}_i = 0$  applies for the diffusion fluxes, a condition emerging from  $\sum_{i=1}^N c_i(\mathbf{r}, t) = 1 \rightarrow \sum_{i=1}^N \dot{c}_i(\mathbf{r}, t) = 0$ . The diffusion fluxes can be then constructed as

$$\mathbf{J}_i := \nu_i \nabla \tilde{\mu}_i \quad (10)$$

(for example), where  $\nu_i > 0$  is the diffusion mobility of component  $i$ , and  $\tilde{\mu}_i = \delta \tilde{F} / \delta c_i = \delta F / \delta c_i - \Lambda(\mathbf{r}, t)$  is the generalized non-equilibrium chemical potential. Note that in equilibrium  $\tilde{\mu}_i \rightarrow \tilde{\mu}_i^0$  (constant), thus indicating  $\mathbf{J}_i = 0$  and (consequently)  $\dot{c}_i = 0$ . The Lagrange multiplier can be expressed as  $\nabla \Lambda(\mathbf{r}, t) = \sum_{i=1}^N \tilde{\nu}_i \nabla(\delta F / \delta c_i)$ , where  $\tilde{\nu}_i = \nu_i / \sum_{j=1}^N \nu_j > 0$ . Using this in Eq. (9), and introducing  $\nu_i := \kappa_i \Sigma$  (where  $\Sigma = \sum_{k=1}^N \kappa_k$ ) results in

$$\mathbf{J}_i = \sum_{j=1}^N \kappa_{ij} \nabla \left( \frac{\delta F}{\delta c_i} - \frac{\delta F}{\delta c_j} \right), \quad (11)$$

where  $\kappa_{ij} = \kappa_i \kappa_j$ . Comparing Eq. (11) and (6), however, indicates  $\mathbf{J}_i = 0$  in equilibrium for *arbitrary*  $\kappa_{ij}$ 's. The only condition for the mobilities emerges from the symmetry argument, that the variables should not be labeled, where labeling means that the time evolution of the system is not invariant under re-labeling the variables. The condition of no labeling yields [26]

$$\kappa_{ij} = \kappa_{ji}, \quad (12)$$

in agreement with Onsager's approach of multi-component diffusion [27]. In the Appendix of our recent study [26] we pointed out that elimination of

of the variables by setting up  $\mathbf{J}_i \propto (\delta F / \delta c_i) - (\delta F / \delta c_N)$  for  $i = 1 \dots N - 1$  labels the variables in principle, and contradicts to Onsager's reciprocal relations. The only exception is the fully symmetric system, i.e. when all interface thicknesses, interfacial tensions, and dynamic coefficients are equal. Note, that Eq. (11) and Eq. (12) offer a more general form for the constitutive equation than Eq. (10). In the latter we have only  $N$  independent parameters,  $\tilde{\kappa} = (\kappa_1, \kappa_2, \dots, \kappa_N)$ , and the mobility matrix  $\mathbb{L}$  in the general form  $\rho \dot{\mathbf{c}} = \nabla \cdot (\mathbb{L} \cdot \nabla \tilde{\mu})$  emerge from these as  $\mathbb{L} = \tilde{\kappa} \otimes \tilde{\kappa}$ . In contrast, according to Eq. (11) and (12), we may choose  $N(N - 1)/2$  free parameters  $\{\kappa_{ij}\}$  in general, and the elements of the mobility matrix are calculated as  $L_{ii} = \sum_{j \neq i} \kappa_{ij}$ , and  $L_{ij} = -\kappa_{ij}$  for  $i \neq j$ . Although Eq. (10) and (11) coincide in equilibrium, the general construction becomes significant for  $N \geq 4$ , where the number pairs are greater than  $N$ .

The remaining issue which has to be considered is the condition of "formal reducibility" for the dynamic equations. An elegant solution of the problem introducing mobility matrices on geometric basis was published by Bollada, Jimack and Mullis [28]. The authors proposed symmetric mobility matrices reducing formally. For example, in case of  $\kappa_{ij}(c_i, c_j) = [c_i / (1 - c_i)] [c_j / (1 - c_j)]$  the  $k^{\text{th}}$  row and column of the mobility matrix vanish, and the mobility matrix of an  $N - 1$ -component system is recovered. Note, however, that such a mobility matrix can be "dangerous" with respect to the free energy functional, meaning that non-equilibrium states may become stationary, since the equality of the functional derivative gradients is not a necessary condition for a stationary solution. Speaking mathematically more precisely, the eigenvalue  $s = 0$  (representing stationary solution) of the mobility matrix  $\mathbb{L}$  has multiplicity greater than 1 in case of at least 1 vanishing field. The components of the corresponding eigenvectors are equal at the positions of non-vanishing fields, otherwise they are arbitrary. *Therefore, a stationary state of the dynamics does not necessarily represent equilibrium solution.* Nevertheless, as discussed in our recent paper [26], if one can prove that the  $n+m$ -component natural extensions of all equilibrium solutions emerging from the  $n$ -component model also represent equilibrium in the  $n + m$ -component model for any  $n, m \geq 1$ , then the Bollada-Jimack-Mullis matrix is not dangerous with respect to the free energy functional. Having such a functional, although being necessary, is not satisfactory, since the dynamics must satisfy also the *second law of thermodynamics*, i.e. the entropy production rate must be non-negative. This requirement can be addressed by considering the Kim-Lowengrub model in the constant density limit. The condition for the contribution of the diffusion equations to the entropy production rate reads [24]:

$$\sum_{i=1}^N \nabla \tilde{\mu}_i \cdot \mathbf{J}_i \geq 0. \quad (13)$$

Here  $\tilde{\mu}_i = (\delta F / \delta c_i) + p$ , where  $p$  is the non-equilibrium

thermodynamic pressure. According to Eq. (11),  $\mathbf{J}_i = \sum_{j=1}^N L_{ij} \nabla(\delta F / \delta c_j)$ , where  $\sum_{j=1}^N L_{ij} = 0$ , therefore, Eq. (13) results in

$$\sum_{i,j} L_{ij} \left( \nabla \frac{\delta F}{\delta c_i} \cdot \nabla \frac{\delta F}{\delta c_j} \right) \geq 0, \quad (14)$$

thus indicating that the mobility matrix  $\mathbb{L}$  must be *positive semi-definite*. Therefore, the original Bollada-Jimack-Mullis matrix is modified as

$$\kappa_{ij}(c_i, c_j) := \kappa_{ij}^0 \left| \frac{c_i}{1 - c_i} \right| \left| \frac{c_j}{1 - c_j} \right|, \quad (15)$$

where  $\kappa_{ij}^0 > 0$ 's are arbitrary constants. The absolute value is necessary for a simple reason: The solution may slightly leave the physical regime ( $0 \leq c_i \leq 1$  for  $i = 1 \dots N$ ) in the simulations because of numerical reasons. Nevertheless, small perturbations around *stable* equilibrium solutions relax naturally for a positive semi-definite mobility matrix without any further artificial modifications, such as overwriting the solution. This should be true for at least the bulk components and the binary equilibrium interfaces. The positive semi-definiteness of this matrix has been verified numerically case by case for the particular matrices we used in our calculations and simulations.

## 2. Navier-Stokes equation

The velocity field is governed by the following Navier-Stokes equation (emerging from the momentum balance for the components) [24]:

$$\rho \dot{\mathbf{v}} = \nabla \cdot (\mathbb{R} + \mathbb{D}), \quad (16)$$

where  $\mathbb{R}$  and  $\mathbb{D}$  are the reversible and irreversible stresses, respectively. The viscous stress of a multi-component Newtonian liquid can be approximated as:

$$\mathbb{D} = \eta [(\nabla \otimes \mathbf{v}) + (\nabla \otimes \mathbf{v})^T], \quad (17)$$

where  $\eta = \sum_{i=1}^N c_i \eta_i$  is the local shear viscosity, calculated from the viscosities of the bulk components,  $\eta_i$ . Furthermore, the reversible stress has the general Korteweg form [17, 18]:

$$\mathbb{R} = -p \mathbb{I} + \mathbb{A}, \quad (18)$$

where  $\tilde{p}$  is a non-equilibrium generalization of the equilibrium thermodynamic pressure:

$$-p = \tilde{f} - \sum_{i=1}^N c_i \frac{\delta \tilde{F}}{\delta c_i} = -\tilde{p} + \Lambda(\mathbf{r}, t), \quad (19)$$

where  $\tilde{f}$  is the integrand of  $\tilde{F}$  defined by Eq. (3), and  $-\tilde{p} = f - \sum_{x=1}^N c_x (\delta F / \delta c_x)$ . Furthermore,  $\mathbb{A}$  is a general

non-diagonal tensor, which can be determined from the condition of mechanical equilibrium, often formulated as a generalized Gibbs-Duhem relation [19–21]

$$\nabla \cdot \mathbb{R} = - \sum_{i=1}^N c_i \nabla \frac{\delta \tilde{F}}{\delta c_i}. \quad (20)$$

Using Eq. (18) in (20) then yields

$$\mathbb{A} = - \sum_{i=1}^N \left( \nabla c_i \otimes \frac{\partial f}{\partial \nabla c_i} \right), \quad (21)$$

showing that the flow operator does not contain the Lagrange multiplier. This result is in agreement with previous results [24]. Furthermore, since the liquid mixture is incompressible and all the components have the same density, we also have the condition

$$\nabla \cdot \mathbf{v} = 0. \quad (22)$$

Although this condition results in a *degeneracy* in the velocity field, it is resolved by the Lagrange multiplier  $\Lambda(\mathbf{r}, t)$  in Eq. (19).

## III. MULTI-COMPONENT CAHN-HILLIARD LIQUID

### A. Free energy functional

The free energy functional of a general, multi-component Cahn-Hilliard liquid is formulated as:

$$F = \int dV \left\{ f(\mathbf{c}) + \frac{\epsilon^2(\mathbf{c})}{2} \sum_{i=1}^N (\nabla c_i)^2 \right\}, \quad (23)$$

where the *multi-well* free energy landscape  $f(\mathbf{c})$  is constructed as [26]:

$$f(\mathbf{c}) := w(\mathbf{c}) g(\mathbf{c}) + A_3 f_3(\mathbf{c}), \quad (24)$$

where

$$g(\mathbf{c}) = \frac{1}{12} + \sum_{i=1}^N \left( \frac{c_i^4}{4} - \frac{c_i^3}{3} \right) + \frac{1}{2} \sum_{i < j} c_i^2 c_j^2. \quad (25)$$

In Eq. (25), the double sum stands for a summation for all pairs, i.e.  $\sum_{i < j} = \sum_{i=1}^{N-1} \sum_{j=i+1}^N$ . Following Kazaryan [29], the coefficients  $w(\mathbf{c})$  and  $\epsilon^2(\mathbf{c})$  interpolating between the component pairs read as:

$$w(\mathbf{c}) = \frac{\sum_{i < j} w_{ij} c_i^2 c_j^2}{\sum_{i < j} c_i^2 c_j^2} \quad \text{and} \quad \epsilon^2(\mathbf{c}) = \frac{\sum_{i < j} \epsilon_{ij}^2 c_i^2 c_j^2}{\sum_{i < j} c_i^2 c_j^2}. \quad (26)$$

Furthermore, the "triplet" term is defined as:

$$f_3(\mathbf{c}) := \sum_{i < j < k} |c_i| |c_j| |c_k|, \quad (27)$$

where the sum is for all different  $(i, j, k)$  triplets, i.e.  $i \neq j$ ,  $i \neq k$ , and  $j \neq k$ ,  $i, j, k = 1 \dots N$ . The usual (Gibbs-simplex) representation of the free energy landscape is shown in Fig. 1(a)-(d) for symmetric and asymmetric ternary systems, in case of  $A_3 = 0$  and  $A_3 \neq 0$ , respectively. We note, that similar terms are used by some authors [30, 31] to control the presence of the third component at binary interfaces, however, our approach is quite different than theirs, as it will be shown.

## B. Interfaces, energy hierarchy and stability

When exactly two components are present, i.e.  $c_i(\mathbf{r}) + c_j(\mathbf{r}) = 1$  for  $i \neq j$ , and  $c_k = 0$  for all  $k \neq i, j$ , Eq. (23) reduces to the usual binary Cahn-Hilliard free energy functional:

$$F_{ij} = \int dV \{w_{ij}[c(1-c)]^2 + \epsilon_{ij}^2(\nabla c)^2\}, \quad (28)$$

therefore,  $\epsilon_{ij}^2$ 's and  $w_{ij}$ 's can be related to the interfacial tension ( $\sigma_{ij}$ ) and interface thickness ( $\delta_{ij}$ ) as:

$$w_{ij} = 3(\sigma_{ij}/\delta_{ij}) \quad \text{and} \quad \epsilon_{ij}^2 = 3(\sigma_{ij}\delta_{ij}), \quad (29)$$

where the interface thickness is defined by the binary equilibrium interface solution

$$c_{ij}(x) = \{1 + \tanh[x/(2\delta_{ij})]\}/2, \quad (30)$$

while the interfacial tension reads

$$\sigma_{ij} = \int_{-\infty}^{+\infty} dx \{w_{ij}[c_{ij}(x)]^2[1 - c_{ij}(x)]^2 + \epsilon_{ij}^2[\partial_x c_{ij}(x)]^2\}. \quad (31)$$

The general functional defined by Eq. (23) has two practical features:

- $F$ , together with  $\delta F/\delta c_i$  reduce formally, i.e. writing up  $F$  (and  $\delta F/\delta c_i$ ) for  $N$  fields, then applying  $c_N \equiv 0$  results in the expressions derived directly in the  $N - 1$ -component model. This, together with Eq. (15) result in the formal reducibility of the dynamic equations too;
- All two-component equilibrium interfaces  $c_{kl}(x) = \{[1 + \tanh[x/(2\delta_{kl})]]\}/2$  represent equilibrium in the complete,  $N$ -component model. In other words, the binary planar interfaces represent equilibrium in the  $N$ -component system (see Appendix A for details).

We mention, that the latter does not apply for almost any of previous multiphase/multicomponent descriptions [26]. Nevertheless, it is an essential feature because of the followings: Eq. (30) represents only a *conditional* extremum, since it is calculated in the  $c_i(\mathbf{r}) + c_j(\mathbf{r}) = 1$  binary subspace. Therefore, there's no guarantee that it is also a solution of the complete variational problem defined by Eq (6). In case of several existing multiphase descriptions the case is indeed this, the equilibrium

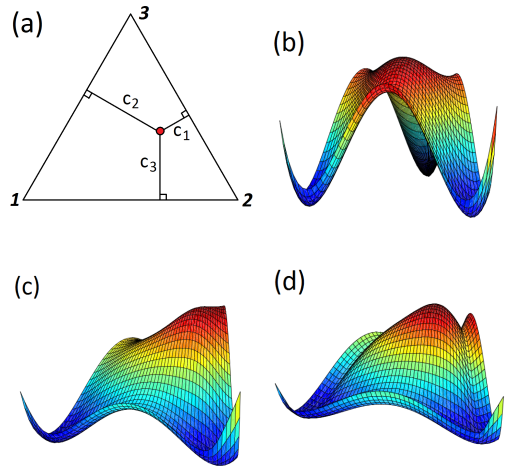


FIG. 1. Gibbs simplex and free energy landscapes  $f(\mathbf{c})$  in ternary systems. (a) Gibbs simplex in a ternary system. The compositions in the red dot are measured perpendicular to the edges of the triangle. If all the edges measure 1 unit,  $c_1 + c_2 + c_3 = 1$ . The vertices (denoted by bold numbers) correspond to bulk components, i.e.  $c_i = 1$  at vertex  $i$ , where  $i = 1, 2, 3$ . (b) Free energy density in the symmetric system without triplet term (i.e.  $A_3 = 0$ ). (c-d) Free energy landscapes in an asymmetric ternary system ( $w_{12} = 1.5 w_0$ ,  $w_{13} = 1.0 w_0$ ,  $w_{23} = 0.5 w_0$ ) in case of  $A_3 = 0$  (panel c) and  $A_3 = 1.0 w_0$  (panel d). The minima of the free energy landscapes correspond to the vertices of the Gibbs simplex displayed in panel a.

two-component interfaces do not represent equilibrium of the general,  $N$ -component model, due to the inconsistent generalization of the free energy functional. The problem is resolved on various ways, including the introduction of non-variational dynamics / degenerated mobility matrix, or penalizing free energy terms for ternary states, as also discussed in details in our recent work [26]. In contrast, our description is totally free of these artificial modifications.

In a symmetric system ( $\epsilon_{ij}^2 \equiv \epsilon_0^2$  and  $w_{ij} \equiv w_0$ ) without triplet energy contribution ( $A_3 = 0$ ), Eq. (24) is a finite-degree polynomial penalizing the multi-component states as follows:

$$f(\mathbf{c}_n) = \frac{1}{12} \left(1 - \frac{1}{n^2}\right), \quad (32)$$

where  $\mathbf{c}_n = \mathcal{P}[\{1/n, 1/n, \dots, 1/n, 0, 0, \dots, 0\}]$ . Here  $\mathcal{P}[\dots]$  stands for an arbitrary permutation of the components of the vector argument  $\{c_1, c_2, \dots, c_N\}$ , where  $n$  elements have the value  $1/n$  and all the others are 0, while  $n = 1 \dots N$ . Eq. (24) then penalizes equally the  $n$ -component states, and the energy increases strictly monotonously as a function of the number of components being present.

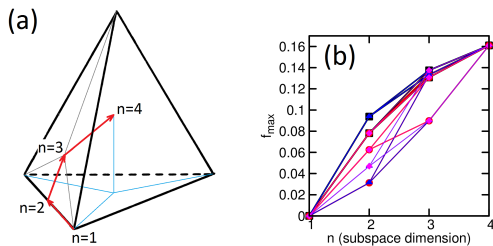


FIG. 2. Degeneracy of the subspace extrema in an asymmetric quaternary system ( $w_{12} = 1.25 w_0$ ,  $w_{13} = 1.5 w_0$ ,  $w_{23} = 0.5 w_0$ ,  $w_{14} = 1.25 w_0$ ,  $w_{24} = 1.0 w_0$ ,  $w_{34} = 0.75 w_0$ ), for  $A_3 = 1.0 w_0$ . (a) A possible path starts in a vertex ( $n = 1$ ) representing the absolute minimum of the free energy density, then passes the location of a binary ( $n = 2$ ) and a ternary ( $n = 3$ ) maximum, while finally arrives at the location of the single quaternary ( $n = 4$ ) maximum, which is the absolute maximum of the free energy density. (b) Sequences of subspace extrema along all possible paths illustrated in panel a.

This feature also applies for *arbitrary*  $A_3 \geq 0$  in the symmetric system for the triplet term defined by Eq. (27) (see Appendix B for the derivation).

Interestingly, the strictly monotonous tendency of the subspace extrema seems to be valid even for asymmetric systems, however, both  $f(c_n)$  and  $c_n$  have now degeneracy, since both the location and the value of the subspace maxima can be different. This is illustrated in Fig. 2, which shows the degenerated hierarchy of the subspace extrema in case of asymmetry for  $N = 4$ . Since the  $n = 2$  and 3-component subspace maxima of the Gibbs simplex now can be different, one can define a "path" on the Gibbs simplex as follows. A path starts in a vertex (representing a bulk component), then jumps to the location of the maximum of one of the connecting edges [denoted by  $n = 1$  and  $n = 2$  in Fig. 2(a), respectively]. From here, we jump to the location of the maximum of one of the connecting planes ( $n = 3$ ), while the final point is the location of the global maximum inside the tetrahedron. Fig. 2(b) shows the energy density in the subspace maxima (symbols) along all possible bulk  $\rightarrow$  binary  $\rightarrow$  ternary  $\rightarrow$  quaternary paths (denoted by the connecting lines). It seems that all the 24 possible paths prescribe strictly monotonously increasing energy sequence. If the free energy landscape does not have any other extrema, and all the extrema except the vertices represent maxima, then this behavior, together with the fact, that the free energy functional penalizes any spatial variation of the fields, suggest, that an  $N$ -component system undergoes spinodal decomposition, and without becoming trapped into a high-order state, i.e., the system never prefers high order multiple junctions, independently from the number of components.

Although we constructed a free energy functional, which is expected to result in spinodal decomposition for an energy minimizing dynamics, and for which the

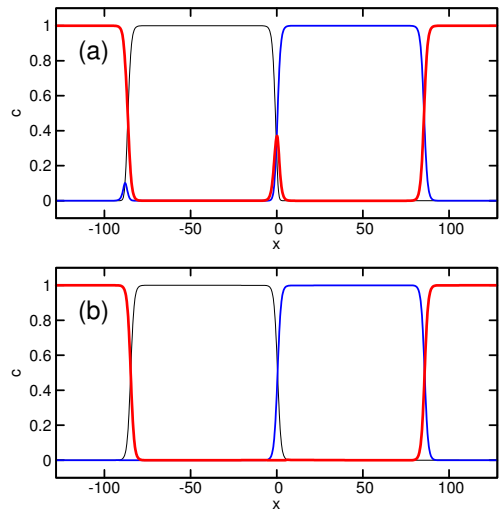


FIG. 3. Two-component equilibrium interfaces in an asymmetric ternary system ( $w_{12} = 1.5 w_0$ ,  $w_{13} = 1.0 w_0$ ,  $w_{23} = 0.5 w_0$ ) in case of (a)  $A_3 = 0$  and (b)  $A_3 = 1.0 w_0$ . Note that, in case of  $A_3 = 0$ ,  $c_3$  (thick red) and  $c_2$  (normal blue) appear on the (1, 2) and (1, 3) interfaces, respectively, while  $c_1$  (thin black) does not appear on the (2, 3) interface, which has the lowest energy. Applying the triplet term then prevents the appearance of the third component at any two-component interfaces.

binary planar interfaces together with the bulk states are equilibrium solutions, the interfaces may become unstable in case of asymmetry for  $A_3 = 0$ . The reason is, that the  $A_3 = 0$  free energy landscape is "weak" for the multi-component states, meaning that the energy increases too slowly as a function of  $n$ : the energy difference between  $f(1, 0, \dots)$  and  $f(1/2, 1/2, 0, \dots)$  is much more significant than that of between  $f(1/2, 1/2, 0, \dots)$  and  $f(1/3, 1/3, 1/3, 0, \dots)$  [and so on, see Fig. 1(b) and Eq. (32)]. This means, that in case of asymmetry [see Fig. 1(c)], the shift in the location of three-component maximum can be significant, and therefore it can destabilize the binary planar interface on the closest edge (or, as a matter of fact, on any other edges, except the one with the lowest interfacial tension). To stabilize the (otherwise equilibrium) binary planar interfaces, we apply the triplet term described by Eq. (27). Choosing a sufficiently large amplitude  $A_3$  shifts the location and increases the value of the ternary maximum of the free energy landscape [see Fig 1(d)], thus resulting in the restabilization of the interfaces. The phenomenon is also illustrated in Fig 3. The figure shows the numerical solution of the 1-dimensional Euler-Lagrange problem in an asymmetric ternary system for  $A_3 = 0$  [panel (a)] and  $A_3 \neq 0$  [panel (b)]. We used finite difference method

with explicit time stepping to solve the Euler-Lagrange problem  $\nabla(\delta F/\delta c_i) = \nabla(\delta F/\delta c_j)$ , together with periodic boundary conditions. As one can see, the third component appears at both the (1, 2) and (1, 3) interfaces in case of  $A_3 = 0$  [see panel (a)], showing that the free energy landscape is weak with respect to the gradient term, and the binary planar interfaces, although representing equilibrium, are not stable. The only stable interface is the (2, 3) interface, which has the lowest energy. Nevertheless, choosing  $A_3 = 1$  solves the problem [see panel (b)], since as the three-component maximum of the free energy landscape increases, the interfaces become stable.

Summarizing, Eq. (23) prescribes a multi-component free energy functional, which results in stable bulk states and binary interfaces in equilibrium, even for asymmetric systems, while high-order multiple states are penalized increasingly as a function of the components. This behavior results in spinodal decomposition in a system of arbitrary number of components. Therefore, Eq. (23) is a suitable generalization of the binary Cahn-Hilliard free energy functional. The triplet term  $f_3(\mathbf{c})$  has no effect on the bulk ( $n = 1$ ) and binary states ( $n = 2$ ), and on the structure and hierarchy of the subspace extrema of the free energy landscape, but controls the energy of multi-component (ternary and up) states. Therefore, it is an ideal tool to control the *stability* of the binary planar interfaces.

### C. Parameters and scaling

To anchor the mobilities  $\kappa_{ij}^0$  in Eq. (15) to measurable quantities, we first take Eq. (9) in the binary limit  $c_i = u$ ,  $c_j = 1 - u$ , and  $c_k = 0$  for  $i \neq j$  and  $k \neq i, j$ . In case of  $\mathbf{v} = 0$  it yields

$$\rho \frac{\partial u}{\partial t} = \kappa_{ij}^0 \nabla \frac{\delta F}{\delta u} , \quad (33)$$

and  $\partial c_k/\partial t = 0$  for  $k \neq i, j$ . The functional derivative reads  $\delta F/\delta u = 2 \{w_{ij}[u(1-u)(1-2u)] - \epsilon_{ij}^2 \nabla^2 u\}$ . For  $u = \delta u \rightarrow 0$ , Eq. (33) becomes  $\rho(\partial_t \delta u) = 2\kappa_{ij}^0 w_{ij}(\nabla^2 \delta u)$ , yielding thus the diffusion constant  $D_{ij} = (2\kappa_{ij}^0 w_{ij})/\rho$  of the  $i^{\text{th}}$  component in the bulk  $j^{\text{th}}$  component. The mobility is then related to the diffusion constant via

$$\frac{2w_{ij}\kappa_{ij}^0}{D_{ij}} = \frac{2w_{ij}\kappa_{ij}^0}{D_{ji}} = \rho , \quad (34)$$

where the second equation emerges from the symmetry of  $\kappa_{ij}^0$ . Therefore, the diffusion constant of the  $j^{\text{th}}$  component in the  $i^{\text{th}}$  one is the same as that of the  $i^{\text{th}}$  component in the  $j^{\text{th}}$  one in our approach. Scaling the length as  $\mathbf{r} := \lambda \hat{\mathbf{r}}$ , and introducing  $D_{ij} := D_0 \hat{D}_{ij}$  yields the time scale  $\tau = \lambda^2/D_0$  in  $t := \tau \hat{t}$ , while using  $w_{ij} := w_0 \hat{w}_{ij}$ , and  $\epsilon_{ij}^2 := \epsilon_0^2 \hat{\epsilon}_{ij}^2$  result in the dimensionless diffusion equations

$$\frac{dc_i}{d\hat{t}} = \hat{\nabla} \cdot \hat{\mathbf{J}}_i . \quad (35)$$

The dimensionless diffusion fluxes read

$$\hat{\mathbf{J}}_i = \sum_{j=1}^N \hat{\kappa}_{ij}^0 h(c_i, c_j) \hat{\nabla} \left( \frac{\delta \hat{F}}{\delta c_i} - \frac{\delta \hat{F}}{\delta c_j} \right) \quad (36)$$

$$\frac{\delta \hat{F}}{\delta c_i} = \frac{\partial(\hat{w}g + \hat{A}_3 f_3)}{\partial c_i} + \frac{\delta_0^2}{\lambda^2} \left[ \frac{\partial \hat{\epsilon}^2}{\partial c_i} (\hat{\nabla} \mathbf{c})^2 - \hat{\epsilon}^2 \hat{\nabla}^2 c_i \right] \quad (37)$$

where  $\delta_0^2 = \epsilon_0^2/w_0$ . Furthermore,  $h(c_i, c_j) = |c_i/(1-c_i)| |c_j/(1-c_j)|$  and

$$2\hat{\kappa}_{ij}^0 = \hat{D}_{ij}/\hat{w}_{ij} . \quad (38)$$

The dimensionless coefficients read as

$$\hat{w} = \frac{\sum_{i<j} \hat{w}_{ij} c_i^2 c_j^2}{\sum_{i<j} c_i^2 c_j^2} \quad \text{and} \quad \hat{\epsilon}^2 = \frac{\sum_{i<j} \hat{\epsilon}_{ij}^2 c_i^2 c_j^2}{\sum_{i<j} c_i^2 c_j^2} , \quad (39)$$

while  $\hat{A}_3 = A_3/w_0$ . Introducing the dimensionless interfacial tensions  $\sigma_{ij} := \sigma_0 \hat{\sigma}_{ij}$  and interface thicknesses  $\delta_{ij} := \delta_0 \hat{\delta}_{ij}$ , and considering  $\epsilon_{ij}^2 = 3(\sigma_{ij} \delta_{ij})$  and  $w_{ij} = 3(\sigma_{ij}/\delta_{ij})$  yield the scales

$$\epsilon_0^2 = 3(\sigma_0 \delta_0) \quad \text{and} \quad w_0 = 3(\sigma_0/\delta_0) , \quad (40)$$

and

$$\hat{\epsilon}_{ij}^2 = \hat{\sigma}_{ij} \hat{\delta}_{ij} \quad \text{and} \quad \hat{w}_{ij} = \hat{\sigma}_{ij}/\hat{\delta}_{ij} . \quad (41)$$

Furthermore,  $\epsilon_0^2/w_0 = \delta_0^2$  in Eq. (37). The dimensionless Navier-Stokes equation reads:

$$\frac{d\hat{\mathbf{v}}}{d\hat{t}} = \hat{\nabla} \cdot \hat{\mathbb{P}} , \quad (42)$$

where

$$\hat{\mathbb{P}} = \hat{\mathbf{a}} \hat{\mathbb{A}}(\mathbf{c}) + \hat{\eta} \hat{\mathbb{D}}(\hat{\mathbf{v}}) . \quad (43)$$

Here the dimensionless flow field generator  $\hat{\mathbb{A}}(\mathbf{c})$  and the viscous stress  $\hat{\mathbb{D}}(\hat{\mathbf{v}})$  read:

$$\hat{\mathbb{A}}(\mathbf{c}) = -\hat{\epsilon}^2 \sum_{i=1}^N (\hat{\nabla} c_i \otimes \hat{\nabla} c_i) \quad (44)$$

$$\hat{\mathbb{D}}(\hat{\mathbf{v}}) = (\hat{\nabla} \otimes \hat{\mathbf{v}}) + (\hat{\nabla} \otimes \hat{\mathbf{v}})^T , \quad (45)$$

respectively, whereas the dimensionless amplitudes are

$$\hat{\mathbf{a}} = \frac{3\sigma_0 \delta_0}{D_0 \rho} \quad \text{and} \quad \hat{\eta} = \frac{\eta}{D_0 \rho} . \quad (46)$$

Finally, the incompressibility condition simply becomes

$$\hat{\nabla} \cdot \hat{\mathbf{v}} = 0 . \quad (47)$$

#### IV. NUMERICAL METHOD

The system of dynamic equations described by (35), (42) and (47) are solved numerically on a fully periodic 2-dimensional domain by using an operator-splitting based quasi-spectral semi-implicit time stepping scheme [32] combined with the spectral Chorin's projection method as follows. The dynamic equations can be re-written in the form

$$\frac{\partial \mathbf{y}}{\partial t} = \mathbf{f}(\mathbf{y}, \nabla \mathbf{y}) , \quad (48)$$

where  $\mathbf{y} = (c_1, c_2, \dots, c_n, v_x, v_y)$ , and  $\mathbf{f}(\mathbf{y}, \nabla \mathbf{y})$  is the (generally nonlinear) right-hand side.  $\mathbf{f}(\mathbf{y}, \nabla \mathbf{y})$  is calculated at time point  $t$ , while  $\partial y_i / \partial t$  is discretized simply as

$$\frac{\partial y_i}{\partial t} \approx \frac{y_i^{t+\Delta t} - y_i^t}{\Delta t} . \quad (49)$$

Next, we add the general linear term  $\hat{s}[y_i] = \sum_{i=1}^{\infty} (-1)^i s_i \nabla^{2i} y_i$  (where  $s_i \geq 0$ ) to both sides of Eq. (48). We consider this term at  $t + \Delta t$  at the left-hand side, but at  $t$  on the right-hand side of the equation. This concept, together with Eq. (49) results in the following, explicit spectral time stepping scheme:

$$y_i^{t+\Delta t}(\mathbf{k}) = y_i^t(\mathbf{k}) + \frac{\Delta t}{1 + s_i(\mathbf{k})\Delta t} \mathcal{F}\{f_i[\mathbf{y}^t(\mathbf{r}), \nabla \mathbf{y}^t(\mathbf{r})]\} , \quad (50)$$

where  $s_i(\mathbf{k}) = \sum_{j=1}^{\infty} s_j^{(i)}(\mathbf{k}^2)^j$ , and  $\mathcal{F}\{\cdot\}$  stands for the Fourier transform. The *splitting constants*  $\{s_j^{(i)}\}$  must be chosen so that Eq. (50) is stable. Suitable splitting constants can be found by expanding the right-hand side of the differential equations, then identifying terms of the form  $(-1)^{n+1} f(\mathbf{y}) \nabla^{2n} y_i$  in the equation for  $y_i$ .  $\max\{0, \max\{f(\mathbf{y})\}\}$  then provides a theoretical splitting constant  $\hat{s}_n^{(i)}$ . Since the equations are coupled and highly non-linear, a unique experimental multiplier  $s$  is applied, i.e. the splitting constants are chosen as  $s_n^{(i)} := s \hat{s}_n^{(i)}$ . In our case, we used  $s = 5$ .

Considering the Navier-Stokes equation, note that the new velocity field  $\mathbf{v}^{t+\Delta t}(\mathbf{k})$  does not satisfy Eq. (47) in general. Introducing  $\mathbf{v}^{t+\Delta t} := \mathbf{v}^* + \delta \mathbf{v}$ , where  $\mathbf{v}^*$  is calculated from Eq. (50), and the correction is given in the form  $\delta \mathbf{v} := \nabla s(\mathbf{r})$ , where  $s(\mathbf{r})$  is a scalar field, and using Eq. (47) yields the spectral solution

$$\delta \mathbf{v}(\mathbf{k}) = -\frac{\mathbf{k} \otimes \mathbf{k}}{\mathbf{k}^2} \cdot \mathbf{v}^*(\mathbf{k}) . \quad (51)$$

Using Eqns. (50) and (51), the velocity field is then generated by the following sequence:

$$\mathbf{v}^*(\mathbf{k}) = \mathbf{v}^t(\mathbf{k}) + \frac{\Delta t}{1 + s_v(\mathbf{k})\Delta t} \mathcal{F}\{\mathbf{f}^t(\mathbf{r})\} \quad (52)$$

$$\mathbf{v}^{t+\Delta t}(\mathbf{k}) = [\mathbb{I} - \mathbb{P}(\mathbf{k})] \cdot \mathbf{v}^*(\mathbf{k}) , \quad (53)$$

where  $s_v(\mathbf{k})$  is a splitting function emerging from the viscous stress,  $\mathbf{f}^t(\mathbf{r}) = \nabla \cdot \hat{\mathbb{P}}$ , where  $\hat{\mathbb{P}}$  defined by Eq.

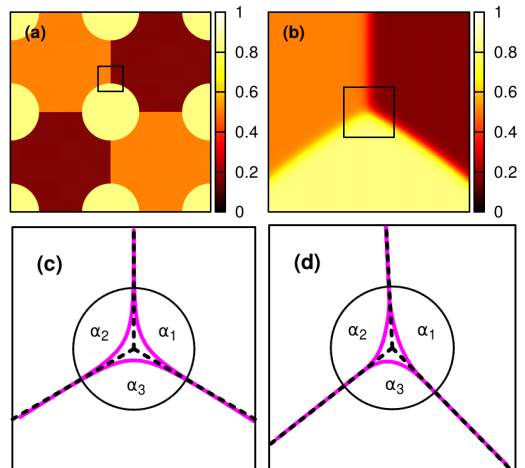


FIG. 4. Contact angle measurement in a ternary system: (a) Initial condition, and (b) converged (equilibrium) solution in a symmetric system in the area indicated by the black square on panel a. On both panels  $\sum_{i=1}^3 c_i(\mathbf{r})[(i - 0.5)/3]$  is shown. (c) Contour lines  $[c_i(\mathbf{r}) = 0.5]$  of the fields at a trijunction in the area indicated by the black square on panel b, and (d) the same as panel c in case of asymmetric system.

(43), while  $\mathbb{P}(\mathbf{k}) = (\mathbf{k} \otimes \mathbf{k})/\mathbf{k}^2$  is the operator generating the divergent part of a vector field. Indeed, in Eq. (53)  $\mathbb{I} - \mathbb{P}(\mathbf{k})$  eliminates the divergence of  $\mathbf{v}^*$ .

It is important to note that our numerical scheme is *unbounded*, meaning that the spatial solution  $c_i(\mathbf{r}, t)$  might become negative or greater than 1 because of numerical errors. Nevertheless, the construction of the free energy functional and the modified Bollada-Jimack-Mullis mobility matrix ensure that no artificial modification of the solution is needed after a time step, as discussed before. Instead, the system naturally finds the bulk states and the two-component interfaces. Finally we mention, that the generalized Chorin's projection method presented here is compatible with equilibrium. In equilibrium the diffusion fluxes vanish, i.e.  $\mathbf{J}_i = 0$  for  $i = 1 \dots N$ , resulting in  $\dot{\mathbf{c}} = 0$ . Furthermore,  $\nabla \cdot \hat{\mathbb{A}}$  becomes the gradient of a scalar function in equilibrium, which is then eliminated by the Chorin's projection method (i.e. no flow is generated). Since the viscous term vanish for a homogeneous velocity field,  $\mathbf{v}(\mathbf{r}) = \text{const}$  is the general equilibrium solution.

#### V. RESULTS

The numerical simulations were performed on a 2-dimensional, uniform rectangular grid with spatial resolution  $h = 0.5$  and different time steps. The phys-

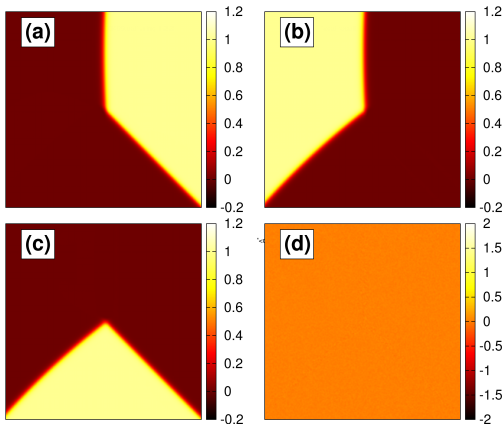


FIG. 5. Spatial distribution of the individual components (a-c) in the vicinity of the equilibrium trijunction in an asymmetric ternary system, and (d) error of the local sum of the variables,  $\epsilon := 10^{14} [\sum_{i=1}^3 c_i(\mathbf{r}) - 1]$ . Note that the third component is not present at the binary interfaces, while the error of the local sum is negligible.

ical parameters were chosen to model realistic binary, ternary and quaternary (4-component) systems mimicking the oil/water/CO<sub>2</sub> interfaces. The scales then read  $\rho = 1000 \text{ kg/m}^3$ ,  $D_0 = 5 \times 10^{-10} \text{ m}^2/\text{s}$ ,  $\sigma_0 = 50 \text{ mJ/m}^2$ ,  $\delta_0 = 1.25 \text{ \AA}$ , and

$$\eta(\mathbf{c}) := \eta_0 \sum_{i=1}^N c_i x_i, \quad (54)$$

where  $x_i = \eta_i/\eta_0$ , and the viscosity scale reads  $\eta_0 = 1 \text{ mPas}$ .

### A. Contact angles

The validation of the model started with equilibrium contact angle measurements in both symmetric ( $\hat{\sigma}_{ij} = \hat{\delta}_{ij} = 1$ ) and asymmetric systems. As discussed in Section III, the function  $h(c_i, c_j) = |c_i/(1-c_i)||c_j/(1-c_j)|$  in Eq. (36) might generate "dangerous" solutions (i.e. stationary solutions which do not represent equilibrium), therefore, the dynamic equations were solved by applying  $h(c_i, c_j) \equiv 1$  (and  $\hat{\kappa}_{ij} = 1/2$ ) in this case. Since we are interested exclusively in equilibrium, but not the time evolution of the system, this step does not influence the results. The initial condition for the velocity field was  $\mathbf{v}(\mathbf{r}, 0) = 0$ , while the initial distribution of the components is shown in Fig. 4(a). For better visualization,  $h_3(\mathbf{r}, t) := \sum_{i=1}^3 c_i(\mathbf{r}, t)[(i-0.5)/3]$  is shown, thus indicating bulk components at  $h = 1/6, 1/2$  and  $5/6$  for  $i = 1, 2$  and  $3$ , respectively. The calculations were performed on

a  $1024 \times 1024$  grid with time step  $\Delta t = 0.001$ . After  $10^6$  time steps the flow field vanished, and the system practically reached equilibrium [the convergence criterion for equilibrium was  $\bar{v} := 1/(N_x N_y) \sum_{i,j} \sqrt{\mathbf{v}_{i,j}^2} < 10^{-4}$  for the average velocity, which corresponds to 1 pixel shift in the solution in  $10^6$  time steps]. The amplitude of the triplet term was  $A_3 = 0$  and  $1/2$  in the symmetric and asymmetric system, respectively.

In order to measure the contact angles at a trijunction, we plotted the  $c_i(\mathbf{r}) = 1/2$  contours for  $i = 1, 2$  and  $3$ , as shown in Fig. 4(c), then fitted straight lines (dashed in the figure) for the unperturbed binary interfaces ("far" from the trijunction). The crossing point of these lines defines the trijunction point. As expected, the contact angle  $\alpha_1 = \alpha_2 = \alpha_3 = 120^\circ$  was detected in the symmetric system. In contrast, asymmetric systems establish different contact angles. For instance, for the interface tensions  $\hat{\sigma}_{12} = 1.2$ ,  $\hat{\sigma}_{13} = 1.0$  and  $\hat{\sigma}_{23} = 0.8$  (the corresponding interface thicknesses were  $\hat{\delta}_{12} = 1.1$ ,  $\hat{\delta}_{13} = 0.9$  and  $\hat{\delta}_{23} = 1.0$ , respectively), the theoretical contact angles can be determined from the condition of mechanical equilibrium, yielding:

$$\alpha_1^0 = \pi - \cos^{-1} \left( \frac{\hat{\sigma}_{12}^2 + \hat{\sigma}_{13}^2 - \hat{\sigma}_{23}^2}{2\hat{\sigma}_{12}\hat{\sigma}_{13}} \right) = 138.6^\circ \quad (55)$$

$$\alpha_2^0 = \pi - \cos^{-1} \left( \frac{\hat{\sigma}_{12}^2 + \hat{\sigma}_{23}^2 - \hat{\sigma}_{13}^2}{2\hat{\sigma}_{12}\hat{\sigma}_{23}} \right) = 124.23^\circ \quad (56)$$

$$\alpha_3^0 = \pi - \cos^{-1} \left( \frac{\hat{\sigma}_{13}^2 + \hat{\sigma}_{23}^2 - \hat{\sigma}_{12}^2}{2\hat{\sigma}_{13}\hat{\sigma}_{23}} \right) = 97.181^\circ. \quad (57)$$

From the simulation, the contact angles  $\alpha_1 = 137.3^\circ$ ,  $\alpha_2 = 126.37^\circ$ , and  $\alpha_3 = 96.33^\circ$  have been measured [see Fig 4(d)], showing then 1.7% maximal relative error compared to the theoretical values, which can be attributed to the uncertainty of the measurement.

Figure 5 shows the individual compositions (panels a-c) and the sum of the fields (panel d) in the neighborhood of the trijunction displayed in Figure 4(d). The spatial distribution of the individual fields demonstrate the effect of the triplet term. In accordance with Figure 3(b) and 4(d), all of the two-component interfaces are practically free of the third component. Furthermore, Figure 5(d) shows that the error of the local sum of the variables is in the range of the truncation error of double precision floating point numbers.

The calculations were repeated in an asymmetric 4-component (quaternary) system as well (see Fig 6), with  $\hat{\sigma}_{12} = 1.0$ ,  $\hat{\sigma}_{13} = 1.1$ ,  $\hat{\sigma}_{14} = 0.75$ ,  $\hat{\sigma}_{23} = 0.9$ ,  $\hat{\sigma}_{24} = 1.25$  and  $\hat{\sigma}_{34} = 1.0$ . The interface thicknesses were equal, i.e.  $\hat{\delta}_{ij} = 1.0$  was used, while the amplitude of the triplet term was  $A_3 = 1$ . The contact angle measurements resulted in less than 1.5% relative error again compared to the theoretical values for all the 4 different trijunctions [illustrated in Fig 6(c)-(f)]. According to our experience, the unperturbed binary planar interfaces contain no additional components, similarly to the ternary case.



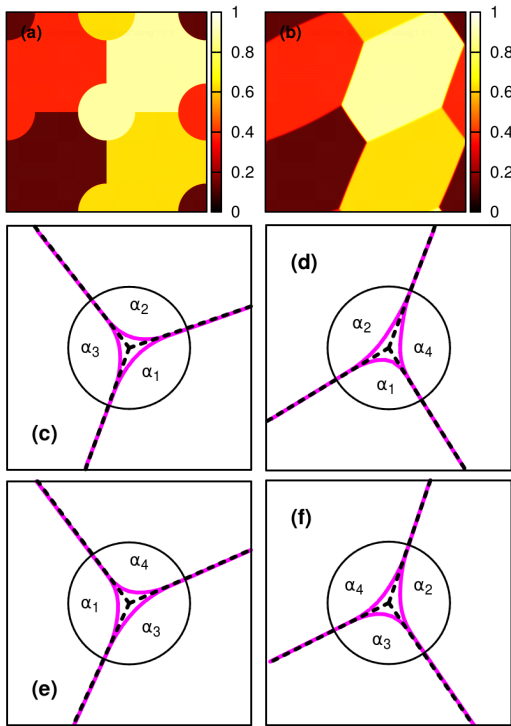


FIG. 6. Contact angles in an asymmetric quaternary system (for parameters, see the main text): (a) initial condition, (b) equilibrium state, (c)-(d) contour lines for the fields in the vicinity of the 4 different trijunctions from panel b, analogously to Fig 4. On panels a and b,  $h_4(\mathbf{r}, t) = \sum_{i=1}^4 [(i - 1/2)/4]c_i(\mathbf{r}, t)$  is shown.

## B. Spinodal decomposition

Since we're now interested in the time evolution of the system, the modified Bollada-Jimack-Mullis matrix defined by Eq. (15) is used henceforth.

### 1. Binary system

Spinodal decomposition was studied first in the binary limit. Technically we performed calculations in a ternary system, where the third component was set to 0 initially, i.e.  $c_3(\mathbf{r}, 0) = 0$  was used. In this case, the dynamic equations, together with the Navier-Stokes equation naturally reduce to the dynamic equations of a traditional, one order parameter, flow assisted Cahn-Hilliard system. Therefore, the reference calculation was based on the surfactant assisted liquid phase separation model

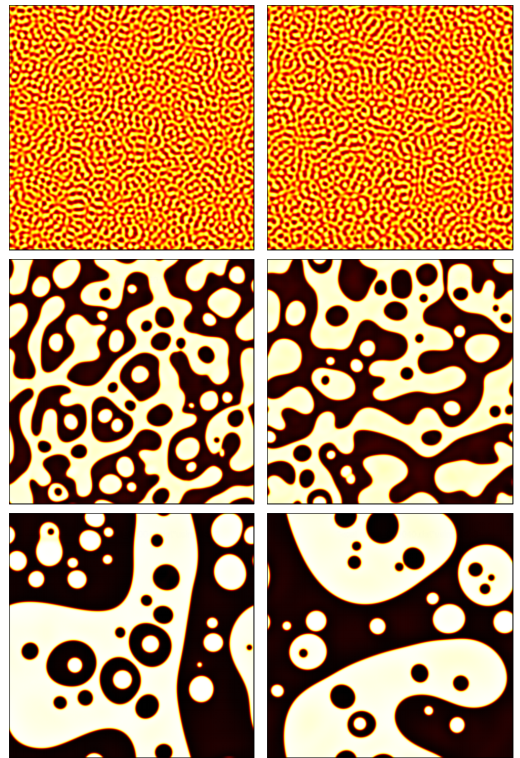


FIG. 7. Pattern coarsening during liquid-flow assisted spinodal decomposition of a binary liquid, as predicted by the Ginzburg-Landau theory of surfactant assisted liquid phase separation of Tóth and Kvamme (left column), and the present model (right column). The snapshots of the simulations were taken at  $t = 62.5, 125,$  and  $250,$  respectively (from top to bottom).

of Tóth and Kvamme for incompressible liquid flow, in the surfactant-free case. The dynamic equations read

$$\dot{\phi} = \nabla^2[(\phi^3 - \phi) - 2\nabla^2\phi] \quad (58)$$

$$\dot{\mathbf{v}} = \nabla \cdot (\mathbb{A} + \mathbb{D}) \quad (59)$$

$$\mathbb{A} = -2\tilde{w}(\nabla\phi \otimes \nabla\phi) \quad (60)$$

$$\mathbb{D} = \tilde{\mu}[(\nabla \otimes \mathbf{v}) + (\nabla \otimes \mathbf{v})^T] \quad (61)$$

$$0 = \nabla \cdot \mathbf{v} \quad (62)$$

The transformation of the fields read  $c_1 = (1 + \phi)/2$  and  $c_2 = (1 - \phi)/2$ , yielding  $\hat{h}_{12}^0 = 1$ ,  $\hat{\eta} = \hat{\eta}_0(c_1 x_1 + c_2 x_2)$  corresponding to  $\tilde{\mu} = \tilde{\mu}_0[x_1(1 + \phi)/2 + x_2(1 - \phi)/2]$  with  $\hat{\eta}_0 = \tilde{\mu}_0$ , and  $\hat{a} = 4\tilde{w}$ . We used  $\tilde{\mu}_0 = 2857.0$ ,  $x_1 = 1.0$  and  $x_2 = 1633.0/\tilde{\mu}_0$  in Eq. (54), and  $\tilde{w} = 1.73 \times 10^4$ . The initial condition was  $\phi(\mathbf{r}, 0) = A\mathcal{R}[-1, +1]$  [and  $c_1(\mathbf{r}, 0) = 0.5 + (A/2)\mathcal{R}[-1, +1]$ , correspondingly], where  $\mathcal{R}[-1, 1]$  is a uniformly distributed random number on

$[-1, 1]$ , and  $|A| \ll 1$ . Since the homogeneous state  $\phi = 0$  (and  $c_1 = 0.5$ ) represents unstable equilibrium, the system undergoes phase separation for  $A \neq 0$ . Since the implementation of the equations in solving the different models are different, we do not expect exactly the *same* result from the same initial condition. Nevertheless, we are interested only in the characteristic behavior of the system. Therefore, we used different random numbers (but the same amplitude  $A$ ) in setting up the initial conditions for  $\phi$  and  $c_1$ . In this case  $\Delta t = 0.0025$  was chosen. Snapshots of the simulations are presented in Fig 7. It is quite clear that the patterns roughen similarly as a function of time in both cases, indicating that the dynamic equations of the present model reduce naturally to the conventional binary model. In addition, no appearance of the third component was detected in our model during the simulation, due to the Bollada-Jimack-Mullis type mobility matrix.

## 2. Asymmetric ternary and quaternary flows

In our first multi-component simulation an asymmetric ternary system was considered with dimensionless interfacial tensions  $\hat{\sigma}_{12} = 1.2$ ,  $\hat{\sigma}_{13} = 1.0$ , and  $\hat{\sigma}_{23} = 0.8$ , and dimensionless interface thicknesses  $\hat{\delta}_{12} = 1.1$ ,  $\hat{\delta}_{13} = 0.9$  and  $\hat{\delta}_{23} = 1.0$ . The amplitude of the triplet term was  $A_3 = 1/2$ , which was enough to stabilize the binary planar interfaces. The pairwise diffusion constants were also asymmetric, we used  $\hat{D}_{12} = 1.0$ ,  $\hat{D}_{13} = 2.0$ , and  $\hat{D}_{23} = 0.5$ , whereas the dimensionless viscosities in Eq. (54) were  $x_1 = 0.5$ ,  $x_2 = 1.0$  and  $x_3 = 2.0$ , respectively. The initial condition reads  $c_1(\mathbf{r}, 0) = 0.2 + A \mathcal{R}[-1, 1]$ ,  $c_2(\mathbf{r}, 0) = 0.3 + A \mathcal{R}[-1, 1]$ , and  $c_3(\mathbf{r}, 0) = 1 - [c_1(\mathbf{r}, 0) + c_2(\mathbf{r}, 0)]$ , where  $A = 0.01$  was chosen. The simulation has been performed on a  $1024 \times 1024$  computational grid with  $h = 0.5$  and  $\Delta t = 0.005$ . Snapshots of the simulation are shown in Fig. 8(a)-(d) at different dimensionless times. As one can see, the system is unstable in its initial state, and undergoes spinodal decomposition. Although the system is still far from equilibrium at  $t = 3125$ , the individual fields of the components [see panels (e)-(g)] suggest, that the third component vanishes at the evolving binary interfaces. It is nevertheless important to mention, that pure binary interfaces exist only in equilibrium, while non-equilibrium curved interfaces may contain the third component. This effect is not prevented by applying a mobility matrix of the Bollada-Jimack-Mullis type, which is responsible only for preventing the appearance of a component when it is not present in a calculation *at all* [26]. Despite these, the third component tends to vanish at even non-equilibrium curved interfaces, showing the robustness of the construction of the free energy functional.

The simulations were repeated in a quaternary system as well (see Fig. 9), where the dimensionless interfacial tensions were  $\hat{\sigma}_{12} = 1.0$ ,  $\hat{\sigma}_{13} = 1.1$ ,  $\hat{\sigma}_{14} = 0.75$ ,  $\hat{\sigma}_{23} = 0.9$ ,  $\hat{\sigma}_{24} = 1.25$  and  $\hat{\sigma}_{34} = 1.0$ , while all in-

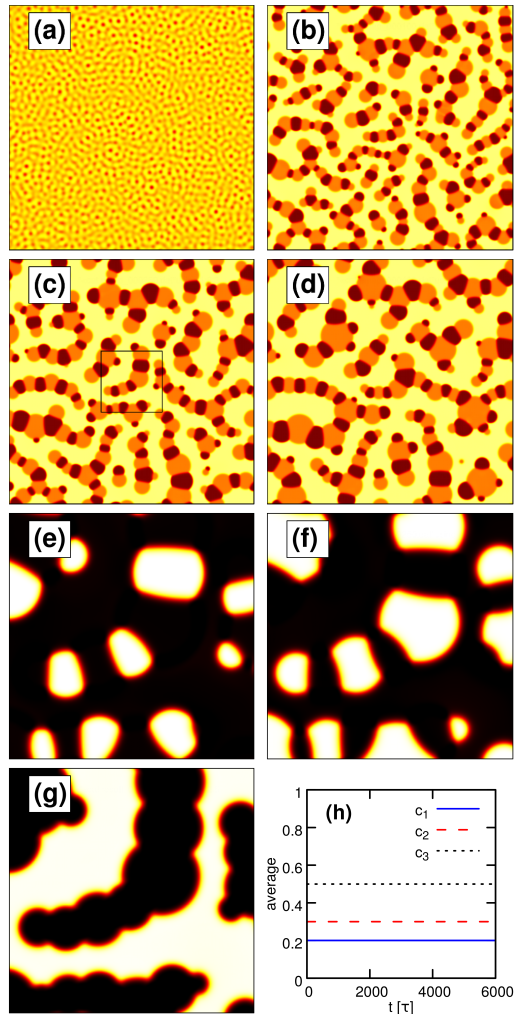


FIG. 8. Spinodal decomposition in an asymmetric ternary system. Snapshots of the simulation at  $t = 312.5, 1250, 3125$  and  $6250$  (from panels a to d), respectively. Coloring is the same as in Figure 6. Panels e-g show the individual mass fractions  $c_1(\mathbf{r}, t)$ ,  $c_2(\mathbf{r}, t)$  and  $c_3(\mathbf{r}, t)$ , respectively, in the area indicated by the black square on panel c. (Black corresponds to  $c = 0$  and white to  $c = 1$ .) The time evolution of the total concentrations are shown by panel h, thus indicating global conservation for all components.

terface thicknesses and diffusion constants were chosen to be equal, i.e.,  $\hat{\delta}_{ij} = \hat{D}_{ij} = 1.0$ . Furthermore, we chose  $A_3 = 1.0$  to stabilize all the binary planar interfaces. The dimensionless viscosities were  $x_1 = x_3 = 1.0$ ,

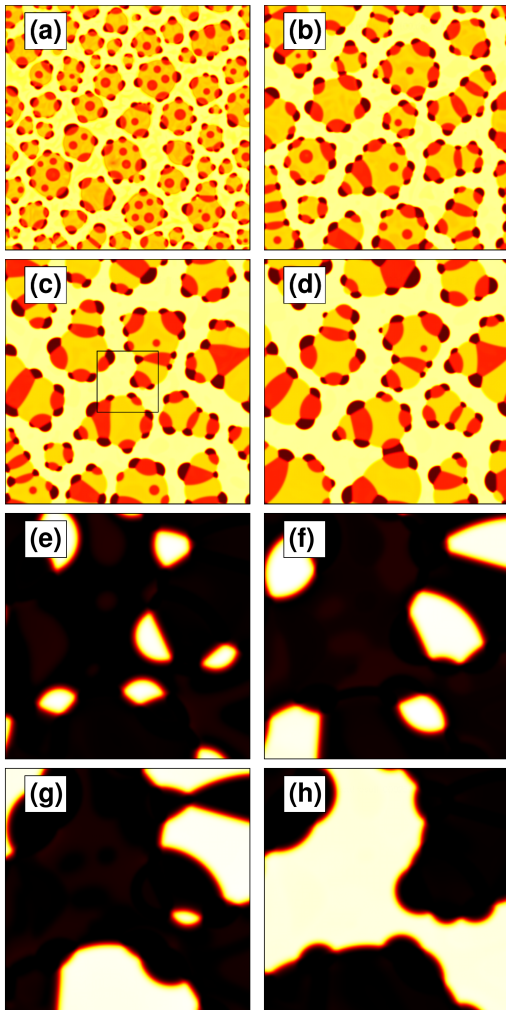


FIG. 9. Spinodal decomposition in an asymmetric quaternary (4-component) system. Snapshots at dimensionless times  $t = 312.5, 1250, 3125$  and  $6250$ , respectively. The individual fields  $c_1(\mathbf{r}, t)$ ,  $c_2(\mathbf{r}, t)$ ,  $c_3(\mathbf{r}, t)$  and  $c_4(\mathbf{r}, t)$  are shown in panels e-f in the black square indicated in panel c.

$x_2 = 0.5$  and  $x_4 = 2.0$ , respectively. Our experience was quite the same as in the ternary case: The system prepared in a high-energy, strongly non-equilibrium, homogeneous multi-component state undergoes phase separation, which is enhanced by the liquid flow. In the forming pattern, the bulk – interface – trijunction topology dominates, as expected from the free energy functional and the energy minimizing dynamics. Furthermore, the

additional components vanish at evolving interfaces and trijunctions in time. The forming patterns are also quite similar in the two cases, mostly due to the fact that we had a majority component ( $c_3$  and  $c_4$  in the ternary and quaternary system, respectively), in which "bubbles" of the minority phases started to form. The final (equilibrium) pattern, however, remains a question: the system has to find a configuration containing the least possible amount of interfaces and trijunctions, and representing minimum of the free energy functional. Such a configuration, nevertheless, can be a strong function of the volume fractions of the components. For example, in a binary system with a volume fraction  $1/2 : 1/2$  binary planar interfaces should form, while in a system of volume fraction  $1/10 : 9/10$ , for example, it is not energetically preferred creating such long interfaces. Instead, a bubble of the minority component forms, thus representing lower energy. In multi-component systems, the solution of the Euler-Lagrange equations can even be degenerated, i.e. it might have multiple solutions representing local minima the system can be trapped in.

Comparing Figs 8 and 9 sheds the light on another important detail. At  $t = 312.5$  [panel (a) in both Figures], the ternary system is still almost homogeneous, at least compared to the ternary system, which shows a much more developed pattern. Although both systems had similar initial conditions,  $A = 1/2$  and  $A = 1$  were used in the ternary and quaternary case, respectively. This, together with Fig. 1 (c-d) give a good impression of how the triplet term works: increasing  $A_3$  means increasing penalization for multi-component states (ternary and above, as discussed in Section III. B), which forces the system to get rid of the multi-component states faster and faster. Indeed,  $A_3 = 1$  (Fig. 9) means a stronger penalization than  $A_3 = 1/2$  (Fig. 8), therefore, the quaternary system eliminates the high-order states.

The long time effect of  $A_3$  on the evolving pattern is, however, expected to be negligible. As long as  $A_3$  is roughly in the same order of magnitude as  $\max[g(\mathbf{c})]$ , small perturbations around binary interfaces produce small variation in the energy relative to the interfacial tension. The key is, again, that the triplet term is used solely to stabilize the binary planar interfaces, thus resulting in a strongly finite  $A_3$ . In contrast, in previous multi-phase/multi-component descriptions the binary interfaces are not equilibrium solutions, and the triplet term is applied to suppress the third component, which is definitely present at the binary planar interface. In these cases, the binary planar interface solution is recovered for  $A_3 \rightarrow \infty$ , which then may significantly affect the dynamics of the quasi-binary interfaces even if only a small amount of the third component is present. Summarizing, the purpose of applying the triplet term is essentially different in the two cases.

## VI. CONCLUSIONS

In this work we presented a generalization of the Cahn-Hilliard theory of liquid phase separation for arbitrary number of components. It has been shown that the generalization can be done on a systematic way. First a general, physically and mathematically consistent, entropy producing advection-diffusion dynamics has been set up, which then has been extended with the generalization of the Cahn-Hilliard free energy functional for many components. The extension has been done on phenomenological basis, resulting in a model, which (i) reduces/extends naturally on the level of both the free energy functional and the dynamic equations when removing/adding a component, (ii) recovers the standard Cahn-Hilliard model for  $N = 2$ . Furthermore, (iii) the bulk states and the two-component interfaces are *stable* equilibrium solutions of the multi-component model, (iv) the free energy functional penalizes the high-order multi-component states strictly monotonously as a function of the number of components being present, and (v) the pairwise interfacial properties (interfacial tension and interface thickness) can be chosen independently.

We have shown that (i) a simple triplet energy term can be used to *stabilize the binary planar interfaces*, (ii) the equilibrium contact angles are in perfect agreement with theoretical values. Furthermore, we demonstrated, that (iii) the system undergoes spinodal decomposition, when starting from a high-energy non-equilibrium state, and converges to equilibrium by developing the bulk – interface – trijunction topology in 2 dimensions in asymmetric ternary and quaternary systems.

Our results might significantly contribute to the continuum theory of multi-component liquids, since controlled pattern formation in these systems is of increasing importance in several practical applications. For instance, surfactant controlled nanoshell formation opened a new chapter in targeted drug delivery [33]. Another crucial field is energy: a controlled emulsion  $\rightarrow$  emulsion transition in the CO<sub>2</sub>/water/heavy crude oil system would result in an efficient and environmentally sound combination of CO<sub>2</sub> storage and Enhanced Oil Recovery [34, 35].

## VII. ACKNOWLEDGEMENT

The authors thank Prof. László Gránásy and Prof. Tamás Pusztai from the Wigner Research Center for Physics, Hungary, Prof. Valeriy I. Levitas from Iowa State University, IA, USA, and Dr. Kumar Ankit from Karlsruhe University, Germany. This work has been supported by the VISTA basic research programme project No. 6359 "Surfactants for water/CO<sub>2</sub>/hydrocarbon emulsions for combined CO<sub>2</sub> storage and utilization" of the Norwegian Academy of Science and Letters and the Statoil.

## APPENDIX

### A. Energy hierarchy

In a symmetric system, the free energy landscape reads:

$$\frac{f(\mathbf{c})}{w_0} = g(\mathbf{c}) + a f_3(\mathbf{c}) \quad , \quad (63)$$

where

$$g(\mathbf{c}) = \frac{1}{12} + \sum_{i=1}^N \left( \frac{c_i^4}{4} - \frac{c_i^3}{3} \right) + \frac{1}{2} \sum_{i<j} (c_i c_j)^2 \quad , \quad (64)$$

$a = A_3/w_0 \geq 0$ , and

$$f_3(\mathbf{c}) = \sum_{i<j<k}^{N,N,N} |c_i| |c_j| |c_k| \quad . \quad (65)$$

For  $\mathbf{c}_n = \mathbb{P}[(1/n, 1/n, \dots, 1/n, 0, 0, \dots, 0)]$ , Eq. (63) read as:

$$f(n) = \frac{1}{12} \left( 1 - \frac{1}{n^2} \right) + a \left[ \frac{n(n-1)(n-2)}{6} \left( \frac{1}{n} \right)^3 \right] \quad , \quad (66)$$

which must be monotonously increasing as a function of  $n = 1, 2, 3, \dots$ . The increment for  $n \rightarrow n+1$  components then reads:

$$f(n+1) - f(n) = \frac{1 + 2n + 2a(n-1)(2+3n)}{12n^2(1+n)^2} \geq 0 \quad , \quad (67)$$

which is trivially true for  $n = 1$  (and  $a \geq 0$ ), and results in

$$a \geq d(n) = \frac{1 + 2n}{4 + 2n + 6n^2} \quad (68)$$

for  $n > 1$ . Since  $d(n) < 0$ , and  $\lim_{n \rightarrow \infty} d(n) = 0$ , the strictly monotonously increasing tendency of the  $n$ -component multiple states on the free energy landscape applies for arbitrary  $A_3 \geq 0$ . We note, however, that this tendency is not true for higher order triplet terms, such as  $(c_i c_j c_k)^2$ , for example, when  $f(n)$  shows a maximum for any positive  $A_3$ .

### B. Equilibrium solutions

In the multi-component system thermodynamic equilibrium is defined by the extrema of the free energy functional. The corresponding Euler-Lagrange equations of the complete multi-component problem read:

$$\nabla \frac{\delta F}{\delta c_i} = \nabla \frac{\delta F}{\delta c_j} \quad (69)$$

for any  $i \neq j$  pairs,  $i, j = 1 \dots N$ . The functional derivatives read:

$$\frac{\delta F}{\delta c_i} = \frac{\partial f}{\partial c_i} - \nabla \cdot \frac{\partial f}{\partial \nabla c_i}, \quad (70)$$

where

$$f = w(\mathbf{c})g(\mathbf{c}) + A_3 f_3(\mathbf{c}) + \frac{\epsilon^2(\mathbf{c})}{2} \sum_{i=1}^N (\nabla c_i)^2 \quad (71)$$

is the integrand of the free energy functional defined by Eq. (23). Using this in Eq. (70) yields

$$\begin{aligned} \frac{\delta F}{\delta c_i} = & \frac{\partial w}{\partial c_i} g(\mathbf{c}) + \frac{\partial \epsilon^2}{\partial c_i} \left[ \frac{1}{2} \sum_{i=1}^N (\nabla c_i)^2 \right] + \\ & w(\mathbf{c}) \frac{\partial g}{\partial c_i} + A_3 \frac{\partial f_3}{\partial c_i} - \nabla \cdot \left[ \epsilon^2(\mathbf{c}) \nabla c_i \right], \end{aligned} \quad (72)$$

where

$$\frac{\partial \epsilon^2}{\partial c_i} = 2 c_i \frac{\sum_{j \neq i} [\epsilon_{ij}^2 - \epsilon^2(\mathbf{c})] c_j^2}{\sum_{k < l} c_k^2 c_l^2} \quad (73)$$

$$\frac{\partial w}{\partial c_i} = 2 c_i \frac{\sum_{j \neq i} [w_{ij} - w(\mathbf{c})] c_j^2}{\sum_{k < l} c_k^2 c_l^2} \quad (74)$$

$$\frac{\partial g}{\partial c_i} = c_i (c^2 - c_i) \quad (75)$$

$$\frac{\partial f_3}{\partial c_i} = \text{sgn}(c_i) \sum_{(j < k) \neq i} |c_j| |c_k|. \quad (76)$$

Since Eq. (72)-(76) vanish for  $c_i(\mathbf{r}) = 0$ , the functional derivative vanishes for a vanishing field, i.e.  $(\delta F / \delta c_i)_{c_i=0} = 0$ . Therefore, in the binary limit  $c_I(\mathbf{r}) + c_J(\mathbf{r}) = 1$  and  $c_K(\mathbf{r}) = 0$ , the functional derivatives read:

$$\frac{\delta F}{\delta c_I} = w_{IJ} \frac{\partial g}{\partial c_I} - \epsilon_{IJ}^2 \nabla^2 c_I \quad (77)$$

$$\frac{\delta F}{\delta c_J} = w_{IJ} \frac{\partial g}{\partial c_J} - \epsilon_{IJ}^2 \nabla^2 c_J \quad (78)$$

$$\frac{\delta F}{\delta c_K} = 0, \quad (79)$$

where  $\partial g / \partial c_I = -\partial g / \partial c_J = c_I \{ [c_I^2 + (1 - c_I)^2] - c_I \} = c_I (1 - c_I) (1 - 2c_I)$ , i.e.  $\left. \frac{\partial g}{\partial c_I} \right|_{c_I+c_J=1} = \{ \frac{\partial}{\partial c} [c^2(1-c)^2] \}_{c=c_I}$ . It is easy to see that the triplet term has no contribution to the free energy at all, since only 2 components are present, while  $\text{sgn}(0) = 0$  ensures the vanishing derivative in the equation for vanishing  $c_K$ . In addition, the derivatives of the Kazaryan polynomials also vanish for  $c_I + c_J = 1$ , since in this case the sums in the nominators vanish. Substituting  $c_I(x) = \{1 + \tanh[x/(2\delta_{IJ})]\}/2$ ,  $c_J(x) = 1 - c_I(x)$ , and  $c_K(x) = 0$  into Eqns. (77) and (78) then yields

$$\delta F / \delta c_i = 0 \quad (80)$$

for  $i = 1 \dots N$ , i.e. the binary planar interfaces are equilibrium solution of the multi-component problem.

- |   |   |
|---|---|
| <p>[1] M. F. Haase and J. Brujic, <i>Angewandte Chemie</i> <b>126</b>, 11987 (2014).</p> <p>[2] T. Shukutani, T. Myojo, H. Nakanishi, T. Norisuye, and Q. Tran-Cong-Miyata, <i>Macromolecules</i> <b>47</b>, 4380 (2014).</p> <p>[3] G. Ahearn, <i>Journal of the American Oil Chemists Society</i> <b>46</b>, 540A (1969).</p> <p>[4] S. Iglauer, Y. Wu, P. Shuler, Y. Tang, and W. A. G. III, <i>Journal of Petroleum Science and Engineering</i> <b>71</b>, 23 (2010).</p> <p>[5] S. Q. Tunio, A. H. Tunio, N. A. Ghirano, and Z. M. El Adawy, <i>Intl. J. Appl. Sci. Tech.</i> <b>1</b>, 143 (2011).</p> <p>[6] Z. Song, Z. Li, M. Wei, F. Lai, and B. Bai, <i>Computers &amp; Fluids</i> <b>99</b>, 93 (2014).</p> | <p>[7] J. W. Cahn and J. E. Hilliard, <i>The Journal of Chemical Physics</i> <b>28</b> (1958).</p> <p>[8] H. Cook, <i>Acta Metallurgica</i> <b>18</b>, 297 (1970).</p> <p>[9] J. Langer, <i>Annals of Physics</i> <b>65</b>, 53 (1971).</p> <p>[10] J. Langer, <i>Acta Metallurgica</i> <b>21</b>, 1649 (1973).</p> <p>[11] D. D. Fontaine, <i>Journal of Physics and Chemistry of Solids</i> <b>33</b>, 297 (1972).</p> <p>[12] D. D. Fontaine, <i>Journal of Physics and Chemistry of Solids</i> <b>34</b>, 1285 (1973).</p> <p>[13] J. Morral and J. Cahn, <i>Acta Metallurgica</i> <b>19</b>, 1037 (1971).</p> <p>[14] J. Hoyt, <i>Acta Metallurgica</i> <b>37</b>, 2489 (1989).</p> <p>[15] J. Hoyt, <i>Acta Metallurgica et Materialia</i> <b>38</b>, 227 (1990).</p> |
|---|---|

- [16] S. Maier-Paape, B. Stoth, and T. Wanner, *Journal of Statistical Physics* **98**, 871 (2000).
- [17] D. J. Korteweg, *Arch. Neerl. Sci. Ex. Nat.* **6**, 1 (1901).
- [18] R. Evans, *Advances in Physics* **28**, 143 (1979).
- [19] R. Salmon, *Annual Review of Fluid Mechanics* **20**, 225 (1988).
- [20] A. A. Wheeler and G. B. McFadden, *Proceedings of the Royal Society of London. Series A: Mathematical, Physical and Engineering Sciences* **453**, 1611 (1997).
- [21] D. Anderson, G. McFadden, and A. Wheeler, *Physica D: Nonlinear Phenomena* **135**, 175 (2000).
- [22] D. M. Anderson, G. B. McFadden, and A. A. Wheeler, *Annual Review of Fluid Mechanics* **30**, 139 (1998).
- [23] G. Tegze, T. Pusztai, and L. Gránásy, *Materials Science and Engineering: A* **413414**, 418 (2005), international Conference on Advances in Solidification Processes.
- [24] J. Kim and J. Lowengrub, *Intf. Free Bound.* **7**, 435 (2005).
- [25] J. Kim, *Commun. Comput. Phys.* **12**, 613 (2012).
- [26] G. I. Tóth, T. Pusztai, and L. Gránásy, *Phys. Rev. B* **92**, 184105 (2015).
- [27] L. Onsager, *Ann. N. Y. Acad. Sci* **46**, 241 (1945).
- [28] P. Bollada, P. Jimack, and A. Mullis, *Physica D: Nonlinear Phenomena* **241**, 816 (2012).
- [29] A. Kazaryan, Y. Wang, S. A. Dregia, and B. R. Patton, *Phys. Rev. B* **61**, 14275 (2000).
- [30] K. Ankit, B. Nestler, M. Selzer, and M. Reichardt, *Contributions to Mineralogy and Petrology* **166**, 1709 (2013).
- [31] V. I. Levitas and A. M. Roy, *Phys. Rev. B* **91**, 174109 (2015).
- [32] G. Tegze, G. Bansal, G. I. Tóth, T. Pusztai, Z. Fan, and L. Gránásy, *Journal of Computational Physics* **228**, 1612 (2009).
- [33] M. M. De Villiers and Y. M. Lvov, “Nanoshells for drug delivery,” in *Nanotechnologies for the Life Sciences* (Wiley-VCH Verlag GmbH & Co. KGaA, 2007).
- [34] G. I. Tóth and B. Kvamme, *Phys. Rev. E* **91**, 032404 (2015).
- [35] G. I. Tóth and B. Kvamme, *Phys. Chem. Chem. Phys.* **17**, 20259 (2015).



---

## **PAPER VII**

**STAGES IN DYNAMICS OF HYDRATE FORMATION  
AND CONSEQUENCES FOR DESIGN OF  
EXPERIMENTS FOR HYDRATE FORMATION IN  
SEDIMENTS**



Article

# Stages in the Dynamics of Hydrate Formation and Consequences for Design of Experiments for Hydrate Formation in Sediments

Bjørn Kvamme <sup>1,\*</sup>, Richard B. Coffin <sup>1</sup>, Jinzhou Zhao <sup>1</sup>, Na Wei <sup>1</sup>, Shouwei Zhou <sup>1</sup>, Qingping Li <sup>2</sup>, Navid Saeidi <sup>3</sup>, Yu-Chien Chien <sup>4</sup>, Derek Dunn-Rankin <sup>3,4</sup>, Wantong Sun <sup>1</sup> and Mojdeh Zarifi <sup>5</sup>

<sup>1</sup> State Key Laboratory of Oil and Gas Reservoir Geology and Exploitation, Southwest Petroleum University, Xindu Road No.8, Chengdu 610500, China

<sup>2</sup> CNOOC Research Institutes Limited Liability Company, Taiyanggong South Road No.6, Beijing 10027, China

<sup>3</sup> Environmental Engineering Department, University of California, Irvine, CA 92697-3975, USA

<sup>4</sup> Mechanical and Aerospace Engineering Department, University of California, Irvine, CA 92697-3975, USA

<sup>5</sup> Department of Physics and Technology, University of Bergen, Bergen 5007, Norway

\* Correspondence: bkvamme@strategic-carbonllc.com; Tel.: +86-47-93451956

Received: 8 July 2019; Accepted: 23 August 2019; Published: 3 September 2019



**Abstract:** Natural gas hydrates in sediments can never reach thermodynamic equilibrium. Every section of any hydrate-filled reservoir is unique and resides in a stationary balance that depends on many factors. Fluxes of hydrocarbons from below support formation of new hydrate, and inflow of water through fracture systems leads to hydrate dissociation. Mineral/fluid/hydrate interaction and geochemistry are some of the many other factors that determine local hydrate saturation in the pores. Even when using real sediments from coring it is impossible to reproduce in the laboratory a natural gas hydrate reservoir which has developed over geological time-scales. In this work we discuss the various stages of hydrate formation, with a focus on dynamic rate limiting processes which can lead to trapped pockets of gas and trapped liquid water inside hydrate. Heterogeneous hydrate nucleation on the interface between liquid water and the phase containing the hydrate former rapidly leads to mass transport limiting films of hydrate. These hydrate films can delay the onset of massive, and visible, hydrate growth by several hours. Heat transport in systems of liquid water and hydrate is orders of magnitude faster than mass transport. We demonstrate that a simple mass transport model is able to predict induction times for selective available experimental data for CO<sub>2</sub> hydrate formation and CH<sub>4</sub> hydrate formation. Another route to hydrate nucleation is towards mineral surfaces. CH<sub>4</sub> cannot adsorb directly but can get trapped in water structures as a secondary adsorption. H<sub>2</sub>S has a significant dipole moment and can adsorb directly on mineral surfaces. The quadrupole-moment in CO<sub>2</sub> also plays a significant role in adsorption on minerals. Hydrate that nucleates toward minerals cannot stick to the mineral surfaces so the role of these nucleation sites is to produce hydrate cores for further growth elsewhere in the system. Various ways to overcome these obstacles and create realistic hydrate saturation in laboratory sediment are also discussed.

**Keywords:** hydrate; phase transitions; nucleation; hydrate films

## 1. Introduction

Natural gas hydrates are crystalline compounds which are mainly stabilized by hydrogen bonds that forms cavities which enclathrate small hydrocarbons. Inorganic gases, like for instance CO<sub>2</sub> and H<sub>2</sub>S, also form hydrates. The extra stabilization of the water structure by the inclusion of these “guest” molecules makes hydrates stable also for temperatures above zero Celsius if the pressure

is high enough. The formation of these ice-like compounds during processing and transport of hydrocarbons has motivated substantial amounts of hydrate research in the past. The enormous quantity of natural gas hydrates spread around the world stimulates creativity in development of new methods for commercial dissociation and use of these energy sources. Adding steam or hot water for thermal dissociation of the hydrate is very expensive. Substantial portions of the added heat are lost to minerals. Adding chemicals is also very expensive. The pressure reduction method is the approach that has drawn the most attention in the past. In this method the local pressure is reduced to below the stability limit pressure of the hydrate. One drawback of the pressure reduction method is that the heat necessary for dissociation of the hydrate still needs to be supplied. Studies conducted on pilot plant scale [1–4] have so far not been successful, and freezing down (from the heat drawn away by dissociation demand) has been only one of several problems. Production of sand and water are other drawbacks. In addition to the stability limit considerations, hydrate dissociation in sediment is limited by the transport processes across a thin interface (1.2 nm) between the hydrate and surrounding phases. These phase transition dynamics are implicitly coupled to the dynamics of the flow and all phase transitions in every pore. Finally, the coupled dynamics of all pores are connected to the reservoir flow. Pressure reduction attacks the top level of dynamics. The transfer of the impact all the way down to the phase transition dynamics will impose significant delays. Hence, pressure reduction is a slow method from a theoretical point of view. An experimental challenge for pressure reduction is to establish realistic boundary conditions that can supply heat from surrounding sediments. Many published experiments even report pressure reduction experiments at constant temperature as controlled by surrounding heat baths. Temperature changes, on the other hand, distribute very rapidly through liquid water and hydrate, making thermal approaches dynamically efficient.

The strong focus on reduction of CO<sub>2</sub> emissions during the latest two decades has also triggered rapid development of various ways to utilize CO<sub>2</sub>, like for instance the use of CO<sub>2</sub> for enhanced oil recovery. The use of CO<sub>2</sub> for production of natural gas hydrate is another option. The exchange between CH<sub>4</sub> hydrate and CO<sub>2</sub> hydrate is possible through two primary mechanisms. The first mechanism is a solid-state exchange which has been verified experimentally for temperatures substantially inside the ice region for water [5,6] and also theoretically through molecular dynamics (MD) simulations [7]. For temperatures above freezing the water surrounding the hydrate in the pores is a combination of liquid water and pore bounded water. A typical hydrate saturation for Alaska is 75% or lower, like in the area used for the Ignik Sikimu pilot test [8,9]. Hydrate saturation is the percentage of available pore volume that is filled with hydrate. For temperatures in the liquid water region another mechanism [10,11] than solid state conversion is possible. Injected CO<sub>2</sub> will form new hydrate with free pore water. Released heat from this hydrate formation, and other factors, will dissociate the in situ hydrate. Similar to the formation of CH<sub>4</sub> hydrate the formation of a new CO<sub>2</sub> hydrate will also go through the various stages of the hydrate formation process. From a physical point of view any fluid/solid phase transition in the classical regime consists of two stages. The nucleation of hydrate requires that the free energy change of the formation be negative and the free energy difference has to be large enough to supply the work needed to push away the molecules in the original phases. The necessary hydrate particle volume needed to win the competition between benefits of the phase transition, and the penalty of the push work, is the critical size hydrate core. After this first nucleation stage the hydrate will grow steadily, but will compete with other hydrate cores for mass, and may diminish in competition with more stable cores. And also in the steady growth stage the heat released from the growth of neighboring hydrate cores can lead to dissociation. Also, as discussed further later, dilution of fluid phases will lead to dissociation. Even the two physically well-defined stages of hydrate growth are fairly complex in non-equilibrium systems. Rapid formation of hydrate films on the interface between hydrate former phase and water leads to a dramatic slow-down in supply of hydrate formers from typical liquid phase diffusivity (coefficients in the order of 10<sup>-7</sup> m<sup>2</sup>/s to 10<sup>-8</sup> m<sup>2</sup>/s) down to diffusivity for transport through hydrate (coefficient from 10<sup>-15</sup> m<sup>2</sup>/s to 10<sup>-17</sup> m<sup>2</sup>/s). Dramatic reduction in mass transport rates and limited shear forces (limited or no flow) lead to very

long times, relative to the typical nanoseconds time scale for nucleation, before visible hydrate can be observed at millimeter scales. In addition to the nucleation stage and the growth stage the term induction frequently occurs in the open literature. This time can be defined as the time to reach visible hydrate or to reach the onset of massive hydrate growth rate (depends on monitoring method resolution).

We utilize classical nucleation theory (CNT) and residual thermodynamics to examine the dynamics of hydrate formation. This is used as the basis for considering various ways to break hydrate films and increase formation rate. The primary goal is to shed light on how to design laboratory experiments for hydrate formation between water and CH<sub>4</sub> or CO<sub>2</sub> in sediments. Reducing trapped gas pockets and trapped liquid water to a minimum will be an important step towards creating hydrates in sediments that in important ways can be compared to natural gas hydrates in nature.

**2. Methodologies**

Kvamme and Tanaka [12] used MD simulations to calculate the chemical potentials of water in ice and empty clathrates of structures I and II hydrate. They then used experimental data for heat of freezing at zero Celsius and experimental data for specific heat capacity of liquid water in order to get a continuous description of water chemical potential. Ideal gas chemical potential for the three phases (ice, empty clathrate of structure I and empty clathrate of structure II) were trivially sampled from momentum space during the MD simulations. The values calculated by Kvamme and Tanaka [12] are plotted in Figure 1 along with parameters listed in Table 1. Gas (or fluid phases) of CH<sub>4</sub> and CO<sub>2</sub> are modelled using residual thermodynamics in the manner that is similar for gas/liquid equilibrium in hydrocarbon systems. For this purpose we utilize the Soave-Redlich-Kwong (SRK) equation of state [13]. The only difference is that we use chemical potential rather than fugacity. For that reason, the gas phase needs model molecules for the ideal gas term for CH<sub>4</sub> and CO<sub>2</sub>. CH<sub>4</sub> is modelled as a spherical molecule and the ideal gas chemical potential is an analytical integral over the Boltzmann factors of translational momentums in the x, y and z directions. The equations for this can be found in any textbook on physical chemistry or statistical mechanics and are not repeated here. The model we use for CO<sub>2</sub> is a linear molecule with only two independent rotational degrees of freedom with equal moments of inertia due to the symmetry. The translational part is given by the molecular weight and the center of mass. For completeness we also give the three rotational momentums for the water model utilized in our earlier study so that it will be possible to reproduce the results presented in this work in Table 2 below.

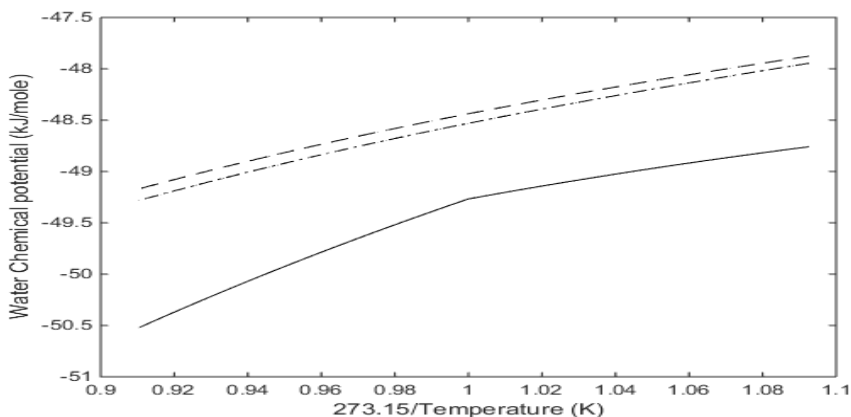


**Figure 1.** Water chemical potential empty hydrate of structure I (dashed) and empty hydrate of structure II (dash-dot) and liquid water (solid) in the region (273.15/1.1–0.9) and liquid region (273.15/1.0–1.1) is presented by a solid curve.

More advanced theories, like for instance phase field theories [14–18], may be more rigorous in the implicit couplings between the various contributions to the phase transition dynamics but are also more complex in terms of distinguishing between the various stages of hydrate growth. Classical nucleation theory (CNT) is still rigorous enough to illustrate nucleation times. In principle

**Table 1.** Coefficients  $a_i$  for chemical potential of water in various phases;  $\mu_{H_2O} = \sum_{i=1}^{i=6} a_i \left( \frac{T_{C_{H_2O}}}{T} \right)^{(i-1)}$  with  $T_{C_{H_2O}} = 647.096$  K.

| $i$ | Str. I<br>$a_i$ (kJ/mole) | Str. II<br>$a_i$ (kJ/mole) | Liquid<br>$a_i$ (kJ/mole) | Ice<br>$a_i$ (kJ/mole) |
|-----|---------------------------|----------------------------|---------------------------|------------------------|
| 1   | −90.48377                 | −92.72076                  | −109.03432                | −87.13485              |
| 2   | 42.46997                  | 45.09842                   | 58.33379                  | 41.31529               |
| 3   | −14.61482                 | −15.72658                  | −19.48522                 | −17.71143              |
| 4   | 1.76419                   | 1.92639                    | 2.32631                   | 3.88149                |
| 5   | 0                         | 0                          | 0                         | −0.43451               |
| 6   | 0                         | 0                          | 0                         | 0.01971                |

**Table 2.** Moments of inertia for H<sub>2</sub>O and CO<sub>2</sub> models utilized.

| Axis | H <sub>2</sub> O Moment of Inertia (kg·m <sup>2</sup> ) | CO <sub>2</sub> Moment of Inertia (kg·m <sup>2</sup> ) |
|------|---|--|
| x    | 2.938·10 <sup>−47</sup>                                 | 0.7173·10 <sup>−45</sup>                               |
| y    | 1.020·10 <sup>−47</sup>                                 | 0.7173·10 <sup>−45</sup>                               |
| z    | 1.918·10 <sup>−47</sup>                                 | 0  |

More advanced theories, like for instance phase field theories [14–18], may be more rigorous in the implicit couplings between the various contributions to the phase transition dynamics but are also more complex in terms of distinguishing between the various stages of hydrate growth. Classical nucleation theory (CNT) is still rigorous enough to illustrate nucleation times. In principle CNT can be used to determine two parameters related to volume and shape of a hydrate core [19] in transition to growth. For the main goal of this work, however, we stick to a spherical model. A critical size hydrate core is defined as the size when the hydrate core enters the stable growth period.

We also limit ourselves to some of the important hydrate phase transitions involved in hydrate formation in porous media. Formation of hydrate on the interface between a separate phase containing hydrate formers, and hydrate formation towards mineral surfaces, are the two fastest routes. When these two routes have created a hydrate film there will also be some hydrate formation from dissolved hydrate former in water. For methane this is limited by fairly low solubility, while the higher solubility of CO<sub>2</sub> in water makes this route far more significant.

In order for a hydrate particle to reach critical size, the hydrate former molecules must be transported from an outer boundary on the liquid water side and through an interface layer of gradually increased water structure. The more structured the water, the slower the transport. The necessary time for enough hydrate former molecules to reach surface of the hydrate core at critical size is the nucleation time. Further growth through the hydrate film is very slow as indicated above. Since heat transport is very fast, and maybe two to three orders of magnitude faster than mass transport in liquid water, it will be several orders of magnitude faster than mass transport through hydrate. Assuming a constant mass transport rate through the hydrate film in order to supply the hydrate film with hydrate formers we are then able to estimate hydrate film thickness as a function of time. This will provide a basis for evaluating the necessary dynamics needed to break hydrate films, and correspondingly ensure that measures can be taken to prevent blocking hydrate films.

### 2.1. Hydrate Formation from Water and a Separate Phase Containing Hydrate Formers

Hydrate phase transition along the equilibrium curve is reversible. At equilibrium the free energy changes of the hydrate formation from liquid water (or ice) and hydrate formers coming from

gas, liquid or fluid state is zero. Outside of equilibrium the molar free energy change, as given by Equation (1) below, has to be negative.

$$\Delta G^{(H_1)} = x_{H_2O}^{H_1} \left( \mu_{H_2O}^{H_1}(T, P, \vec{x}^{H_1}) - \mu_{H_2O}^{water}(T, P, \vec{x}) \right) + \sum_i x_i^{H_1} \left( \mu_i^{H_1}(T, P, \vec{x}^{H_1}) - \mu_i^{gas}(T, P, \vec{y}^{gas}) \right) \quad (1)$$

The superscript  $H_1$  denotes this specific heterogeneous phase transition.  $T$  is temperature,  $P$  is pressure.  $x$  is mole-fraction in either liquid or hydrate (denoted with a superscript  $H$ ).  $y$  is mole-fraction in gas (or liquid, or fluid) hydrate former phase;  $i$  is an index for hydrate formers. Superscript water denotes a water phase. Generally this is ice, liquid or adsorbed water on mineral surfaces. In this work we only consider liquid water;  $\mu$  is chemical potential.  $x$  is mole-fraction in liquid water or hydrate (as given by superscripts). Vector sign denote mole-fractions of all components in the actual phase.

Symmetric excess formulation for liquid water chemical potential is given by:

$$\mu_{H_2O}^{water}(T, P, \vec{x}) = \mu_{H_2O}^{pure, H_2O}(T, P) + RT \ln[x_{H_2O} \gamma_{H_2O}(T, P, \vec{x})] \approx \mu_{H_2O}^{pure, H_2O}(T, P) + RT \ln[x_{H_2O}] \quad (2)$$

$\lim(\gamma_{H_2O}) = 1.0$  when  $x_{H_2O}$  approaches unity.

Water as superscript on the left-hand side distinguishes liquid water phase from water in the hydrate phase. A right-hand side approximation of Equation (2) is not necessary but good enough for the purpose of this work. The alternative would be to use a model for the activity coefficient or utilization of the Gibbs-Duhem relation. In our phase field theory (PFT) modelling of  $CO_2$  hydrate phase transition dynamics studies [14,15] we used the latter approach. Our PFT models are fairly complex and a simpler kinetic model might be more useful in order to visualize the various stages of the hydrate formation.

Water chemical potential in the hydrate structure is given by [16]:

$$\mu_{H_2O}^H = \mu_{H_2O}^{O,H} - \sum_{k=1,2} RT v_k \ln \left( 1 + \sum_i h_{ij} \right) \quad (3)$$

$H$  denotes hydrate and superscript  $O$  on first term on right hand side denotes empty clathrate. Calculated values for water chemical potentials in empty hydrates of structure I and II are readily available from model water (TIP4P) simulations [12] as discussed above. Cavities per water in structure I hydrate,  $v_k$  is 1/23 for small cavities and 3/23 for large cavities.  $h_{ki}$  is the canonical partition function for  $s$  guest of type  $i$  in cavity type  $k$ . For a rigid water lattice the result is a Boltzmann integral over all possible water-guest and guest-guest interactions and a function of the free energy of the huest molecule [12]. This is the most common way to calculate  $h_{ki}$  in various available codes for hydrate equilibrium. A different formulation of  $h_{ki}$  utilize a perturbation approach in which the movements of the guest molecule, relative to energy minimum position in the cavity, is approximated by an harmonic oscillator. The advantage of this approach is that some frequencies of guest movements may interfere with the water lattice librational frequencies. As such we directly also get calculations for these effects, which are typically included as empirical correction, incorporated. For  $CO_2$  a comparison with a rigid lattice calculations and the harmonic oscillator approach reveal a destabilization effect of 1 kJ/mole due to  $CO_2$  movements in the large cavity of structure I [12]:

$$h_{ki} = e^{\beta[\mu_{ki} - \Delta g_{ki}]} \quad (4)$$

$\beta$  is the inverse of the universal gas constant times temperature.  $\mu_{ki}$  is the chemical potential of guest molecule  $i$  in hydrate cavity of type  $k$ . At equilibrium this chemical potential is equal to the chemical potential for the same molecule in the phase it comes from during the hydrate formation. For Equation (1) that means gas, liquid or fluid as a separate phase. In a non-equilibrium situation the

guest chemical potentials are adjusted for distances from equilibrium through a Taylor expansion, as discussed later. The free energies of inclusion (latter term in the exponent) are given in Table 3 below.

**Table 3.** Coefficients  $a_i$  for free energy of guest type  $j$  inclusion in cavity type  $k$ ;  $\Delta g_{kj} = \sum_{i=1}^{i=6} a_i \left(\frac{T_{C_i}}{T}\right)^{(i-1)}$  with  $T_{C_{CH_4}} = 190.56$  K and  $T_{C_{CO_2}} = 304.13$  K.

| $i$ | CH <sub>4</sub> |            | CO <sub>2</sub> Large |              | CO <sub>2</sub> Small |
|-----|-----------------|------------|-----------------------|--------------|-----------------------|
|     | Large           | Small      | T ≤ 283.14 K          | T > 283.14 K |                       |
| 1   | 17.97150        | -42.47683  | 41.52168              | -17.87093    | 0.19929               |
| 2   | -23.44013       | 119.24124  | -41.96874             | -17.89249    | -28.28735             |
| 3   | -161.81535      | -183.19565 | -70.72691             | 17.38136     | -11.94528             |
| 4   | 45.20561        | 128.39252  | -11.81084             | -29.68940    | -2.66250              |
| 5   | 36.67261        | -54.98784  | 16.73045              | -19.90321    | 3.85653               |
| 6   | 138.00217       | -78.55671  | 21.91621              | 25.22112     | 3.21040               |

Filling fractions in the various cavities, and mole-fractions in the hydrate are given by:

$$\theta_{ki} = \frac{h_{ki}}{1 + \sum_j h_{kj}} \quad (5)$$

$\theta_{ki}$  is the filling fraction of component  $i$  in cavity type  $k$ :

$$x_i^H = \frac{\theta_{large,i} \nu_{large} + \theta_{small,i} \nu_{small}}{1 + \theta_{large,i} \nu_{large} + \theta_{small,i} \nu_{small}} \quad (6)$$

$\nu$  is fraction of cavity per water. Corresponding mole-fraction water is then given by:

$$x_{H_2O}^H = 1 - \sum_i x_i^H \quad (7)$$

The associated hydrate free energy is then:

$$G^{(H)} = x_{H_2O}^H \mu_{H_2O}^H + \sum_i x_i^H \mu_i^H \quad (8)$$

where  $\mu$  is chemical potential.  $H_2O$  subscripts denote water.  $i$  are hydrate formers.  $H$  superscripts denote hydrate.  $x$  is mole-fraction in hydrate (superscript  $H$ ) and  $G$  is free energy.

Guest molecule  $i$  (in the case of this work either  $CO_2$  or  $CH_4$ ) chemical potential that enters Equations (4) and (8) at equilibrium is given by:

$$\mu_i(T, P, \vec{y}) = \mu_i^{pure, idealgas}(T, P, \vec{y}) + RT \ln[y_i \phi_i(T, P, \vec{y})] \quad (9)$$

where  $y_i$  is the mole-fraction of component  $i$  in the gas (or liquid or fluid) mixture.  $\phi_i$  is the fugacity coefficient for component  $i$ . Chemical potential for a monoatomic model of methane in ideal gas state is trivial and analytical from statistical mechanics and the Boltzmann integral over translational momentums. For the rigid  $CO_2$  model there are two additional rotational contributions. The necessary moments of inertia are given in Table 2. The resulting ideal gas chemical potential ends up as trivial functions of temperature and density. The SRK [13] equation of state is utilized for calculating the fugacity coefficient, and also the density needed for the ideal gas chemical potential calculations.

## 2.2. Temperature and Pressure as Driving Forces for Heterogeneous Hydrate Formation on Water/Hydrate Former Interface

With two components (one hydrate former and water) and three phases (water, hydrate former phase and hydrate), there are 12 independent thermodynamic variables, while the sum of conservation laws and conditions for thermodynamic equilibrium cover 11 variables. Hence, when both temperature and pressure are given locally in a reservoir, the system is over determined by 1, and there is no unique equilibrium state. But a pressure temperature equilibrium curve will still represent asymptotic limits at which hydrate formation ends (or enter a modus on infinite time to continue) at that two-dimensional projection of the thermodynamic variables.

For the heterogeneous case we therefore first calculate the equilibrium curve. For pure  $\text{CH}_4$  or pure  $\text{CO}_2$ , and a defined temperature, the chemical potential for the guest is given by Equation (9) for a variable pressure. This chemical potential enters Equation (4) along with the free energy of inclusion, which is a function of temperature only for small and large cavities. Equations (2) and (3) are solved for the same chemical potential of water in liquid state and hydrate given the equilibrium pressure. For completeness the free energies of inclusion are given in Table 3 below. Calculated equilibrium curves for  $\text{CH}_4$  and  $\text{CO}_2$  are compared to experimental data in Figure 2. It is important to keep in mind that the parameters for the free energy of inclusion have been calculated from MD simulations with the procedure described in Kamuro and Tanaka [12] for temperatures up to 280 K for  $\text{CH}_4$ . As such all calculated results are predictions, and results for temperatures above 280 K are all extrapolations. For  $\text{CO}_2$  on the other hand, on the other hand, a system of nine unit cells of hydrate structure I was simulated on all sides with a  $\text{CO}_2$  thick layer. The system was at 273.15 K at 273.15 K and 288 K using SRK in order to keep consistency in our calculations with our calculations in this work that utilize the SRK equation of state. The first two curves for 284 K and 290 K are both in the dense  $\text{CO}_2$  region. The essential difference between the low temperature results and the high temperature results are the impact of the surrounding  $\text{CO}_2$  molecules on the water lattice vibrations. The water lattice structure is dominated by the 75% large cavities and the small cavity does not even benefit much from  $\text{CO}_2$  stabilization size and shape of the molecule. For the small cavities it is a statistical justification of distinguishing between gas or liquid  $\text{CO}_2$  around gas or liquid  $\text{CO}_2$ .

The models for extending thermodynamic properties of water and fluid phases are discussed in detail elsewhere [19–21] and will not be repeated here due to space limitations.

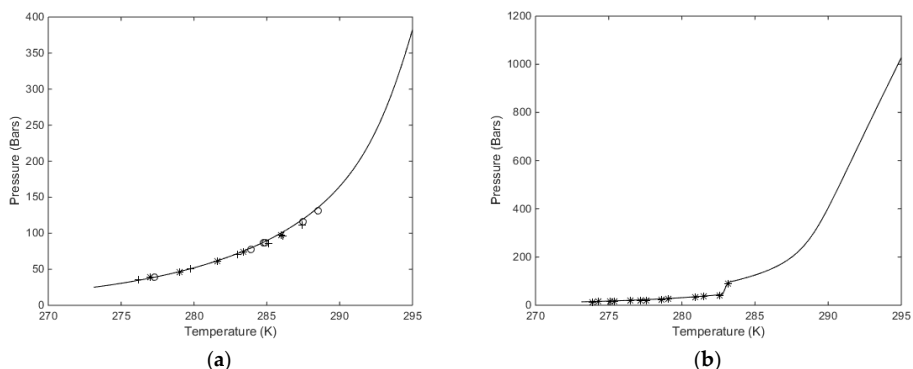


**Figure 2.** (a) Equilibrium curve for  $\text{CH}_4$  hydrate. Calculated values (solid) and experimental data from Bown and van den Broek [21] (f), [22] (b), and [23] (a), [24] (c), [25] (e). (b) Equilibrium curve for  $\text{CO}_2$  hydrate (solid) and experimental data from [25] (\*).

Two aspects regarding Figure 2a,b are worth mentioning. The equilibrium curve for  $\text{CO}_2$  in Figure 2b does not have a discontinuity but there is a rapid change in density related to a phase transition. This leads to a rapid decrease in fugacity coefficients and a corresponding higher pressure needed to reach hydrate equilibrium. Some researchers actually presents Figure 2b as a continuous smooth curve without any rapid change. A second aspect is illustrated in Figure 2a. As can be seen, the equilibrium pressures for  $\text{CO}_2$  hydrate are higher than the equilibrium pressures for  $\text{CH}_4$  after the  $\text{CO}_2$  density increase. This is often wrongly interpreted as a higher stability for the  $\text{CH}_4$  hydrate

Two aspects regarding Figure 2a,b are worth mentioning. The equilibrium curve for CO<sub>2</sub> in Figure 2b does not have a discontinuity but there is a rapid change in density related to a phase transition. This leads to a rapid decrease in fugacity coefficients and a corresponding higher pressure needed to reach hydrate equilibrium. Some researchers actually presents Figure 2b as a continuous smooth curve without any rapid change. A second aspect is illustrated in Figure 2a. As can be seen, the equilibrium pressures for CO<sub>2</sub> hydrate are higher than the equilibrium pressures for CH<sub>4</sub> after the CO<sub>2</sub> density increase. This is often wrongly interpreted as a higher stability for the CH<sub>4</sub> hydrate above the temperature for the CO<sub>2</sub> phase transition. Pressure and temperature are independent thermodynamic variables. Free energies are the corresponding thermodynamic responses for the level of thermodynamic stability. In Figure 2b we plot free energies of CH<sub>4</sub> and CO<sub>2</sub> hydrate as function of temperature along the equilibrium pressures for the two types of hydrates.

Along the curves in Figure 2 the free energy changes in Equation (1) are trivially zero. Outside equilibrium all properties of fluids are continuous and can be calculated for any pressure and temperature. The necessary pressure correction for water chemical potential in Equation (2) is available from the molar volume of liquid water, which is almost constant and independent of temperature and pressure, time pressure minus equilibrium pressure for the actual temperature. Hydrate water chemical potential, on the other hand, is based on an equilibrium theory. The derivation [12] from the grand canonical ensemble in statistical mechanics leads to a Langmuir type of adsorption theory as expressed by Equation (3). For:

$$G_{\text{Non-equilibrium}}^H(T, P, \vec{x}) = G^{H,\text{Eq.}}(T^{\text{Eq.}}, P^{\text{Eq.}}, \vec{x}^{\text{Eq.}}) + \sum_r \left. \frac{\partial G^H}{\partial x_r} \right|_{P, T, x_{i \neq r}} (x_r - x_r^{\text{Eq.}}) + \left. \frac{\partial G^H}{\partial P} \right|_{T, \vec{x}} (P - P^{\text{Eq.}}) + \left. \frac{\partial G^H}{\partial T} \right|_{P, \vec{x}} (T - T^{\text{Eq.}}) \quad (10)$$

we choose  $T$  to be equal to an equilibrium temperature, for which equilibrium pressure and compositions are calculated according to the equation and discussion above. The correction for pressure change is related to the partial molar volumes of water and hydrate formers in hydrate. Water partial molar volume is given by the structure of the hydrate while the occupation volume of the guest molecules can be calculated from Monte Carlo simulations according to the procedures described by Kvamme and Lund [26] and Kvamme and Førreidahl [27]. The calculated volumes are 164.2 Å<sup>3</sup>/molecule and 89.2 Å<sup>3</sup>/molecule for CH<sub>4</sub> in large and small cavities, respectively. Corresponding values for CO<sub>2</sub> are 135.6 Å<sup>3</sup>/molecule and 76.9 Å<sup>3</sup>/molecule for large and small cavities, respectively. The value for CO<sub>2</sub> in small cavities is not practically interesting since the filling fractions of CO<sub>2</sub> in small cavities is practically zero.

Classical nucleation theory (CNT) for a spherical hydrate particle can be written as:

$$J = J_0 e^{-\beta \Delta G^{\text{Total}}} \quad (11)$$

where  $J_0$  is the mass transport flux supplying the hydrate growth. The phase transition in Equation (1) it will be the supply of CH<sub>4</sub> or CO<sub>2</sub> across an interface of gradually more structured water towards the hydrate core, as discussed in Kvamme et al. [19–21]. The units of  $J_0$  will be moles/m<sup>2</sup>s for heterogeneous hydrate formation on the growing surface area of the hydrate crystal.  $\beta$  is the inverse of the gas constant times temperature and  $\Delta G^{\text{Total}}$  is the molar free energy change of the phase transition. This molar free energy consists of two contributions (Equation (1) with Equation (10)) to correct for hydrate properties outside of equilibrium which are the free energy benefit of the phase transition and the second contribution is the penalty related to the work of pushing aside old phases. Even for a hydrate forming on the gas/water interface any hydrate core below critical size will be covered by water also on the side facing the gas due to capillary forces. Molar densities of liquid water and hydrate are reasonably close. It is therefore a fair approximation to multiply the molar free energy of the phase transition with molar density of hydrate times the volume of hydrate core. The penalty of the push



work is the interface free energy times the surface area of the hydrate crystal. The total free energy change in extensive formulation (underlines indicate Joule units):

$$\underline{\Delta G}^{Total} = \underline{\Delta G}^{Phasetransition} + \underline{\Delta G}^{Pushwork} \quad (12)$$

The simplest possible geometry of a crystal is a sphere and for a core radius  $R$  the result is:

$$\underline{\Delta G}^{Total} = \frac{4}{3}\pi R^3 \rho_N^H \Delta G^{Phasetransition} + 4\pi R^2 \gamma \quad (13)$$

where  $\rho_N^H$  is the molar density of the hydrate and  $\gamma$  is the interface free energy between the hydrate and the surrounding phase. There is no reliable value for interface free energy between hydrate and liquid water since the measurement of such a property is extremely difficult. We have not found any value in the open literature. Interface free energy between liquid water and ice is available [28] and the reported value is 29.1 mJ/m<sup>2</sup>. We have used this value as an approximation for interface free energy between liquid water and hydrate in the last term of Equation (13).

Differentiation of (13) with respect to  $R$  gives the solution for maximum free energy radius (the critical core size):

$$R^* = -\frac{2\gamma}{\rho_N^H \Delta G^{Phasetransition}} \quad (14)$$

Superscript \* denotes critical nuclei radius. Calculated critical radii for CH<sub>4</sub> hydrate at two different temperatures are given in Figure 3a. The associated nucleation times are based on integration of Fick's law:

$$t(R) - t(0) = \int_{C_{CH_4}(R=0)}^{C_{CH_4}(R=12)} \frac{\partial C_{CH_4}(z)}{\left[-D_{CH_4}(z) \frac{\partial^2 C_{CH_4}(z)}{\partial z^2}\right]} \quad (15)$$

Energies 2019, 12, x FOR PEER REVIEW

10 of 19

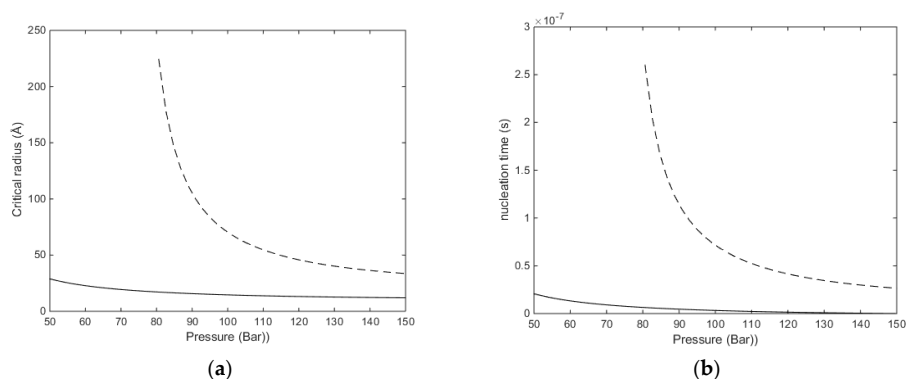


**Figure 3.** (a) Critical radius for CH<sub>4</sub> hydrate as a function of pressure for two different temperatures. Solid curve is for 273.15 K and dashed curve is for 283.15 K. (b) Nucleation time for CH<sub>4</sub> hydrate as a function of pressure for 273.15 K (solid) and 283.15 K (dashed).

The concentration profiles for CH<sub>4</sub> as a function of distance from the liquid side of the interface ( $z = 0$  Å) to the hydrate side of the interface ( $z = 12$  Å) is available from Kvamme [19,20] and Kvamme et al. [21]. The diffusivity coefficient profile for CH<sub>4</sub> was tuned to be the same as for CO since the diffusion of CH<sub>4</sub> and CO through the liquid hydrate interface is dominated by the gradually increasing transport and dynamic situations of partial local dissociation and reformation. See Kvamme et al. [21] for a brief summary of reported diffusivities of hydrate-formers through hydrate. In summary the diffusivities range from 10<sup>-15</sup> m<sup>2</sup>/s to 10<sup>-17</sup> m<sup>2</sup>/s. Quite a number of the studies are based on Monte Carlo studies of “cavity jumping” and rarely reflect any mechanism for how guest molecules are actually able to move around in the hydrate structure. Based on our MD studies [12] the mechanism seems more like a temporary destabilization of water hydrogen bonding structures between filled cavities and empty neighbor cavities. Nevertheless, more detailed studies are needed to verify these observations in a scientifically satisfactory manner. For our purpose in the context of this work we then might expect diffusivity coefficients which are higher than the range indicated above due to the

structure of water towards the hydrate side of the interface. The profile is given by Figure 8a in Kvamme [19] and fitted to Equation (16) with the parameters in Table 4 below.

$$\left[ \frac{D(z)_j}{D_{liquid,j}} \right] = 9.5 \cdot 10^{-9} \sum_{i=1}^9 a_i (a \tan [(0.5z \frac{\pi}{2})/12])^{i-1} \quad (16)$$

**Table 4.** Parameters for Equation (16).

| <i>i</i> | Parameter | <i>i</i> | Parameter | <i>I</i> | Parameter |
|----------|-----------|----------|-----------|----------|-----------|
| 1        | 0.979242  | 4        | 171.673   | 7        | −9649.96  |
| 2        | 15.5427   | 5        | 6.76975   | 8        | 14,779.7  |
| 3        | −88.5112  | 6        | 1939.55   | 9        | −7496.15  |

Using  $D_{liquid,j}$  equal to  $1.0 \cdot 10^{-08} \text{ m}^2/\text{s}$  and integrating Equation (15) to critical size. That is, for every supply of hydrate-former needed to grow a hydrate core, the transport has to cross the interface thickness at the mass transport penalty given by Equation (16). The number of transported molecules is then recalculated to provide a corresponding radius added to the core size. This latter recalculation involves the calculated filling fraction and the corresponding volume of hydrate water. With reference to the equilibrium curve in Figure 2a note that the equilibrium pressure for 283.16 K is around 80 bars and that is the reason for the exponential increase in critical size when the pressure approaches 80 bar. As expected, there is a substantial increase in nucleation time between these two temperatures. At 273.16 K and 150 bar the calculated critical radius is 12.0 Å and nucleation time is essentially instantaneous (less than one ns). Calculated critical radius at 283.16 K and 150 bars is 33.6 Å, and nucleation time is 26.5 ns.

For transport of  $\text{CH}_4$  through the hydrate, in order to continue the growth of the film, it is now assumed that the diffusivity coefficient, and associated diffusion rate at the hydrate side of the interface, is equal to a stationary transport through the hydrate. This rate is expected to be slightly higher than regular diffusion through a block of hydrate without dynamics of couplings to heat transport and dynamic situations of partial local dissociation and reformation. See Kvamme et al. [21] for a brief summary of reported diffusivities of hydrate-formers through hydrate. In summary the diffusivities range from  $10^{-15} \text{ m}^2/\text{s}$  to  $10^{-17} \text{ m}^2/\text{s}$ . Quite a number of the studies are based on Monte Carlo studies of “cavity jumping” and rarely reflect any mechanism for how guest molecules are actually able to move around in the hydrate structure. Based on our MD studies [12] the mechanism seems more like a temporary destabilization of water hydrogen bonding structures between filled cavities and empty neighbor cavities. Nevertheless, more detailed studies are needed to verify these observations in a scientifically satisfactory manner. For our purpose in the context of this work we then might expect diffusivity coefficients which are higher than the range indicated above due to the couplings with heat transport dynamics rapid local dissociation/refreezing effects. The heat transport dynamics is implicitly coupled through the relationship:

$$\frac{\partial \left[ \frac{\Delta G^{\text{Total}}}{RT} \right]_{P,\bar{N}}}{\partial T} = - \left[ \frac{\Delta H^{\text{Total}}}{RT^2} \right] \quad (17)$$

which then connects Equations (12), (13) and (1) for any hydrate core since the number of moles in the actual radius of the core is simply the volume of the core times the molar density of the hydrate core. In the simple calculations below we disregard effects of heat transport dynamics. Based on our earlier calculations [15–18], and also in accordance with other sources in the literature, the heat transport rate through liquid water is 2–3 times faster than the corresponding mass transport rate. This ratio will be orders of magnitude higher for transport through hydrate. In accordance with this we expect that the mass transport rate is only affected by heat transport due to fast local phase transitions.

Within the focus of this work we simply examine a couple of values for  $D_{liq}$  in (16) and plot the time needed to reach 1 mm hydrate film thickness. In Figure 4 we plot results for  $D_{liq} = 5 \cdot 10^{-08} \text{ m}^2/\text{s}$  in Equation (16) and the condition of temperature and pressure equal to that used in a magnetic resonance imaging experiment conducted at the ConocoPhillips research laboratory in Bartlesville (OK, USA). The experiment was conducted at a temperature of 276.25 K and 83 bars with initial equal volumes of liquid water and  $\text{CH}_4$ . See Kvamme et al. [29] for more details on the experiment. The container was made of plastic and as such was methane-wetting.

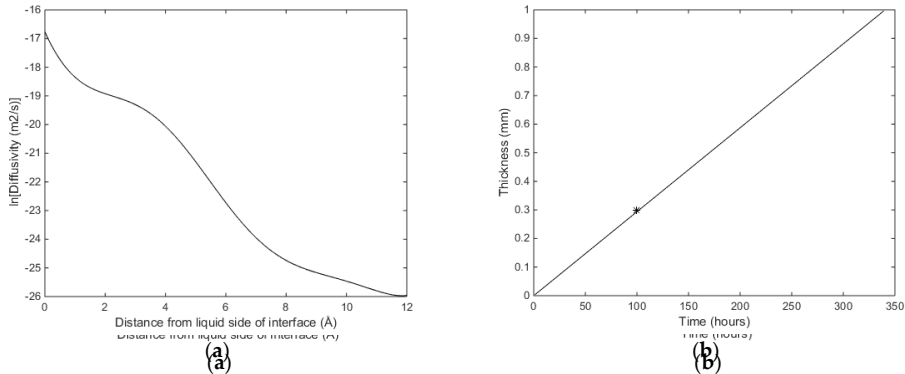


**Figure 4.** (a) Diffusivity profile for  $D_{liq} = 5 \cdot 10^{-08} \text{ m}^2/\text{s}$  in Equation (16) as applied for  $\text{CH}_4$  hydrate. (b) Calculated hydrate film thickness as function of time (solid) and experimental observation from Magnetic Resonance Imaging (MRI) experiment [29,30] for  $\text{CH}_4$  hydrate based on a resolution of 300 micron.

Nucleation studies for  $\text{CO}_2$  have been published in a recent paper [19] and in order to save space we limit ourselves to estimates of growth as illustrated in Figure 5. Nucleation studies for  $\text{CO}_2$  have been published in a recent paper [19] and in order to save space we limit ourselves to estimates of growth as illustrated in Figure 5.

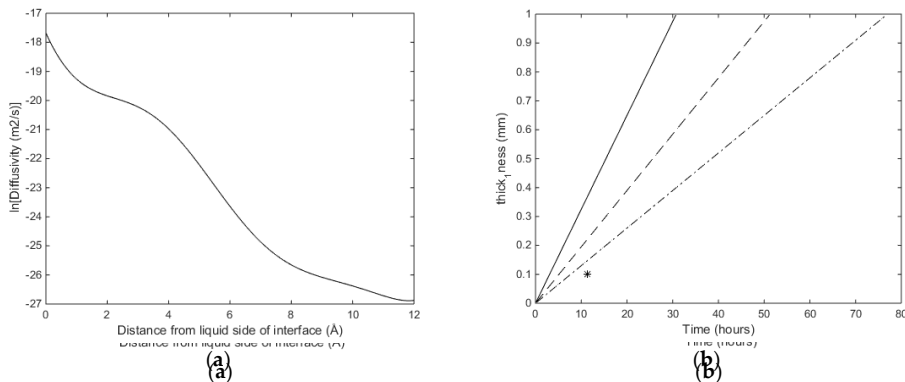


**Figure 5.** (a) Diffusivity profile for  $D_{liq} = 2 \cdot 10^{-08} \text{ m}^2/\text{s}$  in Equation (16) for  $\text{CO}_2$  hydrate. (b) Calculated hydrate film thickness as function of time for  $D_{liq} = 5 \cdot 10^{-08} \text{ m}^2/\text{s}$  (solid),  $D_{liq} = 3 \cdot 10^{-08} \text{ m}^2/\text{s}$  (dashed) and  $D_{liq} = 2 \cdot 10^{-08} \text{ m}^2/\text{s}$  (dash-dot). The experimental point (\*) is rather uncertain and based on a reading of a picture in Uchida et al. [31] for a water droplet exposed to  $\text{CO}_2$  under hydrate forming conditions.

Based on the methods of Kvamme and Tanaka [12] it is easy to see that water molecules between a filled cavity and a neighboring empty cavity have higher librational movements and hydrogen bonding structures can temporarily break and let guest molecules move to the empty movements. And these open neighboring structures while for the larger  $\text{CO}_2$  and the largest cavity neighbors can participate in such transports. For  $\text{CH}_4$  this can happen for all cavities while for the larger  $\text{CO}_2$  only large cavity neighbors can participate in such transports. As such it is reasonable that the diffusivity coefficient for  $\text{CO}_2$  through hydrate is lower than the corresponding values for  $\text{CH}_4$ . And just as macroscopic heat transport is orders of magnitude faster than mass transport so is the local molecular heat transport involved in breaking and reforming hydrogen water hydrogen bonds during migration of a guest involved in breaking and reforming hydrogen water hydrogen bonds during migration of a guest

in such transports. As such it is reasonable that the diffusivity coefficient for CO<sub>2</sub>, through hydrate, is lower than the corresponding values for CH<sub>4</sub>. And just as macroscopic heat transport is orders of magnitude faster than mass transport so is the local molecular heat transport involved in breaking and reforming hydrogen water hydrogen bonds during migration of a guest molecule between cavities.

The mechanical strength of hydrate films in a pore depends on the cross section area, thickness and strength of connection to the mineral surfaces. As discussed in several papers, for instance [32,33] the papers referenced therein, hydrate can never touch the surface of minerals. From a thermodynamic point of view, the thickness of the first adsorbed water layer on mineral surfaces of water, hematite and kaolinite is on the order of three times the density of liquid water. The associated chemical potential is very low and far lower than is even possible for water in hydrate. Even the average chemical potential of adsorbed water layer on minerals such as calcite, hematite, and kaolinite is only a few percent of the average chemical potential of water in hydrate. Even the first five layers of water adsorbed on Hematite are calculated to be 1/3 the chemical potential of water in liquid adsorbed on it. The reason is the strong Coulombic lower interaction with water. The reason is also an easy to see that the regular distribution of mineral charges on water regular distribution of partial charges on water hydrogens and oxygens in a hydrate crystal can never favorably match the distribution of positive and negative charges on the mineral surfaces.

What we have presented above provides a tool for analyzing how rapidly the hydrate film will grow, and for specific porosity and minerals, when and at what frequency we need to shock the system in order to break these hydrate films during the formation of hydrate. The specific sediment (or soil) used in the experiment (or in a lab) is not a laboratory for this purpose. We need a higher resolution time scale of the growth, and in Figure 6 we plot the times needed to reach 100 nm and 100 nm and 10,000 nm (10,000 nm).

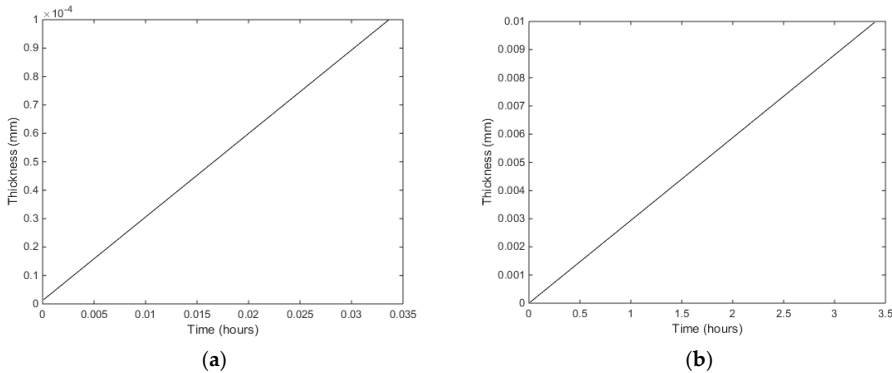


Figure 6. (a) Time to grow 100 nm CH<sub>4</sub> hydrate film. (b) Time to grow 100 micrometer hydrate film.

As discussed above it is a straightforward mechanical calculation to determine the magnitude of a mechanical pulse. If 10<sup>11</sup> nm is an acceptable thickness then the frequency of a mechanical shock needs to be on the average 2 μm. Depending on the laboratory setup this pulse can be generated by sound, mechanical shaking of the sediment, or electric. The important thing is that the sediment section is kept in place relative to the fluid and that the mechanical pulse is intended to break the hydrate film in moderate amounts in order to break the hydrate films. The necessary forms needed is sensitive to many factors like for instance pore size, geochemical issues (mineral type and salinity) as well as temperature and pressure. Calculations and necessary forces to break the hydrate films using mechanical pulses are therefore too case specific to discuss in a more general paper like this. In a more general paper on hydrate production [8,9,11] large amounts of N<sub>2</sub> were added and the thermodynamic driving force for creating a new CO<sub>2</sub> hydrate was practically zero. Instead of mechanically breaking the hydrate film with efficient surfactants can break the water/CO<sub>2</sub> interface free of blocking hydrate and permit for more continuous hydrate formation from the injected CO<sub>2</sub> free of blocking hydrate and permit for more continuous hydrate formation from the injected CO<sub>2</sub>. Even methanol has surfactant properties but is too soluble in water to be interesting. And methanol is of course poisonous and not desirable to use. But some general insight can be found from a recent study [21].

Even methanol has surfactant properties but is too soluble in water to be interesting. And methanol is of course poisonous and not desirable to use. But some general insight can be found from a recent study [21].

Hydrate can nucleate and grow from dissolved hydrate formers as discussed in a number of papers [9,10,14–16,18,19,21,29,30]:

Hydrate can nucleate and grow from dissolved hydrate formers (discussed in a number of papers [9,10,14–16,18,19,21,29,30]):

$$\Delta G^{(H_2)} = \left[ \sum_{H_2O} x_{H_2O}^{H_2} (\mu_{H_2O}^{H_2}(T, P, \vec{x}^{H_2}) - \mu_{H_2O}^{water}(T, P, \vec{x})) + \sum_{H_2} x_{H_2}^{H_2} (\mu_{H_2}^{H_2}(T, P, \vec{x}^{H_2}) - \mu_{H_2}^{water}(T, P, \vec{x})) \right] \quad (12)$$

$$\Delta G^{(H_2)} = \left[ \sum_{H_2O} x_{H_2O}^{H_2} (\mu_{H_2O}^{H_2}(T, P, \vec{x}^{H_2}) - \mu_{H_2O}^{water}(T, P, \vec{x})) + \sum_{H_2} x_{H_2}^{H_2} (\mu_{H_2}^{H_2}(T, P, \vec{x}^{H_2}) - \mu_{H_2}^{water}(T, P, \vec{x})) \right] \quad (18)$$

Chemical potential for water as solvent for CH<sub>4</sub> is not affected significantly by the very low concentrations of CH<sub>4</sub>. For CO<sub>2</sub> dissolved in water the approximation in Equation (2) is considered to be good enough for the purpose of this work. Models for chemical potential of the hydrate former, which appear in the last term of Equation (18) are discussed in more detail in [19–21] and will not be repeated here. These chemical potentials also enter the canonical partition function for guest molecules in the two types of cavities through Equation (4). The actual film thickness that can be added through this route is limited for CH<sub>4</sub> and significant for CO<sub>2</sub>.

There are several implications of the calculations illustrated in Figure 7. Dissociation of hydrate leads to a combination of gas bubbles and supersaturation of hydrate former in the surrounding water. This can then in turn lead to reformation of hydrate from dissolved hydrate former in concentration ranges between the blue and the black curve. If water surrounding the hydrate is diluted below the black curve then hydrate will dissociate. Also keep in mind that every unique concentration of hydrate former in between the blue and black curves will lead to a unique hydrate composition due to the chemical potential dependency of hydrate former as a function of concentration. Mathematically this means that an infinite number of different hydrates are possible. Stability will of course vary substantially.

There are several implications of the calculations illustrated in Figure 7. Dissociation of hydrate concentration ranges between the blue and the black curve. If water surrounding the hydrate is diluted below the black curve then hydrate will dissociate. Also keep in mind that every unique concentration of hydrate former in between the blue and black curves will lead to a unique hydrate composition due to the chemical potential dependency of hydrate former as a function of concentration. Mathematically this means that an infinite number of different hydrates are possible. Stability will of course vary substantially.

There are several implications of the calculations illustrated in Figure 7. Dissociation of hydrate concentration ranges between the blue and the black curve. If water surrounding the hydrate is diluted below the black curve then hydrate will dissociate. Also keep in mind that every unique concentration of hydrate former in between the blue and black curves will lead to a unique hydrate composition due to the chemical potential dependency of hydrate former as a function of concentration. Mathematically this means that an infinite number of different hydrates are possible. Stability will of course vary substantially.

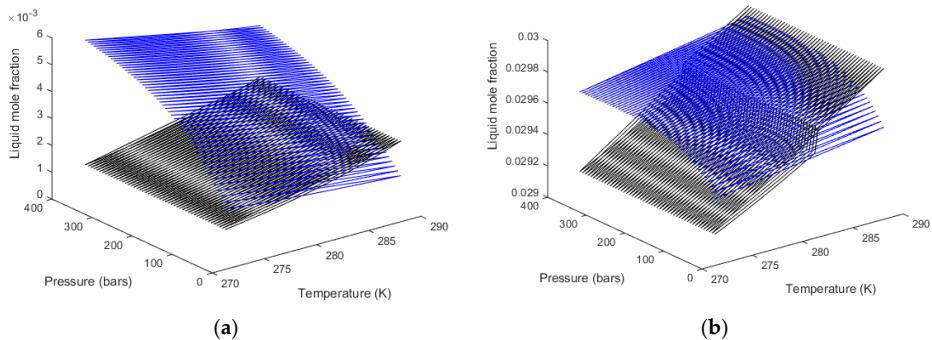


**Figure 7.** (a) Solubility of CH<sub>4</sub> in liquid water (blue) and lower limit of hydrate stability (black). (b) Solubility of CO<sub>2</sub> in liquid water (blue) and lower limit of hydrate stability (black). Hydrate formation concentration ranges between the blue and black curves. Concentrations of hydrate formers in surrounding water less than the black curves lead to hydrate dissociation. Possible concentration of hydrate formers in water above the blue curves lead to degassing from water solution. Examples of the free energies of hydrates from water and CH<sub>4</sub>, and water and CO<sub>2</sub> are given in figure 10b as function of temperature and pressure. Free energies for hydrates of homologs from solution and different different than the typical picture CH<sub>4</sub> hydrate, CH<sub>2</sub> and CO<sub>2</sub> hydrates are similar.

Figure 8 illustrates a bit more clearly the regions for which it is not possible to grow hydrate from dissolved hydrate formers in water, i.e., regions for which the blue curves are lower in free energy. As expected, the differences in hydrate free energies between CH<sub>4</sub> hydrate formed from

Figure 8 illustrates a bit more clearly the regions for which it is not possible to grow hydrate from solution in slightly formable water.  $\text{CO}_2$  hydrate forms from the solution. But the differences are hardly significant compared to the corresponding differences in free energies formed heterogeneously from gas (or fluid) hydrate from a phase and liquid water. But the differences are hardly significant compared to the corresponding differences in free energies formed heterogeneously from gas (or fluid) hydrate from a phase and liquid water.

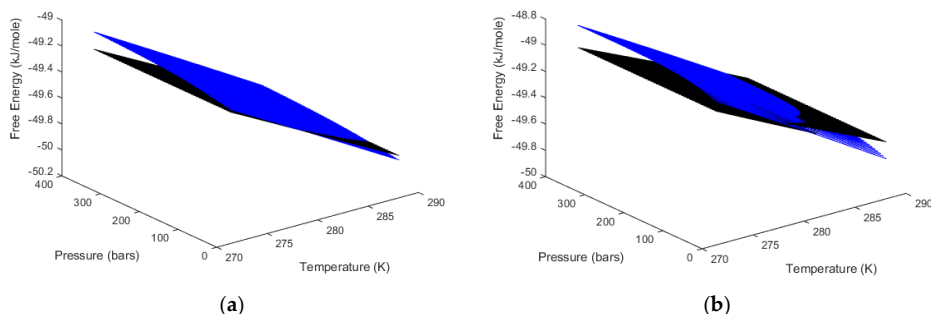


**Figure 8.** (a) Free energy of aqueous solution of  $\text{CH}_4$  (blue) and free energy of  $\text{CH}_4$  hydrate at stability limit toward liquid water (black). (b) Free energy of aqueous solution of  $\text{CO}_2$  (blue) and free energy of  $\text{CO}_2$  hydrate at stability limit toward liquid water (black). The black color in the illustration is the dynamic lines for dry hydrate formation for hydrate solution in the black color. The black color is the free energy of the hydrate but the free hydrate behavior of creating hydrate for the specific conditions the hydrate formation rate of hydrate in water as given in Figure 7.

## 2.4. Hydrate Nucleation from Primary and Secondary Adsorption of Hydrate Formers on Mineral Surfaces

$\text{CH}_4$  is non-polar and cannot adsorb directly on charged mineral surfaces in competition with water, but  $\text{CH}_4$  molecules can get trapped in structured water as illustrated in some recent MD studies at the University of Bergen [34]. These studies indicate that methane gets dynamically trapped in structured water—typically from the third minimum in the water density as a function of distance from the calcite surface. As long there is a separate methane phase outside of the water layer in contact with the calcite a methane/water region, or phase, exists inside the water. Average water/methane distances in this separate phase are close to the characteristic of a small hydrate cavity. But the dynamics of the structure makes it hard to evaluate associated chemical potentials for methane with sufficient confidence. Work is in progress to overcome these challenges. Some illustrative animations from the MD simulations are available from the first author of the current work.

Direct adsorption is possible for polar and slightly polar hydrate formers like  $\text{H}_2\text{S}$ , which has a significant dipole moment and adsorbs well on the same type of minerals as water due to similarities in molecular structures. Although we do have a variety of chemical potentials for different interaction models for  $\text{H}_2\text{S}$  the limitation is that the results cannot be evaluated. Chemical potentials of adsorbed molecules cannot be measured directly but the density profiles of adsorbed molecules can be derived from measured structure factors. One of our examples for adsorbed  $\text{CO}_2$  on Calcite [33] is illustrated in Figure 9 below. The finer details of the molecular simulations are too extensive in the context of this paper so the reader is directed to the original work [33] which is available for free download or can be provided by the first author of this paper. In the context of this paper we only use the calculated value for chemical potential as an example. The average value is of course sensitive to temperature and we can only solve for the hydrate stability pressure for this particular temperature, which is 17.0 bar when liquid water chemical potential is used for the water. This can be compared to a stability limit pressure of 15.7 bars for the same temperature and using  $\text{CO}_2$  from gas. This is work in progress and more detailed studies of the chemical potentials of  $\text{CO}_2$  and water that actually makes the nuclei is needed.

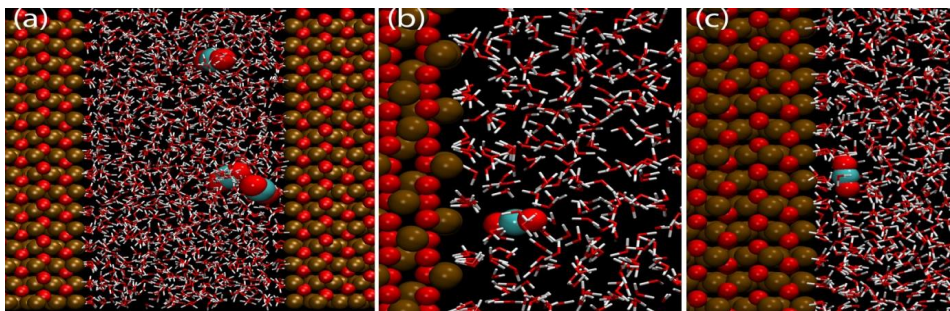


**Figure 9.** Snapshots of various configurations of trapped  $\text{CO}_2$  and indirectly adsorbed  $\text{CO}_2$  on a calcite surface at 274 K. Red on calcite is oxygens and brown is calcium, but upscale relative to size of water.  $\text{CO}_2$  is upscale, with red for oxygens and cyan for carbon. Water molecules have white hydrogens and red oxygens. The average value of  $\text{CO}_2$  chemical potential is  $39.27 \text{ kJ/mol}$ .

### 3. Discussion

Hydrates in sediments can form from many different phases. The most important routes to hydrates are however initial nucleation on the interface between water and hydrate or phase nucleation towards mineral surfaces. These two routes are very different in the sense that hydrate that appear to nucleate on mineral surfaces will be able to nucleate towards mineral surfaces and the other hand nucleation of hydrate by the interface between hydrate former phase and water, on the other hand can lead to a slow down of growth due to mass transport limitation of hydrate through the hydrate film. Visual observations of hydrate formation techniques with the use of the lead to the correct interpretation of reduction of nucleation delay as time increases.

The problem of hydrate films that slow down hydrate growth often leads to a typical misunderstanding that  $\text{CO}_2$  is not efficient for producing hydrates. The opposite might actually be the case with the right additives to  $\text{CO}_2$ , but this is the subject for a subsequent paper. In the paper by the paper of [19–21] gives some insights.

Another frequent misunderstanding is that methane hydrate is more stable than  $\text{CO}_2$  hydrate above a certain temperature, as illustrated in the combined Figure 2a,b above and Figure 10b below. Temperature and pressure are independent thermodynamic variables and the free energy is what determines phase stability and relative stability. Free energies of  $\text{CH}_4$  and  $\text{CO}_2$  hydrates along the equilibrium conditions are plotted in Figure 10b. There are consequences of these differences and that will be discussed further in the subsequent paper.

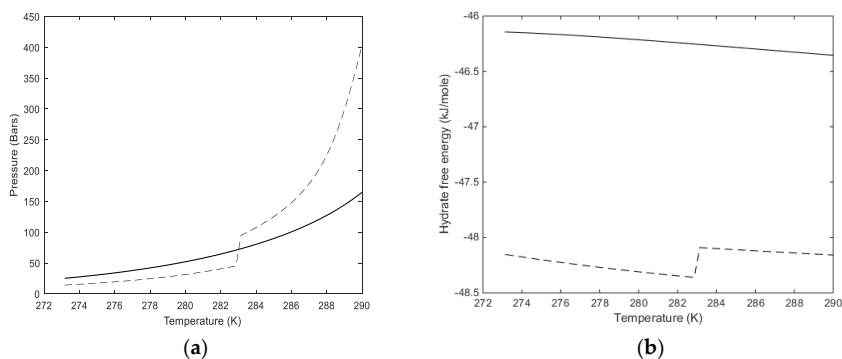


**Figure 10.** (a) Pressure temperature equilibrium curves for  $\text{CH}_4$  hydrate (solid) and  $\text{CO}_2$  hydrate (dash). (b) Free energies for hydrates of  $\text{CH}_4$  (solid) and  $\text{CO}_2$  (dash) hydrates along their equilibrium conditions of temperature and pressure.

above a certain temperature, as illustrated in the combined Figure 2a,b above and Figure 10b below. Temperature and pressure are independent thermodynamic variables and the free energy is what determines phase stability and relative stability. Free energies of CH<sub>4</sub> and CO<sub>2</sub> hydrates along the equilibrium conditions are plotted in Figure 10b. There are consequences of these differences and this will be discussed further in a subsequent paper.

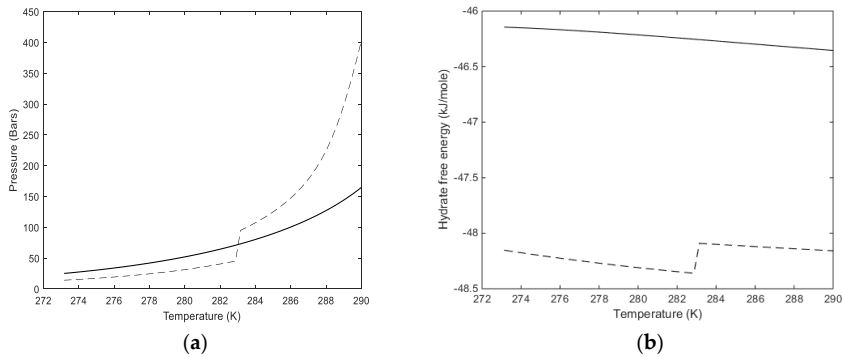


**Figure 10.** (a) Pressure-temperature equilibrium curves for CH<sub>4</sub> hydrate (solid) and CO<sub>2</sub> hydrate (dashed). (b) Free energies for hydrates of CH<sub>4</sub> (solid) and CO<sub>2</sub> (dashed) hydrates along their equilibrium conditions of temperature and pressure.

Even if the diffusivity of hydrate formers through hydrate films is faster than is represented by diffusivity coefficients on the order of  $10^{-15}$  m<sup>2</sup>/s or less due to local dissociation mechanisms, a solid state transition [5,6] is highly unlikely for temperatures above freezing, as is also discussed elsewhere [11,16,19,35,36]. The thermodynamic driving force for such a transition would be the difference in free energy derived from Figure 10b. In such a system water is either hydrate or frozen water except in the mineral/water interface and the water hydrate interface, which are both nano scale in thickness. The only other exception is water trapped in small pores and unlikely to form hydrate due to mechanical strain in the hydrate lattice and a relatively large impact of mineral surfaces. The experiments at temperatures far below zero have limited value for relevant hydrate reservoirs since the solid state conversion is likely never going to play any role in reservoirs. Another confusion caused by these experiments is the inclusion of CO<sub>2</sub> in small cavities. It is theoretically possible but not thermodynamically feasible at realistic reservoir temperatures above zero.

The only feasible formation concept is, therefore, that injected CO<sub>2</sub> forms a new CO<sub>2</sub> hydrate and that the released hydrate heat of formation dissociates CH<sub>4</sub> hydrate. There is actually excess heat available for this process since the heat of formation of CO<sub>2</sub> hydrate is higher than is needed to dissociate CH<sub>4</sub> hydrate, as illustrated in Figure 11a above [19,20]. Adding large amounts of nitrogen in the CO<sub>2</sub>, or using fuel gas dominated by nitrogen is not a good solution, as discussed earlier in several papers, e.g., [9], and illustrated in Figure 11b for 146 bar. At 276 K more than 30% CO<sub>2</sub> is needed in order to make new hydrate with water. At temperatures above slightly more than 286 K chemical potential for liquid water is also lower than chemical potential of water in hydrate from pure CO<sub>2</sub> and water, which is also illustrated by the equilibrium curve in Figure 2b. A limited amount of nitrogen can be useful for increasing the permeability of the injection gas. And since nitrogen can enter the 25% small cavities of a structure I hydrate primarily stabilized by CO<sub>2</sub>, any addition of nitrogen reduces the thermodynamic driving force for making a new CO<sub>2</sub> hydrate. Large amounts of N<sub>2</sub> (or even air) will lead to dissociation of CH<sub>4</sub> hydrate because the N<sub>2</sub> phase (or air) is undersaturated with CH<sub>4</sub> relative to the chemical potential of CH<sub>4</sub> in the hydrate, and if the N<sub>2</sub> (or air) is dry relative to water saturation with reference to water in hydrate that will be an additional driving force for CH<sub>4</sub> hydrate dissociation. Figure 1 in the recent paper by Darnell et al. [37] is therefore wrong since the N<sub>2</sub> hydrate stability limit curve (green curve) is not relevant for the actual processes. The CO<sub>2</sub> hydrate curve, as well as the CO<sub>2</sub> fluid curves is also wrong since CO<sub>2</sub> goes through a phase transition. This has been discussed elsewhere in this work. See also Figure 2. See also Figures 10 and 11 which illustrate the need for a thermodynamic analysis rather than plots in independent thermodynamic variable P and T. A simulation model without real phase transition analysis in terms of free energy based functions are therefore of limited value. Lack of heat transport analysis is also a limitation of this work. The free



energy difference between  $\text{CH}_4$  in the hydrate and in the outside  $\text{N}_2$ , as one example, will enter as the thermodynamic benefit but this driving force is implicitly coupled to mass—and heat—transport dynamics. See also Kvamme [19,20] and Kvamme et al. [21] for more details.

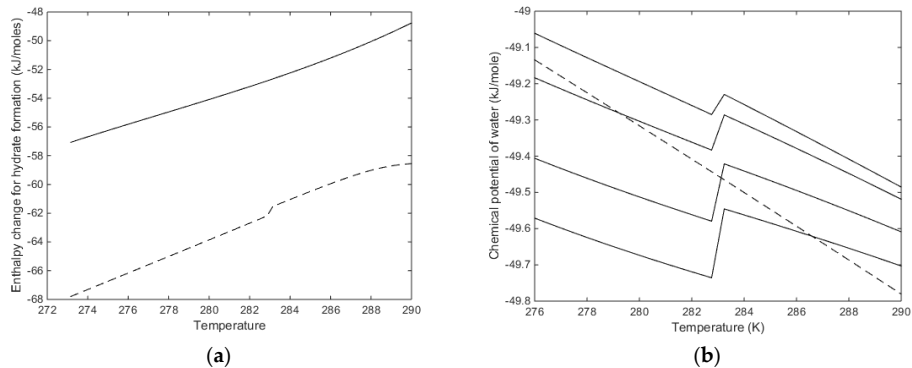


**Figure 11.** (a) Enthalpy of  $\text{CH}_4$  hydrate formation (solid) along the hydrate equilibrium curve and enthalpy of  $\text{CO}_2$  hydrate formation (dashed) along the hydrate equilibrium curve. (b) Chemical potentials for water in hydrates formed from  $\text{CO}_2$  and  $\text{N}_2$  mixtures at 146 bars. Solid curves are chemical potentials for pure  $\text{CO}_2$ , next solid curve is for 70 mole percent  $\text{CO}_2$ , then 40 mole percent  $\text{CO}_2$  and the top is for 20 mole percent  $\text{CO}_2$ .

The key to efficient additives is illustrated in the paper by Kvamme et al. [27]. Small amounts of methanol in water will have a hydrate activating effect due to its surfactant properties. First of all the concentration of methanol at the water/ $\text{CH}_4$  interface will keep the interface open and free of blocking hydrate films. A second effect is increased transport rates for  $\text{CH}_4$  into water. The third effect is a higher solubility of  $\text{CH}_4$  in the water below the methanol concentrated layer. The hydrate activator effect of small amounts of methanol is well known from industrial experience and the Tommelien study [38]. Methanol is of course not a desirable additive since it will dissolve in water, and will eventually also disappear from the interface, but adding small surfactants to  $\text{CO}_2$  is a good approach. Large water/ $\text{CO}_2$  surfactants, on the other hand, are not of useful activities for enhancing the detection of  $\text{CO}_2$ . The heavy surfactants are the order of magnitude weights of some few thousands as like to cause problems of surfactant clogging and block in the flow pathways between the hydrate and mineral surfaces. The breaking of hydrate films is an alternative. The study of hydrate film formation and growth are still useful to be together with energy balance for calculation of heating/cooling frequencies and necessary heat impulses for breaking desired film thickness.

#### 4. Conclusions

Hydrates can nucleate from many phases. Except for cases of extremely small thermodynamic driving forces it is nano-scale phenomenon in both time and volume, as illustrated in this work using classical nucleation theory. The values for critical hydrate sizes obtained in this work are very much in accordance with earlier results that we have calculated from far more theoretically advanced approaches. Transport through hydrate films established through heterogeneous hydrate formation on the interface between liquid water and hydrate former phase is extremely slow. Simplified mass transport limitation models are able to verify the long induction times that are frequently observed in hydrate experiments. This type of information is critical since it can be used to design experimental equipment for efficient formation of hydrate film on hydrate former phase. It can be used to calculate the necessary frequencies for mechanical shock pulses for breaking mass transport-limiting hydrate films and ensure efficient conversion of water and hydrate-formers in the sediment pores. These calculations will also be useful if cycles of heating/cooling are used to break hydrate films and reform hydrate. The existence of these mass transport limiting films is also a critical issue in the use of  $\text{CO}_2$  for combined production of  $\text{CH}_4$  from hydrate and safe storage of  $\text{CO}_2$  in the form of hydrate. Adding nitrogen in small amounts increases gas permeability but it is absolutely critical that the amount of nitrogen be balanced so that there is still a significant driving

These calculations will also be useful if cycles of heating/cooling are used to break hydrate films and reform hydrate. The existence of these mass transport limiting films is also a critical issue in the use of CO<sub>2</sub> for combined production of CH<sub>4</sub> from hydrate and safe storage of CO<sub>2</sub> in the form of hydrate. Adding nitrogen in small amounts increases gas permeability but it is absolutely critical that the amount of nitrogen be balanced so that there is still a significant driving force for creating a new CO<sub>2</sub>-dominated hydrate from the injection gas. Adding specially designed small surfactants will keep interfaces open and free of blocking hydrate films.

**Author Contributions:** All authors have been involved in Methodology, formal analysis and writing-review & editing.

**Funding:** This research received no external funding

**Conflicts of Interest:** The authors declare no conflict of interest.

## References

1. Dallimore, S.R.; Uchida, T.; Collett, T.S. *Scientific Results from JAPEX/JNOC/GSC Mallik 2L-38 Gas Hydrate Research Well, Mackenzie Delta, Northwest Territories, Canada*; Bulletin 544; Geological Survey of Canada: Ottawa, ON, Canada, 1999.
2. Hancock, S.H.; Collett, T.S.; Dallimore, S.R.; Satoh, T.; Inoue, T.; Huenges, E.; Hennings, J.; Weatherill, B. *Overview of Thermal-Stimulation Production-Test Results for the JAPEX/JNOC/GSC et al. Mallik 5L38 Gas Hydrate Production Research Well*; Bulletin 585; Geological Survey of Canada: Ottawa, ON, Canada, 2005.
3. Konno, Y. Oral Presentation. In Proceedings of the Nanotechnology and Nano-Geoscience in Oil and Gas Industry, Kyoto, Japan, 4–8 March 2014.
4. Tenma, N. Recent Status of Methane Hydrate R&D Program in Japan. In Proceedings of the 11th International Methane Hydrate Research and Development, Corpus Christie, TX, USA, 5–8 December 2017.
5. Lee, H.; Seo, Y.; Seo, Y.-T.; Moudrakovski, I.L.; Ripmeester, J.A. Recovering methane from solid methane hydrate with carbon dioxide. *Angew. Chem. Int. Ed.* **2003**, *42*, 5048–5051. [[CrossRef](#)] [[PubMed](#)]
6. Falenty, A.; Genov, G.; Hansen, T.C.; Kuhs, W.F.; Salamat, A.N. Kinetics of CO<sub>2</sub>-hydrate formation from water frost at low temperatures: Experimental results and theoretical model. *J. Phys. Chem. C* **2010**, *115*, 4022–4032. [[CrossRef](#)]
7. Kuznetsova, T.; Kvamme, B.; Morrissey, K. An alternative for carbon dioxide emission mitigation: In situ methane hydrate conversion. *AIP Conf. Proc.* **2012**, *1504*, 772–775.
8. Schoderbek, D.; Farrell, H.; Hester, K.; Howard, J.; Raterman, K.; Silpngarnlert, S.; Lloyd Martin, K.; Smith, B.; Klein, P. *ConocoPhillips Gas Hydrate Production Test Final Technical Report (1 October 2008–30 June 2013)*; ConocoPhillips Company for United States Department of Energy National Energy Technology Laboratory: Houston, TX, USA, 2013.
9. Kvamme, B. Thermodynamic limitations of the CO<sub>2</sub>/N<sub>2</sub> mixture injected into CH<sub>4</sub> hydrate in the Ignik Sikumi field trial. *J. Chem. Eng. Data* **2016**, *61*, 1280–1295. [[CrossRef](#)]
10. Baig, K. Nano to Micro Scale Modeling of Hydrate Phase Transition Kinetics. Ph.D. Thesis, University of Bergen, Bergen, Norway, 2017.
11. Baig, K.; Kvamme, B.; Kuznetsova, T.; Bauman, J. The impact of water/hydrate film thickness on the kinetic rate of mixed hydrate formation during CO<sub>2</sub> injection into CH<sub>4</sub> hydrate. *AIChE J.* **2015**, *61*, 3944–3957.
12. Kvamme, B.; Tanaka, H. Thermodynamic stability of hydrates for ethane, ethylene, and carbon dioxide. *J. Phys. Chem.* **1995**, *99*, 7114–7119. [[CrossRef](#)]
13. Soave, G. Equilibrium constants from a modified Redlich–Kwong equation of state. *Chem. Eng. Sci.* **1972**, *27*, 1197–1203. [[CrossRef](#)]
14. Kvamme, B.; Graue, A.; Aspenes, E.; Kuznetsova, T.; Gránásy, L.; Tóth, G.; Pusztai, T.; Tegze, G. Kinetics of solid hydrate formation by carbon dioxide: Phase field theory of hydrate nucleation and magnetic resonance imaging. *Phys. Chem. Chem. Phys.* **2004**, *6*, 2327–2334. [[CrossRef](#)]
15. Tegze, G.; Pusztai, T.; Tóth, G.; Gránásy, L. Multiscale approach to CO<sub>2</sub> hydrate formation in aqueous solution: Phase field theory and molecular dynamics. Nucleation and growth. *J. Chem. Phys.* **2006**, *124*, 234710. [[CrossRef](#)]
16. Kivelä, P.-H.; Baig, K.; Qasim, M.; Kvamme, B. Phase field theory modeling of methane fluxes from exposed natural gas hydrate reservoirs. *AIP Conf. Proc.* **2012**, *1504*, 351–363.

17. Qasim, M. *Microscale Modeling of Natural Gas Hydrates in Reservoirs*. Ph.D. Thesis, University of Bergen, Bergen, Norway, 2012.
18. Svandal, A. *Modeling Hydrate Phase Transitions Using Mean-Field Approaches*. Ph.D. Thesis, University of Bergen, Bergen, Norway, 2006.
19. Kvamme, B. Environmentally friendly production of methane from natural gas hydrate using carbon dioxide. *Sustainability* **2019**, *11*, 1964.
20. Kvamme, B. Enthalpies of hydrate formation from hydrate formers dissolved in water. *Energies* **2019**, *12*, 1039. [[CrossRef](#)]
21. Kvamme, B.; Selvåg, J.; Aromada, S.A.; Saeidi, N.; Kuznetsova, T. Methanol as hydrate inhibitor and hydrate activator. *Phys. Chem. Chem. Phys.* **2018**, *20*, 21968–21987. [[CrossRef](#)] [[PubMed](#)]
22. Bavoh, C.B.; Partoon, B.; Laland, B.; Keong, L.K. Methane hydrate liquid–vapour–equilibrium phase condition measurements in the presence of natural amino acids. *J. Nat. Gas Sci. Eng.* **2017**, *37*, 425–434. [[CrossRef](#)]
23. Tumba, K.; Reddy, P.; Naidoo, P.; Ramjugernath, D.; Eslamimanesh, A.; Mohammadi, A.H.; Richon, D. Phase equilibria of methane and carbon dioxide clathrate hydrates in the presence of aqueous solutions of tributylmethylphosphonium methylsulfate ionic liquid. *J. Chem. Eng. Data* **2011**, *56*, 3620–3629. [[CrossRef](#)]
24. Sabil, K.M.; Nashed, O.; Lal, B.; Ismail, B.; Japper-Jaafar, A. Experimental investigation on the dissociation conditions of methane hydrate in the presence of imidazolium-based ionic liquids. *Thermodyn. J. Chem.* **2015**, *84*, 7–13.
25. Herri, J.-M.; Bouchemoua, A.; Kwaterski, M.; Fezoua, A.; Ouabbas, Y.; Cameirao, A. Gas hydrate equilibria for CO<sub>2</sub>–N<sub>2</sub> and CO<sub>2</sub>–CH<sub>4</sub> gas mixtures—Experimental studies and thermodynamic modelling. *Fluid Phase Equilibria* **2011**, *301*, 171–190. [[CrossRef](#)]
26. Kvamme, B.; Lund, A. The influence of gas–gas interactions on the Langmuir–constants for some natural gas hydrates. *Fluid Phase Equilibria* **1993**, *90*, 15–44. [[CrossRef](#)]
27. Kvamme, B.; Førriisdahl, O.K. Polar guest–molecules in natural gas hydrates. *Fluid Phase Equilibria* **1993**, *83*, 427–435. [[CrossRef](#)]
28. Harris, J.G.; Yung, K.H. Carbon dioxide’s liquid–vapor coexistence curve and critical properties as predicted by a simple molecular model. *J. Phys. Chem.* **1995**, *99*, 12021–12024. [[CrossRef](#)]
29. Kvamme, B.; Graue, A.; Kuznetsova, T.; Buanes, T.; Erslund, G. Storage of CO<sub>2</sub> in natural gas hydrate reservoirs and the effect of hydrate as an extra sealing in cold aquifers. *Int. J. Greenh. Gas Control* **2007**, *1*, 236–246. [[CrossRef](#)]
30. Buanes, T. *Mean-Field Approaches Applied to Hydrate Phase Transition*. Ph.D. Thesis, University of Bergen, Bergen, Norway, 2006.
31. Uchida, T.; Ikeda, I.Y.; Takeya, S.; Ebinuma, T.; Nagao, J.; Narita, H. CO<sub>2</sub> hydrate film formation at the boundary between CO<sub>2</sub> and water: Effects of temperature, pressure and additives on the formation rate. *J. Cryst. Growth* **2002**, *237–239 Pt 1*, 383–387. [[CrossRef](#)]
32. Kvamme, B.; Kuznetsova, T.; Kivelæ, P.-H. Adsorption of water and carbon dioxide on hematite and consequences for possible hydrate formation. *Phys. Chem. Chem. Phys.* **2012**, *14*, 4410–4424. [[CrossRef](#)] [[PubMed](#)]
33. Van Cuong, P. *Transport and Adsorption of CO<sub>2</sub> and H<sub>2</sub>O on Calcite and Clathrate Hydrate*. Ph.D. Thesis, University of Bergen, Bergen, Norway, 2012.
34. Mohammad, N. *Heterogeneous Hydrate Nucleation on Calcite {1014} and Kaolinite {001} Surfaces: A Molecular Dynamics Simulation Study*. Master’s Thesis, University of Bergen, Bergen, Norway, 2016.
35. Qasim, M.; Kvamme, B.; Baig, K. Modeling Dissociation and Reformation of Methane and Carbon Dioxide Hydrate using Phase Field Theory with implicit hydrodynamics. In *Proceedings of the 7th International Conference on Gas Hydrate (ICGH7)*, Edinburgh, Scotland, 17–21 July 2011.
36. Qasim, M.; Baig, K.; Kvamme, B.; Bauman, J. Mix Hydrate formation by CH<sub>4</sub>–CO<sub>2</sub> exchange using Phase Field Theory with implicit Thermodynamics. *Int. J. Energy Environ.* **2012**, *6*, 479–487.

37. Darnell, K.N.; Flemings, P.B.; DiCarlo, D. Nitrogen-Driven Chromatographic Separation During Gas Injection into Hydrate-Bearing Sediments. *Water Resour. Res.* **2019**. [[CrossRef](#)]
38. Austvik, T.; Hustvedt, E.; Gjertsen, L.H. Formation and Removal of Hydrate Plugs—Field Trial at Tommeliten. In Proceedings of the 76 Annual Meeting of the Gas Processors Association (GPA), San Antonio, TX, USA, 10–12 March 1997; p. 249.



© 2019 by the authors. Licensee MDPI, Basel, Switzerland. This article is an open access article distributed under the terms and conditions of the Creative Commons Attribution (CC BY) license (<http://creativecommons.org/licenses/by/4.0/>).



---


## **PAPER VIII**

**MODELLING HEAT TRANSPORT IN SYSTEMS OF  
HYDRATE FILLED SEDIMENTS USING RESIDUAL  
THERMODYNAMICS AND CLASSICAL NUCLEATION  
THEORY**



Article

# Modeling Heat Transport in Systems of Hydrate-Filled Sediments Using Residual Thermodynamics and Classical Nucleation Theory

Mojdeh Zarifi <sup>1,\*</sup>, Bjørn Kvamme <sup>2</sup> and Tatiana Kuznetsova <sup>1</sup> 

<sup>1</sup> Department of Physics and Technology, University of Bergen, Allegaten 55, 5007 Bergen, Norway; tatyana.kuznetsova@uib.no

<sup>2</sup> Hyzen Energy, 26701 Quail Creek, Laguna Hills, CA 92656, USA; Bkvamme@hyzenenergy.com

\* Correspondence: mojdeh.zarifi@uib.no; Tel.: +47-416-45-284

**Abstract:** As in any other phase transition, hydrate phase transition kinetics involves an implicit coupling of phase transition thermodynamic control and the associated dynamics of mass and heat transport. This work provides a brief overview of certain selected hydrate film growth models with an emphasis on analyzing the hydrate phase transition dynamics. Our analysis is based on the fundamental properties of hydrate and hydrate/liquid water interfaces derived from molecular modeling. We demonstrate that hydrate phase transitions involving water-dominated phases are characterized by heat transport several orders of magnitude faster than mass transport, strongly suggesting that any hydrate phase transition kinetic models based on heat transport will be entirely incorrect as far as thermodynamics is concerned. We therefore propose that theoretical studies focusing on hydrate nucleation and growth should be based on concepts that incorporate all the relevant transport properties. We also illustrate this point using the example of a fairly simplistic kinetic model, that of classical nucleation theory (CNT), modified to incorporate new models for mass transport across water/hydrate interfaces. A novel and consistent model suitable for the calculation of enthalpies is also discussed and appropriate calculations for pure components and relevant mixtures of carbon dioxide, methane, and nitrogen are demonstrated. This residual thermodynamic model for hydrate is consistent with the free energy model for hydrate and ensures that our revised CNT model is thermodynamically harmonious.

**Keywords:** heat transfer; mass transfer; methane hydrates; carbon dioxide storage; carbon dioxide hydrate; classical nucleation theory



**Citation:** Zarifi, M.; Kvamme, B.; Kuznetsova, T. Modeling Heat Transport in Systems of Hydrate-Filled Sediments Using Residual Thermodynamics and Classical Nucleation Theory. *Appl. Sci.* **2021**, *11*, 4124. <https://doi.org/10.3390/app11094124>

Academic Editor:  
Javier Rodríguez-Martín

Received: 3 March 2021

Accepted: 21 April 2021

Published: 30 April 2021

**Publisher's Note:** MDPI stays neutral with regard to jurisdictional claims in published maps and institutional affiliations.



**Copyright:** © 2021 by the authors. Licensee MDPI, Basel, Switzerland. This article is an open access article distributed under the terms and conditions of the Creative Commons Attribution (CC BY) license (<https://creativecommons.org/licenses/by/4.0/>).

## 1. Introduction

Gas clathrate hydrate has long been a subject of many studies in the oil and gas-related industries, with hydrates as a flow hazard historically being both the focus and the main funding source for hydrate research. The basic building blocks of hydrates are hydrogen-bonded water cages which can trap molecules of certain non-polar substances. These encaged molecules (often referred to as “guest” species or hydrate formers) vary from light hydrocarbons such as methane and ethane, to acid gases such as carbon dioxide and hydrogen sulfide, and to compounds popular as refrigerants in the past. A great number of gas hydrate deposits exist both onshore and offshore all around the world, many of them considered viable potential sources of natural gas [1]. While the natural gas hydrates in sediments are rapidly becoming more and more relevant as an energy source, hydrate-related hydrocarbon fluxes into seawater and atmosphere poses a climate concern, with the geo-hazard aspects related to hydrate-filled sediments now coming to the forefront of hydrate research.

A fairly recent innovative approach to hydrate production calls for exchanging carbon dioxide for methane in natural gas hydrate reservoirs, providing a win–win scenario



of methane production combined with simultaneous safe CO<sub>2</sub> storage in the form of hydrate. This concept has often been envisaged as occurring at pressures needed for the CO<sub>2</sub> hydrate formation, which will be significantly lower than those of CH<sub>4</sub> hydrate at the same temperature. However, strictly speaking, those conditions are far from being relevant for practical implementations, since they are only relevant for the solid-state exchange mechanism, proven experimentally for temperatures far below zero by Kuhs et al. [2] and more recently Lee et al. [3]. Above the freezing point, hydrate deposits in the pores will always be in contact with free liquid water [4]. Even in Alaska permafrost, the average hydrate saturation amounts to only about 75%, with hydrate-filled sediment with saturation exceeding 80% being a very rare occurrence. These circumstances will give rise to a very fast mechanism for formation of new CO<sub>2</sub> hydrate from the injected CO<sub>2</sub>. Heat released by this phase transition will be rapidly transported through the aqueous phases and assist in the dissociation of in situ CH<sub>4</sub> hydrate [3,5,6]. Since this is a liquid-state mechanism, its kinetic rates will be several orders of magnitude higher than those of a solid-state mechanism. Moreover, the two hydrate phases (in situ CH<sub>4</sub> hydrate and the newly formed CO<sub>2</sub> one) will not be actually in contact with each other, making the pressure–temperature equilibrium curves not particularly relevant for the purposes of analysis and illustration. The “exchange” phenomenon is rather a process of replacement, where a new hydrate fills the pore space originally filled with CH<sub>4</sub> hydrate.

The use of CO<sub>2</sub> for hydrate production is just one of many technologies currently considered for the purposes of releasing CH<sub>4</sub> from in situ hydrates while at the same time storing CO<sub>2</sub> in solid form as a hydrate. Regardless of the technology platform chosen, two criteria must be satisfied. The free energy change associated with the process has to be sufficient to dissociate the hydrate, and the necessary heat for hydrate melting must be supplied. Pressure reduction has long been the method of choice for dissociation of hydrates in natural gas hydrate reservoirs since it is easy to choose the production conditions lying outside hydrate stability limits based on the temperature–pressure stability curve of CH<sub>4</sub> hydrate. However, the question of the dissociation heat supply still remains. Limited temperature gradients will be established by the pressure reduction itself, as well as geothermal gradients. It is outside the focus of this work to discuss whether these gradients will be sufficient to sustain the melting process.

It would require far too much space to review all the various methods used in experiments and pilot-plant tests for CH<sub>4</sub> hydrate production. We have three decades of experience in experiments on CO<sub>2</sub>/CH<sub>4</sub> exchange, and there is a plethora of literature already available on the topic. Similarly, there are numerous publications devoted to pressure reduction and studies of other methods. The focus in this work is mainly on the best way to model the phase transition thermodynamics and its associated kinetics. An important issue here is the need for a theoretically based model platform that accounts for all the implicit dynamic contributions to the phase transition. In order to accomplish this, we apply a fairly simple kinetic model based on theoretical considerations [7]. Yet, another important requirement to satisfy is a consistent thermodynamic model to describe the enthalpy changes taking place in hydrate phase transitions. With temperature, pressure, and concentrations as independent thermodynamic variables, Gibbs free energy will be the thermodynamic function determining phase stability. We need our models for enthalpy changes to be consistent with those for the Gibbs free energy.

Another area where hydrate phase transition dynamics become relevant is the transport of CO<sub>2</sub> in pipelines, which is a routine process in offshore Norway and many places around the world. Given the high pipeline pressures and low seafloor temperatures on the seafloor (typically below 6 °C), residual water present in the CO<sub>2</sub> stream may drop out either via condensation in bulk or adsorption on rusty pipeline walls and subsequently form a hydrate. Hydrate formation on small droplets liquid water will involve a dynamic balance between the driving force for hydrate formation (Gibbs free energy) and the transport of released heat through the insulating CO<sub>2</sub> fluid surrounding the forming hydrate core. Hydrate formation on liquid water films adsorbed on the rusty walls will also involve

the need to get rid of formation heat. While the liquid water and the pipeline wall will act as efficient heat conductors, pipeline insulation and the “bulk” CO<sub>2</sub> stream will hinder heat transport.

The examples presented above present just a few samples of practical scenarios involving implicit coupling between phase transition dynamics and heat transport dynamics. Theoretical physics provides a number of platforms suitable for modeling phase transition dynamics. Common to all of them is the implicit coupling between the mass transport dynamics characterizing the phase transition, the thermodynamics control (a function of Gibbs free energy change), and the heat transport.

The main focus of this work was to review some of the more recent and popular models applied to study hydrate phase transition dynamics in terms of actual kinetic rate limiting factors. Our secondary objective was to shed more light on the connection between nanoscale transition dynamics and hydrodynamic flow (which happens across a thin interface of 1–1.5 nm). Our third objective was related to the need for thermodynamic consistency. Many models describing enthalpy changes related to hydrate phase transitions are disconnected from the formal thermodynamic coupling between phase transition thermodynamics (Gibbs free energy changes) and the enthalpy changes related to heat transport requirements.

The paper is organized as follows. Section 2 provides an overview of popular models used to describe hydrate formation and dissociation dynamics in terms of characteristic transition properties. In Section 3, we outline a theoretical concept to serve as a basis for alternative kinetic models comprehensively accounting for implicit coupling between mass transport, heat transport, and thermodynamic control. It is important to point out here that the model we used is just an example chosen for illustration purposes. The need to include all the implicit dynamic contributions and to ensure thermodynamic consistency within the model are the important messages. Modeling results and associated discussion can be found in Section 4, while Section 5 provides the conclusions.

## 2. Literature Overview

Over the last several decades, a number of theoretical studies focusing on hydrate film formation along water/guest-fluid interfaces have been carried out by research groups worldwide [8–20]. The bulk of the studies considered either a planar gas–liquid interface, a water droplet surface in the gas phase, or the gas–bubble interface, with the theoretical research focusing on the impact of heat transfer on the growth of hydrates at the interface. As this paper aims to develop a more realistic kinetic model for hydrate film formation, we will mostly focus on the theoretical investigation by various researchers rather than experimental results.

The first theoretical models of hydrate film formation were developed by Shindo et al. [8], Lund et al. [9], and Teng et al. [10]; these studies can be broadly grouped together since their models describe the hydrate film as a diffuse layer suspended in the liquid hydrate former. Shindo et al. [8] treated each hydrate film as a concentration boundary layer, hypothesizing that water molecules will diffuse into the liquid CO<sub>2</sub> phase and subsequently give rise to hydrate nucleation, with the newly formed hydrate clusters slowly diffusing towards the aqueous phase. Lund et al. [9] extended the model by adding the possibility of hydrate cluster dissociating. Teng et al. [10] “reversed” the two models by presuming that hydrate will form more easily in the water-rich phase. However, all of the original three models have been shown to disagree with the experimental observations of a sharp solid–liquid interface and hydrate film tensile strength measurements by Sugaya et al. [11]

The second group of researchers utilized models that treated the hydrate film as a solid plate. For example, Hirai et al. 1996 [12] and Mori and Mochizuki 1997 [13] modeled the film as a CO<sub>2</sub>-permeable micro-perforated plate model and a water-permeable micro-perforated plate, respectively. Unfortunately, the Hirai et al. [12] model failed to explain the driving force for the liquid CO<sub>2</sub> flow through the holes across the hydrate film, and

also used the unrealistic assumption of a mosaic water-side surface to explain the melting and crystallization of hydrates.

Later, Mori and Mochizuki 1997 [13] proposed a model similar to that of Hirai et al. [12] with respect to geometry and structure of the hydrate film. Their model assumes the hydrate film to be a uniform plate with constant thickness and evenly distributed micro-perforations. Their key difference in their description compared to Hirai et al. [12] was that it was the liquid water rather than the CO<sub>2</sub> that permeated the hydrate film and filled its capillaries. The process was driven by capillary pressure induced at the interface, with the aqueous phase inside the capillaries being saturated in guest species. The model assumed that CO<sub>2</sub> transfer into the aqueous phase and subsequent hydrate formation and dissociation processes will be rate controlled by mass transfer. A somewhat controversial point of this model was its assumption of hydrate melting and crystallization present even in the case of a vanishing driving force, as well as the lack of any consideration of kinetics governing the two processes. In 1998, Mori suggested a model describing the formation of hydrate film around a CO<sub>2</sub> droplet [14]. This new model was based on three new assumptions introduced to retard the dissolution of CO<sub>2</sub> in water. The first supposition involved the reduction in the droplet surface mobility due to hydrate film formation and the decrease in the convective mass transfer coefficient. The second assumption was the reduction in the solubility of CO<sub>2</sub> due to hydrate film formation, and the third one suggested that the effective viscosity of water and mass diffusion coefficient will increase because of hydrate cluster consumption of CO<sub>2</sub>.

In 1999, Uchida et al. [15] experimentally observed hydrate film formation at the interface between water and CO<sub>2</sub>. Their paper has also presented a theoretical analysis of the two-dimensional formation of a hydrate film, which is uniform in thickness and has a semicircular front. This model assumes that, firstly, the hydrate will only form at the film front where the temperature remains constant at the corresponding triple point (water/guest fluid/hydrate) value, and secondly, the rate of heat released by hydrate formation will be equal to the rate of heat removal by means of conduction through the film surfaces. Their study estimated the hydrate film thickness based on the lateral growth rate alongside the interface (still not fully reliable).

In 2001, Mori [16] extended their 1997 model by incorporating both heat and mass transfer involved in hydrate film formation and dissociation. Their steady-state (more accurately, quasi steady-state) one dimensional simulation of mass and heat transfer included the exothermic effect of hydrate formation and its inverse in the case of hydrate melting. They have also investigated the transient heat and mass transfer processes occurring during hydrate film formation, with their conclusion being that some mechanism other than heat transfer dominates the hydrate film formation, and heat transfer can be safely neglected when dealing with hydrate film thinner than 0.3 µm. In 2001, Freer et al. [17] applied a moving boundary model of heat transfer for the film hydrate formation to estimate the film thickness. They compared the obtained value with their own experimental result from a water/methane hydrate film and concluded that heat conduction was the dominant driving force. However, they denied the validity of their own conductive heat transfer model and proposed a model combining interfacial attachment kinetics via the Arrhenius expression and convective heat transfer instead.

In 2006, Mochizuki and Mori [18] carried out a numerical study of heat transfer across the water/hydrate-former phase boundaries. They applied two analytic models for methane and CO<sub>2</sub> hydrate film formation, derived by assuming two different film front geometries. Both models presumed a uniform film with constant thickness, with the thermodynamic triple point temperature set as the film front temperature. Their model assumed two-dimensional conductive heat transfer from the film front to hydrate formation sites and was able to predict the film formation rate if provided the film thickness. They estimated that a CO<sub>2</sub> hydrate film will be much thinner than a methane hydrate one at the same sub-cooling range. In addition, both CO<sub>2</sub> and methane films have exhibited a tendency to become thinner as the sub-cooling rate increased.

There is a need for a realistic kinetic model able to describe how the coupled processes of mass and heat transport will impact the formation and dissociation of hydrate, while accounting for all independent thermodynamic variables.

The bulk of available hydrate film formation studies fall into the hydrodynamic spatial range (micrometer and up), i.e., far beyond the scale of phase transitions itself. Phase transitions are nano-scale phenomena occurring across a thin interface only several nanometers in thickness. Many of the studies are based solely on estimates of film front propagation in terms of  $V_f$  and hydrate film thickness, while other papers also theoretically model the axial growth of hydrate films [19]. An obvious limitation of all models listed in Table 1 is that they account for heat transport only and ignore mass transport. This is an interesting and unusual assumption since heat transport through aqueous systems will be faster by a factor of two or three than mass transport [21,22]. The main assumptions of various models mentioned above include:

- Hydrate film having a homogeneous structure at the macroscopic level;
- Infinitely extending aqueous and guest-fluid phases and the interfaces between them;
- Spatially uniform hydrate film with thickness that does not vary with time;
- Hydrate crystal formation occurring only at the front of the hydrate film;
- The front temperature remaining constant at the three-phase equilibrium value;
- No advection occurring in either of the aqueous or guest-fluid phases.

**Table 1.** Properties needed for hydrate kinetic modeling, including details missing in hydrate phase transition models proposed by various research groups.

| Hydrate Phase Transition Characteristics | 1st Group <sup>a</sup> | 2nd Group <sup>b</sup> | Mori and Mochizuki 1997, 1998 | Uchida et al. 1999 | Mori and Mochizuki 2001 | Freer et al. (2001) | Mochizuki et al. (2006) | Mochizuki et al. (2017) | Liu et al. (2018) | This Work Model |
|--|------------------------|------------------------|-------------------------------|--------------------|-------------------------|---------------------|-------------------------|-------------------------|-------------------|-----------------|
| Score <sup>c</sup>                       | 1                      | 1                      | 1                             | 1                  | 1                       | 1                   | 2                       | 3                       | 3                 | 4               |
| Phase transition thermodynamic control   | – <sup>d</sup>         | –                      | –                             | –                  | –                       | –                   | √ <sup>d</sup>          | √                       | √                 | √               |
| Phase transition mass transport kinetics | √                      | √                      | √                             | √                  | √                       | –                   | √                       | √                       | √                 | √               |
| Phase transition heat transport kinetics | –                      | –                      | –                             | √                  | √                       | √                   | √                       | √                       | √                 | √               |
| Irregular hydrate surfaces               | –                      | –                      | –                             | –                  | –                       | –                   | –                       | –                       | –                 | –               |
| Inhomogeneous (heterogeneous) hydrate    | –                      | –                      | –                             | –                  | –                       | –                   | –                       | –                       | –                 | –               |
| Hydrodynamic level mass flow             | –                      | –                      | –                             | –                  | –                       | –                   | –                       | –                       | –                 | √               |
| Hydrodynamic level heat flow             | –                      | –                      | –                             | –                  | –                       | –                   | –                       | –                       | –                 | –               |
| Enthalpy changes                         | –                      | –                      | –                             | –                  | –                       | –                   | –                       | –                       | –                 | √               |
| Changes in heat capacity                 | –                      | –                      | –                             | –                  | –                       | –                   | –                       | –                       | –                 | √               |
| Changes in volume                        | –                      | –                      | –                             | –                  | –                       | –                   | –                       | –                       | –                 | √               |

<sup>a</sup>: Shindo et al. [8], Lund et al. [9], and Teng et al. [10], <sup>b</sup>: Hirai et al. 1996 [12] and Mori and Mochizuki 1997 [13]. <sup>c</sup> Scores are on a 0–5 scale based on the major aspects accounted for by each model; a model able to fully cover all the three aspects would be scored at 5. <sup>d</sup> (–) Hyphen indicates that the model in question ignores this aspect altogether; while (√) checkmark indicates that this aspect is accounted for, to a certain degree. The overall score reflects our opinion on the general comprehensiveness of the theoretical treatment as a whole.

Based on experimental observations of important dynamic features such as hydrate film thickness as a function of time and comparison to their previous studies, Mori and Mochizuki [19] have recently introduced two major interlinked assumptions:

- Spatial non-uniformity of temperature at the film edge;
- A variation in the guest concentration on the aqueous-phase side (i.e., mole fraction of water/hydrate at the two-phase equilibrium over the film front surface).

The most recent study in this overview, that of Liu et al. [20], considered natural convective heat transfer along with the gas–liquid interface. Unlike the previous studies, this model does contain a quantitative relation between the hydrate film formation and experimental temperature. Their model also proposes a sub-cooling correlation and an assumption that heat exchange between gas and aqueous phases will not influence the diffusion of hydrate film.

In Table 1 we briefly list certain basic physical quantities we believe to be essential for the kinetics of hydrate formation and dissociation. The three first rows describe the level of handling of the implicit coupling between mass transport, heat transport, and thermodynamic control of a given hydrate phase transition.

One can apply mass flux equation from the classical nucleation theory (CNT) to relate the two first hydrate transition properties of Table 1. The associated enthalpy change can be then directly coupled to the free energy change present in the thermodynamic control term via a trivial thermodynamic relationship. In more advanced theories, the coupling is slightly different and even more implicit. However, for screening purposes, even a complete description in accordance with the CNT would be scored as 5. Anything in between is based on a subjective evaluation. These first three elements are intimately related to the initial nucleation stage and are thus nanoscale in both space and time dimensions. The main purpose of the table was to provide a better basis for selection of models that have potential as platforms for further improvements. The fourth element contains both nanoscale aspects and higher level aspects. Several studies probing the phenomena at nano- to mesoscale have clearly demonstrated that nucleation is favored in inclinations or regions of restricted space between solid surfaces because molecules (both water and hydrate formers) become trapped there. Even if this trapping only lasts for a limited interval, the molecules will still take more time to rearrange into a hydrate as compared to a “bulk” or interfacial solution of hydrate formers in water. However, if the inclinations are too narrow, a destabilization of the hydrate core is more likely due to mechanical strain on a small hydrate nucleus squeezed in between solid surfaces.

A thermodynamically non-equilibrium situation will remove the chemical equilibrium constraint (equality of chemical potentials for all components in all the phases), leading to components with the highest affinity for water and the lowest volatility to be the best candidates to form hydrates first. In this study, we limit ourselves to components forming structure I and II hydrates. While the three first rows are directly related to the phase transition itself, the hydrodynamic conditions outside of the growing or decaying hydrates will provide either a reservoir or a sink for heat and mass, hence the need for rows 6 and 7.

The availability of either experimental data or models suitable for the estimation of heat that has to be transported to and from hydrates is the reason for the next two rows. The estimates for volume changes will be required for various purposes, including the application of the Clapeyron equation.

### 3. Methods

This work uses a fairly basic model to describe the kinetics of hydrates, the classical nucleation theory (CNT). There were two reasons for this. The first one is that this theory makes the various contributions to the phase transitions quite obvious, with their relative impact for the various phase transitions of interest easy to compare.

The second reason stems from the fact that the model’s simplicity makes it easy to incorporate into software used for hydrate reservoir modeling and hydrate risk evaluation. Using a multiphase flow simulator to evaluate the risk of hydrate formation during the processing and transport of hydrate-forming fluids such as hydrocarbon, CO<sub>2</sub>, and H<sub>2</sub>S is a computationally expensive endeavor requiring a numerically simple model. It is, however, very important to stress that our CNT version is very different from the original one. The

$$\Delta G^{(H)} = \left[ \begin{aligned} &x_{H_2O}^H (\mu_{H_2O}^H(T, P, \vec{x}^H) - \mu_{H_2O}^{water}(T, P, \vec{x})) \\ &+ \sum_j x_j^H (\mu_j^H(T, P, \vec{x}^H) - \mu_j^{gas}(T, P, \vec{y}^{gas})) \end{aligned} \right] \quad (2)$$

where  $\mu$  denotes chemical potential. Subscripts H:O and  $j$  denote water and hydrate formers, respectively. Superscripts H, water, and gas stand for hydrate, liquid water, and gas phases, respectively.  $x$  is the corresponding mole fraction in either the liquid or hydrate phase (superscript H) and  $y$  is the mol fraction in the hydrate former phase.  $T$  and  $P$  are temperature and pressure. Due to the implicit and consistent coupling between free energy and enthalpy in the phase stability boundary approach, it makes sense to relate the changes in enthalpy to the phase stability boundary. This connection in the free energy change of the phase transition (see Equation (2) below). At the hydrate stability limit, this free energy change will vanish (various solutions of Equation (2) are plotted in Figure 1) and been verified through comparison with experimental hydrate phase boundaries. However, the interfacial free energy barrier, this means that the chemical potential and free energies involved in Equation (2) have also been confirmed. Figure 1 is actually constructed so as to ensure that the free energy change given by Equation (2) is equal to zero.

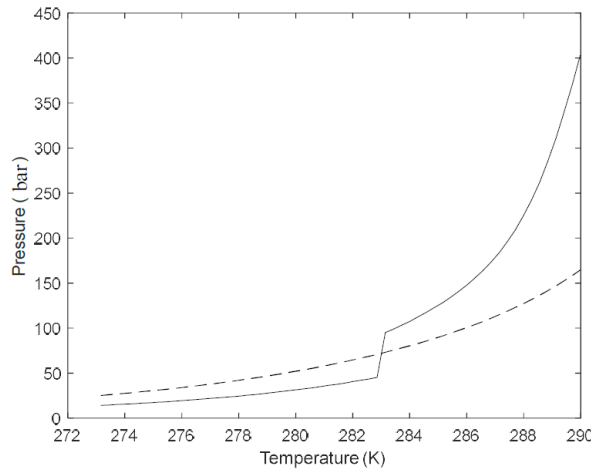


**Figure 1.** Hydrate stability region in the P-T projection of the stability regimes. The solid curve is for CO<sub>2</sub>, and the dashed curve is for CH<sub>4</sub>.

In summary, the treatment of classical thermodynamics in this work is principally different from that of reference and other studies that rely on classical thermodynamics for non-based. Residual thermodynamic states, the link through fluid states (a) and (b) from the pressure and temperature of the reference state, is not taken from the gas state groups. The first state is certain state in high quality pure fluid and the second state is the state of hydrate phase of energy site. However, in this study, we are based on gas as a reference state, simply a pure component of pure reference state. In this model, any other property of pure component will be of gas limited to the state of pure component. The first stage is the high pressure and the second stage is the low pressure and the third stage is the low pressure and the low temperature. The relevant properties and the ideal mixing changes through the state of pure component [29]. Superscript total in Equation (1) signifies the

A substantial advantage of utilizing ideal gas as a reference state is the direct linkage to classical molecular dynamics simulations (MD). In the classical limit, the momentum space (ideal gas) is orthonormal to the configurational space (residual properties). MD simulations sample the ideal gas properties from molecular velocities, rotational velocities, and velocities related to intramolecular movements, while the residual properties are estimated based on molecular interactions. The application of residual thermodynamics for hydrate and liquid water has been made possible via the modeling of the chemical potential of water in empty hydrate structures, ice, and liquid water [7]. This approach provides comparable free energies for all phases potentially co-existing in systems of hydrate formers and water. We also can obtain free energies of different hydrate phases

and thus compare their relative stability [21,24–28]. Given the limited space, the reader is directed to our earlier work on the fundamentals of CNT as applied to hydrates [29]. In this work, we mainly focus on heat release during the formation of hydrates.

Unlike many other models describing enthalpy changes associated with hydrate formation and melting, our residual thermodynamic model is directly related to the free energy changes as illustrated by Equation (1) below. The heat transport kinetics will be implicitly coupled to Equation (1), and a trivial application of statistical mechanics will prove that using Equation (1) for enthalpy will provide a consistent coupling between free energy and enthalpy changes. The residual, or configurational partition function, will be directly linked to the phase structure. Consistent descriptions of enthalpy and free energy will be needed in order to provide the correct entropy change for the phase transition; to the best of our knowledge, Equation (5) is the only enthalpy model in the available literature that satisfies this requirement.

Equation (1) below is a fundamental classical thermodynamics relationship; its derivation is available in any textbook and requires no further explanations.

$$\frac{\partial \left[ \frac{\Delta G^{Total}}{RT} \right]_{P, \vec{N}}}{\partial T} = - \left[ \frac{\Delta H^{Total}}{RT^2} \right] \quad (1)$$

where  $G$  is free energy and  $H$  is enthalpy. The  $\Delta$  symbol is the change in free energy and enthalpy, respectively. The subscripts on the left brackets denote constant pressure and mol numbers. The free energy change related to the formation of hydrate on the interface between a separate hydrate former phase and liquid water can be expressed as

$$\Delta G^{(H)} = \left[ \begin{array}{l} x_{H_2O}^H (\mu_{H_2O}^H(T, P, \vec{x}^H) - \mu_{H_2O}^{water}(T, P, \vec{x})) \\ + \sum_j x_j^H (\mu_j^H(T, P, \vec{x}^H) - \mu_j^{gas}(T, P, \vec{y}^{gas})) \end{array} \right] \quad (2)$$

where  $\mu$  denotes chemical potential. Subscripts  $H_2O$  and  $j$  denote water and hydrate formers, respectively. Superscripts  $H$ , water, and gas stand for hydrate, liquid water, and gas phases, respectively.  $x$  is the corresponding mole fraction in either the liquid or hydrate phase (superscript  $H$ ), and  $y$  is the mol fraction in the hydrate former phase.  $T$  and  $P$ ; are temperature and pressure. Due to the implicit and consistent coupling between free energy (a function that determines phase stability) and enthalpy, it makes sense to relate the changes in enthalpy to the phase stability boundaries. This connection is illustrated by the link between the pressure–temperature hydrate phase stability boundaries in Figure 1. The validity and accuracy of the calculations involved in the construction of Figure 1 have been verified through comparison with experimental data in many of our previous papers. For all the practical purposes, this means that the chemical potentials and free energies involved in Equation (2) have also been confirmed. Figure 1 is actually constructed so as to ensure that the free energy change given by Equation (2) is equal to zero.

In summary, the treatment of enthalpy changes in this work is entirely different from that used in many other enthalpy models. All our calculations are based on residual thermodynamics and the link through Equations (1) and (2). For this same reason, we do not refer to many publications from other research groups. There are certainly many high-quality publications dedicated to calculations of enthalpy changes in hydrate phase transitions. However, since they are based on very different thermodynamic platforms and reference systems, a review of these models would require too much space and will be of limited value for the main focus of this paper.

The liquid water chemical potential has been calculated using the symmetric excess conventions as described in Kvamme et al. [29] and Kvamme [30]. Equations (1) and (2) are coupled to an implicit equation for mass transport flux and thermodynamic control through Equation (22) in Kvamme et al. [29]. Superscript total in Equation (1) signifies the sum of Equation (2) and the penalty due to the work required to push aside the surrounding

phases to make room for the hydrate. This penalty term is proportional to the interfacial free energy (see Kvamme et al. [7] for more details).

The chemical potential for water in the hydrate structure is given by [5]

$$\mu_{H_2O}^H = \mu_{H_2O}^{O,H} - \sum_{k=1,2} RTv_k \ln \left( 1 + \sum_i h_{ij} \right) \quad (3)$$

in which superscript H denotes hydrate, with the superscript "O" in the first term on right-hand side referring to an empty clathrate lattice. These chemical potentials are readily available from model water (TIP4P) simulations of Kvamme and Tanaka [7]. The number of cavities per water  $v_k$  is 1/23 for small cavities of structure I and 3/23 for large cavities. CO<sub>2</sub> is not able to provide significant stabilization of small cavities and has only been detected there at temperatures far below zero. The lack of liquid water interface under these ice conditions entails an entirely dissimilar hydrate formation mechanism where the gas side of the interface plays a different part. At temperatures above the freezing point and with CO<sub>2</sub> as the only guest, the sum over canonical partition functions for small and large cavities will include large cavities only:

$$h_{ij} = e^{-\beta[\mu_{ij} + \Delta g_j]} \quad (4)$$

where  $\beta$  is the inverse of the universal gas constant times temperature. At equilibrium, the chemical potential of guest molecule  $j$  in hydrate cavities will be equal to its chemical potential in the co-existing phase it originated from.

### 3.1. Enthalpies of Phase Transitions from Residual Thermodynamics

A residual thermodynamics route to calculations of enthalpies of hydrate formation and dissociation has been recently proposed by Kvamme [30]. We refer the reader to that work for the details of all intermediate steps involved in the derivation of the right-hand side of Equation (3) using Equation (1), and only the final result is provided here:

$$H_{H_2O}^H = -RT^2 \frac{\partial \left[ \frac{\mu_{H_2O}^{O,H}}{RT} \right]_{P,\vec{N}}}{\partial T} + \left[ \sum_{k=1,2} v_k \frac{\sum_i h_{ki} \left[ \left( H_{ki} - \Delta g_{ki} + T \frac{\partial \Delta g_{ki}}{\partial T} \right) \right]}{\left( 1 + \sum_i h_{ki} \right)} \right] \quad (5)$$

Enthalpies involved on the liquid water side of the phase transition can be trivially obtained by numerical differentiation of the polynomial fit of chemical potential as described in Kvamme and Tanaka [7], with the thermodynamic properties of the hydrate former phase and water in Equation (5) also being trivial to obtain. In the relevant temperature range of about 10 degrees (273 K–283 K), the differences in enthalpies as calculated from Equation (5) using Monte Carlo data do not vary substantially and can even be set as constant for the purposes of this work. This result is rather expected due to the hydrate water lattice being fairly rigid. The average motion of water atoms will mostly identical, while the sampled cavity partition functions will, of course, vary significantly over the same temperature range (see also the fitted functions of  $T$  in Kvamme and Tanaka [7]). The enthalpies of various guest molecules in the two types of cavities were evaluated by means of Monte Carlo simulations along the lines described in Kvamme and Lund [31] and Kvamme and Førreisdahl [32]. For a limited range of roughly 15 K from 273.15 and up, the residual energies remained virtually constant and amounted to  $-16.53$  kJ/mol,  $-17.73$  kJ/mol, and  $-27.65$  kJ/mol for CH<sub>4</sub> in a large cavity, CH<sub>4</sub> in small cavity, and CO<sub>2</sub> in large cavity, respectively. The associated sampled volumes of movement/occupation were  $164.2 \text{ \AA}^3$ ,  $89.21 \text{ \AA}^3$ , and  $135.6 \text{ \AA}^3$ , respectively.



### 3.2. Heat Transport Related to Hydrate Phase Transitions

The two primary ways of heat transport relevant for the systems discussed in this work are conduction and convection. In the discussion that follows, we will consider systems where the initial amounts of water and CO<sub>2</sub> are large enough to not be consumed during the hydrate growth.

In the case of hydrate nucleation and growth inside a pipeline, the new mass will continuously be supplied by the flow stream. Offshore methane gas hydrates in sediments are typically characterized by methane coming from below through the fracture systems. A continuous inflow of water through fractures connected to the seafloor above will ensure a supply of liquid water but will also cause the hydrate to dissociate due to severe lack of dissolved methane. The chemical potential of CH<sub>4</sub> in the incoming water will therefore be close to its infinite dilution chemical potential, which is typically substantially lower than the chemical potential of CH<sub>4</sub> in hydrate. A typical sediment example in the case of CO<sub>2</sub> will involve aquifer storage of CO<sub>2</sub> in reservoirs that contain regions favorable for hydrate formation. Liquid water is available in the sediments, and a continuous inflow of CO<sub>2</sub> will lead to the formation of hydrate films that will reduce vertical CO<sub>2</sub> migration. In addition to the presence of natural sealing (clay, shale), these hydrate films reduce risk of CO<sub>2</sub> leakage to the surroundings above the storage site. These two practical examples alone illustrate the importance of having a model that assumes that the original “bulk” phases of the water and hydrate former phase will not be totally consumed and disappear. There are numerous other relevant examples.

A typical simplified heat transport model in our scenarios will involve heat conduction through the water over the growing film. The simplest approach would be a sum of symmetric heat conduction from below the hydrate growth site and heat conduction through the hydrate film towards the CO<sub>2</sub> phase. When the temperature on the hydrate surface reaches the hydrate melting point, an additional term of hydrate dissociation dynamics will enter the mass and energy balances. Additionally, mineral bedrock may also play a part in the overall energy balance, and it is entirely feasible to include the associated heat transport even within the framework of a very simple model. When the liquid water phase has been depleted in the CO<sub>2</sub> to the level of quasi-equilibrium with the CO<sub>2</sub> hydrate, a new hydrate can only form in one of the two ways: (1) CO<sub>2</sub> transport through the hydrate film and into the liquid water side of the hydrate film, or (2) water transport through the hydrate film and into the CO<sub>2</sub> side of the hydrate film.

The diffusion of CO<sub>2</sub> through hydrate will be very slow and most probably limited by the existence of empty cavities; this process will trigger the temporary local destabilization of the water hydrate lattice and induce a counter diffusion of water molecules.

In the absence of “fresh” building blocks, the first and second laws of thermodynamics will lead to a dynamic process in which the least stable hydrates (those with highest free energy) are undergoing melting to support the growth of hydrate regions with lower free energy [29]. Even by themselves, these processes can generate mass fluxes across the hydrate membrane film. Ultimately, these local free energy-governed processes can even lead to the creation of holes in the hydrate membrane, allowing for the supply of new building blocks.

A common approximation in hydrate modeling, as well as in the interpretation of experimental data, is, therefore, to lump both these contributions together into an apparent conductivity:

$$\dot{Q} = K \frac{V^{film}}{A_{\perp}} \Delta T \quad (6)$$

where  $A_{\perp}$  is area normal to the heat transport direction, and  $V^{film}$  is the volume of hydrate film.

Heat transport through liquid water and hydrate will be very fast, and two to three orders of magnitude faster than mass transport [21,22]. Work is in progress on a more detailed review of available theoretical estimates of diffusion through hydrate. The available values range from 10<sup>-15</sup> m<sup>2</sup>/s to 10<sup>-17</sup> m<sup>2</sup>/s for diffusivity of CH<sub>4</sub> through hydrate, with

the corresponding CO<sub>2</sub> values likely to be slightly lower. However, the huge variation illustrates the existing uncertainty in the correct way to handle this transport, with the bulk of the studies based on some sort of cavity-jumping Monte Carlo calculations. This is basically a mathematical–statistical method, and other types of approaches might be required. One hypothesis suggests that the more vigorous process of water librations in empty cavities facilitates a temporary destabilization of the water lattice due to the motion of guest molecules in the neighboring cavities. This may eventually allow the guest molecules to enter into the previously empty cavity. This hypothesis is based on the observation of Kvamme and Tanaka [7] and how various guest molecules interfere with water lattice librations. Regardless of the mechanism, these phenomena will result in increased diffusion, with the mass transport through a hydrate film accordingly expected to be proportional to the square root of time with a constant rate. The first part of a film growth model is simply the time a guest molecule will need to travel across the hydrate film. The resulting heat of the hydrate formation will be distributed locally as heat transport through liquid (K<sub>w</sub>) and through hydrate (K<sub>H</sub>) up to the hydrate dissociation temperature. The remaining fraction of the released heat will lead to the local partial dissociation of the hydrate film.

The curves characterizing heterogeneous (water and a separate hydrate former phase) hydrate dissociation or hydrate formation will be given by the temperature–pressure projection of hydrate stability conditions, see Figure 1 for examples in the case of CH<sub>4</sub> and CO<sub>2</sub>. See Kvamme [24] and Kvamme and Aromada [25] for verification of the model behind Figure 1 through comparisons with experimental data. As mentioned before, the plotted curves are the solutions of Equation (2) when the free energy change is set to zero. The chemical potential for water in hydrate is calculated from Equation (3) using guest partition functions from Equation (4). The estimation of the liquid water chemical potential utilized the pure liquid water chemical potential from Kvamme and Tanaka [7], with activity correction added in the case of additives such as alcohols or ions present. Setting the chemical potentials of the hydrate former in the hydrate equal to its value in the separate hydrate former phase will allow one to solve Equation (2) by means of iterations.

Additionally, note a very sharp increase in the hydrate stability curve in the case of CO<sub>2</sub> due to its phase transition from gas to liquid with a significantly higher density and a corresponding shift in thermodynamic properties. This changeover is frequently ignored in the published hydrate equilibrium data, with artificial smoothing of the CO<sub>2</sub> hydrate equilibrium curve creating a bias in quite a number of published datasets.

A simple model describing the dynamic progress of the system following the hydrate former reaching the liquid water side will be given by

$$\left( dJ_{formation} A_{H_{formation}} \Delta H_{formation}^{formation}(T, P) \right) = K_w \Delta T_w dR_w + K_H \Delta T_H dR_H + K_m \Delta T_m dR_m + dJ_{dissociation} A_{H_k} \Delta H_{k,dissociation}(T_k, P) \quad (7)$$

The “*formation*” superscript over the delta *H* denotes the enthalpy change of hydrate formation associated with the guest molecules entering the liquid water side. The simplest scenario will be represented by an evenly distributed growth flux across a planar surface of initial hydrate film. *R* is the distance of heat transport. Subscript *w* denotes liquid water, subscript *H* stands for hydrate film, and *m* indicates minerals. In the case of liquid water and hydrate, the reference temperature is that of hydrate formation; it is approximated by the average of the surface area normal to the mean mass flux through the sediment in the case of minerals.

For the hydrate film, the heating contribution (the second term) will continue to increase up to the hydrate dissociation point corresponding to the actual pressure (see Figure 1). After that, heat transported in this direction will be split between the dissociation of hydrate and raising the hydrate temperature.

As can be seen from Table 2 below and the associated discussion, the reported experimental values of heat conductivity through hydrate vary significantly. The difference in

liquid water heat conductivity is, however, limited. If the K-values for hydrate and liquid water are assumed to be identical, then the temperature difference from one time step to the next will be the same whether the conduction is through liquid water or hydrate. To simplify conductivity for both the hydrate and water phase, they are the same up to two limits. The first limit is when hydrate dissociation begins; another limit is if the heat transport through the hydrate approaches the hydrate former phase, which is almost heat insulating.

If we ignore the mineral surfaces for a moment, Equation (7) can be rewritten into the following one-dimensional form:

$$\left( dJ_{formation} A_{\perp} \Delta H^{formation}(T, P) \right) = K \Delta T_w d\vec{R} + K \Delta T_H d\vec{R} + dJ_{dissociation} A_{\perp} \Delta H_{\alpha}^{dissociation}(T_{\alpha}, P) \quad (8)$$

The purpose of vectorial  $R$  is only to indicate the direction relative to a reference point. With the reference point set so that  $R = 0$  at the hydrate surface, the hydrate former entering the aqueous phase will correspond to positive  $R$ , while transport through the hydrate film will be indicated by negative  $R$  values. The second reasoning behind the vector notation in the context of (8) is to ensure absolute values for both the first and the second terms. Both the left-hand side and the third term on the right-hand side, are also absolute values, allowing Equation (8) to describe the distribution of heat released during hydrate formation.

While Equation (8) is clearly oversimplified, there is some justification for it for the systems in consideration. Heat transport through liquids is normally two to three orders of magnitudes faster than mass transport [21–29], which also explains the difference in flux rather than associated heat release (or consumption). Transporting the guest molecules through a hydrate film from the gas side to the liquid side to sustain the growth may be 8 to 10 orders of magnitudes slower than diffusion of the same molecules through liquid water. As such, it will be fairly safe to assume that any guest molecules that reach the liquid water side will instantly dispose the hydrate formation heat due to the combination of the three terms in Equation (8).

A number of theoretical methods for estimating thermal conductivity are available in the literature as well as substantial amounts of experimental data from different research groups worldwide. It is far outside the focus of this work to conduct a detailed review of theoretical models and experimental data for thermal conductivities of relevance to this work. As such, the literature values in Table 2 are listed with reference to the actual sources without any additional comment.

Generally, gas hydrates exhibit a glass-like behavior where it comes to the temperature and pressure dependence of their thermal conductivity. This feature makes them drastically different in comparison to ice and other molecular crystals [33]. In hydrates, the water framework is much more distorted, with the hydrogen bond more strained than in ice. This results in the inhibition of long-range modes and spatial localization of energy, suggesting that their low thermal conductivity is not only due to guest–host interactions. The rigidity of the framework and hydrate lattice structures will also contribute lower thermal conductivity of clathrates compared to ice. Both available models and experimental data point to a typical hydrate thermal conductivity of 0.45–0.7 W/(m·K) within the temperature range 265 K to 280 K. Taking methane hydrate as an example, thermal conductivity measured in compacted samples using a needle probe at conditions similar to those in natural environments amounted to  $0.62 \pm 0.02$  W/(m·K) [33]. The only reported value for the CO<sub>2</sub> hydrate thermal conductivity is 0.49 W/(m·K) [34].

**Table 2.** Thermal conductivity of different hydrate components in various phases

| Material                   | Thermal Conductivity (Experimental Values) W/(m·K) <sup>1</sup> |  |
|----------------------------|---|--|
| CH <sub>4</sub> (liq)      | Aquas Phase   | [36]   |
| Liquid Water (273 K–283 K) |   | 0.57–0.58 [37]                                   |
| Sea Water                  | Gas Phase   | 0.56–0.57 [35]                                   |
| CH <sub>4</sub> (liq)      |   | 0.0297 (260 K, 1 MPa) [36]                       |
| CH <sub>4</sub> (gas)      |   | 0.035 (at 4.98 MPa, 277 K) [37]                  |
| CO <sub>2</sub> (gas)      | Gas Phase   | 0.093512 [37]                                    |
| CH <sub>4</sub> (gas)      |   | 0.0297 (260 K, 1 MPa) 0.035 (at 4.98 MPa, 277 K) |
| CO <sub>2</sub> (gas)      | Minerals  | 0.093512 [37]                                    |
| Quartz                     | Minerals  | 6.6–8.4 [38]                                     |
| Calcite                    |   | 3–4.5 [38]                                       |
| Quartz                     |   | 6.6–8.4 [38]                                     |
| Kaolinite                  |   | 1.8–3 [38]                                       |
| Kaolinite                  | Hydrate Phase   | 1.8–3 [38]                                       |
| CH <sub>4</sub> Hydrate    | Hydrate Phase   | 0.57 (263 K) [33]                                |
|                            | CH <sub>4</sub> Hydrate   | 0.57 (263 K) [33] 0.68 (261.5–277.4) [33]        |
|                            | CO <sub>2</sub> Hydrate   | 0.68 (261.5–277.4) [33]                          |
| CO <sub>2</sub> Hydrate    |   | 0.49 [34]  |

<sup>1</sup> Thermal conductivity: W/ (m·K) =

<sup>1</sup> Thermal conductivity above (Equation (8)) has been reformulated in terms of the mass transport across the hydrate/liquid water interface during the hydrate formation:

In view of the above, Equation (8) has been reformulated in terms of the mass transport across the hydrate/liquid water interface during the hydrate formation:

$$A_{\perp} \left( \frac{dJ_{formation}}{dR} \right) \Delta H_{formation}(T, P) = K\Delta T_w + K\Delta T_H + \tag{9}$$

$$A_{\perp} \left( \frac{dJ_{dissociation}}{dR} \right) \Delta H_{dissociation}(T, P) \tag{9}$$

The diffusivity across the interface from the liquid water side ( $R \equiv 0 \text{ \AA}$ ) to the hydrate side of the interface ( $R \equiv 12 \text{ \AA}$ ) is not known and is difficult to model using Molecular Dynamics simulations or other approaches. The profile in Figure 2 is therefore based on selected experimental data through some interpretation of water movements during the dissociation of hydrates. It is considered sufficient for the purposes of this work.

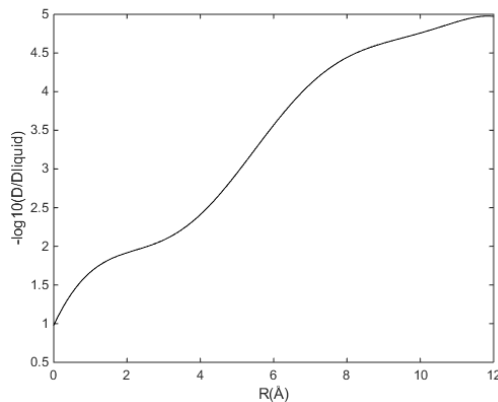


**Figure 2.** Relative diffusivities of CO<sub>2</sub> across the interface from liquid water side side to hydrate side side.

A mathematical fit to the profile in Figure 2 is

A mathematical fit to the profile in Figure 2 is

$$-\log_{10} \left[ \frac{D(R)_j}{D_{liquid,j}} \right] = \sum_{i=1}^9 a_i \left( a \tan \left[ \left( 0.5R \frac{\pi}{2} \right) / 12 \right] \right)^{i-1} \tag{10}$$

$$-\log_{10} \left[ \frac{D_{hydrate,j}}{D_{liquid,j}} \right] = \sum_{i=1}^9 a_i \left( a \tan \left[ \left( 0.5R \frac{\pi}{2} \right) / 12 \right] \right)^{i-1} \tag{10}$$

j = CO<sub>2</sub>, CH<sub>4</sub>, with parameters given in Table 3.

$j = \text{CO}_2, \text{CH}_4$ , with parameters given in Table 3.

**Table 3.** Parameters for Equation (10).

| i | i | Parameter    | i | i | Parameter    | i | i | Parameter     |
|---|---|--------------|---|---|--------------|---|---|---------------|
| 1 | 1 | 0.9799479242 | 4 | 4 | 171.6731673  | 7 | 7 | -9649.9649.96 |
| 2 | 2 | 15.54275427  | 5 | 5 | 6.769776975  | 8 | 8 | 14.7794779.7  |
| 3 | 3 | -88.51135112 | 6 | 6 | 1939.5939.55 | 9 | 9 | -7496.7496.15 |

However, in the context of this work, the most important aspect is to shed more light on the relative importance of various contributions to the implicitly coupled mass and heat transport dynamics related to hydrate phase transitions.

Fick's law will give:

$$J(R) = \left[ -D_{CO_2}(R) \frac{\partial C(R)}{\partial R} \right] \tag{11}$$

while the derivative of mass flux across the interface can be written as

$$\frac{dJ(R)}{dR} = \left[ - \left( \frac{dD_{CO_2}(R)}{dR} \right) \left( \frac{\partial C(R)}{\partial R} \right) - D_{CO_2}(R) \frac{\partial^2 C(R)}{\partial R^2} \right] \tag{12}$$

The appropriately derived concentration profile of CO<sub>2</sub> across the water interface is illustrated in Figure 3 below:

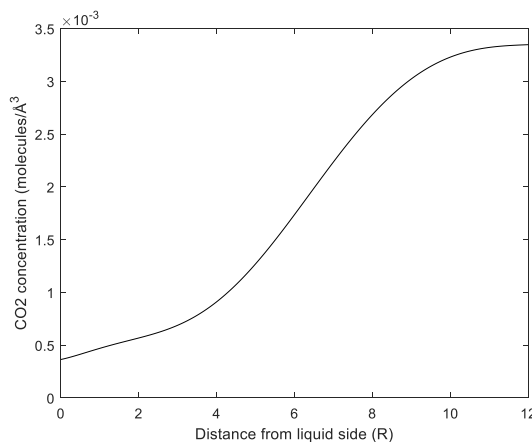


**Figure 3.** Concentration profile for CO<sub>2</sub> across water (R=0) hydrate (R=12) interface [39,41].

### 4. Results and Discussion

The stability of a hydrate phase will ultimately depend on all independent thermodynamic variables of the systems. These include temperature, pressure, and concentrations of the components. In order to proceed in phase space, it is possible to do various projections of hydrate stability onto a subset of independent thermodynamic variables, with temperature and pressure projections being the most typical example, as illustrated by stability limits of CH<sub>4</sub> and CO<sub>2</sub> hydrates in Figure 1. As noted previously, the phase transition undergone by CO<sub>2</sub> will significantly affect the temperature-pressure projection of its hydrate existence region. Given that temperatures and pressures are independent thermodynamic variables, it is the hydrated Gibbs free energy that will determine the phase stability. The free energies of hydrates formed along the corresponding hydrate stability limits of Figure 1 are plotted in Figure 4. CO<sub>2</sub> will form a more stable hydrate than CH<sub>4</sub> for the whole range of thermodynamic conditions covered in Figure 1. In order to illustrate impact of a typical hydrate inhibitor, we also present the curves of Gibbs free

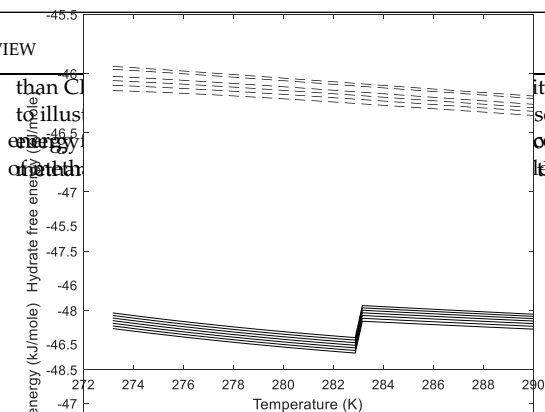


**Figure 4.** Calculated free energies of CO<sub>2</sub> hydrates (solid) and CH<sub>4</sub> hydrates (dashed). For each set of curves, the lowest curve is the free energy of hydrate formed from pure water, with the curves above corresponding to the following methanol content: 2 mol %, 4 mol %, 6 mol %, 8 mol %, 10 mol % and finally 12 mol % for the topmost curves of CO<sub>2</sub> and CH<sub>4</sub>, respectively.

Since Figure 5 may not be easily interpreted, the understanding of its plots should benefit from an additional reading of the two related 2D figures. Figure 5 shows the covariation of pressure and temperature, while Figure 6 below shows enthalpy changes along the temperature projection of CO<sub>2</sub> hydrate (solid) and CH<sub>4</sub> hydrate (dashed). For each set of curves, the lowest curve is the free energy of hydrate formed from pure water, with the curves above corresponding to the following methanol content: 2 mol %, 4 mol %, 6 mol %, 8 mol %, 10 mol % and finally 12 mol % for the topmost curves of CO<sub>2</sub> and CH<sub>4</sub>, respectively.

Since Figure 5 may not be easily interpreted, the understanding of its plots should benefit from an additional reading of the two related 2D figures. Figure 5 shows the covariation of pressure and temperature, while Figure 6 below shows enthalpy changes along the temperature projection of Figure 4.

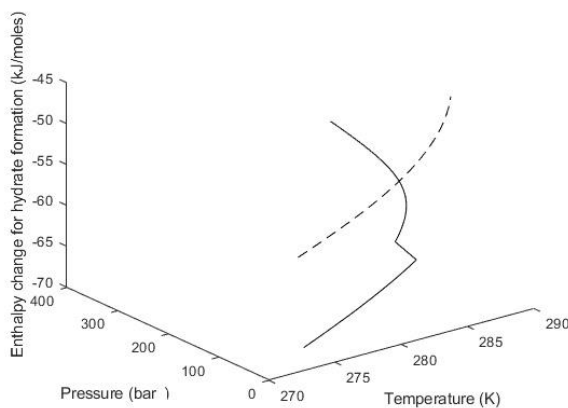


**Figure 5.** Enthalpy changes associated with hydrate formation along the hydrate P-T equilibrium curves for CO<sub>2</sub> hydrate (solid) and CH<sub>4</sub> hydrate (dashed). Units are kJ/mol hydrate former.

What is even more important in the context of this work are the differences in enthalpies of hydrate formation along the hydrate formation curves presented in Figure 6. One of the reasons for presenting the data for varying concentrations of methanol in the aqueous phase in Figure 4 is the fact that methanol also will act as a surfactant where the water/hydrate-former phase is concerned. This can be used to stimulate the CO<sub>2</sub>/CH<sub>4</sub>

**Figure 5.** Enthalpy changes associated with hydrate formation along the hydrate P-T equilibrium curves for CO<sub>2</sub> hydrate (solid) and CH<sub>4</sub> hydrate (dashed). Units are kJ/mol hydrate former.

are the differences in enthalpies presented in Figure 6. The addition of methanol in the aqueous phase acts as a surfactant where the water/hydrate-former phase is concerned. This can be used to stimulate the CO<sub>2</sub>/CH<sub>4</sub> exchange and the formation of a seal.

temperatures within the hydrate stability region will be very small. Figure 6 will therefore present the enthalpies for pure CH<sub>4</sub> hydrate, pure CO<sub>2</sub> hydrate, as well CO<sub>2</sub>/CH<sub>4</sub> mixtures with 98 mol % CO<sub>2</sub>, 95 mol % CO<sub>2</sub>, and 90 mol % CO<sub>2</sub> plotted as functions of temperature along with the corresponding temperature–pressure stability limits. A similar plot in Figure 7 shows the enthalpies of hydrate formation as functions of pressure along the temperature–pressure stability limits. Since a CO<sub>2</sub> molecule is too large to provide any stabilization of small cavities, 25% of small cavities will be empty for these ranges of conditions in the case of a pure CO<sub>2</sub> hydrate. As can be seen from Figures 6 and 7 below, the addition of CH<sub>4</sub> will therefore result in larger (negative) values for enthalpies of hydrate formation. exchange process since the methanol-enriched interface will hinder the formation of a sealing hydrate film between water and hydrate-former phases.

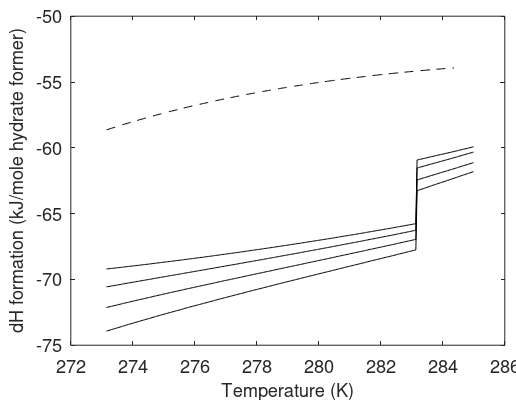


**Figure 6.** Enthalpies of hydrate formation in kJ/mol hydrate former as function of temperature. For temperatures below the CO<sub>2</sub> phase transition point (roughly 283.4 K), the bottom solid curve corresponds to CO<sub>2</sub>/CH<sub>4</sub> mixture with 10 mol % CH<sub>4</sub>; the top solid curve is pure CO<sub>2</sub>; 5 mol % CH<sub>4</sub> corresponds to CO<sub>2</sub>/CH<sub>4</sub> mixture with 10 mol % CH<sub>4</sub>; the top solid curve is pure CO<sub>2</sub>; 5 mol % CH<sub>4</sub> and 2 mol % CH<sub>4</sub> curves fall in between. For temperatures above the CO<sub>2</sub> phase transition point, the order of curves is reversed. The dashed curve is the corresponding results for pure CH<sub>4</sub> hydrate.

In accordance with Figure 5, the heat of hydrate formation will be about 10 kJ per mol of hydrate former larger for the CO<sub>2</sub> hydrate compared to methane hydrate. Heat released when new CO<sub>2</sub> hydrate is created from the injected mixture of CO<sub>2</sub> and surfactant will be transported through the aqueous phase in front of the CO<sub>2</sub> plume. A portion of heat will be lost to the heating of the bedrock; an increased concentration of ions due to pore water being consumed by the forming CO<sub>2</sub> hydrate is another important side effect of this process. The latter phenomenon is where Figure 5 comes into play more directly, since CH<sub>4</sub> will dissolve more vigorously when the ion activity goes up.

The injection of CO<sub>2</sub> into CH<sub>4</sub> hydrate-filled sediments will lead to the formation of new CO<sub>2</sub> hydrate from injected CO<sub>2</sub> and free pore water. It is rare to find hydrates with a hydrate saturation exceeding 85% of the pore volume, with 75% or less hydrate filling being more common. The primary mechanism for dissociation of in situ CH<sub>4</sub> hydrate will be driven by the latent heat of the CO<sub>2</sub> hydrate formation. In a general case, it is safe to assume that CH<sub>4</sub> released by the dissociating methane hydrate will migrate away from the CO<sub>2</sub> hydrate, whose surface will contain hydrate films separating the fluid CO<sub>2</sub> from the released CH<sub>4</sub>. In the case where we can expect a degree of mixing between the released CH<sub>4</sub> and CO<sub>2</sub>, it will be instructive to examine how this will affect the enthalpies of formation. For ease of implementation, we will use 2D plots of hydrate formation enthalpies evaluated along the hydrate formation pressure limits. These plots should still yield fairly relevant conclusions for hydrate formation enthalpies since any Poynting pressure corrections within the hydrate stability region will be very small. Figure 6 will therefore present the enthalpies for pure CH<sub>4</sub> hydrate, pure CO<sub>2</sub> hydrate, as well CO<sub>2</sub>/CH<sub>4</sub> mixtures with 98 mol % CO<sub>2</sub>, 95 mol % CO<sub>2</sub>, and 90 mol % CO<sub>2</sub> plotted as functions of temperature along with the corresponding temperature–pressure stability limits. A similar plot in Figure 7 shows the enthalpies of hydrate formation as functions of pressure along the temperature–pressure stability limits. Since a CO<sub>2</sub> molecule is too large to provide any stabilization of small cavities, 25% of small cavities will be empty for these ranges of conditions in the case of a pure CO<sub>2</sub> hydrate. As can be seen from Figures 6 and 7 below, the addition of CH<sub>4</sub> will therefore result in larger (negative) values for enthalpies of hydrate formation.

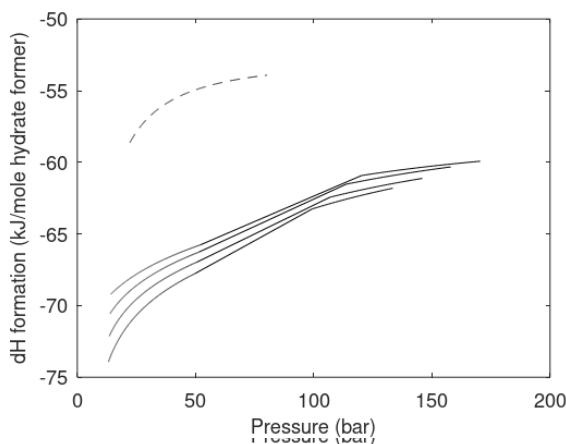


**Figure 7.** Enthalpies of hydrate formation in kJ/mol hydrate former as function of pressure. The bottom solid curve corresponds to  $\text{CO}_2/\text{CH}_4$  mixture with 10 mol %  $\text{CH}_4$ ; the top solid curve is pure  $\text{CO}_2$ ; the middle curves fall in between. The dashed curve is the corresponding results for pure  $\text{CH}_4$  hydrate.

The results presented in Figures 6 and 7 will also be relevant when the injected  $\text{CO}_2$  comes from a separation plant used for removal of sour gases from hydrocarbons. As an example, millions of tons of  $\text{CO}_2$  from the Sleipner field are separated and injected into the Utsira formation. The injection gas contains approximately 5 mol % of  $\text{CH}_4$  [42]. In Figures 8 and 9, we plot the enthalpies of hydrate formation as a function of temperature and pressure along the hydrate stability limit curve.

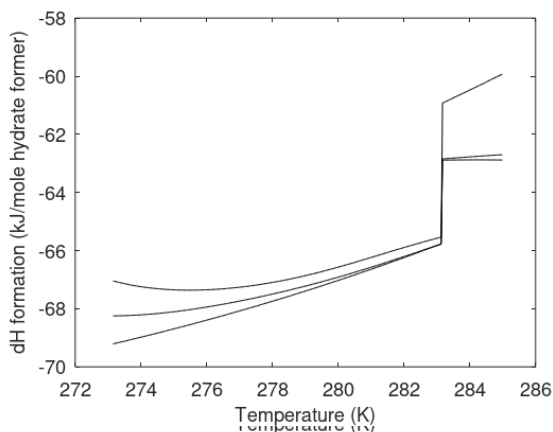


**Figure 8.** Enthalpies of hydrate formation in kJ/mol hydrate former as function of temperature. For temperatures below the  $\text{CO}_2$  phase transition (around 283.5 K), the bottom solid curve corresponds to pure  $\text{CO}_2$  hydrate; the top solid curve is 20 mol %  $\text{N}_2$  in  $\text{CO}_2/\text{N}_2$  mix; the middle curve is 10 mol %  $\text{N}_2$  in  $\text{CO}_2/\text{N}_2$  mix. Above the  $\text{CO}_2$  phase transition, the order of the curves is reversed: 10 mol %  $\text{N}_2$  in  $\text{CO}_2/\text{N}_2$  mix. Above the  $\text{CO}_2$  phase transition, the order of the curves is reversed.

The use of pure component values for the enthalpies of hydrate formation will substantially simplify the modeling, with the motivation for including Figures 6–9 being to facilitate a qualitative picture of the sensitivity of hydrate formation enthalpies with respect to certain relevant additives. Other uncertainties taken into account, using pure component



values for modeling will provide a fair approximation only for temperatures below and fairly close to the CO<sub>2</sub> phase transition temperature, as illustrated in Figures 6–9.

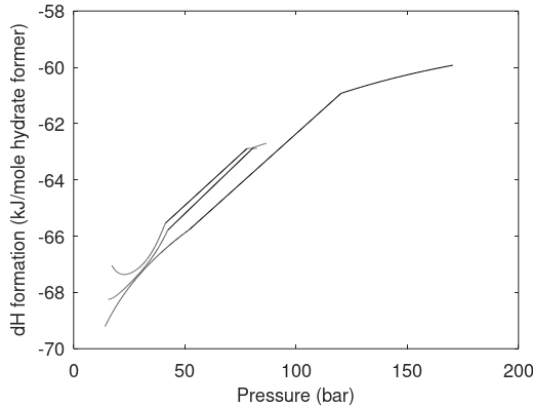
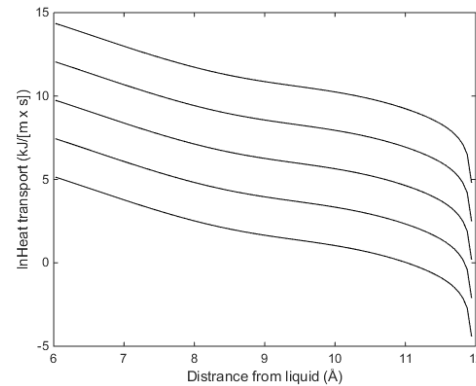


**Figure 9.** Enthalpies of hydrate formation in kJ/mol hydrate former as function of pressure. The bottom solid curve is pure CO<sub>2</sub> hydrate; the middle one is 10 mol % N<sub>2</sub> in the CO<sub>2</sub>/N<sub>2</sub> mix; the top solid curve is for pure CO<sub>2</sub> hydrate; the middle one is 10 mol % N<sub>2</sub> in the CO<sub>2</sub>/N<sub>2</sub> mix; the top solid curve is for 20 mol % N<sub>2</sub>.

The use of pure component values for the enthalpies of hydrate formation will substantially simplify the modeling, with the motivation for including Figures 6–9 being to facilitate a qualitative picture of the sensitivity of hydrate formation enthalpies with respect to certain relevant additives. One uncertainty taken into account, using pure publication data on hydrate phase transitions [23,22], is that it is, therefore disappointing that so many earlier theories are based on heat transport models rather than the associated mass transport limitations.

As noted previously, heat transport in aqueous systems is faster than mass transport by an order of two or three, which is a well-known fact verified by several of our earlier publications of interfaces typical for CH<sub>4</sub> and CO<sub>2</sub> hydrates [39–41]. Recently, a number of experimental studies have studied the use of CO<sub>2</sub> with limited admixture of N<sub>2</sub> intended to avoid the blocking of pores by newly formed CO<sub>2</sub> hydrate and to increase the flow permeability of the injection gas at the same time (see for instance Kvamme [24],

low permeability of the injection gas at the same time (see for instance Kvamme [24], Kvamme et al. [25], and Kvamme et al. [26]). The following profile (Figure 10) is based on data obtained from the molecular modeling of interfaces typical for CH<sub>4</sub> and CO<sub>2</sub> hydrates [39–41]. Recently, a number of experimental studies have studied the use of CO<sub>2</sub> with limited admixture of N<sub>2</sub> intended to avoid the blocking of pores by newly formed CO<sub>2</sub> hydrate and to increase the flow permeability of the injection gas at the same time (see for instance Kvamme [24], Kvamme et al. [25], and Kvamme et al. [26]).



enthalpy varies along the value amounted to -67.8 kJ/mol CO<sub>2</sub>. in Equation (9), and the limiting heat transport rate. rent values of diffusivity rate limiting portions of

**Figure 10.** Calculated heat transport rates through hydrate liquid-water interfaces as a function of liquid-side diffusivity coefficient in Equation (10). Upper curve is for D liquid in Equation (10) equal to 10<sup>-10</sup> m<sup>2</sup>/s (top), 1 × 10<sup>-11</sup> m<sup>2</sup>/s (middle), 1 × 10<sup>-12</sup> m<sup>2</sup>/s (bottom), and 1 × 10<sup>-13</sup> m<sup>2</sup>/s (bottom). Absolute minimum heat transport rates are 1.4 × 10<sup>-10</sup> kJ/(m × s), 1.4 × 10<sup>-11</sup> kJ/(m × s), 1.4 × 10<sup>-12</sup> kJ/(m × s), and 1.4 × 10<sup>-13</sup> kJ/(m × s) for the same curves.

heat cannot be transported faster than it moves across the rate-limiting section, with many dynamic changes related to the mass and heat transport drastically changing the mass and heat transport rates. As an example, the calculated heat transport rates corresponding to the distance of 6 Å from the liquid side would be four orders of magnitude higher than the values used Figure 10. On the other hand, the heat conduction coefficient of 0.57 W/(m·K) (see Table 2), i.e., 5.7 × 10<sup>-4</sup> kJ/(m·s·K), will still translate into heat transfer orders of magnitude faster than the mass transport-controlled rates on the left-hand side

As illustrated in Figure 5, the heat of hydrate formation enthalpy varies along the hydrate stability limit. At 273.16 K and 14.19 bars, the calculated value amounted to  $-67.8$  kJ/mol  $\text{CO}_2$ , with the corresponding value at 290 K and 403 bars equal to  $-58.5$  kJ/mol  $\text{CO}_2$ . Inserting the former value as the enthalpy of hydrate formation in Equation (9), and the profiles in Figures 2 and 3 in Equation (12), one can find the limiting heat transport rate. These calculations are illustrated in Figure 10 below for five different values of diffusivity on the liquid side of the interface (in Equation (10)) for the most rate limiting portions of the interface.

Heat cannot be transported faster than it moves across the rate-limiting sections, with many dynamic changes related to the mass and heat transport drastically changing the mass and heat transport rates. As an example, the calculated heat transport rates corresponding to the distance of 6 Å from the liquid side would be four orders of magnitude higher than the values used Figure 10. On the other hand, the heat conduction coefficient of  $0.57$  W/(m·K) (see Table 2), i.e.,  $5.7 \times 10^{-4}$  kJ/(m·s·K), will still translate into heat transfer orders of magnitude faster than the mass transport-controlled rates on the left-hand side of Equation (9).

The heat transport models along the lines presented here can be incorporated into simple kinetic models such as the classical nucleation theory (CNT) for use in hydrate phase transition modeling at the pore level in reservoir simulation. Yet, other applications are kinetic extensions of our hydrate risk evaluation models (see, for instance, [24,25]).

In this work, we have shown that mass transport through hydrate/liquid water interface is very slow. This issue is likely to limit hydrate film growth, and this may interfere the balance between distribution of released heat and temperature increase in surroundings. This may lead to partial re-dissociation of the hydrate film. As an illustration of the slow transport through hydrate films, we will utilize a simple version of CNT for spherical hydrate cores. CNT can be formulated as

$$J = J_0 e^{-\beta \Delta G^{Total}} \quad (13)$$

where  $J_0$  is the mass transport flux supplying the hydrate growth. For the phase transition in Equation (1), it will be a supply of  $\text{CO}_2$  across an interface of gradually more structured water towards the hydrate core, as discussed in Kvamme et al. [29] and illustrated above (see Figures 2 and 3). The units of  $J_0$  will be mol/m<sup>2</sup>s for heterogeneous hydrate formation on the growing surface area of the hydrate crystal.  $\beta$  is the inverse of the gas constant times temperature, and  $\Delta G^{Total}$  is the molar free energy change of the phase transition. This molar free energy contains two contributions: the phase transition free energy as described by Equation (1), and the penalty work incurred by pushing aside the old phases. Since the molar densities of liquid water and hydrate are reasonably close, it would be a fair approximation to obtain it as a product of molar free energy of the phase transition times the molar density of the hydrate times the volume of the hydrate core. The push work penalty term is simply given by the interface free energy times the surface area of the hydrate crystal. Using the underscore symbol to indicate extensive properties (in Joule):

$$\underline{\Delta G}^{Total} = \underline{\Delta G}^{Phasetransition} + \underline{\Delta G}^{Pushwork} \quad (14)$$

For the simplest possible geometry of a crystal, a sphere with radius  $R$ , we will obtain

$$\underline{\Delta G}^{Total} = \frac{4}{3}\pi R^3 \rho_N^H \Delta G^{Phasetransition} + 4\pi R^2 \gamma \quad (15)$$

where  $\rho_N^H$  is the hydrate molar density, and  $\gamma$  is the interfacial free energy between hydrate and the surrounding phase. Even if the hydrate core is floating on the water surface, one would expect small crystals to be covered by water on the gas side as well due to capillary forces facilitating the transport of water molecules from the liquid water side.

$$\Delta G_{Total} = \Delta G_{Phase\ transition} + \Delta G_{Push\ work} \quad (14)$$

For the simplest possible geometry of a crystal, a sphere with radius  $R$ , we will obtain

$$\Delta G_{Total} = \frac{4}{3} \pi R^3 \rho_N^H \Delta G_{Phase\ transition} + 4\pi R^2 \gamma \quad (15) \quad 20\ of\ 26$$

where  $\rho_N^H$  is the hydrate molar density, and  $\gamma$  is the interfacial free energy between hydrate and the surrounding phase. Even if the hydrate core is floating on the water surface, one would expect small crystals to be covered by water on the gas side as well due to energy gain (the critical core size) yields the usual result.

Differentiating Equation (15) with respect to  $R$  and solving for the maximum free energy radius (the critical core size) yields the usual result:

$$R^* = - \frac{\rho_N^H \Delta G_{Phase\ transition}}{\rho_N^H \Delta G_{Phase\ transition}} \quad (16)$$

where superscript \* denotes critical nucleus radius. The critical radius for two different temperatures is given in Figure 11 below. For the temperature below the transition to liquid  $CO_2$ , the trend is very similar to that observed in Phase Field Theory (PFT) modeling (see [39, 42] and the references therein).

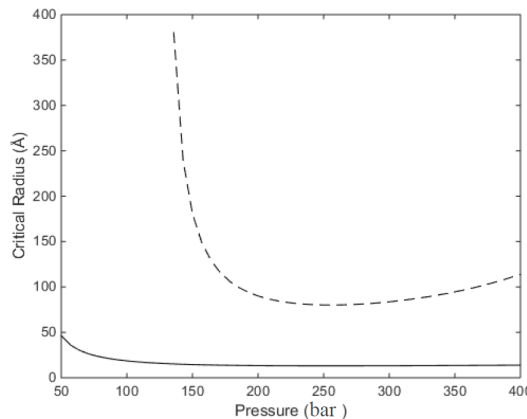


Figure 11. Calculated critical radius for heterogeneous nucleation of hydrate from  $CO_2$  and liquid water as a function of pressure for 280 K (solid) and 285 K (dashed).

The transition into the liquid phase will dramatically increase the critical radius, although it will remain in the nanoscale, except for the lowest pressures. Figure 12 presents nucleation times corresponding to heterogeneous hydrate formation from  $CO_2$  and water phase at 280 K and 285 K, with the nucleation time above the carbon dioxide transition point much higher at lower pressures.

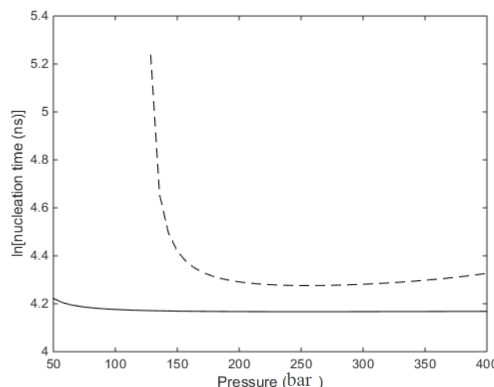


Figure 12. Calculated nucleation times for heterogeneous hydrate formation from  $CO_2$  and liquid water. Solid curve is for 280 K, and dashed curve is for 285 K.

As noted earlier, diffusion through the initial hydrate film will be very slow. Since most estimates available in the literature are based on molecular modeling simulations, using specific approximations and assumptions, at least 12 different values can be found in journal papers; they range between 10 and 15  $m^2/s$  and 10–17  $m^2/s$ . As long a hydrate is formed, it will be the lowest free energy phase for water. The hydrate will therefore decide the minimum level of  $CO_2$  in the contacting aqueous phase. This means that hydrates can grow from  $CO_2$  dissolved in water from its solubility limit and down to the  $CO_2$  hydrate stability limit (see Kvamme et al. [29] for more details).

using specific approximations and assumptions, at least 12 different values can be found in journal papers; they range between 10 and 15 m<sup>2</sup>/s and 10–17 m<sup>2</sup>/s. As long a hydrate is formed, it will be the lowest free energy phase for water. The hydrate will therefore decide the minimum level of CO<sub>2</sub> in the contacting aqueous phase. This means that hydrates can grow from CO<sub>2</sub> dissolved in water from its solubility limit and down to the CO<sub>2</sub> hydrate stability limit (see Kvamme et al. [29] for more details).

Hydrate formation from the aqueous phase side will preferentially occur towards the already established hydrate film due to the presence of adsorbed and structured water in contact with the hydrate surface. However, the supply of hydrate former needed to sustain the growth will still occur via diffusion. Assuming a quasi-equilibrium between liquid water and water adsorbed on the hydrate surface, one can obtain a fair estimate of hydrate nucleation rate from CO<sub>2</sub> dissolved in water. Figure 13 presents the critical radius calculated for homogeneous hydrate formation from CO<sub>2</sub> dissolved in water for 280 K and 100 bars as an example. The corresponding nucleation times are plotted in Figure 14.

Appl. Sci. 2021, 11, 4124 FOR PEER REVIEW

We should note that this route to hydrate formation is characterized by almost “instant” hydrate nucleation in the macroscopic sense (nucleation time of mere seconds).

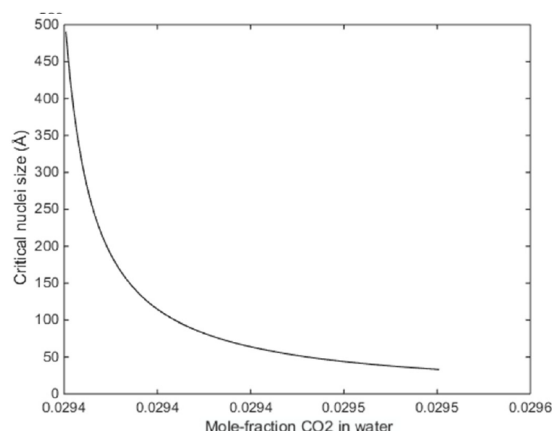


Figure 13. Calculated critical radius in the case of homogeneous hydrate formation from liquid water and CO<sub>2</sub> dissolved in water at 280 K and 100 bars as function of mole fraction of CO<sub>2</sub> in liquid water.

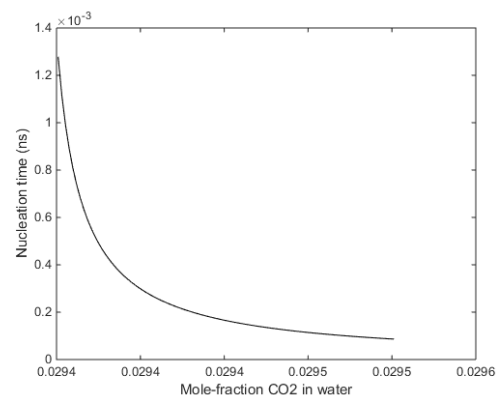
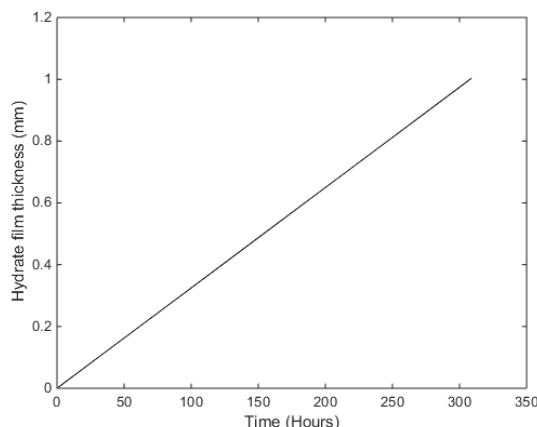


Figure 14. Calculated nucleation times in nanoseconds in the case of homogeneous hydrate formation from liquid water and CO<sub>2</sub> dissolved in water at 280 K and 100 bars.

Figure 15 presents the growth rates calculated by using the value of  $D_{\text{film}} = 10^{-10} \text{ m}^2/\text{s}$  in Equation (10). The time for visible hydrate film appears to be in a good agreement with the observations of Uchida et al. [16], as well as our own observations of CH<sub>4</sub> hydrate film growth [40] that showed visible (Magnetic Resonance Imaging) hydrate on a resolution scale of approximately 300 microns after 100 h.

It is beyond the scope of this work to provide a more detailed analysis of the induc-

Figure 15 presents the growth rates calculated by using the value of  $D_{liq} = 10^{-08} \text{ m}^2/\text{s}$  in Equation (10). The time for visible hydrate film appears to be in a good agreement with the observations of Uchida et al. [10], as well as our own observations of  $\text{CH}_4$  hydrate film growth [40] that showed visible (Magnetic Resonance Imaging) hydrate on a resolution scale of approximately 300 microns after 100 h.



**Figure 15.** Calculated  $\text{CO}_2$  hydrate film thickness as a function of time for a liquid side diffusivity in Equation (10) equal to  $D_{liq} = 10^{-08} \text{ m}^2/\text{s}$ .

While they had the transport of this work to systems more detailed, an analysis of the induction hydrate formation sets of a transport that interests and that highly promises in the conditions of an ically feasible process in this work will be applied to water modeling of hydrate side and in structure themselves into the dynamics of hydrate to be able to grow quickly in this part of hydrate formation containing dissolving factor since the enthalpy of creating the hydrate core needs to be transported through a heat insulator such as hydrocarbon gas.

MDT be this component difficult to use in this theory that is equally as simple and cannot be generally applied to practical applications that require quickly solved kinetic models. The heat transport modeling in this work will also find its way into our present level of Phase Field Theory (PFT) models. See, for instance, [24–26, 38–40] for representative examples.

The important point here is that any specific case has to be analyzed in detail in terms of coupled mass transport, heat transport, and thermodynamic control. The main problem for hydrate formation, from water dissolved in pure water, and this process is thermodynamically feasible. Mass transport is slow since about 150 water molecules must assemble and structure themselves into a hydrate nucleus for it to be able to grow steadily. In this case, kinetic models for hydrate phase transitions are based on physically wrong assumptions.

heat transport will be the rate limiting factor since the enthalpy of creating the hydrate core needs to be transported through a heat insulator such as hydrocarbon gas. If the heat is numerically simple, it still incorporates a newly developed mass transport term based on modern theoretical concepts and results from molecular dynamics simulations. The implicit heat transport model we employ is equally numerically simple but has the advantage of being coupled to a new model for enthalpy calculations completely consistent with the free energies in hydrate and all co-existing phases.

A very important aspect of this work is our use of a thermodynamically consistent approach for all phases, residual thermodynamics. It is slightly outside the main focus of this work to show all the derivations that prove both the consistency and its implications. While the kinetic model for hydrate phase transitions presented in this work (CNT) is numerically simple, it still incorporates a newly developed mass transport term based on maintaining the connection between entropy and structure will require consistent calculations of modern theoretical concepts and results from molecular dynamics simulations. The implicit calculations of both free energy and enthalpy. That is why it was important for us to demonstrate that our free energy calculations are correct as illustrated by Figure 1 and the comparison with experimental data in our previously published work.

being coupled to a new model for enthalpy calculations completely consistent with the free energies in hydrate and all co-existing phases.

Then, the appropriate simplifications and approximations can be performed based on physical arguments. Far too often, including examples mentioned here, kinetic models for hydrate phase transitions are based on physically wrong assumptions.

**5. Conclusions**

Kinetic models found in the literature aiming to describe the kinetics of heterogeneous hydrate film formation and growth are frequently incomplete and lack a fundamental connection to physics-based theoretical platforms. In this work, we propose and demonstrate a theoretical approach able to derive fairly rigorous kinetic models that include im-

A very important aspect of this work is our use of a thermodynamically consistent approach for all phases: residual thermodynamics. It is slightly outside the main focus of this work to show all the derivations that prove both the consistency and its implications. In brief, the combination of statistical mechanics and classical thermodynamics shows that maintaining the connection between entropy and structure will require consistent calculations of both free energy and enthalpy. That is why it was important for us to demonstrate that our free energy calculations are correct as illustrated by Figure 1 and the comparison with experimental data in our previously published work.

## 5. Conclusions

Kinetic models found in the literature aiming to describe the kinetics of heterogeneous hydrate film formation and growth are frequently incomplete and lack a fundamental connection to physics-based theoretical platforms. In this work, we propose and demonstrate a theoretical approach able to derive fairly rigorous kinetic models that include implicit coupling between mass transport, heat transport, and phase transition thermodynamic control. We also show that our scheme allows the evaluation of all relevant thermodynamic properties at the same reference level (ideal gas) for all components in all the phases, enthalpies of hydrate formation and dissociation included.

There is a consensus in the available literature that heat transport in aqueous and hydrate systems will be substantially faster than mass transport. An important consequence of this fact is that any kinetic theory of hydrate nucleation, growth, and dissociation has to be based on comprehensive kinetic models incorporating all the implicit coupling mentioned above. Approximations and simplifications must be based on physical reasoning. We have illustrated these points using a realistic representation of the interface between hydrate and liquid. A frequent misunderstanding found in the literature is that hydrate nucleation times can be measured in hours. This confusion is based on visual observations of hydrates which yields the induction time, i.e., time to onset of massive hydrate growth rather than nucleation. Our results calculated basing on the classical nucleation theory indicate that nucleation will occur on the nanoscale, both in respect to time and critical radius dimensions for both heterogeneous and homogeneous hydrate formation from water and dissolved CO<sub>2</sub>. On the other hand, the diffusion of hydrate formers across the newly formed hydrate film will be a very slow process responsible for the very lengthy interval before hydrate can be observed on the macroscopic scale. Based on all these observations, we highly recommended that all hydrate kinetic modeling should be based on a sound theoretical foundation. Classical nucleation theory, as utilized in this work, has proven fast enough to be implemented into reservoir simulations. Similar arguments apply to the multicomponent diffusive interface theory (MDIT), which is also very simple numerically. On the other hand, the Phase Field Theory (PFT) lies at the opposite end of the spectrum, being quite numerically intensive for integration at the pore scale level, but the heat transport aspects discussed in this work will also be useful as extensions to our PFT theory for detailed mechanistic studies.

**Author Contributions:** All authors have contributed to theoretical development, the writing of the paper and analysis of data, including comparisons with experimental data and scientific discussion. All authors have read and agreed to the published version of the manuscript.

**Funding:** The Research Council of Norway and industrial partners through the following projects: CLIMIT “Safe long term sealing of CO<sub>2</sub> in hydrate,” Research Council of Norway project number 224857; SSC-Ramore, “Subsurface storage of CO<sub>2</sub> e Risk assessment, monitoring and remediation,” project number: 178008/I30; PETROMAKS “CO<sub>2</sub> injection for extra production,” Research Council of Norway project number 801445; PETROMAKS “CO<sub>2</sub> Injection for Stimulated Production of Natural Gas,” Research Council of Norway project numbers 175968 and 230083; and STATOIL, under contract 4502354080.

**Data Availability Statement:** No electronic supplements, refer to the corresponding author for additional details.

**Acknowledgments:** We acknowledge the grants and support from the NFR and Equinor.

**Conflicts of Interest:** The authors declare that there are no conflict of interest.

### Nomenclature

|                     |                             |  |
|---------------------|-----------------------------|--|
| C                   | [molecules/Å <sup>3</sup> ] | Concentration  |
| D                   | [m <sup>2</sup> ·s]         | Diffusivity  |
| T                   | [K]                         | Temperature  |
| T <sub>c</sub>      | [K]                         | Critical temperature [K]   |
| Y                   | [bar or kPa]                | Pressure   |
| H                   | [-]                         | Hydrate phase  |
| ΔG                  | [-]                         | Free energy change   |
| G                   | [kJ/mol]                    | Free energy change   |
| H                   | [-]                         | Hydrate phase  |
| J                   | [mol/m <sup>2</sup> ·s]     | Mass transfer Flux   |
| R                   | [Å]                         | Distance from liquid side  |
| X                   | [-]                         | Mol fraction of liquid   |
| Y                   | [-]                         | Mol fraction of gas  |
| Special characters  |                             |  |
| H <sub>ij</sub>     | [-]                         | Canonical cavity partition function of component j in the cavity i |
| Δg <sub>incij</sub> | [-]                         | Free energy of inclusion of the guest molecules j in the cavity i  |
| μ                   | [kJ/mol]                    | Chemical potential   |
| ∅                   | [-]                         | ∅ Fugacity coefficient   |
| Γ                   | [-]                         | Activity coefficient   |
| Θ <sub>ij</sub>     | [-]                         | Θ <sub>ij</sub> Filling fraction of component j in cavity type i   |
| B                   | [-]                         | Inverse of gas constant times temperature                          |
| x <sub>T</sub>      | [-]                         | Total mol fraction of all guests in the hydrate                    |
| Subscripts          |                             |  |
| H                   |                             | Hydrate phase  |
| M                   |                             | Minerals   |
| N                   |                             | Hydrate Components   |
| P                   |                             | Parent phase   |
| T                   |                             | Total  |
| 0                   |                             | Ambient or reference   |

### References

- Sloan, E.D. Fundamental principles, and applications of natural gas hydrates. *Nature* **2003**, *426*, 353–363. [[CrossRef](#)] [[PubMed](#)]
- Kuhs, W.F.; Chazallon, B.; Klapproth, A.; Pauer, F. Filling isotherms in clathrate hydrates. *Rev. High Press. Sci. Technol.* **1998**, *7*, 1147–1149. [[CrossRef](#)]
- Lee, H.; Seo, Y.; Seo, Y.-T.; Moudrakovski, I.L.; Ripmeester, J.A. Recovering Methane from Solid Methane Hydrate with Carbon Dioxide. *Angew. Chem. Int. Ed.* **2003**, *115*, 5202–5205. [[CrossRef](#)]
- Falenty, A.; Genov, G.; Hansen, T.C.; Kuhs, W.F.; Salamatin, A.N. Kinetics of CO<sub>2</sub>-Hydrate Formation from Water Frost at Low Temperatures: Experimental Results and Theoretical Model. *J. Phys. Chem. C* **2010**, *115*, 4022–4032. [[CrossRef](#)]
- Kvamme, B.; Kuznetsova, T.; Stensholt, B.J.S.; Bauman, B.; Sjöblom, S.; Lervik, K.N. Consequences of CO<sub>2</sub> solubility for hydrate formation from carbon dioxide containing water and other impurities. *Phys. Chem. Chem. Phys.* **2014**, *16*, 8623–8638. [[CrossRef](#)] [[PubMed](#)]
- Kvamme, B.; Kuznetsova, T.; Kivelæ, P.H.; Bauman, J. Can hydrate form in carbon dioxide from dissolved water. *Phys. Chem. Chem. Phys.* **2013**, *15*, 2063–2074. [[CrossRef](#)]
- Kvamme, B.; Tanaka, H. Thermodynamic Stability of Hydrates for Ethane, Ethylene, and Carbon Dioxide. *J. Phys. Chem.* **1995**, *99*, 7114–7119. [[CrossRef](#)]
- Shindo, Y.; Fujioka, Y.; Yanagishita, Y.; Hakuta, T.; Komiyama, H. Formation, and stability of CO<sub>2</sub> hydrate. In Proceedings of the 2nd International Workshop on Interaction between CO<sub>2</sub> and Ocean, Tsukuba-Ibakari, Tsukuba-Ibakari, Japan, 18–22 January 1999; pp. 111–125.
- Lund, P.C.; Shindo, Y.; Fujioka, Y.; Komiyama, H. Study of the pseudo-steady-state kinetics of CO<sub>2</sub> hydrate formation and stability. *Int. J. Chem. Kinet.* **1994**, *26*, 289–297. [[CrossRef](#)]
- Teng, H.; Kinoshita, C.M.; Masutani, S.M. Hydrate formation on the surface of a CO<sub>2</sub> droplet in high-pressure, low-temperature water. *Chem. Eng Sci.* **1995**, *50*, 559–564. [[CrossRef](#)]

11. Sugaya, M.; Mori, Y.H. Behavior of clathrate hydrate formation at the boundary of liquid water and a fluorocarbon in liquid or vapor state. *Chem. Eng. Sci.* **1996**, *51*, 3505–3517. [[CrossRef](#)]
12. Hirai, S.; Okazaki, K.; Araki, N.; Yazawa, H.; Ito, H.; Hijikata, K. Transport phenomena of liquid CO<sub>2</sub> in pressurized water flow with clathrate-hydrate at the interface. *Energy Convers. Manag.* **1996**, *37*, 1073. [[CrossRef](#)]
13. Mori, Y.H.; Mochizuki, T. Mass transport across clathrate hydrate films a capillary permeation model. *Chem. Eng. Sci.* **1997**, *52*, 3613–3616. [[CrossRef](#)]
14. Mori, Y.H. Clathrate Hydrate Formation at the interface between liquid CO<sub>2</sub> and water phases, a review of rival models characterizing hydrate films. *Energy Convers. Manag.* **1998**, *39*, 1537. [[CrossRef](#)]
15. Uchida, T.; Ebinuma, T.; Kawabata, J.; Narita, H. Microscopic observations of formation processes of clathrate-hydrate films at an interface between water and carbon dioxide. *J. Cryst. Growth* **1999**, *204*, 348–356. [[CrossRef](#)]
16. Mori, Y.H. Estimating the thickness of hydrate films from their lateral growth rates: Application of a simplified heat transfer model. *J. Cryst. Growth* **2001**, *223*, 206–212. [[CrossRef](#)]
17. Freer, E.M.; Selim, M.S.; Sloan, E.D. Methane hydrate film growth kinetics. *Fluid Phase Equilib.* **2001**, *185*, 65–75. [[CrossRef](#)]
18. Mochizuki, T.; Mori, Y.H. Clathrate-hydrate film growth along water/hydrate former phase boundaries—Numerical heat-transfer study. *J. Cryst. Growth* **2006**, *290*, 642–652. [[CrossRef](#)]
19. Mochizuki, T.; Mori, Y.H. Simultaneous Mass and Heat Transfer to/from the Edge of a Clathrate-Hydrate Film Causing its Growth along a Water/Guest-Fluid Phase Boundary. *Chem. Eng. Sci.* **2017**, *171*, 61–75. [[CrossRef](#)]
20. Liu, Z.; Li, H.; Chen, L. A New Model of and Insight into Hydrate Film Lateral Growth along the Gas–Liquid Interface Considering Natural Convection Heat Transfer and Baojiang Sun. *Energy Fuels* **2018**, *32*, 2053–2063. [[CrossRef](#)]
21. Svandal, A. Modelling Hydrate Phase Transitions Using Mean-Field Approaches. Ph.D. Thesis, University of Bergen, Bergen, Norway, 2006.
22. Svandal, A.; Kvamme, B.; Granasy, L.; Pusztai, T. The influence of diffusion on hydrate growth. In Proceedings of the 1st International Conference on Diffusion in Solids and Liquids, DSL-2005, Aveiro, Portugal, 6–8 July 2005.
23. Soave, G. Equilibrium constants from a modified Redlich-Kwong equation of state. *Chem. Eng. Sci.* **1972**, *27*, 1197–1203. [[CrossRef](#)]
24. Kvamme, B. Thermodynamic Limitations of the CO<sub>2</sub>/N<sub>2</sub> Mixture Injected into CH<sub>4</sub> Hydrate in the Iknig Sikumi Field Trial. *J. Chem. Eng. Data* **2016**, *3*, 1280–1295. [[CrossRef](#)]
25. Kvamme, B.; Aromada, S.A. Risk of Hydrate Formation during the Processing and Transport of Troll Gas from the North Sea. *J. Chem. Eng. Data* **2017**, *62*, 2163–2177. [[CrossRef](#)]
26. Baig, K. Nano to Micro Scale Modelling of Hydrate Phase Transition Kinetics. Ph.D. Thesis, University of Bergen, Bergen, Norway, 2017.
27. Kvamme, B.; Qasim, M.; Baig, K. Hydrate phase transition kinetics from Phase Field Theory with implicit hydrodynamics and heat transport. *Int. J. Greenh. Gas Control* **2014**, *29*, 263–278. [[CrossRef](#)]
28. Qasim, M. Microscale Modelling of Natural Gas Hydrates in Reservoirs. Ph.D. Thesis, University of Bergen, Bergen, Norway, 2012.
29. Kvamme, B.; Selvåg, J.; Aromada, S.A.; Saeidi, N.; Kuznetsova, T. Methanol as hydrate inhibitor and hydrate activator. *Phys. Chem. Chem. Phys.* **2018**, *20*, 21968–21987. [[CrossRef](#)] [[PubMed](#)]
30. Kvamme, B. Enthalpies of hydrate formation from hydrate formers dissolved in water. *Energies* **2019**, *12*, 1039. [[CrossRef](#)]
31. Kvamme, B.; Lund, A.; Hertzberg, T. The influence of gas-gas interactions on the Langmuir constants for some natural gas hydrates. *Fluid Phase Equilibria* **1993**, *90*, 15–44. [[CrossRef](#)]
32. Kvamme, B.; Førriisdahl, O.K. Polar guest-molecules in natural gas hydrates. *Fluid Phase Equilibria* **1993**, *83*, 427. [[CrossRef](#)]
33. Niall, J.E.; John, S.T. Perspectives on Hydrate Thermal Conductivity. *Energies* **2010**, *3*, 1934–1942.
34. Prah, B.; Rin Yun, R. Heat Transfer and Flow Characteristics of CO<sub>2</sub>-Hydrate Mixture in Pipeline. *Energy Procedia* **2017**, *114*, 6813–6823. [[CrossRef](#)]
35. Sharqawy, M.H.; Lienhard, V.J.H.; Zubair, S.M. Thermophysical properties of seawater: A review of existing correlations and data. *Desalination Water Treat.* **2010**, *16*, 354–380. [[CrossRef](#)]
36. Asgeirsson, L.S.; Ghajar, A.J. Prediction of thermal conductivity and Viscosity for some fluids in the near-critical region. *Chem. Eng. Commun.* **1986**, *43*, 165–184. [[CrossRef](#)]
37. Todd, B.; Young, J.B. Thermodynamic and transport properties of gases for use in solid oxide fuel cell modelling. *J. Power Sources* **2002**, *110*, 186–200. [[CrossRef](#)]
38. Roy, R.F.; Beckand, A.E.; Touloukian, Y.S. Thermophysical Properties of Rocks. *Phys. Prop. Rocks Miner.* **1981**, *198*, 2.
39. Svandal, A.; Kuznetsova, T.; Kvamme, B. Thermodynamic properties and phase transitions in the H<sub>2</sub>O/CO<sub>2</sub>/CH<sub>4</sub> system. *Fluid Phase Equilibria* **2006**, *246*, 177–184. [[CrossRef](#)]
40. Tegze, G.; Pusztai, T.; Toth, G.; Granasy, L.; Svandal, A.; Kuznetsova, T.; Buanes, T.; Kvamme, B. Multi-scale approach to CO<sub>2</sub>-hydrate formation in aqueous solution. *J. Chem. Phys.* **2006**, *124*, 234710. [[CrossRef](#)] [[PubMed](#)]
41. Kvamme, B.; Graue, A.; Buanes, T.; Kuznetsova, T.; Ersland, G. Storage of CO<sub>2</sub> in natural gas hydrate reservoirs and the effect of hydrate as an extra sealing in cold aquifers. *Int. J. Green. Gas Control* **2007**, *1*, 236–246. [[CrossRef](#)]
42. Kvamme, B.; Aromada, S.A. Alternative routes to hydrate formation during processing and transport of natural gas with significant amount of CO<sub>2</sub>: Sleipner gas as a case study. *J. Chem. Eng. Data* **2018**, *63*, 832–844. [[CrossRef](#)]
43. Kvamme, B.; Zhao, J.Z.; Wei, N.; Sun, W.T.; Saeidi, N.; Pei, J.; Kuznetsova, T. Hydrate production philosophy and thermodynamic calculations. *Energies* **2020**, *13*, 673. [[CrossRef](#)]



44. Kvamme, B. Environmentally friendly production of methane from natural gas hydrate using carbon dioxide. *Sustainability* **2019**, *11*, 1964. [[CrossRef](#)]
45. Kvamme, B. Kinetics of Hydrate Formation from Nucleation Theory. *Int. J. Offshore Polar Eng.* **2002**, *12*, 256–263.

---

## **PAPER IX**

**WHY SHOULD WE USE RESIDUAL  
THERMODYNAMICS FOR CALCULATION OF  
HYDRATE PHASE TRANSITIONS?**



Article

# Why Should We Use Residual Thermodynamics for Calculation of Hydrate Phase Transitions?

Bjørn Kvamme <sup>1,\*</sup>, Jinzhou Zhao <sup>1</sup>, Na Wei <sup>1</sup>, Wantong Sun <sup>1</sup>, Mojdeh Zarifi <sup>2</sup>, Navid Saeidi <sup>3</sup>, Shouwei Zhou <sup>4</sup>, Tatiana Kuznetsova <sup>2</sup> and Qingping Li <sup>4</sup>

<sup>1</sup> State Key Laboratory of Oil and Gas Reservoir Geology and Exploitation, Southwest Petroleum University, Xindu Road No.8, Chengdu 610500, China; zhaojz@swpu.edu.cn (J.Z.); 201131010053@swpu.edu.cn (N.W.); wantong.sun@student.uib.no (W.S.)

<sup>2</sup> Department of Physics and Technology, University of Bergen, Allegaten 55, 5007 Bergen, Norway; mojdeh.zarifi@uib.no (M.Z.); nfyta@uib.no (T.K.)

<sup>3</sup> Environmental Engineering Department, University of California, Irvine, CA 92697-3975, USA; saeidin@uci.edu

<sup>4</sup> CNOOC Research Institutes Limited Liability Company, Taiyanggong South Road No.6, Beijing 100027, China; zhoushw@cnooc.com.cn (S.Z.); liqp@cnooc.com.cn (Q.L.)

\* Correspondence: bkvamme@strategic-carbonllc.com; Tel.: +47-9345-1956

Received: 6 December 2019; Accepted: 27 May 2020; Published: 10 August 2020



**Abstract:** The formation of natural gas hydrates during processing and transport of natural has historically been one of the motivations for research on hydrates. In recent years, there has been much focus on the use of hydrate as a phase for compact transport of natural gas, as well as many other applications such as desalination of seawater and the use of hydrate phase in heat pumps. The huge amounts of energy in the form of hydrates distributed in various ways in sediments is a hot topic many places around the world. Common to all these situations of hydrates in nature or industry is that temperature and pressure are both defined. Mathematically, this does not balance the number of independent variables minus conservation of mass and minus equilibrium conditions. There is a need for thermodynamic models for hydrates that can be used for non-equilibrium systems and hydrate formation from different phase, as well as different routes for hydrate dissociation. In this work we first discuss a residual thermodynamic model scheme with the more commonly used reference method for pressure temperature stability limits. However, the residual thermodynamic method stretches far beyond that to other routes for hydrate formation, such as hydrate formation from dissolved hydrate formers. More important, the residual thermodynamic method can be utilized for many thermodynamic properties involved in real hydrate systems. Consistent free energies and enthalpies are only two of these properties. In non-equilibrium systems, a consistent thermodynamic reference system (ideal gas) makes it easier to evaluate most likely distribution of phases and compositions.

**Keywords:** hydrate; phase transitions; statistical mechanics; thermodynamic properties

## 1. Introduction

The problems of hydrate formation in pipelines during transport of hydrocarbons and other hydrate forming components is as old as the modern oil industry itself. The need for calculations of hydrate formation conditions in order to design appropriate measures to counteract problems of pipeline blockings is a continuous effort. During the last three decades there has been a substantial increase in the interest of natural gas hydrates as an energy source, which requires calculation of phase transition conditions and phase transition kinetics. However, also other sides of natural gas hydrates motivate the developments of better and more complete tools for calculations of hydrate phase transitions. Hydrate exposed to inflow of seawater through fracture systems leads to leakage

fluxes of methane to the oceans and potentially also to air. All these dynamics processes may also lead to geo mechanical instability and landslides.

Calculation of hydrate phase transitions has a long history. Many early strategies were based on analogies to calculations of gas/Liquid distributions in hydrocarbon systems. Gas-liquid mole-fraction ratios and K-values are used along with a mass balance to calculate distributions of oil and gas, as well as composition of the phases. In the early days before computers became commercially available, K-value charts for various components were developed. Similar K-value charts were also developed for various hydrate formers in a similar analogy for hydrate equilibrium calculations. It is far beyond the scope of this work to discuss the very old strategies for hydrate equilibrium calculations and for this we refer to some history in Koh & Sloan [1]. Using a semi-grand canonical ensemble, van der Waal & Platteeuw [2] derived a Langmuir-type adsorption theory for hydrate which generated various ways to treat the hydrate phase in a more modern fashion, using equations of state to describe the impact of hydrate formers on thermodynamic equilibrium. One version of the modern way to model hydrate equilibrium was based on the use of a reference hydrate, and mostly credited to Parrish and Prausnitz [1,3]. For review of other methods and more details the reader is directed to other literature such as [1].

In this work we only focus on two different approaches. The first method is what we can call a reference approach since it utilizes a reference state and differences between a pure water phase and empty hydrate of either structure I, II or H. A second method uses residual thermodynamics for all components in all phases, including hydrate.

## 2. Motivation and Overview

Frequently independent thermodynamic variables are often used to evaluate energy processes. One typical example is evaluation of risk for hydrate formation, which is frequently discussed in terms of pressure and temperature stability limits. This projection of the whole stability regime, which also includes concentrations in all co-existing phases do not tell directly if the free energy change needed to create hydrate. Moreover, it does tell anything about how the released heat of hydrate formation and dissociation, is a multi-phase problem in which Gibbs distributed away from the formed hydrate.

This is just one example that tells us that we need a system for analyzing hydrates which is based on thermodynamic responses rather than independent thermodynamic variables. Practically this means that we need to develop model systems which analyze hydrate formation and hydrate dynamics based on free energy changes for the variety of possible (combined first and second law) as responses to changes in temperature, pressure and concentrations. Any phase transition determine phase distributions under constraints of dynamics is implicitly coupled to related mass and heat transport. Pressure and temperature dynamics and heat transport dynamics. We therefore also need a consistent rote to calculations of enthalpies, as the first law response to independent variables like temperature, pressures and concentrations. Similar examples related to hydrates in porous media are just a two-dimensional projection of all independent thermodynamic variables. Concentrations are also discussed in this study.

Another important motivation for this work is that hydrates in porous media can never reach true thermodynamic equilibrium. As we demonstrate in this study there is a lower limit of all hydrate formers and former in surrounding water in all co-existing phases are additional independent thermodynamic variables. One which is needed in order to keep hydrate stable. There is even a lower limit of the objectives water in gas needed in order to prevent the hydrate from sublimation. Overall, there are far too many active phases of this work is to provide a thermodynamic overview of the relevance to hydrate formation and hydrate stability to fulfill the balance between number of some independent variables on one side and conservation laws plus condition of the phase transitions which are often omitted. thermodynamic equilibrium on the other side. When temperature and pressure are both defined in a reservoir or in a pipeline two independent variables are already fixed. Even with only one hydrate former plus water there are three phases when hydrate forms. That leaves only one

independent thermodynamic variable and two are defined. In reality, as also discussed here, hydrate systems in porous media is more mathematically over determined compare tow two fixed independent thermodynamic variables.

This is just one example that tells us that we need a new thermodynamic toolbox which is able to calculate all the hydrate phase transitions of significance for hydrates in sediments or hydrates forming during transport of hydrate formers in a pipeline. This also involves the need for calculation of enthalpies of hydrate phase transitions. Moreover, since hydrate formed from different phases has different stability there is need for a toolbox which also calculated free energies of the various co-existing phases. This is a second objective of this work.

Offshore methane hydrate reservoirs are always in a dynamic state. This implies that fracture systems from below bring in hydrocarbons that lead to formation of hydrate with groundwater. At the same time seawater is leaking into the hydrate filled sediments through fracture systems. As will be discussed in more detail in this study this leads dissociation of hydrates because the seawater content of methane is almost zero. A third objective of this work is to shed more light on important hydrate stability limits, beyond the temperature pressure projection of the stability limits

There are many thermodynamic packages for calculating pressure and temperature stability limits. These are based on very old calculation routes from around 1970. There are many drawbacks related to these old approaches. And a fundamental limitation is that thermodynamic properties like chemical potentials are empirically fitted. Practically these packages only calculate hydrate formation from a separate hydrate former phase and liquid water or ice. It is not

What is new here is a complete concept for calculating hydrate stability limits in various projections. Not only in temperature and pressure, but also for hydrate formation from dissolved hydrate formers and hydrate dissociation towards water under saturated with hydrate former. These types of hydrate phase transitions are critical in the hydrate dynamics related to fracture systems that connects offshore hydrate bearing formations in contact with seawater. However, the most important is a goal of this study to do an extensive comparison of the residual scheme and the reference model. However, it is actually fairly simple to rewrite programs based on the reference over to a residual complete and consistent thermodynamic model system. A fourth objective is therefore to illustrate the thermodynamic similarities, and hopefully, to illustrate what changes are needed to reformulate reference schemes over to residual thermodynamic schemes. That can easily be implemented into hydrate reservoir simulators or hydrate risk evaluation software. This can make substantial steps forward in evaluation of hydrate production scenarios.

The next section gives an overview of the residual thermodynamic concept, along with a brief description of what we call the reference method. The main purpose of this section is to point of advantages and drawbacks of the two different schemes, and also provide a platform for residual thermodynamic analysis of other routes to hydrate dissociation and formation.

In Section 3, we show some examples for hydrate stability limits as based on the residual thermodynamic scheme and on the reference method. Since we do not have any code for the reference method we have used software which is publicly available and documented in many other publications from other groups. Another new element in this section is the estimation of a hydrate curve for CO<sub>2</sub> which also includes the impact of a CO<sub>2</sub> phase transition which is frequently overlooked and smoothened out.

Section 4 focuses on hydrate formation from dissolved hydrate formers as well as the dissociation limits for hydrate in presence of water which in under saturated with hydrate formers. These phase transitions are very important in analysis of hydrate dynamics in sediments, but also during hydrate formation and dissociation in a multiphase flow line containing hydrocarbon oil and gas phases and separate liquid water phase. Hydrate can nucleate and form towards rusty pipeline walls and on water–gas interface (and potentially water–liquid interface). During turbulent flow, these hydrates can dissociate again when exposed to water lean on hydrate formers.

Hydrate dissociation needs two conditions to be fulfilled. The free energy change has to be large enough to efficiently release water and hydrate former from the hydrate. During formation of hydrate there is a barrier related to the push work needed for make space for the new phase. During hydrate dissociation the guest molecules have to cross a thin interface of structured water and correspondingly low diffusivity. In addition to this “penalty” of slow mass transport and need for a significant free energy difference the necessary heat must be supplied. Reducing pressure to below temperature and pressure stability is one method for producing hydrate. The questions are; are the free energy differences sufficient and how is heat supplied. Is there sufficient heat supply? Estimation of consistent enthalpies is crucial in hydrate production. Moreover, the calculations need to be consistent with free energy calculation for the phase transition changes in order to give the correct entropy generation. In Section 5, we discuss thermodynamic models for Gibbs free energy and enthalpy derived from the residual thermodynamic concept.

The study is completed with a discussion in Section 6, followed by our conclusions.

### 3. Thermodynamic Models in Residual Thermodynamics Model and the Reference Models Method

In a thermodynamic description we will use  $\mu_k^m$  as symbol for chemical potential for component k in a phase m. Within the limitations of this work m will be water (ice or liquid), hydrate, gas (hydrate former phase as gas, liquid or supercritical) and adsorbed. Index k will be H<sub>2</sub>O and any other component that distributes over the phases m. This also include possible thermodynamic inhibitors. Fugacity  $f_k^m$  is defined for each component as:

$$d\mu_k^m(T, P, \vec{x}) = RTd \ln f_k^m(T, P, \vec{x}) \quad (1)$$

R is the universal gas constant, T is temperature and P is pressure. Equation (1) is merely a difference equation that requires a reference state. With ideal gas as reference state Equation (1) can be integrated in two steps to:

$$\begin{aligned} \mu_k^{idealgas,mix}(T, P, \vec{x}) - \mu_k^{idealgas,pure}(T, P, \vec{x}) \\ = RT \ln \frac{x_k P}{P} = RT \ln x_k \end{aligned} \quad (2)$$

$$\begin{aligned} \mu_k^m(T, P, \vec{x}) - \mu_k^{idealgas,mix}(T, P, \vec{x}) \\ = RT \ln \frac{f_k^m(T, P, \vec{x})}{x_k P} = RT \ln \phi_k^m(T, P, \vec{x}) \end{aligned} \quad (3)$$

Equations (1)–(3) give two routes to residual thermodynamic description of a phase:

$$\mu_k^m(T, P, \vec{x}) = \mu_k^{idealgas,pure}(T, P, \vec{x}) + RT \ln [x_k \phi_k^m(T, P, \vec{x})] \quad (4)$$

$$f_k^m(T, P, \vec{x}) = x_k \phi_k^m(T, P, \vec{x}) P \quad (5)$$

In the original derivation by van der Waal and Platteeuw [2] the water lattice were assumed to be rigid while a later derivation (Kvamme & Tanaka [4]) permitted movement of the water molecules in the lattice. This latter approach made it possible to investigate the effect of guest movements on the water lattice by using a different evaluation for the impact of the guest movements. The treatment of guest molecule movements in the cavity as a harmonic oscillating spring, from minimum energy state in a molecular dynamics study [4] provides insight into hydrate destabilization effects due to size and mass.

$$\mu_{H_2O}^H = \mu_{H_2O}^{O,H} - \sum_{k=1,2} RTv_k \ln \left( 1 + \sum_i h_{ki} \right) \quad (6)$$

$\mu_{H_2O}^{O,H}$  is the chemical potential for water in an empty clathrate. Number of cavities is  $\nu$ , with subscripts  $k$  for large and small cavities, respectively. For structure I, which is the main focus here,  $\nu_{\text{large}} = 3/24$  and  $\nu_{\text{small}} = 1/24$ . Within the scope of this work we will assume that only one guest molecule can enter a cavity. The harmonic oscillator approach model can be expressed as:

$$h_{ki} = e^{\beta[\mu_{ki} - \Delta g_{ki}]} \quad (7)$$

Chemical potential for molecule type  $i$  in cavity type  $k$ . We will assume that small and large cavities are at equilibrium so that:

$$\mu_{\text{large}i} = \mu_{\text{small}i} \quad (8)$$

For a system at equilibrium then the chemical potential for a guest molecule in a cavity is equal to the chemical potential for the same molecule in the equilibrium phase.  $\Delta g_{ki}$  is the Gibbs free energy change for inclusion for guest molecule  $i$  in a cavity of type  $k$ .

The most classical example is a hydrate former phase (gas, liquid, supercritical) in contact with liquid (or ice) water that form a hydrate. For these three phases there are 12 independent thermodynamic variable, 3 conservation laws and 8 conditions of equilibrium. As is trivially known we can then fix one independent thermodynamic variable, commonly  $T$  or  $P$ . For this particular case equation of equilibrium we have:

$$h_{ki} = e^{\beta[\mu_i^{\text{gas}}(T,P,\vec{x}) - \Delta g_{ki}]} \quad (9)$$

For the equilibrium between the gas and the hydrate.

$$\mu_i^{\text{gas}}(T,P,\vec{x}) = \mu_i^{\text{pure,ideal gas}}(T,P,\vec{x}) + RT \ln[x_i \phi_i(T,P,\vec{x})] \quad (10)$$

In the classical formulation of van der Waal & Platteeuw [3], an alternative formulation for (9) for a rigid water lattice is:

$$h_{ki} = f_i^{\text{gas}}(T,P,\vec{x}) C_{ki}(T) = x_i \phi_i(T,P,\vec{x}) P C_{ki}(T) \quad (11)$$

The Langmuir constant  $C_{ki}(T)$  for a molecule  $i$  in cavity  $k$  and given below as Equation (12). For a molecule like methane the results from (9) and (11) are almost the same while smaller molecules such as  $N_2$  are better represented by (11). For a large molecules like  $CO_2$  the difference in impact on water hydrate chemical potential, Equation (6), is one kJ/mole since the movements of  $CO_2$  interferes with some water lattice librations. In the simplest case of a monoatomic spherical guest molecules the Langmuir constant is a simple integral over the Boltzmann factors of interaction energies between the guest molecule and surrounding waters.

$$C_{ki}(T) = \frac{1}{k_B T} \iiint e^{\beta[\varphi_{iw}(x,y,z)]} dx dy dz \quad (12)$$

For nonlinear multi-atomic representations of guest molecules the integration will involve rotational degrees of freedom. Guest-guest interactions between guest in different are also significant [5]. Polar guest molecules such as  $H_2S$  will also get extra stabilization from coulombic interactions between the partial charges in  $H_2S$  and water molecules in the cavity lattice [6]. For  $CO_2$ , on the other hand, the quadrupole moment will result in a destabilization effect [6]. However, for now Equation (12) serves as sufficient illustration. Various simplifications of (12) can be found in [2].

The most common guest/water interaction model in present versions hydrate equilibrium codes based of the reference method is based on a spherically smeared out version of the Kihara potential for interactions between a water and a guest. The Kihara potential can be expressed as:



$$\phi_{ij}(r_{ij}) = \varepsilon_{ij} \left[ \left( \frac{\sigma_{ij}}{r_{ij} - a_{ij}} \right)^{12} - \left( \frac{\sigma_{ij}}{r_{ij} - a_{ij}} \right)^6 \right] \quad (13)$$

$i$  and  $j$  are molecular indexes while  $r_{ij} - a_{ij}$  is the closest distance between the two molecules.  $\sigma_{ij}$  is a molecular diameter and  $\varepsilon_{ij}$  is a well-depth. For  $a_{ij}$  equal to zero (13) reduces to the Lennard–Jones 12-6 potential which we and many others have utilized in various studies. See for instance references [4–6]. A summation of pairwise interactions in Equation (12) is possible and integration can be conducted efficiently using a Monte Carlo approach [5,6], but it is more common to use an integrated smeared interaction version in which the average water/guest interaction are smeared out over the surface of a spherically smoothed cavity radius  $R$  with  $z$  being the number of waters represented in this spherical shell.  $Z$  is therefore 20 for small cavity and 24 for large cavity. The details of this integration to reach at the spherically smoothed potential is far too extensive to include here. See reference [2] for more details and further references. The final result is for each specific cavity  $k$  is:

$$\varphi_{iw}(r) = 2Z_k \varepsilon_{iw} \left[ \frac{\sigma_{iw}^{12}}{R_k^{11} r} \left( \Delta^{10} + \frac{a_{iw}}{R_k} \Delta^{11} \right) - \frac{\sigma_{iw}^6}{R_k^5 r} \left( \Delta^4 + \frac{a_{iw}}{R_k} \Delta^5 \right) \right] \quad (14)$$

$$\Delta^N = \frac{1}{N} \left[ \left( 1 - \frac{r}{R_k} - \frac{a_{iw}}{R_k} \right)^{-N} - \left( 1 - \frac{r}{R_k} - \frac{a_{iw}}{R_k} \right)^N \right] \quad (15)$$

The spherically symmetric integration version of (12) can then be expressed as:

$$C_{ki}(T) = \frac{4\pi}{k_B T} \int_0^\infty e^{\beta[\varphi_{iw}(x,y,z)]} r^2 dr \quad (16)$$

Some Kihara parameters for the smoother cavity approach are listed below in Table 1. These are of course fitted also with specific fitted parameters when the reference approach is used. As such the Kihara parameters in Table 1 should be used with reference parameters published from the same research groups. List of various published reference properties are listed in Table 1 below. Cavity radii published and coordination numbers published by various research groups are listed in Table 2 below.

**Table 1.** A selection of some available Kihara parameters from open literature for some guest molecules that creates structure I hydrate. Mixing rules for unlike molecules (water and specific guest). Mixing rules are the usual Lorentz–Berthelot:  $\sigma_{iw} = 0.5(\sigma_i + \sigma_w)$ ,  $a_{iw} = 0.5(a_i + a_w)$  and  $\varepsilon_{iw} = \sqrt{\varepsilon_i \varepsilon_w}$ .

| Type           | Kihara Parameters |                       |           |          | Reference |
|----------------|-------------------|-----------------------|-----------|----------|-----------|
|                | $\sigma_g^*$ (Å)  | $\varepsilon_g/k$ (K) | $a_g$ (Å) | $\omega$ |           |
| Methane        | 3.565             | 227.13                | 0.283     | 0.007    | [7]       |
|                | 3.2398            | 153.17                | 0.300     |          | [3]       |
|                | 3.501             | 197.39                | 0.260     | 0.000    | [8,9]     |
|                | 3.1695            | 154.1815              | 0.3834    |          | [10]      |
|                | 3.102             | 161.368               | 0.3834    |          | [11]      |
|                | 3.0367            | 151.7117              | 0.3864    |          | [12]      |
|                | 3.2512            | 153.69                | 0.2950    |          | [13]      |
| Carbon Dioxide | 3.760             | 424.16                | 0.615     |          | [7]       |
|                | 2.9681            | 169.09                | 0.360     |          | [3]       |
|                | 3.407             | 506.25                | 0.677     | 0.225    | [8,9]     |
|                | 2.9040            | 171.97                | 0.7530    |          | [13,14]   |

Table 1. Cont.

| Type                            | Kihara Parameters |                       |           |          | Reference |
|---------------------------------|-------------------|-----------------------|-----------|----------|-----------|
|                                 | $\sigma_g^*$ (Å)  | $\varepsilon_g/k$ (K) | $a_g$ (Å) | $\omega$ |           |
| Ethane                          | 3.4315            | 183.32                | 0.000     |          | [14]      |
|                                 | 4.433             | 202.52                | 0.000     |          | [7]       |
|                                 | 3.3180            | 174.97                | 0.400     |          | [3]       |
|                                 | 4.036             | 393.2                 | 0.574     |          | [8,9]     |
|                                 | 3.3404            | 180.0164              | 0.5651    |          | [10]      |
|                                 | 3.2819            | 164.4899              | 0.5655    |          | [12]      |
| H <sub>2</sub> O of Structure I | $\sigma_w$ (Å)    | $\varepsilon_w/k$ (K) | $a_w$ (Å) |          | [8,9]     |
|                                 | 3.56438           | 102.134               | 0         |          |           |

Table 2. Average smoothed lattice properties of structure I gas hydrates.

| Coordination Number             |   | Average Cavity Radius (Å)       |   | References |
|---------------------------------|---|---------------------------------|---|------------|
| Small Cavity (5 <sup>12</sup> ) | Large Cavity (5 <sup>1,2</sup> 6 <sup>2</sup> ) | Small Cavity (5 <sup>12</sup> ) | Large Cavity (5 <sup>1,2</sup> 6 <sup>2</sup> ) |            |
| 20                              | 24  | 3.95                            | 4.30  | [1]        |
| 20                              | 24  | 3.875                           | 4.152   | [15]       |
| 20                              | 24  | 3.875                           | 4.30  | [16]       |
| 20                              | 24  | 3.94                            | 4.30  | [17]       |
|                                 |   | 3.94                            | 4.30  | [18]       |
| 20                              | 24  | 3.95                            | 4.33  | [2,19,20]  |
|                                 |   | 3.95                            | 4.33  | [11]       |
| 20                              | 24  | 3.95                            | 4.30  | [21]       |

In order to complete the equilibrium calculation for hydrate formation between gas, liquid water and hydrate the symmetric excess formulation of water chemical potential is:

$$\mu_{H_2O}^{water}(T, P, \vec{x}) = \mu_{H_2O}^{pure, H_2O}(T, P) + RT \ln [x_{H_2O} \gamma_{H_2O}(T, P, \vec{x})] \quad (17)$$

$$\lim [\gamma_{H_2O}(T, P, \vec{x})] = 1.0 \text{ when } x_{H_2O} \text{ approaches unity}$$

$\gamma_{H_2O}$  is the activity coefficient of the liquid water as function dissolved hydrate formers as well as additives like methanol and salt. One approach for solving the equilibrium for water is based on residual thermodynamics also for hydrate. For a well defined activity of water according to impacts of solutes the solution of Equation (17) is feasible because liquid water chemical potential as well as empty hydrate chemical potential is known from molecular dynamics simulations and verified in many publications. Some recent examples are [22–30].

$$\mu_{H_2O}^{water}(T, P, \vec{x}) = \mu_{H_2O}^H(T, P, \vec{x}) \quad (18)$$

With known gas composition and a model for the gas fugacity coefficient, we have utilized the SRK [31] equation of state in a number of recent publications. Equations (6) and (17) in (18) can be solved for T if a pressure is given or alternatively for P when temperature is given.

In the absence of data for liquid water chemical potential and water chemical potential for water in empty clathrate of either structure of hydrate Equations (6) and (17) in (18) can be reformulated to:

$$\begin{aligned} \mu_{\text{H}_2\text{O}}^{\text{pure,H}_2\text{O}}(T, P) - \mu_{\text{H}_2\text{O}}^{\text{O,H}}(T, P) = \Delta\mu_{\text{H}_2\text{O}}(T, P) = \\ - \sum_{k=1,2} RTv_k \ln\left(1 + \sum_i h_{ki}\right) - RT \ln[x_{\text{H}_2\text{O}} \gamma_{\text{H}_2\text{O}}(T, P, \vec{x})] \end{aligned} \quad (19)$$

In which either (9) or (11) can be utilized to calculate the cavity partition functions for small and large cavity fillings of the various guest molecules in the system.

Equation (19) is hereafter denoted as the reference method. Direct iterative solution of Equation (18) using chemical potentials for pure liquid water (or ice) as well as empty clathrate water chemical potential in (6) from Kvamme & Tanaka [4] is now the residual thermodynamic method. The chemical potential difference in (19) is typically fitted towards experimental data through the following parameters:

$$\Delta\mu_{\text{H}_2\text{O}}(T_0, P_0) \quad (20)$$

$$\frac{\partial \left[ \frac{\Delta\mu_{\text{H}_2\text{O}}(T, P)}{RT} \right]_{P, N}}{\partial T} = - \left[ \frac{\Delta H_{\text{H}_2\text{O}}(T, P)}{RT^2} \right] \quad (21)$$

$\Delta H_{\text{H}_2\text{O}}(T, P)$  is the enthalpy difference between liquid water enthalpy and empty hydrate water enthalpy.

$$\Delta H_{\text{H}_2\text{O}}(T, P) = \Delta H_{\text{H}_2\text{O}}(T_0, P_0) + \int_{T_0}^T \Delta C p_{\text{H}_2\text{O}}(T) dT + \Delta V_{\text{H}_2\text{O}}(P - P_0) \quad (22)$$

$\Delta C p_{\text{H}_2\text{O}}(T)$  is the specific heat capacity difference between liquid water and empty hydrate for the specific structure in consideration.

Liquid water density does not change much over the limited range of liquid water temperatures for hydrate stability. There is a slight temperature dependency in the hydrate lattice constant [32], but not substantial so a constant  $\Delta V_{\text{H}_2\text{O}}$  in (22) is fair enough, as also indicated in the equation.

In summary the reference approach needs fitted values for (20),  $\Delta H_{\text{H}_2\text{O}}(T_0, P_0)$ , two parameters for  $\Delta C p_{\text{H}_2\text{O}}(T)$  with a linear dependency approximation. Moreover, finally  $\Delta V_{\text{H}_2\text{O}}$ . Altogether 5 parameters that needs to be fitted.

Some selected values from open literature for the parameters discussed above is listed in Table 3 below. There may be many more since the various groups using this method may not always publish their fitted values.

**Table 3.** Selected parameters for reference properties from open literature (Structure I at 273.15 K and 1 bar).

| $\Delta\mu_{\text{H}_2\text{O}}(T_0, P_0)$<br>(J·mol <sup>-1</sup> ) | $\Delta H_{\text{H}_2\text{O}}(T, P)$<br>(J·mol <sup>-1</sup> ) | $\Delta C p_{\text{H}_2\text{O}}(T)$<br>(J·mol <sup>-1</sup> ·K <sup>-1</sup> )      | $\Delta V_{\text{H}_2\text{O}}$<br>(cm <sup>3</sup> ·mol <sup>-1</sup> ) | Reference |
|--|---|--|--|-----------|
| 699  | 0 in ice  |  | 3.0 in ice   | [1]       |
| 1264.172   | 1151.15 in ice;<br>-6012.3518 in liquid water                   | -38.13446 +<br>0.14065(T-273.1)  | 3.0 in ice   | [3]       |
| 1235   | 1684 in ice;<br>-4328 in liquid water                           | -37.32 + 0.179(T-273.15),<br>T > 273.15;<br>0.565 + 0.002(T-273.15),<br>T < 273.15   |  | [33]      |
| 1297   | 1389 in ice   |  |  | [34]      |
| 1120   | 1714 in ice;<br>-4297 in liquid water                           | -34.583 + 0.189(T-273.15),<br>T > 273.15;<br>3.315 + 0.0121(T-273.15),<br>T < 273.15 | 2.9959 in ice;<br>4.5959 in liquid water                                 | [8]       |
| 1299.4   | 1861 in ice   | -37.32   |  | [35]      |

Table 3. Cont.

| $\Delta\mu_{H_2O}(T_0, P_0)$<br>(J·mol <sup>-1</sup> ) | $\Delta H_{H_2O}(T, P)$<br>(J·mol <sup>-1</sup> ) | $\Delta C_{p_{H_2O}}(T)$<br>(J·mol <sup>-1</sup> ·K <sup>-1</sup> )                  | $\Delta V_{H_2O}$<br>(cm <sup>3</sup> ·mol <sup>-1</sup> ) | Reference    |
|--|---|--|--|--------------|
| 1291   | 1451 in ice                                       | 0.65   |  | [36]         |
| 1120   | 1714 in ice;<br>-4297 in liquid water             | -34.583 + 0.189(T-273.15),<br>T > 273.15;<br>3.315 + 0.0121(T-273.15),<br>T < 273.15 | 2.9959 in ice;<br>4.5959 in liquid water                   | [9,17]       |
| 1287   | 931 in ice  | 0  |  | [37]         |
| 1264   | 1151 in ice;<br>-4858 in liquid water             | 39.16  | 3.0 in ice;<br>4.6 in liquid water                         | [38]         |
| 1287   | -5081.35 in liquid water                          | -38.12   | 4.6 in liquid water  | [11]         |
| 1264   | 1151 in ice;<br>-6011 in liquid water             |  | 3.0 in ice;<br>4.6 in liquid water                         | [21]         |
| 1297   | 1389 in ice;<br>-4620.5 in liquid water           | -37.32 + 0.179(T-273.15),<br>T > 273.15;<br>0.565 + 0.002(T-273.15),<br>T < 273.15   | 3.0 in ice;<br>4.601 in liquid water                       | [3,13,33,34] |

In addition to the fitting of fundamental thermodynamic properties the interaction energies between water and guest molecules typically involves fitting of three parameters in a Kihara type of potential for each guest molecule in each type of cavity for the integral in Equation (12). These integrations are normally conducted over a spherically smoothed cavity. See for instance Sloan's book [2]. While the small cavity of structure I is symmetric the large cavity in structure I is asymmetric and on average non-spherical due to the two hexagonal faces.

#### 4. Hydrate Stability Limits in the Pressure–Temperature Projection of Independent Thermodynamic Variable

For one hydrate former and liquid water distributed over 3 phases the number of independent thermodynamic variables are 12 and the sum of conservation laws and conditions of equilibrium is 11. Equilibrium is therefore only possible if one thermodynamic variable is defined. For given temperatures we can therefore solve conditions of equilibrium according to (18) using either the residual thermodynamic scheme or the reference scheme. For the latter alternative we could only find CSMHYD [39] as an open source to compare with, along with experimental data. A comparison is plotted in Figure 1 for CH<sub>4</sub> hydrate. A comparison for CO<sub>2</sub> hydrate is plotted in Figure 2. A comparison between calculated stability limits for a mixture of CO<sub>2</sub> and CH<sub>4</sub> is plotted in Figure 3 and compared to experimental data from open literature. Note that CSMHYD do not estimate the phase transition over to more dense CO<sub>2</sub> phase.

Even if another hydrate former is added so that Gibbs phase rule is achieved it does not mean that the system can reach equilibrium. The reason is three-fold:

- (1) More than one hydrate phase forms due to formation from separate hydrate former and water plus hydrate forming from dissolved hydrate former in water or hydrate former adsorbed on minerals;
- (2) Even for hydrate forming from a separate hydrate former phase and water the various components have different desires to adsorb on liquid water. This depends on the the interaction between each of the hydrate formers and water, as well as the thermodynamic state of the various hydrate formers. In a mixture of CH<sub>4</sub> and CO<sub>2</sub> then CH<sub>4</sub> is supercritical and CO<sub>2</sub> is subcritical. See for instance Kvamme [22] for an illustration of these aspects;

For one hydrate former and liquid water over 3 phases the number of independent thermodynamic variables are 12 and the sum of conservation laws and conditions of equilibrium is 11. Equilibrium is therefore only possible if one thermodynamic variable is defined. For given temperatures we can therefore solve conditions of equilibrium according to (18) using either the residual thermodynamic scheme or the reference scheme. For the latter alternative we could only find CSMHYD [39] as an open source to compare with, along with experimental data. A comparison is plotted in Figure 1 for CH<sub>4</sub> hydrate. A comparison for CO<sub>2</sub> hydrate is plotted in Figure 2. A comparison for CH<sub>4</sub> hydrate formed from CO<sub>2</sub> gas and liquid water is plotted in Figure 3. The combined first and second stability conditions will be used in the next section to find formation and the most stable hydrate first, under conditions of constant T, P and composition. Then the rate will be phase transition to hydrate on cooling.

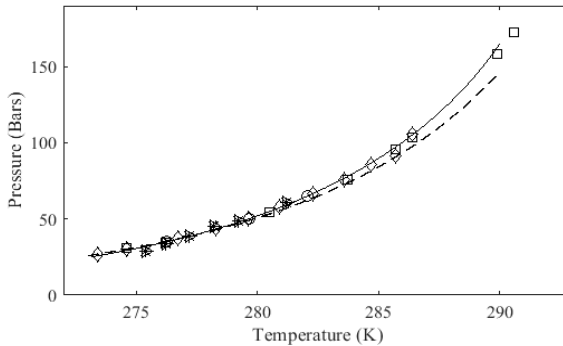


Figure 1. Hydrate formation from liquid water and CH<sub>4</sub> gas, calculated equilibrium for CH<sub>4</sub> hydrate from this work (solid) than CSMHYD (dashed line) [39] and experimental data from Nakamura et al. [40] (□), Service & Englezos [41] (○) and Mohammadi et al. [42] (◇), Takore & Holder [43] (△) and Arisawa et al. [44] (○).  
Sustainability 2020, 12, x FOR PEER REVIEW 10 of 30

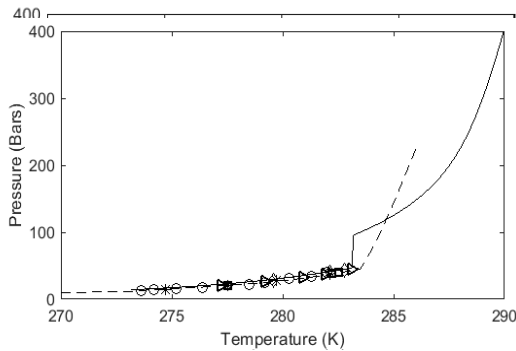


Figure 2. Calculated equilibrium curve for CO<sub>2</sub> hydrate from this work (solid) as compared with CSMHYD (dashed line) [39] and experimental data from Mohammadi et al. [40] (◇), Fan & Guo [45] (○), (●), Ng & Robinson [46] (○), Fan et al. [47] (△), Unruh & Katz [48] (○), Ng & Robinson [46] (○), Fan et al. [47] (△), Unruh & Katz [48] (○).

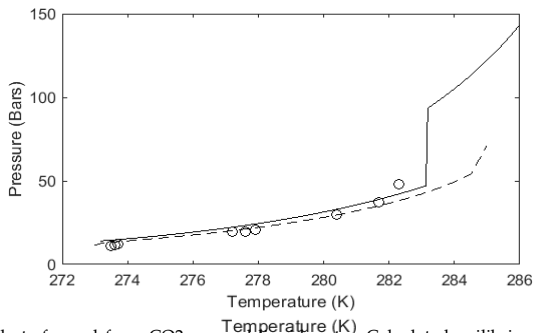
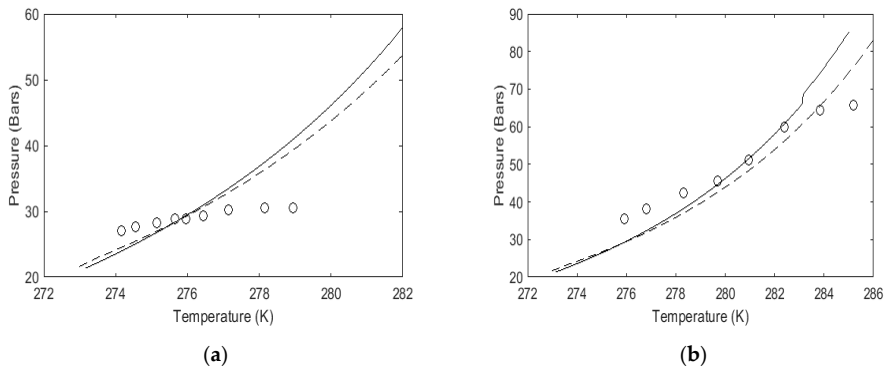


Figure 3. CH<sub>4</sub> hydrate formed from CO<sub>2</sub> gas and liquid water. Calculated equilibrium curve for 3.46% CH<sub>4</sub> + 96% CO<sub>2</sub> hydrate from this work (solid) as compared with CSMHYD (dashed line) [39] and experimental data from Fan and Guo (1999) [45] (circles).

Even if another hydrate former is added so that Gibbs phase rule is achieved it does not mean that the system can reach equilibrium. The reason is three fold: (1) More than one hydrate phase forms due to formation from separate hydrate former and water minerals;

These aspects are illustrated in Figure 4. Each of these two figures is a combination of two equilibrium calculations and results from dynamic experiments published by Lequang et al. [49]. The experimental data point is obtained using two crystallization methods. High rate means that the experiment is started with high supersaturation. This can be a high  $\Delta P$  above hydrate stability limit  $P$  for a defined temperature. Or it can be large  $\Delta T$  below hydrate stability  $T$  for a fixed pressure. The results from high rate experiment is plotted in Figure 4a together with equilibrium data from this work and from GEMHYD. Low rate experimental data are plotted in Figure 4b with equilibrium calculations. For details on the experiments and timeline for pressure/temperature developments the reader is directed to the original study of Lequang et al. [49]. In this context the qualitative aspects are the most important.



**Figure 4.** Hydrate formed from mixed gas and liquid water: (a) (Ca) Critical equilibrium conditions for slow crystallization of 0.95%  $\text{CH}_4$  + 0.03%  $\text{CO}_2$  + 0.02%  $\text{C}_2\text{H}_6$  at 190 bar; (b) Critical equilibrium conditions for fast crystallization of 0.93%  $\text{CH}_4$  + 0.03%  $\text{CO}_2$  + 0.04%  $\text{C}_2\text{H}_6$  at 190 bar. (Solid) results from GEMHYD; (Dashed) parallel experimental data from Lequang et al. [49]; (Open circles) experimental data from Lequang et al. [49]; (Solid lines) equilibrium calculations from this work; (Dashed lines) equilibrium calculations from GEMHYD.

High thermodynamic driving force with the mass transfer impact of pores (2) and (3) is critical for  $\text{CaFC}$  in 305 and 487 bars and for the critical point is at 304 bar and 73 bar/73 bar relative driving force for formation of stable  $\text{CaFC}$  and  $\text{CO}_2$  the supercritical critical conditions in the transition from non-hydrate to hydrate phase is the quadrupole moment of  $\text{CO}_2$  or  $\text{CO}$  is a factor in the interaction with water in the adsorption sites on water molecules for hydrate formation in natural hydrate formation hydrate formation of  $\text{CaFC}$  and  $\text{CO}_2$  hydrate formation than the hydrate crystallization in Figure 4b. Not that a long period of almost invariable response in experiments in the nucleation but the slope transport through hydrate films and thermodynamically controlled rearrangements of hydrate films between hydrate formation phase and water. See for instance Figure 3b and Figure 3c and for discussion on nucleation times and critical sizes for all 2800  $\text{CO}_2$  hydrates in critical diameters and critical scale diameters and associated nucleation times in the order of nanoseconds. In the nucleation time scale in the order of nanoseconds hydrates in nature or industry can never reach full thermodynamic equilibrium because there are two main nature phases of relevance for hydrate formation and dissociation: separate fluid phase liquid water and separate mineral surface hydrate and hydrate phase solution. Separate fluid phase liquid water is applied down full balance of independent thermodynamic variables, whereas separate hydrate and water applications for equilibrium is independent and determined by the exact state for formation of hydrate from dissociation of hydrate can be mathematically speaking for a definite formation of hydrate phase as all the hydrate water will have different composition, different density and different Gibbs free energy. By the thermodynamic definition they are therefore all different phases. This can be seen by looking at how the cavity partition function relate to cavity fillings and corresponding mole-fractions in hydrate. In a non-equilibrium system there is no rule that says that chemical potential is the same for all components in all phases. In contrast to an equilibrium system the phase distribution in a non-equilibrium system is determined by point (3) above. Moreover, then also the distribution of each component in each phase related to a unique chemical potential for each components in each

is no rule that says that chemical potential is the same for all components in all phases. In contrast to an equilibrium system the phase distribution in a non-equilibrium system is determined by point (3) above. Moreover, then also the distribution of each component in each phase related to a unique chemical potential for each components in each phase locally.

$$\theta_{ki} = \frac{h_{ki}}{1 + \sum_j h_{kj}} \quad (23)$$

$\theta_{ki}$  is the filling fraction of component  $i$  in cavity type  $k$

$$x_i^H = \frac{\theta_{large,i} v_{large} + \theta_{small,i} v_{small}}{1 + \theta_{large,i} v_{large} + \theta_{small,i} v_{small}} \quad (24)$$

$v$  is fraction of cavity per water. Subscripts large or small means large and small cavity, respectively and  $i$  is a guest component index. Corresponding mole-fraction water is then given by:

$$x_{H_2O}^H = 1 - \sum_i x_i^H \quad (25)$$

The associated hydrate Gibbs free energy is then:

$$G^{(H)} = x_{H_2O}^H \mu_{H_2O}^H + \sum_i x_i^H \mu_i^H \quad (26)$$

## 5. Hydrate Stability Limits in the Projection of Hydrate Former Concentration in Surrounding Water

Formation of hydrate from solution is possible in between the solubility limit of the actual guest molecule(s) in water and a lower limit of hydrate stability as function of concentration of the same solutes in water. (18) still applies, but for a defined set of  $T$  and  $P$  the mole-fraction of hydrate former in the water solution outside the hydrate is now the unknown variable to be solved for in terms of hydrate stability. The actual mole-fraction found in the lower concentration limit for hydrate stability towards water containing hydrate former(s). The relevant version of (6) is now:

$$h_{ki} = e^{\beta[\mu_i^{aqueous}(T,P,\vec{x}) - \Delta g_{ki}]} \quad (27)$$

in which the superscript aqueous denote chemical potential for the actual hydrate former dissolved in water. For hydrate formers of limited solubility the asymmetric excess convention is the most appropriate to use:

$$\mu_i^{aqueous}(T,P,\vec{x}) = \mu_i^\infty(T,P,\vec{x}) + RT \ln[x_i \gamma_i^\infty(T,P,\vec{x})] \quad (28)$$

$$\mu_{CH_4}^{\infty,Residual} = 3.665 + \frac{40.667}{T_R} - \frac{48.860}{T_R^2} \quad (29)$$

The associated ideal gas chemical potential is trivially given by the temperature and the density of the molecule at infinite dilution in water. We have used experimental data for the infinite dilution of methane in liquid water. This is almost constant for variation of pressure and limited dependent on temperature for the relevant conditions. Parameters for the fitted model of activity coefficients are given in Table 4 for Equation (30).

$$\ln \gamma_{CH_4}^\infty(T,P,\vec{x}) = \sum_{i=1,2}^{39} \left[ a_0(i) + \frac{a_1(i+1)}{T_R} \right] (x_{CH_4})^{[0.05 + \frac{i-1}{30}]} \quad (30)$$

**Table 4.** Parameters for Equation (30).

| <i>I</i> | <i>a</i> <sub>0</sub> | <i>a</i> <sub>1</sub> | <i>I</i> | <i>a</i> <sub>0</sub> | <i>a</i> <sub>1</sub> | <i>i</i> | <i>a</i> <sub>0</sub> | <i>a</i> <sub>1</sub> |
|----------|-----------------------|-----------------------|----------|-----------------------|-----------------------|----------|-----------------------|-----------------------|
| 1        | 1.360608              | 3.796962              | 15       | 11.580192             | 16.384626             | 29       | 23.855418             | 31.720767             |
| 3        | 0.033630              | 0.703216              | 17       | 0.087295              | 13.171333             | 31       | 35.125907             | 37.064849             |
| 5        | 0.656974              | 12.441339             | 19       | 0.558793              | 13.556732             | 33       | 33.675110             | 41.544360             |
| 7        | 1.763890              | 21.119318             | 21       | 23.753020             | 16.573197             | 35       | 27.027285             | 57.609882             |
| 9        | 5.337858              | 33.298760             | 23       | 10.128675             | 13.591099             | 37       | 19.026786             | 54.961702             |
| 11       | 0.024750              | 12.387276             | 25       | −41.212178            | 5.060082              | 39       | 37.872252             | 57.204781             |
| 13       | 48.353808             | 17.261174             | 27       | −31.279868            | 31.289978             |          |                       |                       |

For CO<sub>2</sub>, a slightly different approach is utilized. The density of CO<sub>2</sub> as dissolved in water will correspond to the partial molar volume of CO<sub>2</sub> at infinite dilution. The infinite dilution ideal gas chemical potential is not very sensitive to pressure, so the following approximation to only temperature dependency is considered as adequate:

$$\mu_{\text{CO}_2}^{\infty, \text{ideal gas}} = -130.006 + \frac{163.818}{T_{0,R}} - \frac{64.898}{T_{0,R}^2} \quad (31)$$

where  $T_{0,R}$  is 273.15 K divided by the actual temperature. Equation (31) does not apply to temperatures above 303 K due to the limited range of temperatures for which infinite partial molar volumes are used and for temperatures above 273.15 K.

The fugacity coefficient for CO<sub>2</sub> in water is fitted using the following function:

$$\ln \phi_{\text{CO}_2}^{\text{water}}(T, P, \vec{x}) = \sum_{i=1,2}^{39} \left[ a_0(i) + \frac{a_1(i+1)}{T_R} \right] (x_{\text{CO}_2})^{[0.05 + \frac{i-1}{40}]} \quad (32)$$

where  $T_R$  is reduced temperature and defined as actual  $T$  in Kelvin divided by critical temperature for CO<sub>2</sub> (304.35 K). The lower summation 1, 2 indicates starting from 1 and counting in steps of 2. Parameters are given in Table 5 below. The vector sign on mole-fraction  $x$  denote mole-fractions and any arrow on top of  $x$  denote the vector of all mole-fractions in the actual phase.

**Table 5.** Parameters for Equation (32).

| <i>I</i> | <i>a</i> <sub>0</sub> | <i>a</i> <sub>1</sub> | <i>I</i> | <i>a</i> <sub>0</sub> | <i>a</i> <sub>1</sub> | <i>i</i> | <i>a</i> <sub>0</sub> | <i>a</i> <sub>1</sub> |
|----------|-----------------------|-----------------------|----------|-----------------------|-----------------------|----------|-----------------------|-----------------------|
| 1        | −139.137483           | −138.899061           | 15       | 80.411175             | 88.536302             | 29       | 60.126698             | 64.683147             |
| 3        | −76.549658            | −72.397006            | 17       | 82.710575             | 90.262518             | 31       | 54.782421             | 58.865478             |
| 5        | −20.868725            | −14.715982            | 19       | 82.017332             | 89.094887             | 33       | 49.592998             | 53.235844             |
| 7        | 18.030987             | 24.548835             | 21       | 79.373137             | 85.956670             | 35       | 44.500001             | 47.728622             |
| 9        | 44.210433             | 52.904238             | 23       | 75.429910             | 81.519167             | 37       | 39.869990             | 42.730831             |
| 11       | 63.353037             | 71.596515             | 25       | 70.680932             | 76.270320             | 39       | 35.597488             | 38.125674             |
| 13       | 74.713278             | 82.605791             | 27       | 65.490785             | 70.551406             |          |                       |                       |

The chemical potential for CO<sub>2</sub> that applies to Equations (23) for an equilibrium case is then given as:

$$\mu_{\text{CO}_2}^{\text{aqueous}}(T, P, \vec{y}) = \mu_{\text{CO}_2}^{\infty, \text{ideal gas}}(T, P, \vec{y}) + RT \ln [x_{\text{CO}_2} \phi_{\text{CO}_2}(T, P, \vec{x})] \quad (33)$$

Since the chemical potential of CO<sub>2</sub> is not necessarily the same for dissolved CO<sub>2</sub> in water and CO<sub>2</sub> in gas (or liquid) in a non-equilibrium situation, then hydrate formed according to Equation (2)



will be different from the first hydrate and accordingly denoted H<sub>2</sub>. The composition of this hydrate will be different as seen from the corresponding compositions, which follows from Equations (23)–(25).

Some comparisons with experimental data from Yang et al. [50] are shown in Figure 4 for CH<sub>4</sub>. These comparisons are not directly representative due to the experimental setup and how the experiments are conducted. Furthermore, note that there is a very small pressure dependency in the calculated stability limits, but hardly visible on the scales in Figure 5. These curves are stability limits between two condensed phases. There is a very small Poynting correction on the liquid side and a small Poynting correction on the hydrate side these will almost cancel. The partial molar volume of water in hydrate is slightly larger than partial molar volume of liquid water, but the impact is not visible over the range of pressures in Figure 5a,b. It is also important to keep in mind that all these calculations are pure predictions. Parameters in the cavity Gibbs free energy of inclusions are derived from molecular dynamics and stability limits in the temperature pressure projection of the stability limit window.

For practical purposes of stability limits towards forming water through fractures in sediment and associated associated diagenetic or kinetic of methane hydrate the calculated curves can serve as a rough guide for the purpose and the actual values related to the experiments are fairly uncertain. Another dimension of this is that the hydrate stability window between solubility contour and lowest limit of hydrate stability which is plotted in the figures for the points 278.1 K and 278.2 K are due to the red color of the hydrate stability and the yellow color of the solubility.

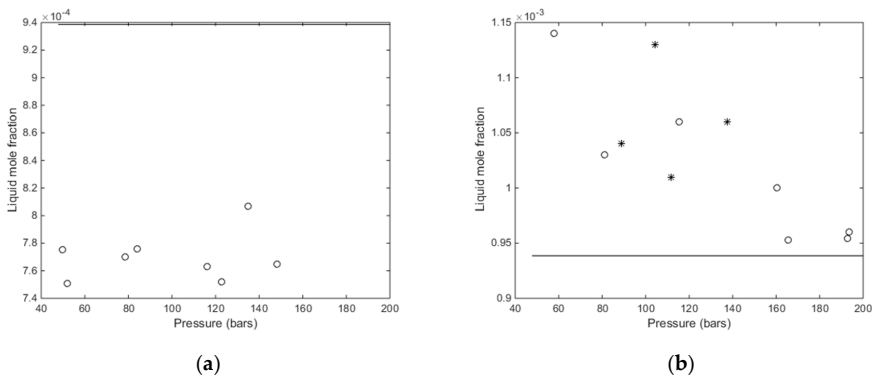


**Figure 5.** (a) Calculated lowest limit mole-fraction of CH<sub>4</sub> in water needed to keep hydrate stable at 273.1 K (solid curve) and experimental data from Yang et al. [50] for 273.1 K (o); (b) calculated lowest limit mole-fraction of CH<sub>4</sub> in water needed to keep hydrate stable at 278.1 K (solid curve) and experimental data from Yang et al. [50] for 278.1 K (o) and 278.2 K (\*).

We could not find any open hydrate codes based on the difference method that can calculate hydrate formation from various concentrations of dissolved hydrate formers in water. These calculations are critical in many natural situations of hydrates in sediments.

Seawater leaking through fractures will lead to hydrate dissociation due to very limited CH<sub>4</sub> in the incoming seawater. This will lead to fluxes of methane bubbling out from the sediments. Two situations can occur, depending on seafloor temperatures and pressures. If temperature and pressure are outside hydrate stability limits then the methane will bubble out through the seawater column in the fracture. Some CH<sub>4</sub> will dissolve and partly be converted through biochemical reactions. If the incoming gas enters hydrate formation conditions of temperature and pressure at the seafloor, then a dynamically unstable situation develops. Hydrate will dissociate towards seawater under saturated with CH<sub>4</sub> from the seafloor side and reform quickly from the reservoir side. This is a complex system in which also the dynamics of biologic consumption of released CH<sub>4</sub> from the top-side can

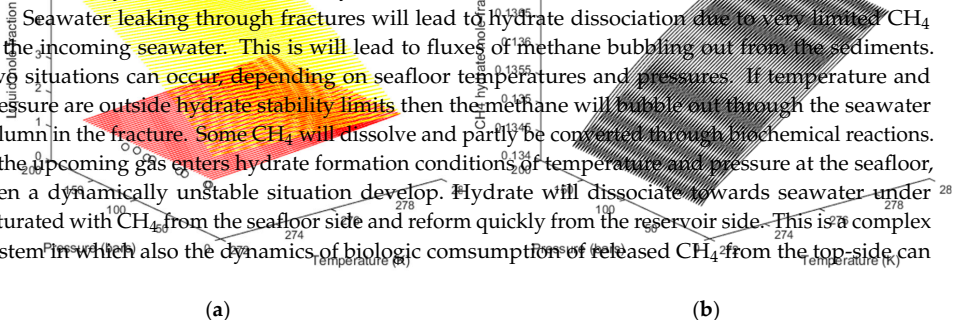


**Figure 6.** (a) Calculated pressure temperature contours of minimum liquid mole-fraction CH<sub>4</sub> mole fraction for hydrate stability (red) and solubility of CH<sub>4</sub> in liquid water (yellow). Experimental data from Yang et al. [50] is plotted as (o)—The values for 278.1 K and 278.2 K are hardly visible here, but can be seen from Figure 6b; (b) mole-fraction CH<sub>4</sub> in hydrate formed from saturated CH<sub>4</sub> in aqueous

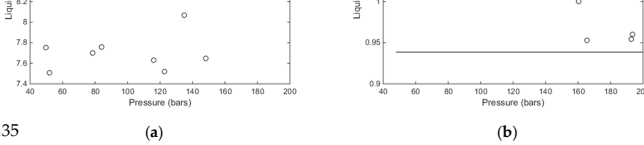


**Figure 5.** (a) Calculated lowest limit mole-fraction of  $\text{CH}_4$  in water needed to keep hydrate stable at 273.16 K (solid curve) and experimental data from Yang et al. [50] for 273.1 K (o); (b) calculated lowest limit mole-fraction of  $\text{CH}_4$  in water needed to keep hydrate stable at 273.1 K (o), 278.1 K (o) and 278.2 K (\*) and experimental data from Yang et al. [50] for 278.1 K (o) and 278.2 K (\*).

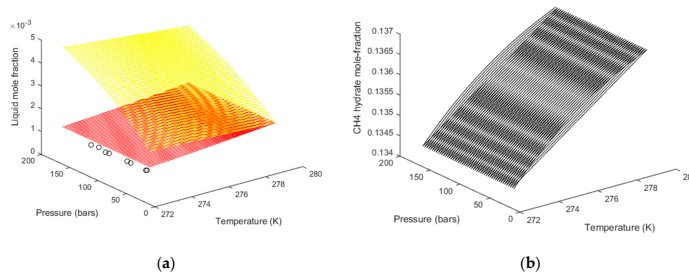


**Figure 6.** (a) Calculated pressure temperature contours of minimum liquid mole-fraction  $\text{CH}_4$  mole fraction for hydrate stability (red) and solubility of  $\text{CH}_4$  in liquid water (yellow). Experimental data from Yang et al. [50] is plotted as (o). The values for 278.1 K and 278.2 K are hardly visible here but can be seen from Figure 6b; (b) mole-fraction  $\text{CH}_4$  in hydrate formed along the minimum hydrate stability limits in Figure 6a (red contour) are slightly higher. Mole-fractions  $\text{CH}_4$  in hydrate formed along the minimum hydrate stability limits in Figure 4a (red contour) are slightly higher.

open hydrate codes based on the difference method that can calculate hydrate formation from various concentrations of dissolved hydrate formers in water. These calculations are critical in many natural situations of hydrates in sediments. In a bigger picture there is a dynamic balance between incoming hydrate formers through fracture systems from below the hydrate formation zones and dissociation of hydrate through fracture systems that brings in seawater from top. If the dissociation flux of hydrate caused by incoming seawater is higher than the flux of new hydrate formation this situation will in the long run lead to depletion of the hydrate. In worst case this can lead to local geo mechanical instabilities and in the worst case landslides.

However, even during hydrate production using for instance pressure reduction hydrate dissociation towards under saturated water can play a significant role. Pumping out water leads to circulation of water from other sections of the sediments through hydrate filled sediments. This incoming water may very well may be water that is under saturated with  $\text{CH}_4$  and as such phase transitions discussed in this section can assist in hydrate dissociation.

Another important aspects of the residual scheme is that all phases are calculated based on ideal gas as reference state. This results in a very transparent comparison of phase stability which is not possible in the same way with the reference scheme, even if specific parameters are used for also being able to calculate phase transitions discussed in this section. Hydrate compositions and free energies calculated from any route discussed above and below are directly comparable in terms of relative stability. Practically this will be a tool for evaluation of which phases that will dissociate first under various changes of conditions. Moreover, even under constant boundary conditions hydrates of higher Gibbs free energy can be consumed in favor of growth of hydrates of lower Gibbs free energy when supply of new mass is limited.

Gibbs free energy minimization methods for calculating most likely phase distribution and associated compositions, is not trivial within a reference scheme model. The difference in reference level between various phases is one challenge. However, there are also several additional challenges and in the final end it boils down to many parameters that are fitted towards pressure temperature stability limit data.

## 6. Thermodynamic Properties

As also discussed above the consistency of free energies for all phases when ideal gas is a universal reference state for all components in all phases is important for calculations of stability limits as well as in kinetic theories on various levels of sophistication, from Classical Nucleation Theory (CNT) [28], Multicomponent Diffuse Interface Theory (MDIT) [51,52], Phase Field Theory (PFT) [53–61] or other

theories derived from statistical mechanics and concepts from Physics. A brief discussion on free energies are discussed in the next section.

Enthalpy changes related to hydrate phase transitions are needed in any concept for production of CH<sub>4</sub> from hydrate. In pressure reduction method the pressure reduction ensures that Gibbs free energy of the system is brought outside of hydrate stability zone, but the enthalpy still has to be primarily supplied from the surrounding formations. Whether the transport capacity and the available heat that can be generated through temperature gradients are sufficient remains to be seen. For the reference method the only possibility is to use the calculated gradients of the pressure temperature in a Clapeyron method as utilized by Anderson [62] or in a simpler scheme as proposed in this work. A much more common approach is the simplified Clausius–Clapeyron which is simplified through neglecting molar volumes of condensed phases. A recently proposed residual thermodynamic scheme for enthalpy calculations [23,63–66] is also discussed in the section Enthalpies below. An advantage of the residual thermodynamic scheme for both Free energies and Enthalpies is also the calculation of consistent entropy changes. This is not a key topic in this work but dynamic entropy generation during various production schemes is an important indicator of production efficiency. This is not a key topic in this work, but dynamic entropy generation during various production schemes is an important indicator of production efficiency.

### 7. Hydrate Free Energies

An important feature of the residual thermodynamic description for all phases is the possibility to compare stability of various hydrates formed from gas/water, dissolved hydrate formers or adsorbed hydrate former and water. As an example we plot Gibbs free energy contours for CH<sub>4</sub> hydrate along the temperature pressure equilibrium curve in Figure 7a below. For comparison we plot free energies of hydrates formed from saturated CH<sub>4</sub> in water solution as function of temperature and pressure in Figure 7b. At the saturation limit contours in Figure 7b the chemical potential of CO<sub>2</sub> in the solution is the same as in the gas. Within the limited range of pressures and temperatures the chemical potential variation for CH<sub>4</sub> is limited and very modest – c.25 kJ/mole. The similar variation for the same range of conditions is only c.30 kJ/mole for the same change of conditions. This difference in the CO<sub>2</sub> hydrate as illustrated in Figure 8a,b.

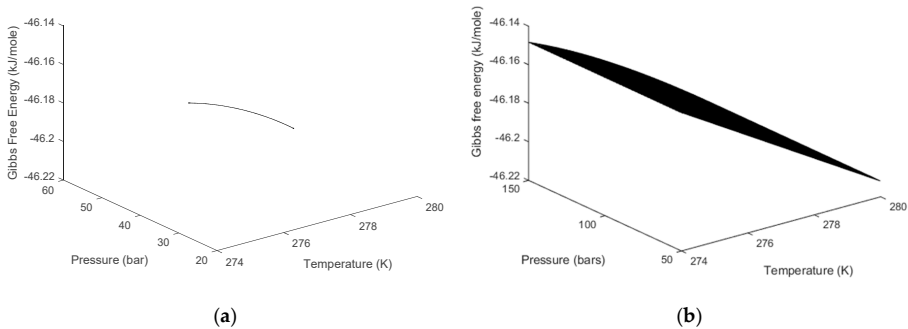


Figure 7. (a) Hydrate Gibbs free energy along the temperature pressure projection of the stability limit of CH<sub>4</sub> hydrate. (b) Gibbs free energy for hydrates formed from saturated solution of CH<sub>4</sub> in water as function of temperature and pressure.

The lower limit of hydrate stability concentration in water surrounding hydrate is found by solving for the concentration of hydrate former in water that gives the same chemical potential for both water and hydrate former in the aqueous phase and the hydrate phase. For CH<sub>4</sub> these chemical potentials are close to infinite dilution chemical potential in water and given by Equation (28), with the associated parameterization. For the same ranges of conditions as in Figure 6b the chemical potential of CH<sub>4</sub> is in the order of –42.6 kJ/mole. The corresponding free energies for hydrate stability limit in terms of concentration of CH<sub>4</sub> varies slightly around –48.6 kJ/mole at 274 K and 50 bar. CO<sub>2</sub> is more solvable

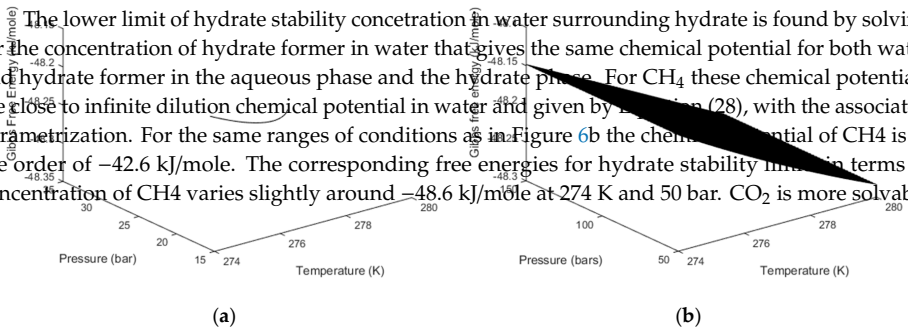
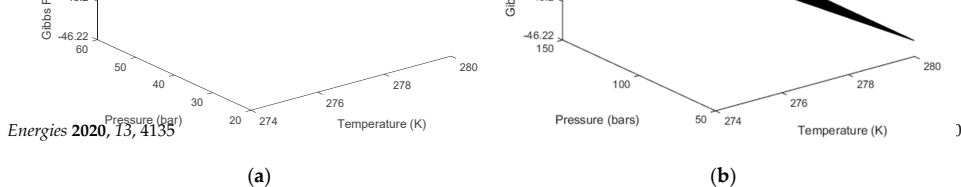
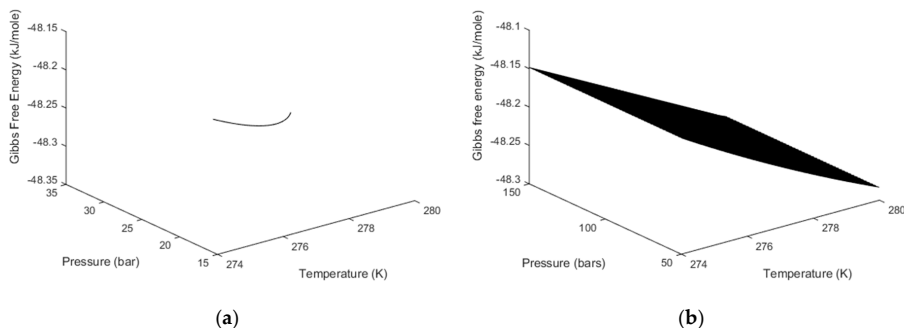


Figure 8. (a) Hydrate Gibbs free energy along the temperature pressure projection of the stability



**Figure 7.** (a) Hydrate Gibbs free energy along the temperature pressure projection of the stability limits of CH<sub>4</sub> hydrate; (b) Gibbs free energy for hydrates formed from saturated solution of CH<sub>4</sub> in water as function of temperature and pressure.



**Figure 8.** (a) Hydrate Gibbs free energy along the temperature pressure projection of the stability limits of CO<sub>2</sub> hydrate; (b) Gibbs free energy for hydrates formed from saturated solution of CO<sub>2</sub> in water as function of temperature and pressure.

## 8. Enthalpies of Hydrate Formation and Dissociation

The Clausius equation for calculating enthalpies of phase transitions is well established and there is no need for a detailed derivation. See for instance Kvamme et al. [66] for a brief review of Anderson's [62] scheme from using the Clapeyron equation:

$$\Delta H = T \Delta V \left( \frac{dP}{dT} \right) \quad (34)$$

Unlike Anderson's scheme we use Monte Carlo simulation to calculate partial molar volume of guest molecules in the various types of cavities. The Monte Carlo procedures are discussed in much details elsewhere [5,6] and will not be repeated here. The calculated values are listed in Table 6 below and are almost not dependent on temperature for the limited range of hydrate stability in the liquid water region.

**Table 6.** Sampled residual energies and cavity occupation volumes for CH<sub>4</sub> and CO<sub>2</sub>.

| Property                   | CH <sub>4</sub> |              | CO <sub>2</sub> |              |
|----------------------------|-----------------|--------------|-----------------|--------------|
|                            | Large Cavity    | Small Cavity | Large Cavity    | Small Cavity |
| $U_{ki}^R$ (kJ/mole)       | -16.53          | -17.73       | -27.65          | -10.58       |
| $V_{ki}$ (Å <sup>3</sup> ) | 164.2           | 89.2         | 135.6           | 76.9         |

The molar volume for guest molecules in the gas phase is directly available from the utilized equation of state (SRK). Liquid water molar volume is almost constant and trivially calculated from liquid water density and molecular weight. Hydrate water molecular volume is then calculated according to the following balance for one guest:

$$V^H = V_{H_2O}^H x_{H_2O}^H + V_{guest}^H (1 - x_{H_2O}^H) \quad (35)$$

The density and average molecular weight for hydrate is trivially calculated from the lattice constant (12.01 Å is used as a constant value throughout this work), calculated filling fractions and the corresponding average mole-fractions of water and guest in the hydrate., i.e.,:

$$V_{H_2O}^H = \frac{V^H - V_{guest}^H (1 - x_{H_2O}^H)}{x_{H_2O}^H} \tag{36}$$

The Clausius equation is then:

$$\Delta V = x_{H_2O}^H (V_{H_2O}^H - V_{H_2O}^{water}) + (1 - x_{H_2O}^H) (V_{guest}^H - V_{guest}^{gas}) \tag{37}$$

Neglecting volumes of condensed phases (including hydrate volume) reduce Equation (19) to the Clausius–Clapeyron equation:

Hydrate formation pressures are generally significant above ideal gas limit for methane and natural gas. Moreover, as discussed above it is not very complicated to calculate the necessary volumes needed for the Clausius equation in (34), so we will not compare results with the Clausius–Clapeyron here. A fundamentally different approach can be derived from the residual thermodynamics model based on chemical potentials for water and guests [63–66]:

$$\frac{\partial \mu_{H_2O}^H}{\partial T} \Big|_{P, \bar{N}} = -RT^2 \frac{\partial}{\partial T} \left[ \frac{\mu_{H_2O}^H}{RT} \right]_{P, \bar{N}} + \left[ \frac{\sum_{k=1,2} v_k \sum_i h_{ki} (\mu_{ki} - \Delta g_{ki}) - T \left( \frac{\partial \mu_{ki}}{\partial T} - \frac{\partial \Delta g_{ki}}{\partial T} \right)}{\left( 1 + \sum_i h_{ki} \right)} \right] \tag{39}$$

For liquid water, the enthalpy is even more trivially obtained by numerical differentiation of the polynomial fit of chemical potential as function of  $T$  given by Kvamme & Tanaka [4]. For water containing salt or other components such as methanol additional contributions according to analytical or numerical differentiation of the activity term in Equation (13). An example for methanol addition is given in Figure 9 below.

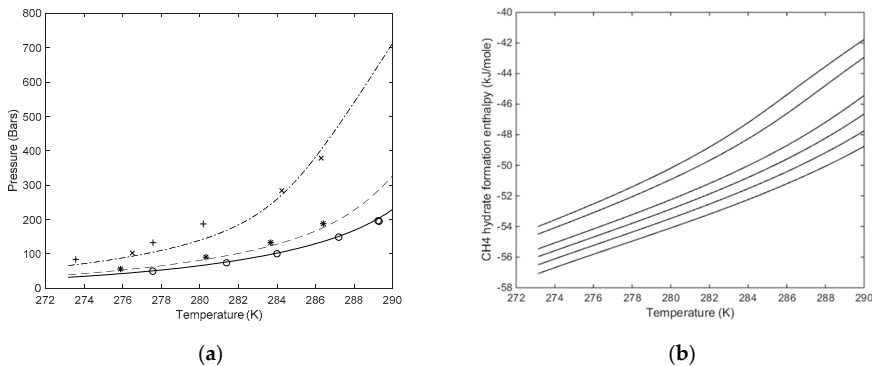


**Figure 9.** (a) CH4 hydrate stability limits in the temperature-pressure projection for 33 different methanol concentrations, 55% mole percent (solid), 100% mole percent (dashed), 200% mole percent (dash-dot), (o) are experimental data from Svartås and Haathus [67], \* are experimental data from Nigg and Robinson [68] and are experimental data from Svartås and Fasmas [69] (b) CH4 hydrate formation enthalpy (kJ/mole) as a function of temperature for pure water and for water with 2%, 4%, 6%, 8%, 10%, 12%, 16%, 20%, 25%, 30%, 35%, 40%, 45%, 50%, 55%, 60%, 65%, 70%, 75%, 80%, 85%, 90%, 95% and 100% methanol in water. Methanol in water for pure water is given by 2%, 4%, 6%, 8%, 10%, 12%, 16%, 20%, 25%, 30%, 35%, 40%, 45%, 50%, 55%, 60%, 65%, 70%, 75%, 80%, 85%, 90%, 95% and 100%.

In an equilibrium situation, the chemical potential of same guest (hydrate former) in the two cavity types must be the same and these must be equal to the chemical potential of the same guest molecule in the phase that it has come from. For the heterogeneous case, this implies chemical potential of the molecule in gas (or liquid) hydrate former phase. However, outside of equilibrium, the gradients in chemical potentials as function of  $T$ ,  $P$  and mole-fractions must reflect how the guest molecule behaves in the cavity.

Enthalpies for various guest molecules in the two types of cavities can be computed by Monte

molecule in gas (or liquid) hydrate former phase. However, outside of equilibrium, the gradients in chemical potentials as function of  $T$ ,  $P$  and mole-fractions must reflect how the guest molecule behaves in the cavity.

Enthalpies for various guest molecules in the two types of cavities can be computed by Monte Carlo simulations along the lines described by Kvamme & Lund [5] and Kvamme & Førrisdahl [6] by sampling guest water interaction energies and efficient volumes from the guest molecules movements. That is:

$$H_{ki}^R = U_{ki}^R + (z_{ki} - 1)RT \quad (40)$$

$U$  refers to energy and superscript R stands for residual (interaction) contribution.  $Z_{ki}$  denotes compressibility factor for the guest molecule  $i$  in cavity  $k$ . Consistent ideal gas values for the same interaction models that were applied in evaluation of the residual values is trivial.

$$z_{ki} = \frac{PV_{ki}}{k_B T} \quad (41)$$

where  $k_B$  means Boltzmann's constant and  $V_{ki}$  stands for the excluded volume of a molecule of type  $i$  in cavity of type  $k$ . This latter volume can be evaluated from the sampled volume of center of mass movements plus the excluded volume due to water/guest occupation. Slightly more complex sampling and calculation for molecules which are not monoatomic (or approximated as monoatomic like methane), but still fairly standard [5,6] and explicit discussion on this is not required here.

For a relevant temperature span in the order of 10 K (273 K–283 K), the differences in enthalpies as evaluated from Equation (40) using Monte Carlo sampled data do not vary substantially and could even be approximated as constant for the purpose of this work. This is as expected because the hydrate water lattice is fairly rigid and the average movements are almost the same for the limited temperature range. Sampled cavity partition functions will of course vary remarkably over the same temperature range because of the direct exponential (Boltzmann factor) dependency. The interaction models for methane (CH<sub>4</sub>) and carbon dioxide (CO<sub>2</sub>) used is the same as those used by Kvamme & Tanaka [4]. In addition, note that while there is an average attraction also for carbon dioxide (CO<sub>2</sub>), the sampled Langmuir constant is very small and not substantial. This is also confirmed by the Molecular Dynamics (MD) studies along the lines of Kvamme & Tanaka [4] whereby the movements of carbon dioxide in the small cavity interferes with several water liberation frequencies and the resulting Gibbs free energy of inclusion is not favorable for carbon dioxide in the small cavity. While small cavity occupation of carbon dioxide has been found at extreme conditions in the ice range of temperatures in some studies [69], it remains unclear if there would be any substantial small cavity filling at all for temperatures above zero degrees Celsius.

The most general approach for calculating enthalpy changes related to temperature pressure stability projection of the phase transition for hydrate formation and dissociation is clearly the residual thermodynamic scheme. Although we have only demonstrated this for pure components here the formalism is totally general for mixtures as well. However, there are not many available studies for mixtures to compare with so it makes sense to start with pure components. Moreover, since CH<sub>4</sub> and CO<sub>2</sub> are important in the concept for combined CH<sub>4</sub> production from hydrate and safe long terms storage of CO<sub>2</sub> ([23] and references therein) these data are needed by use and likely others. The Clapeyron scheme by Anderson [52] involves fairly many computational steps since it goes through ice. Anderson's [62] scheme is discussed and compared in more detail elsewhere [66]. A much simpler Clapeyron scheme was proposed in this work. Preliminary comparisons for CH<sub>4</sub> and CO<sub>2</sub> with experimental data as well as the residual scheme are very promising, except for temperatures higher than around 287 K for CH<sub>4</sub> and CO<sub>2</sub>. As expected the Clausius–Clapeyron scheme is inferior and results deviates significantly even for moderate pressures (30 bar) for both CH<sub>4</sub> and CO<sub>2</sub>.

Another aspect that is worthwhile considering is that even for the two very different hydrate formers the enthalpy change as function of temperature is an almost linear function. Practically this means that the specific heat capacity change for the phase transition is almost the same for all the

various pressures signifying the stability curve of the enthalpy change for a fluid as a function of pressure. Figure 10a–d are calculated using a parameter density of CH<sub>4</sub> in Figure 10a and a density of CH<sub>4</sub> in Figure 10b. The density of CH<sub>4</sub> is a function of the pressure and temperature. This is because the density of CH<sub>4</sub> is a function of the pressure and temperature. This is also reflected in the difference between the calculated CO<sub>2</sub> in Figure 10a and the calculated CH<sub>4</sub> in Figure 10c. Even if the enthalpies in the plots in Figure 10a–d, are not orthonormal since both T and P vary simultaneously in these plots the consequence of the reflection above indicates that it may be feasible to propose the construction two approximate orthonormal functions as:

$$\Delta H_{Formation}(T, P) \approx \Delta H_{Formation}(T) + \Delta H_{Formation}(P) \quad (42)$$

$$= \left[ a_0 + a_1 \frac{T_C}{T} \right] + \left[ \sum_{m=1}^{npoly} b_m \left( \frac{P}{P_C} \right)^{m-1} \right] \approx \Delta H_{Formation}(T) + \Delta H_{Formation}(P) \quad (42)$$

$$= \left[ a_0 + a_1 \frac{T_C}{T} \right] + \left[ \sum_{m=1}^{npoly} b_m \left( \frac{P}{P_C} \right)^{m-1} \right]$$

In the most coarse grain approximation a linear approximation of the enthalpy change from the lowest temperature to the highest temperature in Figure 10a,b would practically imply that the pressure dependency in (42) is approximated to zero. In this case calculations of heats of formation and dissociation outside equilibrium curve will be absolutely trivial and the more rigorous approach discussed by Kvamme [51] and Kvamme et al. [53] will not be needed for those cases. Some experimental data are even published without information on pressure, as discussed by Kvamme et al. [53]. In general there are many limitations on available experimental data for enthalpies of hydrate phase transitions. An example fit is illustrated for CH<sub>4</sub> in Figure 11 below. A similar fit for CO<sub>2</sub> is given as Figure 12 below. An example fit is illustrated for CH<sub>4</sub> in Figure 11 below. A similar fit for CO<sub>2</sub> is given as Figure 12 below.

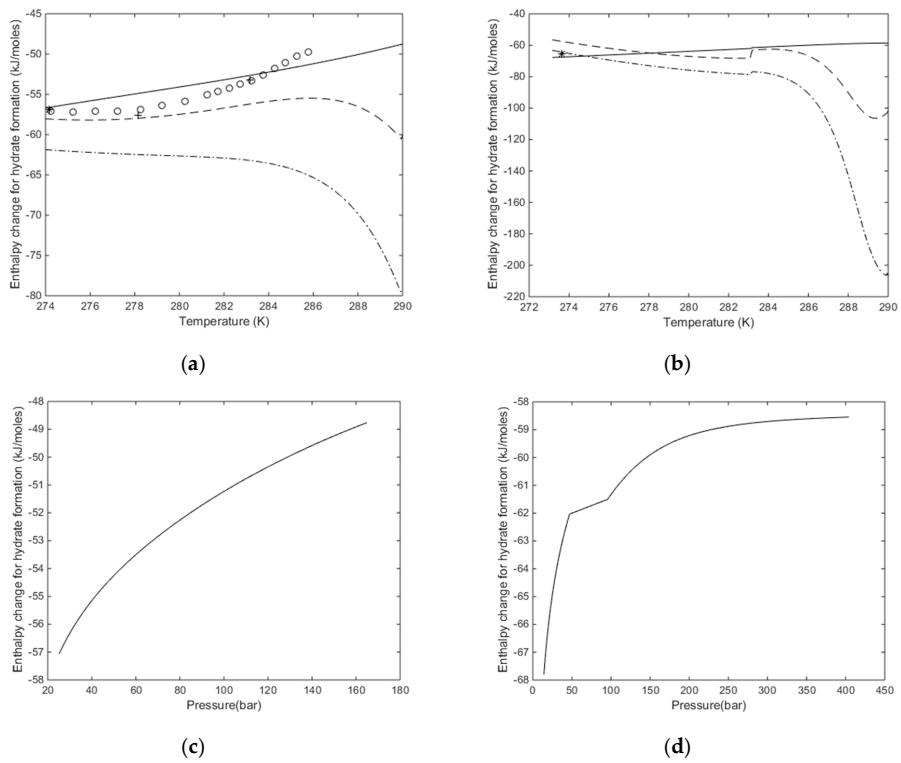


**Figure 10.** (a) Calculated enthalpies of hydrate formation along the pressure-temperature hydrate stability limit curve for CH<sub>4</sub>. Solid is calculated using Equation (39), dashed curve is calculated using the Clausius approach in Equation (34) and dash-dot is calculated using Clausius–Clapeyron, Equation (38) using compressibility factors from SRK [31] equation of state. o are calculated results

the Clausius approach in Equation (34) and dash-dot is calculated using Clausius–Clapeyron Equation (38) using compressibility factors from SRK [31] equation of state. o are calculated results from Nakamura et al. [40] based on Clapeyron. \* is an experimental point measured by Kang et al. [70] using calorimetry. are two points measured by Lievois et al. [71] using calorimetry. (b) calculated enthalpy of hydrate formation along the pressure–temperature stability limit curve for CO<sub>2</sub> Solid is calculated using Equation (39) and dashed curve is calculated using the Clausius–Clapeyron approach in Equation (34) and dash-dot is calculated using Clausius–Clapeyron using compressibility factors from SRK [31] equation of state. \* is an experimental point measured by Kang et al. [70] using calorimetry. (c) pressure projection of the enthalpy change of the CH<sub>4</sub> hydrate formation along the pressure–temperature stability limits. (d) pressure projection of the enthalpy change of the CO<sub>2</sub> hydrate formation along the pressure–temperature stability limits.

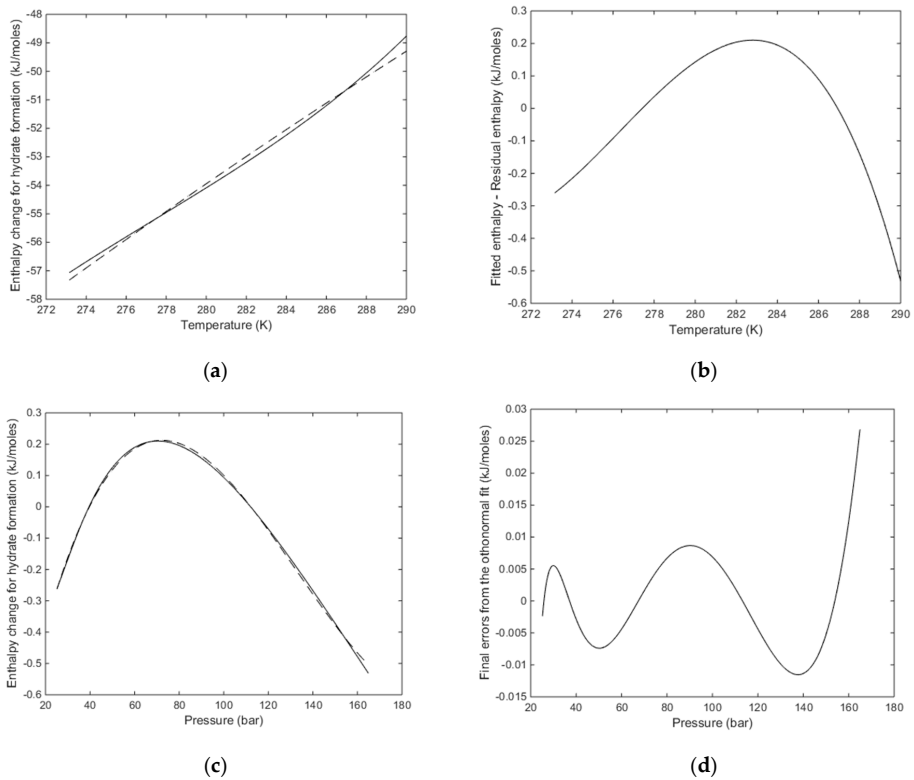


**Figure 11.** (a) Enthalpy change for hydrate formation as calculated from Equation (39) (solid) for CH<sub>4</sub> along the temperature–pressure stability limit and the temperature part of Equation (42) (dashed). Critical temperature  $T_{C1}$  in the first term in Equation (42) is 190.56 K for CH<sub>4</sub>;  $a_8 = 8.108 \text{ kJ/mol}$  and  $a_7 = 1.983 \text{ kJ/mol}$ . (b) Difference between enthalpy change calculated from Equation (39) and only a linear function in temperature (first term on the hand side of Equation (42)) as had been done in Figure 11a. (c) Fit of the orthonormal pressure term in Equation (42) to the error after the linear temperature fit; Figure 11b. Critical pressure for  $P_{C1}$  for CH<sub>4</sub> is 45.99 bar. Number of terms in the last term of Equation (42),  $m_{poly}$ , is 4 and the parameters from  $m = 1$  to  $m = 4$  is  $-1.0314, 1.8105, -0.7924, 0.0916$ ; (d) final errors between calculations from Equation (39) and the orthonormal fit in Equation (42).



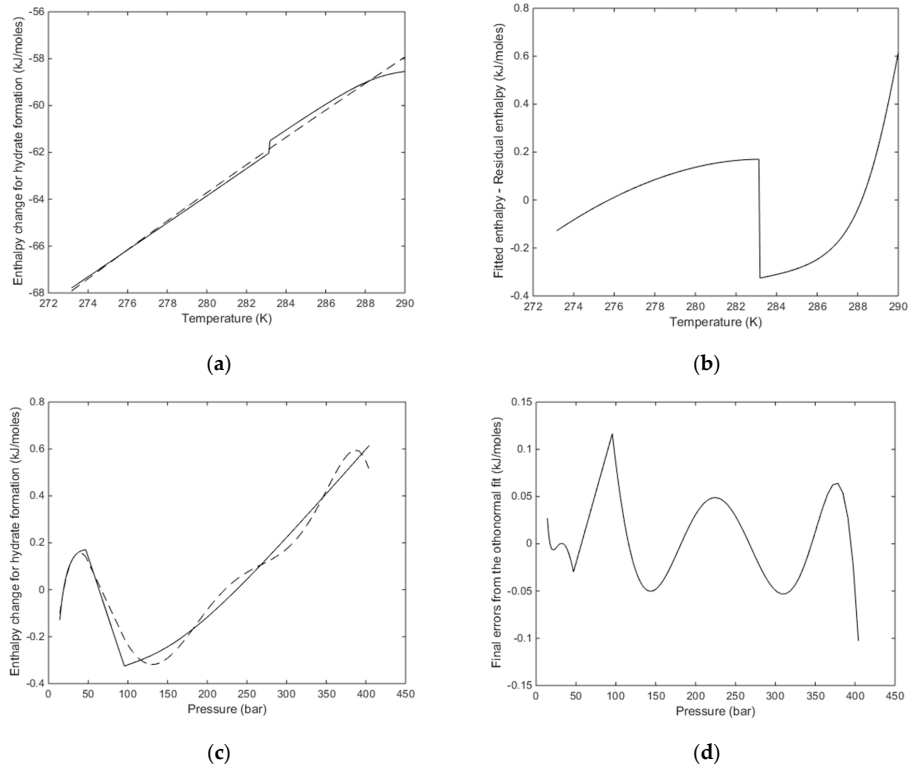


**Figure 12.** (a) Enthalpy change for hydrate formation as calculated from Equation (39) (solid) for  $\text{CO}_2$  along the temperature–pressure stability limit and the temperature part of Equation (42) (dashed). Critical temperature  $T_c$  in the first term in Equation (42) is 31.1 °C for  $\text{CO}_2$  ( $A_0 = 1 \text{ kJ/mol}$  and  $a = 1.5 \text{ kJ/mol}$ ). (b) Difference between enthalpy calculated from Equation (39) and a linear fit of the enthalpy in the first term in Equation (42) (dashed line) in Figure 2a. (c) Fit of the orthonormal pressure term in Equation (42) to the error after the linear temperature fit (Figure 1b). Critical pressure for  $\text{PP}$  for  $\text{CO}_2$  is 73.9 bar. Number of terms in the last term of Equation (42) is 4 and the parameters in the term are  $m = 17$ ,  $n_0 = 61793$ ,  $3.636693$ ,  $5.783651$ ,  $3.578863$ ,  $8.157322$ ,  $0.141922$ ,  $-0.06992$ . (d) Final errors in the orthonormal calculation of Equation (42) on the orthonormal in Equation (42).

The total dominance in temperature dependency is not very surprising in a residual thermodynamic formulation. As also mentioned before, temperature and pressure are independent thermodynamic variables, so using gradients in temperature and pressure is an indirect way to calculate enthalpy. Enthalpy has been used to calculate enthalpy as a function of temperature and pressure in a residual thermodynamic framework. If we first look at the water look at the water the combination of the two considered for two phases, one for two phases can be written as:

$$d \left( \frac{\bar{H}_i^{H,L} - \bar{H}_i^{Aq}}{\bar{H}_i^{H,L} - \bar{H}_i^{Aq}} \right) \leq \left( T^0, H, S_i^{H,L} - T^0, H, S_i^{Aq} \right) dT + \left( \bar{V}_i^{H,L} - \bar{V}_i^{Aq} \right) dP \quad (43)$$

Superscripts  $H$  and  $Aq$  denote Hydrate and liquid water phase, respectively. The flat line on the symbols  $H$ ,  $S$  and  $V$  denote partial molar quantities for enthalpy, entropy and volumes, respectively for component  $i$ . The superscript  $o, H$  and  $o, Aq$  denote surrounding temperature facing hydrate and liquid water, respectively. There is a limited partial molar volume difference between water in the water, two phases, but it is still small volumes. The entropy differences for water in the first term, on the other hand, is substantial between the ordered hydrate and the relative more chaotic liquid water

phase. For the guest molecules the enthalpy for guests in cavities was discussed above and for the liquid state and in fluids (gas, liquid, supercritical) the relevant expression for the pure components is separated into the contribution from the fluid phase and in the cavities so the only differences are in the residual contribution. In summary the pressure sensitivity in the enthalpy is expected to be limited to the same extent as the pressure part of the equation (42) in the data presented on Figure 13 and 14. The residual enthalpy contribution of the various components is given in the (29) enthalpy expression by splitting in two approximation the pressure part of Equation (30). However, the results from Figure 12 may be more accurate for the analysis of the various relative to other Equation (39). Moreover, a state-of-the-art and available experimental data are very incomplete and inconsistent for (42) may be accurate enough for many practical purposes relative to other uncertainties. Moreover, as also noted in the discussion of the (29) experimental data the limitation to temperature, pressure gradients, which are in the calculation of Clapeyron heat during formation of hydrate and the pressure gradient at the interface in liquid water. A model for heat of formation from a hydrate formed from gas phase and water will rapidly liquid water as a transport barrier for formation of hydrate from aqueous phase and particularly hydrate at the existing hydrate film will be released heat that will dynamically interact with the hydrate film towards the existing hydrate film with the release of heat that will dynamically interact with the hydrate film below the growth of the hydrate film, which is the heat of formation of hydrate from gas phase (or liquid phase) and water molecule (Phase Field Theory modeling) [53–61] may shed more insight into these aspects.

In Figure 13, these plot show calculations of heat of formation for hydrate formed from liquid solution of CO<sub>2</sub> in water. Details of the calculation procedure are described in more detail by (2020) in water. Basically the calculation followed the same scheme as in the work of Redinger [52] for gas hydrate formation. In the calculation, the heat of formation for hydrate formed from gas phase and water is accepted as the reference for the magnitude of the heat of formation for hydrate from the difference between the heat of formation of hydrate and the heat of formation of the hydrate from gas phase surrounded by hydrate cavity state. This is in contrast to the existing gas molecules in a cavity. This is a restricted movement and in most cases higher density.

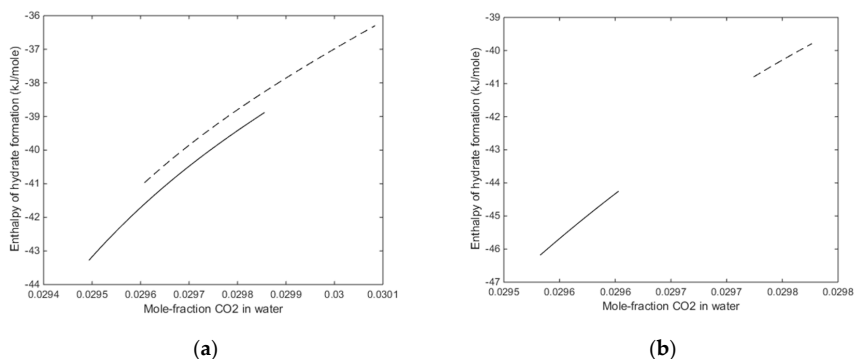


**Figure 13.** (a) Calculated enthalpies of hydrate formation from aqueous solution of CO<sub>2</sub> as function of mole fraction for 274 K and 100 bar (solid) and for 274 K and 200 bar (dashed); (b) calculated enthalpies of hydrate formation from aqueous solution of CO<sub>2</sub> as function of mole fraction for 283 K and 100 bar (solid) and for 283 K and 200 bar (dashed).

Similar plots for CH<sub>4</sub> at the same two temperatures are given in Figure 14 below.

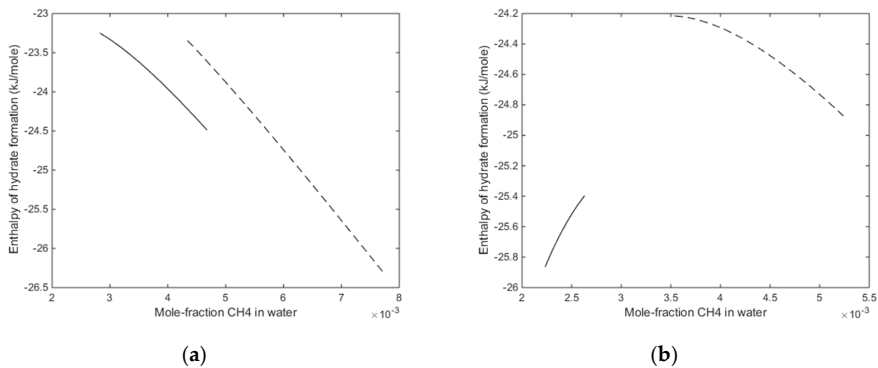


**Figure 14.** (a) Calculated enthalpies of hydrate formation for aqueous solution of CH<sub>4</sub> as a function of mole fraction for 273 K and 100 bar (solid) and 285 K and 100 bar (dashed) and (b) calculated enthalpies of hydrate formation for aqueous solution of CH<sub>4</sub> as a function of mole fraction for 273 K (solid) and 285 K and 200 bar (dashed).

The variation in enthalpies for CH<sub>4</sub> hydrate formation is smaller for CH<sub>4</sub>. The different behavior for the two temperatures reflect that the trapping of CH<sub>4</sub> in the cages activity is not understood naturally in terms of an expansion of CH<sub>4</sub> region of form liquid to cage activity. Due to Equations (40) and (41) there is a turning of the gradient in enthalpies of hydrate formation in the pressure region from 100 bar to 200 bar.

While the illustrations for the heterogeneous hydrate formation in Figures 13 and 14 are only for formation along the long hydrate stability limit, the extensive the extent of the conditions is also a straight forward Kasanise (55) through Taylor (53) partitions initially for expansion of molecular for the formation of hydrate and initiation in Figures 13 and 14.

### 9. Discussion

The reference method of calculation of hydrate stability limits in the temperature-pressure projection of the hydrate stability windows is a very old method with substantial limitations some of which are illustrated in this work. Present level of molecular simulations, as well as molecular models for water and other molecules of relevance for hydrate formation and dissociation is at a very mature level that should make the reference method redundant for the future. The main limitations of this work, fairly old many interaction model (the TIP4P potential [21]) illustrates the extended possibilities of the possible in a dynamic phase transition in a phase hydrate systems and in hydrate hydrates. The fact that a hydrate hydrate in equilibrium at each of the thermodynamic equilibrium conditions is a dynamic equilibrium by balance between competing forces of hydrate formation from the forces of dissociation through the dynamic system bringing in water from above that dissociates hydrate from above at a transition over by the use of residual thermodynamics also for hydrate phases. This will also open up for next generation of hydrate simulations. The old method of reference properties is substantially weakened by the need for many empirical fitting of the fundamental properties (such as properties of the water) and the need for a well as a water/guest interaction fitting limit properties of the hydrates, method (30). The only that part of the temperature projection of the phase stability limits. Other phase transitions such as dissociation of hydrate at high pressure temperature projection for the phase stability limits. The phase transitions, hydrate formation and hydrate formation and dissociation of hydrates is critical in evaluation of hydrate production release in hydrate formation and dissociation in evaluation of dissociation of hydrate plugs and other application related to hydrate phase transitions. Enthalpy calculations are also critical in evaluation of dissociation of hydrate plugs and other application related to hydrate phase transitions.

The use of reactive transport analogy and treating each hydrate phase transition as a pseudo reaction gives a totally different platform for hydrate reservoir simulators [74–78] and includes papers in these theses. Hydrate reservoir simulators based on local free energy minimization of competing phase transitions for hydrate formation and hydrate dissociation, under constraints of local mass- and energy-fluxes, has a wider application. A few of these applications have been discussed in this work, but future possibilities include many extensions, as for example couplings to dynamic geo-bio ecosystems.

In addition to a wider application of a residual scheme comes the value of a consistent route to various thermodynamic properties, as illustrated by a new route for calculation of enthalpies of formation and dissociation [51,53,66], as discussed above. This also includes heat of formation from dissolved hydrate formers in water (and corresponding reverse dissociation). We also propose a new and simple Claussius method for environments that do not have a thermodynamic code, but measured pressure temperature stability limit data.

Similar for industrial systems, like processing and transport of hydrocarbon systems, which also has the same situation of not being able to reach equilibrium due to all the possible routes to hydrate formation, including the impact of solid surfaces like rusty pipelines [22,25–27,29,30,79–81]. Even if hydrate forms in a pipeline it can re-dissociate if the flow surrounding the hydrate results in contact with liquid water under saturated with hydrate former or hydrocarbons which is under saturated with water. Moreover, this is of course not limited to hydrocarbons. Any handling of hydrate forming phases that contains water or is flowing together with a water phase in a multiphase pipeline, has to be analyzed in a non-equilibrium fashion.

The reason for the title of the study is a hope that other research groups should start to think about changing from the reference method over to residual thermodynamics. This is also the reason that we provided a very brief discussion of the old method, which is present in many codes around the world today. It is actually very simple to convert codes over to a residual thermodynamic basis. Moreover, there are many reasons for making this change. As we have discussed here some of the advantages of a residual thermodynamic scheme along the lines described here are:

- (1) The possibility to calculate different hydrate formation and dissociation, phase transitions. This was illustrated for hydrate formation from dissolved hydrate formers and hydrate stability limits;
- (2) In a general non-equilibrium situation, the advantage of a residual thermodynamic scheme is that every component in every co-existing phase has the same reference state (ideal gas). Direct comparisons of chemical potentials and Gibbs free energies for different phases will therefore also provide a direct comparison of relative phase stabilities and thermodynamic driving forces for phase transitions;
- (3) Residual thermodynamics link directly into Molecular Dynamics simulations for providing model molecule properties for active phases for which experimental data are impossible to measure. One example is hydrate formers adsorbed on mineral surfaces and subsequent hydrate nucleation toward mineral surfaces. It is possible to measure structures of fluids adsorbed on solid surfaces, but there is no direct coupling over to thermodynamic properties;
- (4) As illustrated here the advantage is that residual thermodynamic description along the lines described here gives direct and consistent routes to many important thermodynamic properties, as demonstrated with enthalpy of hydrate formation. To our knowledge it is the only available method for calculation of enthalpies of hydrate formation for mixtures;
- (5) Hydrate nucleation theories are implicit couplings between thermodynamics of the phase Transition (Gibbs free energy change), mass transport dynamics and heat transport dynamics. All the thermodynamic properties involved in various nucleation theories are available from the concept demonstrated here;
- (6) Present stage of modeling hydrate production was very limited by lack of consistent thermodynamic tools that is able to address the variety of calculations needed for all the

phase transitions involved. The non-equilibrium nature of hydrates in sediments [79–81] requires a residual thermodynamic scheme that is able to address competing phase transitions for hydrate formation and hydrate dissociation. Work is therefore in progress [76–80] on the development of a new hydrate reservoir simulator, which is fundamentally different from any other hydrate reservoir simulators because it utilizes a reactive transport platform in which all hydrate phase transitions are treated as pseudo reactions. Each of the theses in references [76–80] contain 6 to 12 Journal publications. The theses can be downloaded from University of Bergen for free or they can be sent from the leading author of this study;

- (7) The residual thermodynamic scheme described in this work was applied to discussion on maximum water that can be tolerated in various hydrate forming systems during transport in pipelines [22,25–30]. This also includes impact of mineral surfaces (rust) on concentration limit of water in gas before drop-out.

With reference to the title of the study, we have demonstrated that a residual thermodynamic scheme can be a platform for complete thermodynamic description of hydrates in sediments, as well as hydrates forming in industrial situation. To date, we have illustrated this through various hydrate stability limit region, like temperature, pressure and hydrate stability towards surrounding water or gas. Moreover, we have illustrated that the same model can be used to calculate thermodynamic responses like free energy changes and enthalpy changes that are needed in hydrate production and in many other applications. The residual thermodynamic scheme for enthalpies discussed here is quite unique because it can be used for the same multicomponent mixtures as used in other calculations. It is also a consistent scheme since it is derived from the free energy model. Presently the residual scheme as discussed here is the most extensive and general thermodynamic model for hydrate. That does not imply that other researchers need to follow our basic models for residual properties of ice, liquid water and empty hydrate. Molecular Dynamics simulations are very easy today in terms of modern computers, many new models for water–water interactions and many open software packages for conducting the simulations. The message is simply that we should turn over from a limited concept from 1970's to a more complete thermodynamic model system for more general use. This will open up for a totally different platform that can address many natural systems in a different and more accurate way. This includes dynamic hydrate systems that forms from upcoming gas and dissociates towards incoming seawater and it also includes conventional hydrate seeps that enters seafloor at hydrate forming conditions. The need to understand these systems from a more fundamental thermodynamic point of view is very important in the discussion on changes of carbon fluxes into the oceans. Moreover, hydrate energy is becoming increasingly important for many countries. The residual thermodynamic concept presented here can provide all necessary thermodynamic calculations involved.

## 10. Conclusions

The reference method for calculating hydrate stability limits in the temperature pressure projection has many limitations. It is not theoretically sound to fit chemical potentials and enthalpies to a range of different hydrate using a semi-empirical model for the cavity partition functions. While the theoretical platform is a Langmuir type of adsorption theory the semi-empirical aspect comes in how the water lattice is treated as not being disturbed by the guest molecule movements in the cavities. This is fair for small guest molecules like  $\text{CH}_4$ , but may be wrong by one kilojoule per mole for a guest molecule like  $\text{CO}_2$  in large cavity of structure I. Other semi-empirical aspects are related to various approximations in the evaluation of the Langmuir-constant and the models for interactions between guest molecules and the water molecules in the lattice. Practically all the fitting of parameters in the reference method to a two-dimensional (temperature pressure) projection of the hydrate stability limits is a limitation which makes the concept less useful to address modern hydrate challenges. The rapidly growing interest in hydrate energy requires more accurate thermodynamic description of all dimensions of hydrate stability limits. This involves all phases that can contribute to hydrate formation and hydrate dissociation like aqueous phases and dissolved hydrate formers and adsorption on mineral surfaces.

With the rapid development of interaction models for water and other relevant components for hydrate, including mineral surfaces it is time to make more use of molecular dynamics simulations to establish residual thermodynamic models for all phases of relevance for hydrate formation. In this work we have demonstrated that residual thermodynamic modeling for all phases is able to describe a wider range of the hydrate stability limits. Moreover, in addition we have demonstrated that also enthalpies of hydrate formation and dissociation can be predicted by residual thermodynamics. Being able to predict stability limits (free energy related) as well as enthalpies is a good sign of consistency also for entropy development. We have also proposed a promising simple Clapeyron scheme as alternative to other more complex schemes.

The residual thermodynamic scheme presented and illustrated here is totally superior to the old reference method. One of the reasons is that the residual scheme because it provides a consistent scheme for a very wide range of properties that are need in practical applications in natural hydrate systems, as well as and in industrial hydrate systems. This does not mean that other groups need to use our model systems for chemical potentials of water as ice or liquid and water in empty hydrates. The equations that we have presented for hydrate thermodynamic properties, including enthalpy calculations can be applied with any sets of chemical potentials for water derived from molecular modeling.

**Author Contributions:** All authors have contributes in theoretical development, writing of paper and analysis of data, including comparisons with experimental data. All authors have read and agreed to the published version of the manuscript.

**Funding:** This research was supported by National Key Research and Development Program (No. 2019YFC0312302, No. 2019YFC0312303 and No. 2018YFC0310203), National Natural Science Foundation Item of China (No. 51874252 and No. 5177041544), Basic Applied Research Key Projects of Science and Technology Department of Sichuan Province (No. 2019YJ0419 and No. 2019YJ0351).

**Conflicts of Interest:** There are no conflict of interests.

## References

1. Sloan, E.D.; Koh, C.A. *Clathrate Hydrates of Natural Gases*; Informa UK Limited: Colchester, UK, 2007.
2. van der Waals, J.H.; Platteeuw, J.C. Clathrate Solutions. In *Advances in Chemical Physics*; Wiley: Hoboken, NJ, USA, 2007; pp. 1–57.
3. Parrish, W.R.; Prausnitz, J.M. Dissociation Pressures of Gas Hydrates Formed by Gas Mixtures. *Ind. Eng. Chem. Process. Des. Dev.* **1972**, *11*, 26–35. [[CrossRef](#)]
4. Kvamme, B.; Tanaka, H. Thermodynamic Stability of Hydrates for Ethane, Ethylene, and Carbon Dioxide. *J. Phys. Chem.* **1995**, *99*, 7114–7119. [[CrossRef](#)]
5. Kvamme, B.; Lund, A.; Hertzberg, T. The influence of gas-gas interactions on the Langmuir constants for some natural gas hydrates. *Fluid Phase Equilib.* **1993**, *90*, 15–44. [[CrossRef](#)]
6. Kvamme, B.; Førriisdahl, O.K. Polar guest–molecules in natural gas hydrates. *Fluid Phase Equilib.* **1993**, *83*, 427–435. [[CrossRef](#)]
7. Tee, L.S.; Gotoh, S.; Stewart, W.E. Molecular Parameters for Normal Fluids. Kihara Potential with Spherical Core. *Ind. Eng. Chem. Fundam.* **1966**, *5*, 363–367. [[CrossRef](#)]
8. Holder, G.; John, V. Thermodynamics of multicomponent hydrate forming mixtures. *Fluid Phase Equilib.* **1983**, *14*, 353–361. [[CrossRef](#)]
9. John, V.T.; Papadopoulos, K.D.; Holder, G. A generalized model for predicting equilibrium conditions for gas hydrates. *AIChE J.* **1985**, *31*, 252–259. [[CrossRef](#)]
10. Ballard, A.; Sloan, E.D. Structural transitions in methane+ethane gas hydrates—Part II: Modeling beyond incipient conditions. *Chem. Eng. Sci.* **2000**, *55*, 5773–5782. [[CrossRef](#)]
11. Jager, M.; Sloan, E. The effect of pressure on methane hydration in pure water and sodium chloride solutions. *Fluid Phase Equilib.* **2001**, *185*, 89–99. [[CrossRef](#)]
12. Clarke, M.; Bishnoi, P. Development of an implicit least squares optimisation scheme for the determination of Kihara potential parameters using gas hydrate equilibrium data. *Fluid Phase Equilib.* **2003**, *211*, 51–60. [[CrossRef](#)]

13. Mohammadi, A.H.; Anderson, R.; Tohidi, B. Carbon monoxide clathrate hydrates: Equilibrium data and thermodynamic modeling. *AIChE J.* **2005**, *51*, 2825–2833. [[CrossRef](#)]
14. Tohidi-Kalorazi, B. Gas hydrate equilibria in the presence of electrolyte solutions. Ph.D. Thesis, Herriot-Watt University, Edinburgh, UK, 1995.
15. John, V.T.; Holder, G. Choice of cell size in the cell theory of hydrate phase gas-water interactions. *J. Phys. Chem.* **1981**, *85*, 1811–1814. [[CrossRef](#)]
16. John, V.T.; Holder, G. Langmuir constants for spherical and linear molecules in clathrate hydrates. Validity of the cell theory. *J. Phys. Chem.* **1985**, *89*, 3279–3285. [[CrossRef](#)]
17. Holder, G.; Zetts, S.; Pradhan, N. Phase Behavior in Systems Containing Clathrate Hydrates: A Review. *Rev. Chem. Eng.* **1988**, *5*, 1–70. [[CrossRef](#)]
18. Zele, S.R.; Lee, S.-Y.; Holder, G. A Theory of Lattice Distortion in Gas Hydrates. *J. Phys. Chem. B* **1999**, *103*, 10250–10257. [[CrossRef](#)]
19. Sloan, E.D. Clathrate Hydrates: The Other Common Solid Water Phase. *Ind. Eng. Chem. Res.* **2000**, *39*, 3123–3129. [[CrossRef](#)]
20. Sloan, E. Clathrate hydrate measurements: Microscopic, mesoscopic, and macroscopic. *J. Chem. Thermodyn.* **2003**, *35*, 41–53. [[CrossRef](#)]
21. Yoon, J.-H.; Chun, M.-K.; Lee, H. Generalized model for predicting phase behavior of clathrate hydrate. *AIChE J.* **2002**, *48*, 1317–1330. [[CrossRef](#)]
22. Kvamme, B. Thermodynamic limitations of the CO<sub>2</sub>/N<sub>2</sub> mixture injected into CH<sub>4</sub> hydrate in the Ignik Sikumi field trial. *J. Chem. Eng. Data* **2016**, *61*, 1280–1295. [[CrossRef](#)]
23. Kvamme, B. Environmentally Friendly Production of Methane from Natural Gas Hydrate Using Carbon Dioxide. *Sustainability* **2019**, *11*, 1964. [[CrossRef](#)]
24. Kvamme, B.; Iden, E.; Tveit, J.; Veland, V.; Zarifi, M.; Qorbani, K. Effect of H<sub>2</sub>S content on thermodynamic stability of hydrate formed from CO<sub>2</sub>/N<sub>2</sub> mixtures. *J. Chem. Eng. Data* **2017**, *62*, 1645–1658. [[CrossRef](#)]
25. Kvamme, B.; Aromada, S.A. Risk of Hydrate Formation during the Processing and Transport of Troll Gas from the North Sea. *J. Chem. Eng. Data* **2017**, *62*, 2163–2177. [[CrossRef](#)]
26. Kvamme, B.; Aromada, S.A.; Kuznetsova, T.; Gjerstad, P.B.; Canonge, P.C.; Zarifi, M. Maximum tolerance for water content at various stages of a natural gas production. *Heat Mass Transf.* **2018**, *55*, 1059–1079. [[CrossRef](#)]
27. Kvamme, B.; Aromada, S.A. Alternative Routes to Hydrate Formation during Processing and Transport of Natural Gas with a Significant Amount of CO<sub>2</sub>: Sleipner Gas as a Case Study. *J. Chem. Eng. Data* **2018**, *63*, 832–844. [[CrossRef](#)]
28. Kvamme, B.; Selvag, J.; Saeidi, N.; Kuznetsova, T.; Saedi, N. Methanol as a hydrate inhibitor and hydrate activator. *Phys. Chem. Chem. Phys.* **2018**, *20*, 21968–21987. [[CrossRef](#)] [[PubMed](#)]
29. Aromada, S.A.; Kvamme, B. Impacts of CO<sub>2</sub> and H<sub>2</sub>S on the risk of hydrate formation during pipeline transport of natural gas. *Front. Chem. Sci. Eng.* **2019**, *13*, 616–627. [[CrossRef](#)]
30. Aromada, S.A.; Kvamme, B. New approach for evaluating the risk of hydrate formation during transport of hydrocarbon hydrate formers of sI and sII. *AIChE J.* **2018**, *65*, 1097–1110. [[CrossRef](#)]
31. Soave, G. Equilibrium constants from a modified Redlich-Kwong equation of state. *Chem. Eng. Sci.* **1972**, *27*, 1197–1203. [[CrossRef](#)]
32. Shpakov, V.; Tse, J.; Tulk, C.; Kvamme, B.; Belosludov, V. Elastic moduli calculation and instability in structure I methane clathrate hydrate. *Chem. Phys. Lett.* **1998**, *282*, 107–114. [[CrossRef](#)]
33. Holder, G.; Corbin, G.; Papadopoulos, K.D. Thermodynamic and Molecular Properties of Gas Hydrates from Mixtures Containing Methane, Argon, and Krypton. *Ind. Eng. Chem. Fundam.* **1980**, *19*, 282–286. [[CrossRef](#)]
34. Dharmawardhana, P.B.; Parrish, W.R.; Sloan, E.D. Experimental Thermodynamic Parameters for the Prediction of Natural Gas Hydrate Dissociation Conditions. *Ind. Eng. Chem. Fundam.* **1980**, *19*, 410–414. [[CrossRef](#)]
35. Holder, G.; Malekar, S.T.; Sloan, E.D. Determination of hydrate thermodynamic reference properties from experimental hydrate composition data. *Ind. Eng. Chem. Fundam.* **1984**, *23*, 123–126. [[CrossRef](#)]
36. Yamamuro, O.; Suga, H. Thermodynamic Studies of Clathrate Hydrates. *J. Thermal Anal.* **1989**, *35*, 2025–2064.
37. Handa, Y.P.; Tse, J.S. Thermodynamic properties of empty lattices of structure I and structure II clathrate hydrates. *J. Phys. Chem.* **1986**, *90*, 5917–5921. [[CrossRef](#)]
38. Munck, J.; Skjold-Jørgensen, S.; Rasmussen, P. Computations of the formation of gas hydrates. *Chem. Eng. Sci.* **1988**, *43*, 2661–2672. [[CrossRef](#)]

39. CSM. CSMHYD Software. Available online: <http://hydrates.mines.edu/CHR/Software.html> (accessed on 17 July 2019).
40. Nakamura, T.; Makino, T.; Sugahara, T.; Ohgaki, K. Stability boundaries of gas hydrates helped by methane—structure-H hydrates of methylcyclohexane and cis-1, 2-dimethylcyclohexane. *Chem. Eng. Sci.* **2003**, *58*, 269–273. [[CrossRef](#)]
41. Servio, P.; Englezos, P. Measurement of Dissolved Methane in Water in Equilibrium with Its Hydrate. *J. Chem. Eng. Data* **2002**, *47*, 87–90. [[CrossRef](#)]
42. Mohammadi, A.H.; Anderson, R.; Tohidi, B. *Gas Hydrates 1: Fundamentals, Characterization and Modeling*; Broseta, D., Ruffine, L., Desmedt, A., Eds.; John Wiley & Sons: Hoboken, NJ, USA, 2017.
43. Thakore, J.L.; Holder, G. Solid vapor azeotropes in hydrate-forming systems. *Ind. Eng. Chem. Res.* **1987**, *26*, 462–469. [[CrossRef](#)]
44. Adisasmito, S.; Frank, R.J.; Sloan, E.D. Hydrates of carbon dioxide and methane mixtures. *J. Chem. Eng. Data* **1991**, *36*, 68–71. [[CrossRef](#)]
45. Fan, S.-S.; Guo, T.-M. Hydrate Formation of CO<sub>2</sub>-Rich Binary and Quaternary Gas Mixtures in Aqueous Sodium Chloride Solutions. *J. Chem. Eng. Data* **1999**, *44*, 829–832. [[CrossRef](#)]
46. Ng, H.J.; Chen, C.J.; Robinson, D.B. Ethylene glycol or methanol on hydrate formation in systems containing ethane, propane, carbon dioxide, hydrogen sulfide, or a typical gas condensate. In *Gas Processors Association Research Report 92*; The GPA Midstream Association: Tulsa, OK, USA, 1985.
47. Fan, S.-S.; Chen, G.-J.; Ma, Q.-L.; Guo, T.-M. Experimental and modeling studies on the hydrate formation of CO<sub>2</sub> and CO<sub>2</sub>-rich gas mixtures. *Chem. Eng. J.* **2000**, *78*, 173–178. [[CrossRef](#)]
48. Unruh, C.H.; Katz, D.L. Gas Hydrates of Carbon Dioxide-Methane Mixtures. *J. Pet. Technol.* **1949**, *1*, 83–86. [[CrossRef](#)]
49. le Quang, D.; le Quang, D.; Bouillot, B.; Herri, J.-M.; Glenat, P.; Duchet-Suchaux, P.; le, Q.-D. Experimental procedure and results to measure the composition of gas hydrate, during crystallization and at equilibrium, from N<sub>2</sub>–CO<sub>2</sub>–CH<sub>4</sub>–C<sub>2</sub>H<sub>6</sub>–C<sub>3</sub>H<sub>8</sub>–C<sub>4</sub>H<sub>10</sub> gas mixtures. *Fluid Phase Equilib.* **2016**, *413*, 10–21. [[CrossRef](#)]
50. Yang, S.; Cho, S.; Lee, H.; Lee, C. Measurement, and prediction of phase equilibria for water + methane in hydrate forming conditions. *Fluid Phase Equilib.* **2001**, *185*, 53–63. [[CrossRef](#)]
51. Kvamme, B. Kinetics of hydrate formation from nucleation theory. *Int. J. Offshore Polar* **2002**, *12*, 256–263.
52. Kvamme, B. Droplets of dry ice and cold liquid CO<sub>2</sub> for self-transport of CO<sub>2</sub> to large depths. *Int. J. Offshore Polar* **2003**, *13*, 139–146.
53. Buanes, T. Mean-Field Approaches Applied to Hydrate Phase Transition. Ph.D. Thesis, University of Bergen, Bergen, Norway, 2006.
54. Svandal, A. Modeling hydrate phase transitions using mean-field approaches. Ph.D. Thesis, University of Bergen, Bergen, Norway, 2006.
55. Kvamme, B.; Graue, A.; Buanes, T.; Kuznetsova, T.; Ersland, G. Storage of CO<sub>2</sub> in natural gas hydrate reservoirs and the effect of hydrate as an extra sealing in cold aquifers. *Int. J. Greenh. Gas Control.* **2007**, *1*, 236–246. [[CrossRef](#)]
56. Bauman, J.M. Non-Equilibrium Thermodynamics and Phase Transition Kinetics in Systems of Water, Carbon Dioxide and Methane. Ph.D. Thesis, University of Bergen, Bergen, Norway, 2015.
57. Baig, K. Nano to Micro Scale Modeling of Hydrate Phase Transition Kinetics. Ph.D. Thesis, University of Bergen, Bergen, Norway, 2017.
58. Kvamme, B.; Kuznetsova, T.; Kivelæ, P.-H.; Bauman, J. Can hydrate form in carbon dioxide from dissolved water? *Phys. Chem. Chem. Phys.* **2013**, *15*, 2063–2074. [[CrossRef](#)]
59. Tegze, G.; Pusztai, T.; Tóth, G.; Gránásy, L.; Svandal, A.; Buanes, T.; Kuznetsova, T.; Kvamme, B. Multiscale approach to CO<sub>2</sub> hydrate formation in aqueous solution: Phase field theory and molecular dynamics. Nucleation and growth. *J. Chem. Phys.* **2006**, *124*, 234710. [[CrossRef](#)]
60. Baig, K.; Kvamme, B.; Kuznetsova, T.; Bauman, J. The impact of water/hydrate film thickness on the kinetic rate of mixed hydrate formation during CO<sub>2</sub> injection into CH<sub>4</sub> hydrate. *AIChE J.* **2015**, *61*, 3944–3957. [[CrossRef](#)]
61. Qasim, M. Microscale Modeling of Natural Gas Hydrates in Reservoirs. Ph.D. Thesis, University of Bergen, Bergen, Norway, 2012.



62. Anderson, G.K. Enthalpy of dissociation and hydration number of methane hydrate from the Clapeyron equation. *J. Chem. Thermodyn.* **2004**, *36*, 1119–1127. [[CrossRef](#)]
63. Kvamme, B. Enthalpies of Hydrate Formation from Hydrate Formers Dissolved in Water. *Energies* **2019**, *12*, 1039. [[CrossRef](#)]
64. Aromada, S.A.; Kvamme, B. Modelling of Methane Hydrate Formation and Dissociation Using Residual Thermodynamics. In Proceedings of the 10th EUROSIM Congress on Modelling and Simulation, La Rioja, Logroño, Spain, 1–5 July 2019.
65. Aromada, S.A.; Kvamme, B.; Wei, N.; Saeidi, N. Enthalpies of Hydrate Formation and Dissociation from Residual Thermodynamics. *Energies* **2019**, *12*, 4726. [[CrossRef](#)]
66. Kvamme, B.; Aromada, S.A.; Gjerstad, P.B. Consistent Enthalpies of the Hydrate Formation and Dissociation Using Residual Thermodynamics. *J. Chem. Eng. Data* **2019**, *64*, 3493–3504. [[CrossRef](#)]
67. Svartas, T.M.; Fadnes, F.H. Methane hydrate equilibrium data for the methane-water-methanol system up to 500 bara. In Proceedings of the Second International Offshore and Polar Engineering Conference, San Francisco, CA, USA, 14–19 June 1992; pp. 614–619.
68. Ng, H.-J.; Robinson, D.B. Hydrate formation in systems containing methane, ethane, propane, carbon dioxide or hydrogen sulfide in the presence of methanol. *Fluid Phase Equilib.* **1985**, *21*, 145–155. [[CrossRef](#)]
69. Kuhs, W.F.; Chazallon, B.; Klapproth, A.; Pauer, F. Filling-Isotherms in Clathrate-Hydrates. *Rev. High Press. Sci. Technol.* **1998**, *7*, 1147–1149. [[CrossRef](#)]
70. Kang, S.-P.; Lee, H.; Ryu, B.-J. Enthalpies of dissociation of clathrate hydrates of carbon dioxide, nitrogen, (carbon dioxide+ nitrogen), and (carbon dioxide + nitrogen+ tetrahydrofuran). *J. Chem. Thermodyn.* **2001**, *33*, 513–521. [[CrossRef](#)]
71. Lievois, J.; Perkins, R.A.; Martin, R.; Kobayashi, R. Development of an automated, high pressure heat flux calorimeter and its application to measure the heat of dissociation and hydrate numbers of methane hydrate. *Fluid Phase Equilib.* **1990**, *59*, 73–97. [[CrossRef](#)]
72. Kvamme, B.; Coffin, R.; Zhao, J.; Wei, N.; Zhou, S.; Li, Q.; Saeidi, N.; Chien, Y.-C.; Dunn-Rankin, D.; Sun, W.; et al. Stages in the Dynamics of Hydrate Formation and Consequences for Design of Experiments for Hydrate Formation in Sediments. *Energies* **2019**, *12*, 3399. [[CrossRef](#)]
73. Jorgensen, W.L.; Madura, J. Temperature, and size dependence for Monte Carlo simulations of TIP4P water. *Mol. Phys.* **1985**, *56*, 1381–1392. [[CrossRef](#)]
74. Liu, S. Modelling CO2 Storage in Saline Aquifers with Reactive Transport Simulator RCB. Ph.D. Thesis, University of Bergen, Bergen, Norway, September 2011.
75. Chejara, A. Gas Hydrates in Porous Media: CO2 Storage and CH4 Production. Ph.D. Thesis, University of Bergen, Bergen, Norway, April 2014.
76. Vafaei, M.T. Reactive Transport Modelling of Hydrate Phase Transition Dynamics in Porous Media. Ph.D. Thesis, University of Bergen, Bergen, Norway, May 2015.
77. Jemai, K. Modeling Hydrate Phase Transitions in Porous Media Using a Reactive Transport Simulator. Ph.D. Thesis, University of Bergen, Bergen, Norway, October 2014.
78. Qorbani, K. Non-Equilibrium Modelling of Hydrate Phase Transition Kinetics in Sediments. Ph.D. Thesis, University of Bergen, Bergen, Norway, 15 December 2017.
79. Kvamme, B.; Zhao, J.; Wei, N.; Sun, W.; Saeidi, N.; Pei, J.; Kuznetsova, T. Hydrate Production Philosophy and Thermodynamic Calculations. *Energies* **2020**, *13*, 672. [[CrossRef](#)]
80. Kvamme, B.; Zhao, J.; Wei, N.; Saeidi, N. Hydrate—A Mysterious Phase or Just Misunderstood? *Energies* **2020**, *13*, 880. [[CrossRef](#)]
81. Kvamme, B. Consistent Thermodynamic Calculations for Hydrate Properties and Hydrate Phase Transitions. *Chem. Eng. Data.* **2020**, *65*, 2872–2893. [[CrossRef](#)]




---

# **PAPER X**

**THERMODYNAMICS OF HYDRATE SYSTEMS USING  
A UNIFORM REFERENCE STATE**



# Thermodynamics of hydrate systems using a uniform reference state

Bjørn Kvamme<sup>1</sup>  | Jinzhou Zhao<sup>1</sup> | Na Wei<sup>1</sup> | Qingping Li<sup>2</sup> |  
Navid Saeidi<sup>3</sup> | Wantong Sun<sup>1</sup> | Mojdeh Zarifi<sup>4</sup> | Tatiana Kuznetsova<sup>4</sup>

<sup>1</sup>State Key Laboratory of Oil and Gas Reservoir Geology and Exploitation, Southwest Petroleum University, Chengdu, China

<sup>2</sup>CNOOC Research Institutes Limited Liability Company, Beijing, China

<sup>3</sup>Environmental Engineering Department, University of California, Irvine, California, USA

<sup>4</sup>Department of Physics and Technology, University of Bergen, Bergen, Norway

## Correspondence

Bjørn Kvamme, State Key Laboratory of Oil and Gas Reservoir Geology and Exploitation, Southwest Petroleum University, Chengdu, China.  
Email: bkvamme@strategic-carbonllc.com

## Funding information

Science and Technology Department of Sichuan Province; National Key Research and Development Program

## Abstract

Formation of natural gas hydrates during processing and transport of natural gas has historically been a significant motivator for hydrate research. The last three decades have also seen the focus increasingly shifting towards CH<sub>4</sub> hydrates as a potential energy source. And in the context of climate changes, the impact of hydrate-related processes is coming more to the forefront as well. This interest is not only limited to leakage fluxes of CH<sub>4</sub> from natural gas hydrates but also flux from conventional hydrocarbon systems entering the seafloor at temperature and pressure allowing for hydrate formation. Alternative ways to treat formally overdetermined hydrate systems is an important focus in this work. The most common method used for assessment of hydrate phase transitions involves several fitted parameters to calculate the free energy difference between liquid water and empty hydrate. This technique calls for an empirical fitting of fundamental thermodynamic properties. Numerical codes based on this method limit the models to hydrate formation only from free gas and liquid water. This is at least true for all commercial and academic codes that were examined prior to this work. This work addresses the advantages in using residual thermodynamics for all phases, including hydrates. In addition to making it possible to handle many alternative hydrate routes leading to hydrate formation or dissociation, the presented method also opens a way to calculate a variety of needed thermodynamic properties (e.g., enthalpies of pure components and mixtures) in a simple and consistent way. This approach will be illustrated through calculations of various hydrate phase transitions, examples of free energy calculations for comparison of phase stability, and calculation of enthalpies of hydrate formation. Calculated enthalpies are compared with experimental data as well as results derived from applying the Clapeyron equation. Mechanisms for conversions of in situ CH<sub>4</sub> hydrate to facilitate safe CO<sub>2</sub> storage are also discussed. A very simple Clapeyron-based scheme for calculation of enthalpies for hydrate phase transitions is also proposed.

## KEYWORDS

hydrate, phase transitions, thermodynamic calculations



## 1 | INTRODUCTION

Possible formation of hydrates during processing and transport of hydrocarbons has motivated development of a variety of strategies for preventing associated flow problems during the latest 100 years. For any specific point inside the flowing part of a pipeline or equipment, and in a stationary flow situation, mass is being continuously supplied. None of the original phases (water and hydrocarbons) is totally removed before the pipeline is eventually blocked with hydrate. Another characteristic of the process is that two independent thermodynamic variables will be defined locally at every point. Thermodynamic equilibrium can only be achieved if there is a balance between the number of independent variables and defined constraints. Independent thermodynamic variables are temperature, pressure, and mole fractions of all components in all the phases. Constraints are imposed by conservation equations and conditions ensuring thermodynamic equilibrium. For a system of water and a single hydrate former outside the hydrate stability region, the independent variables are temperature and pressure of water and hydrate former phase plus the mole fractions of each. In total, this gives eight independent thermodynamic variables. The mole fractions in both phases must sum up to unity, resulting in two conservation equations. Thermal and mechanical equilibrium imposes two equilibrium conditions. Chemical equilibrium of the two components between the phases will add two more conditions, leaving us with just 2 degrees of freedom in this example. Fixing temperature and pressure will then define the system as a thermodynamic equilibrium system, and the mutual solubility of components can be calculated.

This counting scheme can easily be extended to the cases of when more phases are present. With only one hydrate phase, the number of independent variables will be equal to 12. The number of constraints is 11 in this case. Equilibrium can therefore only be achieved when only a single independent thermodynamic variable is defined. This has been known since experimental measurements of hydrate equilibrium started around 1940. Typically, hydrate was formed at a defined temperature by increasing pressure. At a defined pressure, the hydrate dissociation temperature was detected by gradually increasing temperature at defined, constant pressure.

Hydrate can form from water and separate hydrate former phase, as well as from dissolved hydrate former and water. In a nonequilibrium situation, these two hydrate phases will not be identical, as discussed in several papers; see, for instance, Kvamme et al.<sup>1</sup> Kvamme,<sup>2,3</sup> and Kvamme et al.<sup>4</sup> This means that no independent variables can be defined if the system

should reach equilibrium. Otherwise, the problem will be mathematically overdetermined. Mineral surfaces can serve as hydrate nucleation sites (Kvamme et al.<sup>5</sup>; Kvamme<sup>6</sup>). In a natural system of hydrates in sediments, both temperature and pressure are locally determined. The system will therefore become even more mathematically overdetermined. For flow in rusty pipelines, the minerals will take the form of rust.

The only thermodynamic variables typically discussed in conventional hydrate risk evaluation schemes are temperature and pressure, and they are normally used to define an equilibrium system. For nonequilibrium system, there is a need for a thermodynamic modeling approach which can evaluate hydrate stability for a variety of independent thermodynamic variables. This need was one of the major motivations and objectives in this work. This is not straightforward within the more conventional thermodynamic scheme that was developed in the 1970s. This scheme, which might be denoted a reference scheme, is based on empirical fitting of water chemical potential difference between empty hydrate and liquid water. And in order to get the pressure and temperature dependency, this method also requires empirical fitting of the difference in partial molar enthalpy difference for water in empty clathrate and liquid water and also corresponding differences in specific heat capacity and partial molar volumes. This will typically limit the possibility for modeling all possible routes to hydrate formation and dissociation. For these reasons, it is not considered as feasible to list many references to the reference approach. The reason that there are many references to Kvamme and Kvamme et al is simply because there are no other hydrate research groups that utilize residual thermodynamics for all phases. In the references provided, there are many simplified models that would make it easy for other research groups to convert old thermodynamic codes based of the reference method over to residual thermodynamics. And that is also why all these simplified correlations are provided.

How will the situation change with additional hydrate formers added to the mixture? A partial answer to this question lies in recognizing the fact that heterogeneous hydrate formation will occur on the interface between the hydrate former phase and the liquid water. In a simplified view, each component in the mixture will feel its own drive to condense at the actual temperature and pressure, as well as unique affinity for the liquid water. An example with some additional theoretical details can be found in Kvamme.<sup>7</sup> In summary, this selective adsorption combined with the first and the second laws of thermodynamics will result in a variety of hydrate phases, each with its own compositions.



Another objective of this work is the need for a thermodynamic model based on a universal (for all phases) reference state which makes it possible to directly compare phase stabilities and driving forces for transport of components between phases. The use of ideal gas as a reference state also for all components in hydrate makes the hydrate phase naturally consistent with other co-existing phases. There is no need for artificial reference states since ideal gas is thermodynamically straightforward in modeling. This reference state also provides a direct bridge between molecular dynamics simulations of model systems since ideal gas is sampled in momentum space and residual contributions are samples in configurational space. This opens up for modeling of hydrate nucleation in many phases. Hydrate nucleation towards mineral surfaces (Kvamme et al<sup>1</sup>) is just one example in this direction. In the context of this work, this is not an important focus and for that reason it is not crucial to spend more space on a literature review on the topic.

Natural gas hydrates in sediments are rapidly becoming more and more relevant as potential energy sources, while the hydrocarbon fluxes into oceanic water and geohazard aspects related to hydrate filled sediments are now in the forefront of hydrate research. Formation and dissociation of hydrates are an example of kinetically coupled dynamics and associated mass and heat transport. How well the coupling of these processes is handled mathematically will depend on the rigorousness of the dynamic model. We have utilized the phase field theory (PFT). Classical nucleation theory (CNT) is simple enough to be easily implemented into reservoir flow models for hydrate systems and risk evaluation tools related to flow in pipelines. A third motivation for this work is the need for a consistent modeling of thermodynamic properties.

The focus of this work is very much centered on the use of physically existing reference state (read: ideal gas) for all components in all phases. This is convenient because all phases, including different hydrate phases formed from different routes (gas/water, water solution, adsorbed on solid surfaces, gas), can be directly compared in terms of stability using Gibbs free energy. It is not known if any other researchers use ideal gas for all components in all phases as reference state, and as such, there are no other publications to refer to. And it is not within the scope of this work to compare and argue for the reference state used in this work as compared with other platforms that use artificially constructed reference state. Quite the opposite, in the papers referred to here that utilize residual thermodynamics, it is demonstrated that the equations can be very easily fitted and represented by very simple equations and correlations that make it very easy for those that want to utilize our residual scheme.

That does not in any sense mean that the many excellent publications from other research groups are not appreciated. On the contrary, the reason for the very few references to these in the context of this work is simply the special and narrow focus of this work. Readers are therefore directed to various books that provides a broader insight into the state-of-the-art hydrate research. The books by Sloan and Koh<sup>8</sup> and Mokogon<sup>9</sup> are just two of many titles.

In a nonequilibrium system, it would make more sense to talk about stability limits in various sets of independent thermodynamic variables, rather than “equilibrium”. Thus, a residual thermodynamic model system for hydrate phase transition is discussed in Section 2. Even if the local condition falls inside the hydrate formation zone in terms of temperature and pressure, the formed hydrate will still dissociate if the surrounding aqueous phase contains less hydrate former than its lowest stability limit. And hydrate can form from solution in water when the concentration of hydrate formers in water is higher than hydrate stability limits. In Section 3, focus is limited to temperature and pressure as stability limits and concentration of hydrate formers in surrounding water as another example. A third example is stability limits of water in gas, which has been discussed in a  $d\mu = RTd\ln f$  number of papers on hydrate risk analysis during transport of natural gas, or CO<sub>2</sub>, containing water (Kvamme & Aromada,<sup>10</sup> Kvamme et al,<sup>11</sup> Kvamme & Aromada,<sup>12</sup> Kvamme et al,<sup>13</sup> Aromada & Kvamme,<sup>14</sup> Aromada & Kvamme<sup>15</sup>).

Another important aspect of the residual thermodynamic approach presented here is the opportunity of calculating free energies for hydrates formed via different pathways. This can be hydrates formed from the same components or stability differences between hydrates of various components or mixtures. This is important for understanding of which hydrates that will dissociate first if the system is exposed to heat, salts, and so forth. Free energy minimizing schemes are frequently used for solving gas/liquid equilibrium or even hydrate equilibrium, like in the approach by Ballard et al (2004) as also applied by Jäger et al.<sup>16</sup> The formalism used in this approach, as proposed by Ballard et al<sup>17</sup> is a development compared with the old way of empirical fitting chemical potential difference between liquid water and empty clathrate. But fugacity is still not directly an energy quantity. Fugacity is convenient in engineering calculations because it is directly a pressure proportional quantity. Fugacity is defined by the following:

$$d\mu = RTd\ln f \quad (1)$$

Even for a pure component, fugacity is not useful without a reference state for integrating Equation (1). For



an equation of state Equation (1) for a pure component fluid, it can be integrated in one step from ideal gas fugacity, which is pressure. Pressure does not directly contain any direct component information. Fugacity is not used in this work for many reasons. Reference state for fugacity in residual thermodynamics is simply pressure and does not distinguish between components. The reason that Equation (1) is put in here is, however, to stress that hydrate as a mixed component does not have a fugacity. Empirical formulations of hydrate fugacity can be found in several journal papers, but the definition is thermodynamically inconsistent. Fugacity is defined on a component basis as given by Equation (1).

In integrated form left-hand side ends up with chemical potential of real gas minus that of ideal gas at same temperature and pressure. Right-hand side simply ends up as the natural logarithm of the fugacity coefficient. In contrast to fugacity, chemical potential is a driving force for chemical work. Sticking to chemical potential formalism for hydrate has the advantage of being directly usable in comparing free energies of hydrate formed from various routes. As one example, the hydrate formed heterogeneously on gas/liquid water interface is different from hydrates formed homogeneously from solution of hydrate formers because composition, density, and Gibbs free energy are different between the two hydrates. Actually, a range of different hydrates can be formed from solution in water depending on the concentration of hydrate former. As will be discussed later, hydrate can form from water solution at concentration in between gas/liquid solubility and minimum concentration for hydrate stability.

Yet another aspect of residual thermodynamic models for hydrate phase transitions is the ability to calculate thermodynamic properties for many other phases that are relevant in natural systems or industrial systems. Examples include mineral surfaces as mentioned above in terms of water adsorption on rust (Kvamme & Aromada,<sup>10</sup> Kvamme et al<sup>11</sup>, Kvamme & Aromada,<sup>12</sup> Kvamme et al,<sup>13</sup> Aromada & Kvamme,<sup>14</sup> Aromada & Kvamme<sup>15</sup>) during transport of hydrate forming fluids containing dissolved and distributed water. Conventional calculation approaches based on empirical models for difference between chemical potential in liquid water and chemical potential for water in empty clathrate is generally able to model the thermodynamics of these phase transitions. In a much wider sense, these are just some examples of a generally totally different platform for thermodynamic properties using residual thermodynamics. State of the art level in molecular dynamics simulations of water systems is on a level that will permit the inclusion of solid surfaces in hydrate phase transitions in sediments. Kvamme et al<sup>1</sup> is just one example of hydrate

nucleation towards mineral surfaces in sediments. While atomistic experimental methods can measure structures of water towards mineral surfaces, the thermodynamic properties need to be calculated using statistical mechanics and molecular dynamics simulations. Fortunately, molecular dynamics simulations also contain samplings of structures that can be verified towards measured structures for real systems. In a wider context, a thermodynamic platform that can be used to bring new knowledge on the dynamic and stationary behavior hydrates in nature and industry is provided. The few examples mentioned, and as published already, are just some few examples of a pathway towards a more complete thermodynamic and kinetic description of hydrates in industrial setting and in nature.

Since the free energy values are also needed in kinetic models and the value of a consistent reference system (ideal gas) for hydrate, liquid water, and hydrate former phase is that free energy minimizing approaches are numerically smooth.

## 2 | RESIDUAL THERMODYNAMICS FOR HYDRATE SYSTEMS

### 2.1 | Residual models for water systems

A thermodynamic model consists of a reference state, a way to describe the entropy effects of ideal mixing, and finally a model estimating the differences between the real system and its ideal mixing representation.

Molecular dynamics simulation in the classical approximation is based on orthonormal splitting of the canonical partition function into momentum space (ideal gas) and configurational space (effects of molecule interactions).

Kvamme and Tanaka<sup>18</sup> utilized a harmonic oscillator approach to calculate chemical potentials for ice and water in empty (see below) hydrate structures I and II. The properties for ice were extrapolated to liquid water using experimental enthalpy of water dissociation at 273.15 K and specific heat capacity for liquid water for temperatures above 273.15 K. The result provided a residual thermodynamic model system for the water phases. The statistical mechanical model for hydrate in our earlier paper (Kvamme and Tanaka<sup>18</sup>) is not dissimilar to that of van der Waals and Platteeuw<sup>19</sup> but more general since it also accounts for effects of flexible water lattice and associated destabilization effect of large guest molecules.

The residual thermodynamic model for water in hydrate is given by:



$$\mu_{H_2O}^H = \mu_{H_2O}^{O,H} - \sum_{k=1,2} RT\nu_k \ln \left( 1 + \sum_j h_{kj} \right) \quad (2)$$

where  $\mu_{H_2O}^{O,H}$  is the chemical potential for water in an empty clathrate for the given hydrate structure. This chemical potential has been derived from molecular dynamics simulations via the harmonic oscillator approach (Kvamme & Tanaka<sup>18</sup>).  $k$  is an index for cavity types and  $j$  is an index for guest molecules in the various cavities. The number of cavities is  $\nu$ , with subscripts  $k$  for large and small cavities, respectively. For structure I, which is the main focus here,  $\nu_{\text{large}} = 3/24$  and  $\nu_{\text{small}} = 1/24$ . For structure II, the corresponding numbers are  $\nu_{\text{large}} = 1/17$  and  $\nu_{\text{small}} = 2/17$ .  $R$  is the universal gas constant, and  $T$  is temperature. The reference pressure for empty clathrate water chemical potential is 1 bar. It is corrected to real pressure through a trivial pointing correction. The molar volume of water in empty clathrate for the relevant structure is trivially calculated from the structure and cell dimensions.

$h_{kj}$  is the canonical partition function for guest molecule of type  $j$  in cavity type  $k$ . This is given by Kvamme and Tanaka<sup>18</sup>:

$$h_{kj} = e^{\beta [\mu_{kj}^H(T, P, \vec{x}^H) - \Delta g_{kj}(T)]} \quad (3)$$

where  $\beta$  is the inverse of the universal gas constant times temperature.  $\Delta g_{kj}(T)$  is the free energy change on including molecule  $j$  in cavity  $k$  (Kvamme et al,<sup>20</sup> Kvamme et al,<sup>21</sup> Qasim,<sup>22</sup> Buanes,<sup>23</sup> Baig,<sup>24</sup> Tegze et al,<sup>25</sup> Svandal et al<sup>26</sup>), as well as less sophisticated CNT (Kvamme et al,<sup>27</sup> Kvamme,<sup>2</sup> Kvamme,<sup>3</sup> Kvamme et al<sup>13</sup>).

The residual thermodynamic based approach for liquid water is given by:

$$\mu_{H_2O}^{\text{water}}(T, P, \vec{x}^{\text{water}}) = \mu_{H_2O}^{\text{pure}, H_2O}(T, P) + RT \ln \left[ \chi_{H_2O}^{\text{water}, \text{water}}(T, P, \vec{x}^{\text{water}}) \right] \quad (4)$$

The first term on the right-hand side is the chemical potential for water as pure liquid, which is also available in Kvamme and Tanaka<sup>18</sup> as a simple analytical expression. Supercripts “water” denotes the liquid water phase, while subscript “H<sub>2</sub>O” means water as a component. The first term in the brackets of the last term is the ideal liquid mixing contribution, while  $\chi_{H_2O}^{\text{water}, \text{water}}$  is the deviation from ideal liquid mixture for water and approaches unity when mole-fraction water approach 1.0.

Correlated chemical potentials for water in ice, liquid water, and empty structures I and II with ideal gas as

reference are given in Table 1 below. These are values estimated at 1 bar and thus have to be corrected to actual pressure with a trivial Poynting correction using the molar volume for water in the different phases listed in Table 1.

## 2.2 | Residual thermodynamics for gas or liquid hydrate former phase and dissolved hydrate formers

$$\mu_j^{\text{gas}}(T, P, \vec{x}) = \mu_j^{\text{ideal gas, pure}}(T, P) + RT \ln \left[ \chi_j \phi_j^{\text{gas}}(T, P, \vec{x}) \right] \quad (5)$$

where  $\chi_j$  is mole fraction of component  $j$  in the gas mixture.  $\vec{x}$  is the mole-fraction vector for the gas mixture.  $P$  is pressure. Ideal gas chemical potential (first term on right-hand side) is trivially given by statistical mechanics from molecular weight and moments of inertia for molecule  $j$ .  $\phi_j^{\text{gas}}$  is the fugacity coefficient for component  $j$  in the gas mixture at the actual  $T$  and  $P$ . This is trivially unity for ideal gas and generally derived from Helmholtz free energy for any given equation of state (the Soave-Redlich-Kwong<sup>28</sup> EoS was used in this work).

Calculation of infinite dilution chemical potential via molecular dynamics simulations can be performed by several well-established techniques. Asymmetric-excess models for CH<sub>4</sub> and CO<sub>2</sub> based on molecular modeling are also available but too space consuming to repeat in this paper. Interested readers are referred to Kvamme<sup>3</sup> and Kvamme.<sup>4</sup>

## 3 | HETEROGENEOUS AND HOMOGENEOUS HYDRATE FORMATION

### 3.1 | Heterogeneous hydrate formation

Figure 1 presents the temperature–pressure projection of hydrate stability limits, while Figure 2 plots free

TABLE 1 Parameters for dimensionless chemical potential functions

| Water phase, $m$               | $\alpha_0$ | $\alpha_1$ |
|--------------------------------|------------|------------|
| Empty structure I              | −21.333    | −18.246    |
| Empty structure II             | −21.374    | −18.186    |
| Ice ( $T < 273.15$ K)          | −21.690    | −19.051    |
| Liquid water ( $T > 273.15$ K) | −21.690    | −16.080    |



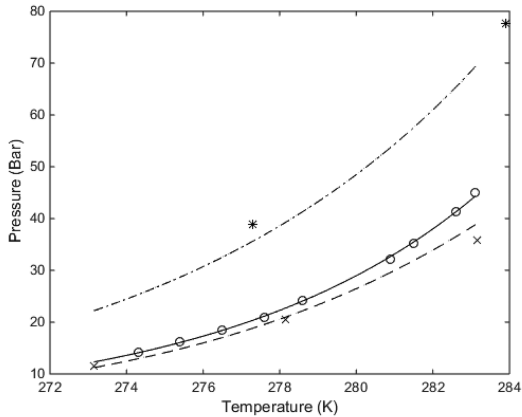


FIGURE 1 Calculated pressure temperature hydrate stability limits for CH<sub>4</sub> (dash dot), CO<sub>2</sub> (solid), CO<sub>2</sub> mixture with 1 mole % H<sub>2</sub>S (dash). \* are experimental data for pure CH<sub>4</sub> from Tumba et al<sup>29</sup>; o are experimental data for pure CO<sub>2</sub> from Herri et al<sup>30</sup>; x are experimental data for CO<sub>2</sub> mixture with 1 mole % H<sub>2</sub>S from Chen et al<sup>31</sup>

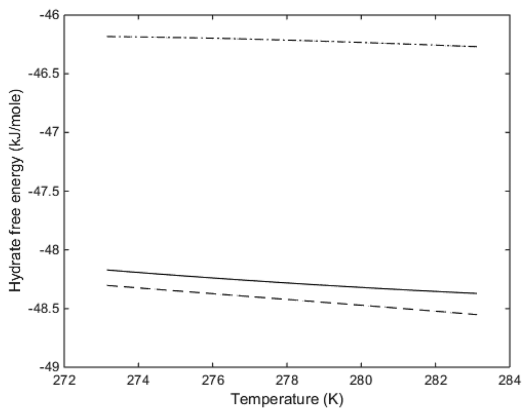


FIGURE 2 Calculated free energies for pure CH<sub>4</sub> hydrate (dash dot), pure CO<sub>2</sub> hydrate (solid), and a mixture with 1 mole % H<sub>2</sub>S in CO<sub>2</sub> (dash)

energies in case of pure CH<sub>4</sub>, pure CO<sub>2</sub> hydrate, and 1 mole % H<sub>2</sub>S-CO<sub>2</sub> mixture. These solutions have been obtained by setting chemical potential for water in hydrate (Equation 2) to be equal to that of liquid water (Equation 4). The chemical potential of guest molecules in gas (Equation 5) is set to be the same as that of guest in hydrate (Equation 3). See Kvamme<sup>3</sup> and Kvamme<sup>4</sup> for values of free energies of inclusion utilized in Equation (3).

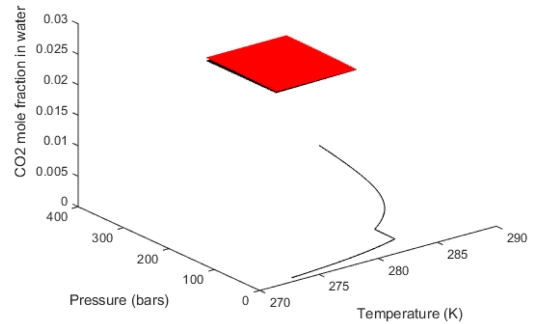


FIGURE 3 Stability limits for hydrate in temperature pressure and liquid water CO<sub>2</sub> concentration limits. Black curve for  $x_{\text{CO}_2} = 0$  is the temperature pressure projection with hydrate region to the left of the curve. Black contour is the minimum  $x_{\text{CO}_2}$  in surrounding water needed to keep the hydrate stable. Red contour is the solubility of CO<sub>2</sub> in water

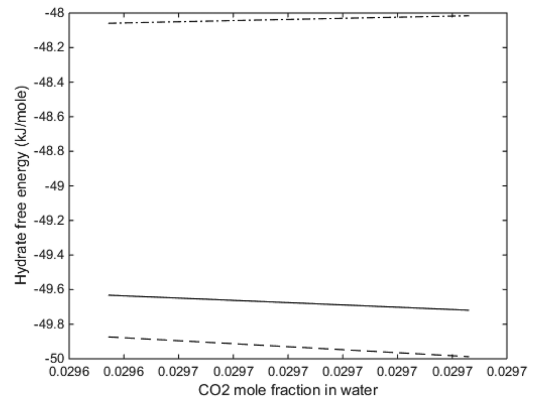


FIGURE 4 Free energy (solid curve) for hydrate formed between minimum hydrate stability mole-fraction and solubility of CO<sub>2</sub> in water at 284 K and 200 bar. Dashed curve is chemical potential for water, and dash dot curve is chemical potential of the dissolved CO<sub>2</sub> in the water

### 3.2 | Homogeneous hydrate formation

Two sets of calculations are relevant for homogeneous hydrate formation from hydrate formers dissolved in water. Solubility of hydrate formers in water will define the limits of available hydrate formers. If the chemical potential of water in liquid is lower than that of water in hydrate, hydrate will dissociate. The lower limit of hydrate stability towards the surrounding aqueous phase becomes relevant when the liquid phase water and hydrate have the same chemical potential, and the guest chemical potential in aqueous solution is the same as in hydrate in Equation (3). An example is given in Figure 3



below. The contours for solubility (red) almost overshadow the black contour corresponding to the minimum aqueous CO<sub>2</sub> concentration required to keep hydrate stable. Hydrate can grow for concentrations in between the black and red contours. Concentration above red will imply degassing.

Figure 4 plots the chemical potentials of components and the free energy of the formed hydrate at 284 K and 200 bar.

#### 4 | HYDRATE NUCLEATION AND GROWTH

Within the limited space of this work, it is not possible to discuss either critical hydrate size or corresponding nucleation times subsequent hydrate growth and induction time. See Kvamme et al<sup>1,4,27</sup> for relevant examples. In CNT, the thermodynamic control term contains the free energy change of the phase transition. The prefactor is the mass transport implicitly coupled to the associated heat transport. In case of hydrate formation, this heat transport combines various transport mechanisms (conduction, convection, radiation). A consistent enthalpy of formation will be given by the following thermodynamic relationship:

$$\frac{\partial \left[ \frac{\Delta G^{\text{Phase transition}}}{RT} \right]_{P, \vec{N}}}{\partial T} = - \left[ \frac{\Delta H^{\text{Phase transition}}}{RT^2} \right] \quad (6)$$

See Kvamme,<sup>4,6</sup> Kvamme et al<sup>32</sup> and Aromada et al<sup>33</sup> for details on the theory. An important difference from the approach of Lee and Holder<sup>34</sup> is that Equation 6 is totally consistent with calculations of Gibbs free energy using the same model. From a basic physical point of view, it means that the entropy of a phase transition is consistent. In ore plain language, it means that when hydrate formation is calculated according to internally consistent free energy and enthalpy, it should end up as a realistic phase in terms of structure as reflected by the entropy of the phase. Another important consistency is in kinetic modeling. In CNT, Gibbs free energy and enthalpy are trivially connected as illustrated by Kvamme et al.<sup>4</sup>

#### 5 | CO<sub>2</sub>/CH<sub>4</sub> HYDRATE EXCHANGE FOR COMBINED SAFE CO<sub>2</sub> STORAGE AND ENERGY PRODUCTION

The CO<sub>2</sub>/CH<sub>4</sub> system is interesting because a pure CO<sub>2</sub> hydrate will have virtually zero filling of small cavities; thus, CH<sub>4</sub> entering them even in a small degree will lower the heat of formation. Similarly, the CH<sub>4</sub> hydrate

will achieve higher stability and lower formation heat by addition of CO<sub>2</sub>. This trend can be observed in Figure 5.

Injection of CO<sub>2</sub> into CH<sub>4</sub> hydrates in sediments is thermodynamically feasible for two reasons. A frequent misunderstanding is that CO<sub>2</sub> hydrate is only more stable than CH<sub>4</sub> hydrate for a limited range of conditions. The basis for this is evaluation of temperature pressure projections of hydrate stability limits like the one in

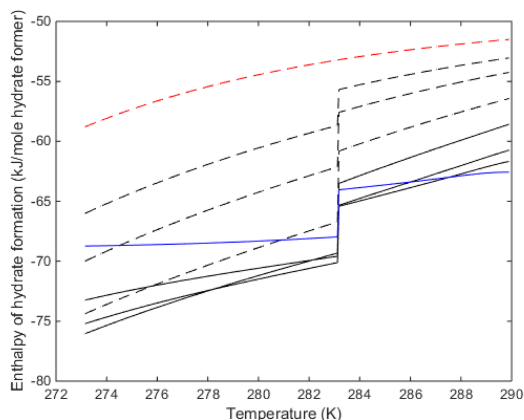


FIGURE 5 Enthalpies of hydrate formation for pure CH<sub>4</sub> hydrate (red dash) along temperature pressure stability limit curve. Solid blue is hydrate formation for pure CO<sub>2</sub> hydrate along temperature pressure stability limit curve. Dashed black curves are enthalpies of hydrate formation for various mixtures which are rich in CH<sub>4</sub>. Curves are for 10 mole% CO<sub>2</sub> (top black dash), then 20 mole% CO<sub>2</sub> (black dash) and 40 mole% CO<sub>2</sub> (bottom black). Solid black curves are for 90 mole% CO<sub>2</sub> (top black), then 80 mole% CO<sub>2</sub> (black dash) and 60 mole% CO<sub>2</sub> (bottom black)

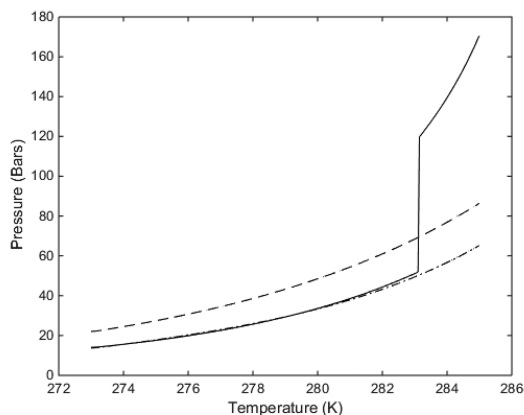


FIGURE 6 Calculated pressure temperature hydrate stability limits for CH<sub>4</sub> (dash), CO<sub>2</sub> (solid), and CH<sub>4</sub>/C<sub>2</sub>H<sub>8</sub> mixture with 10 mole % C<sub>2</sub>H<sub>8</sub> (dash dot)



Figure 6. According to this plot, the hydrate stability region for  $\text{CH}_4$  hydrate and for  $\text{CH}_4$  hydrate formed from 90 mole percent  $\text{CH}_4$  and rest  $\text{C}_2\text{H}_6$  is more favorable than temperature pressure hydrate stability region. For the  $\text{CH}_4/\text{C}_2\text{H}_6$  mixture, it is even almost the same as for  $\text{CO}_2$  hydrate up to the phase transition temperature for  $\text{CO}_2$ . Temperature and pressure are two of many independent thermodynamic variables. For a system controlled by temperature, pressure, and concentrations of all components in all phases, the thermodynamic function for phase stability is Gibbs free energy. With ideal gas as reference state for all components in all co-existing phases, then values for phase free energies for different phases are directly comparable. From Figure 7, it is seen

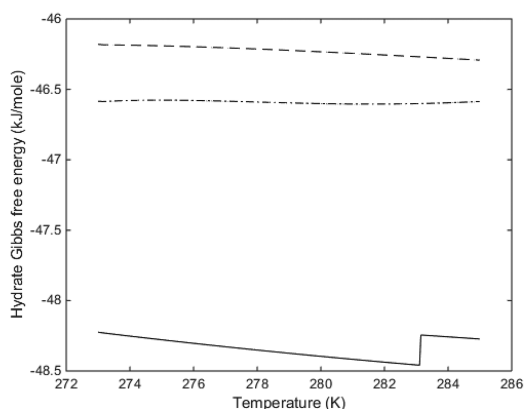


FIGURE 7 Calculated Gibbs free energy for hydrate formed from  $\text{CH}_4$  and water (dash), from  $\text{CO}_2$  and water (solid) and from  $\text{CH}_4/\text{C}_2\text{H}_8$  mixture with 10 mole %  $\text{C}_2\text{H}_8$  and water (dash dot)

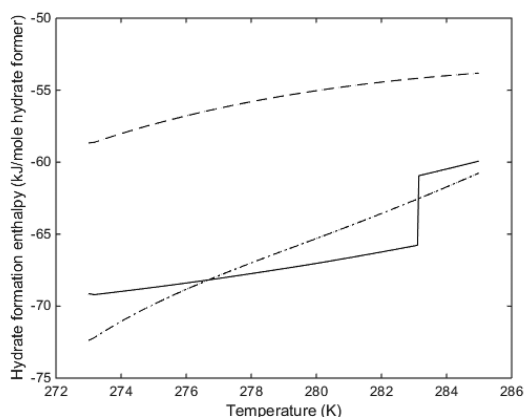


FIGURE 8 Calculated enthalpy for hydrate formation for  $\text{CH}_4$  and water (dash), for  $\text{CO}_2$  and water (solid), and for  $\text{CH}_4/\text{C}_2\text{H}_8$  mixture with 10 mole %  $\text{C}_2\text{H}_8$  and water (dash dot)

that  $\text{CO}_2$  hydrate is significantly more stable than for the  $\text{CH}_4$  hydrate and  $\text{CH}_4/\text{C}_2\text{H}_6$  hydrate. Injection of  $\text{CO}_2$  into  $\text{CH}_4$  hydrate-filled sediment will lead to formation of a new  $\text{CO}_2$  hydrate from pore water and injected  $\text{CO}_2$ . The released heat from this hydrate formation will contribute to a dissociation of the in situ hydrate. In the example case of pure  $\text{CH}_4$  hydrate and the second case of a mixed  $\text{CH}_4/\text{C}_2\text{H}_6$  hydrate, the enthalpies of hydrates formation for the three systems are plotted in Figure 8.

Most natural gas hydrates in nature are formed from biogenic  $\text{CH}_4$  in the upper crust. It does not, however, exclude that slow hydrate dynamic may suppress access for thermogenic hydrates from below. As such, the picture might be much more complex for many systems in a real hydrate production case that stretches over many years and also releases access to thermogenic hydrocarbon sources. This will add hydrate formers like propane and iso-butane as hydrate formers. Potentially, the thermogenic hydrocarbon source will also contain sour gasses like  $\text{H}_2\text{S}$ . In a follow-up to this work, it will therefore be relevant to investigate some real thermogenic mixtures. Due to the hydrocarbon composition, hydrates from these mixtures will typically form mixtures of structure I and II hydrates. Structure H hydrates are more rare, but they are found some places, like in the Gulf of Mexico (Sassen & MacDonald<sup>35</sup>). The example with 10 mole %  $\text{C}_2\text{H}_6$  is not representative for a natural gas system but was used to illustrate that temperature pressure stability limits do not provide the hydrate stability limit information that is needed in production planning. Figure 7 tells us that a new  $\text{CO}_2$  hydrate is sufficiently more thermodynamic stable than the two other hydrates. Figure 8 tells us that formation of a new  $\text{CO}_2$  hydrate releases sufficient heat to dissociate  $\text{CH}_4$  hydrate but may not be sufficient for the mixed hydrate. Injection of  $\text{CO}_2$  with limited amounts of a thermodynamic inhibitor like methanol is likely to produce the mixed hydrate efficiently (Kvamme et al<sup>13</sup>).

A number of interesting papers due to Longinos and Parlaktuna (Longinos & Parlaktuna<sup>36–39</sup>) discuss interesting experiments on hydrate formation dynamics and effects of various types of chemicals that change hydrate formation dynamics. While these are very interesting papers, they stretch outside the main focus of this work. Hydrate phase transition dynamics is by nature on nanoscale. Hydrodynamic effects of various stirring devices and/or hydrodynamic flow are on microscale and up. It is of course connected since hydrodynamics will break hydrate films and increase contacts surfaces and a variety of other effects. Different chemicals have effects on different scales and some will affect interfaces involved in phase transitions as well. These effects are outside the scope of this work. Generally, phase transition for



nucleation and growth is well described in physics. Induction times may be interpreted as onset of massive growth and is sensitive to hydrodynamics. It is not well defined and depends on resolution of monitoring methods. In the absence of induced hydrodynamics, it has been demonstrated that slow mass transport through blocking hydrate films can predict experimental induction times (Kvamme et al<sup>27</sup>). Another aspect related to the papers by Longinos and Parlaktuna<sup>36–39</sup> is the effect of selective adsorption of hydrate that forms on water surfaces, which, for instance, implies that adsorption of propane on liquid water surface will dominate compared with adsorption of methane (Kvamme<sup>7</sup>). In summary, comparison with theories and experimental papers on hydrodynamic level requires a different theoretical approach than what is discussed here. The primary focus here is thermodynamics of hydrate phase transitions. Efficient numerical algorithms make it possible to extend PFT<sup>20,25,40–48</sup> to mm scale and can make it possible to incorporate many of the effects studied by Longinos and Parlaktuna.<sup>36–39</sup>

## 6 | CONCLUSIONS

A consistent residual thermodynamic model system is demonstrated in this work. One advantage of applying residual thermodynamics for all the phases is ensuring the same reference state for all components in all the phases. In case of nonequilibrium systems like hydrate-filled sediments and hydrate in transport and industrial processes, this will make free energy minimization easier and more transparent. Another benefit of our approach is that it makes it possible to handle the variety of stability limits and routes of hydrate formation and dissociation within the same framework. Specifically, it is argued that there is a need for a more complete hydrate stability description that also includes concentration of hydrate formers in surrounding water. And finally, the model provides free energies and enthalpies of hydrate phase transitions, which are crucial for analyzing the dynamics of real-life hydrate formation and dissociation in nature. As an example, it demonstrated that the free energy of CO<sub>2</sub> hydrate is roughly 2 kJ/mole hydrate more stable than CH<sub>4</sub> hydrate, which is important when these two types of hydrates are in the same sediment. Practically, this means that the hydrates of highest free energy will dissociate first when salinity increases or other factors affect hydrate stability in the pores. The implicit model for enthalpy of hydrate formation is simple, consistent, and general for mixtures. Calculations of enthalpies of hydrate formation have been illustrated for mixtures of CH<sub>4</sub> and CO<sub>2</sub>.

## ACKNOWLEDGEMENTS

This research was supported by the National Key Research and Development Program (No. 2019YFC0312302, No. 2019YFC0312303, and No. 2018YFC0310203), the National Natural Science Foundation Item of China (No. 51874252 and No. 5177041544), and the Basic Applied Research Key Projects of Science and Technology Department of Sichuan Province (No. 2019YJ0419 and No. 2019YJ0351). Support from Hyzen Energy Inc. is appreciated.

## ORCID

Bjørn Kvamme  <https://orcid.org/0000-0003-3538-5409>

## REFERENCES

1. Kvamme B, Zhao J, Wei N, et al. Hydrate production philosophy and thermodynamic calculations. *Energies*. 2020; 13(3):672.
2. Kvamme B. Enthalpies of hydrate formation from hydrate formers dissolved in water. *Energies*. 2019;12(6):1039-1058.
3. Kvamme B. Environmentally friendly production of methane from natural gas hydrate using carbon dioxide. *Sustainability*. 2019;11(7):1964-1987.
4. Kvamme B, Aromada S, Saeidi N, Hustache-Marmou TPJ, Gjerstad P. Hydrate nucleation, growth and induction. *ACS Omega*. 2020;5(6):2603-2619.
5. Kvamme B, Kuznetsova T, Kivelæ, P.-H. Adsorption of water and carbon dioxide on hematite and consequences for possible hydrate formation. *Phys Chem Chem Phys*. 2012;2012(14): 4410-4424.
6. Kvamme B. Consistent thermodynamic calculations for hydrate properties and hydrate phase transitions. *Chem Eng Data*. 2020;65(5):2872-2893.
7. Kvamme B. Thermodynamic limitations of the CO<sub>2</sub>/N<sub>2</sub> mixture injected into CH<sub>4</sub> hydrate in the Ignik Sikumi field trial. *J Chem Eng Data*. 2016;61(3):1280-1295.
8. Sloan ED, Koh CA. *Clathrate Hydrates of Natural Gases*. 3rd ed. Boca Raton, USA: CRC Press; 2007.
9. Mokogon Y. F. 1997. *Hydrate of Hydrocarbons, Pennwell Corp, 1 edition (September 1, 1997)*.
10. Kvamme B, Aromada SA. Risk of hydrate formation during processing and transport of Troll gas from the North Sea. *J Chem Eng Data*. 2017;62(7):2163-2177.
11. Kvamme B, Aromada SA. Alternative routes to hydrate formation during processing and transport of natural gas with significant amount of CO<sub>2</sub>: Sleipner gas as a case study. *J Chem Eng Data*. 2018;63(3):832-844.
12. Kvamme B, Aromada SA, Kuznetsova T, Gjerstad PB, Canonge PC, Zarifi M. Maximum tolerance for water content at various stages of a Natuna production. *Heat Mass Transfer*. 2018;55:1059-1079.
13. Kvamme B, Selvåg J, Aromada SK, Saeidi N, Kuznetsova T. Methanol as hydrate inhibitor and hydrate activator. *Phys Chem Chem Phys*. 2018;20(34):21968-21987.
14. Aromada SA, Kvamme B. Impacts of CO<sub>2</sub> and H<sub>2</sub>S on the risk of hydrate formation during pipeline transport of natural gas. *Front Chem Sci Eng*. 2019;13(3):616-627.



15. Aromada SA, Kvamme B. New approach for evaluating the risk of hydrate formation during transport of hydrocarbon hydrate formers of sI and sII. *AIChE J.* 2019;65(3):1097-1110.
16. Jäger A, Vinš V, Span R, Hrubý J. Model for gas hydrates applied to CCS systems part III. Results and implementation in trend 2.0. *Fluid Phase Equilib.* 2016;429:55-66.
17. Ballard AL, Sloan ED Jr. The next generation of hydrate prediction I. Hydrate standard states and incorporation of spectroscopy. *Fluid Phase Equilibria.* 2002;194:371-383.
18. Kvamme B, Tanaka H. Thermodynamic stability of hydrates for ethylene, ethane and carbon dioxide. *J Phys Chem.* 1995; 99(18):7114-7119.
19. Van der Waals JH, Platteeuw JC. Clathrate solutions. *Adv Chem. Phys.* 1059(2):1-57.
20. Kvamme B, Kuznetsova T, Kivelæ PH, Bauman J. Can hydrate form in carbon dioxide from dissolved water? *Phys Chem Chem Phys.* 2013;15(6):2063-2074.
21. Kvamme B, Graue A, Buanes T, Kuznetsova T, Ersland G. Storage of CO<sub>2</sub> in natural gas hydrate reservoirs and the effect of hydrate as an extra sealing in cold aquifers. *Int J Greenh Gas con.* 2007;2007(1):236-246.
22. Qasim M. *Microscale Modeling of Natural Gas Hydrates in Reservoirs.* Bergen, Norway: PhD thesis, University of Bergen; 2012.
23. Buanes T. *Mean-Field Approaches Applied to Hydrate Phase Transition.* Bergen, Norway: PhD thesis, University of Bergen; 2006.
24. Baig K. *Nano to Micro Scale Modeling of Hydrate Phase Transition Kinetics.* Bergen, Norway: PhD thesis, University of Bergen; 2017.
25. Tegze G, Pusztai T, Tóth G, Gránásy L. Multiscale approach to CO<sub>2</sub> hydrate formation in aqueous solution: phase field theory and molecular dynamics. *Nucleation Growth J Chem Phys.* 2006;124(23):234710-234722.
26. Svandal A, Kuznetsova K, Kvamme B. Thermodynamic properties and phase transitions in the H<sub>2</sub>O/CO<sub>2</sub>/CH<sub>4</sub> system. *Phys Chem Chem Phys.* 2006;8(14):1707-1713.
27. Kvamme B, Coffin RB, Wei N, et al. Stages in dynamics of hydrate formation and consequences for design of experiments for hydrate formation in sediments. *Energies.* 2019;12: 3399-3419.
28. Soave G. Equilibrium constants from a modified Redlich-Kwong equation of state. *Chem Eng Sci.* 1972;27(6):1197-1203.
29. Tumba K, Reddy P, Naidoo P, et al. Phase equilibria of methane and carbon dioxide clathrate hydrates in the presence of aqueous solutions of tributylmethylphosphonium methylsulfate ionic liquid. *J Chem Eng Data.* 2011;56(9):3620-3629.
30. Herri J-M, Bouchemoua A, Kwaterski M, Fezoua A, Ouabbas Y, Cameirao A. Gas hydrate equilibria for CO<sub>2</sub>-N<sub>2</sub> and CO<sub>2</sub>-CH<sub>4</sub> gas mixtures—Experimental studies and thermodynamic modelling. *Fluid Phase Equilibria.* 2011;301(2): 171-190.
31. Chen L, Lu H, Ripmeester JA. Dissociation conditions and Raman spectra of CO<sub>2</sub> + SO<sub>2</sub> and CO<sub>2</sub> + H<sub>2</sub>S hydrates. *Ind Eng Chem Res.* 2015;54(21):5543-5549.
32. Kvamme B, Aromada SA, Berge Gjerstad P. Consistent enthalpies of the hydrate formation and dissociation using residual thermodynamics. *J Chem Eng Data.* 2019;64(8): 3493-3504.
33. Aromada SA, Kvamme B, Wei N, Saeidi N. Enthalpies of hydrate formation and dissociation from residual thermodynamics. *Energies.* 2019;12:4726-4752.
34. Lee S-Y, Holder GD. Model for gas hydrate equilibria using a variable reference chemical potential: Part 1. *AIChE J.* 2002; 48(1):161-167.
35. Sassen R, MacDonald IR. Evidence of structure H hydrate, Gulf of Mexico Continental Slope. *Organic Geochem.* 1994;22(6): 1029-1032.
36. Longinos SN, Parlaktuna M. Kinetic analysis of dual impellers on methane hydrate formation. *Int J Chem Reactor Eng.* 19(2): 155-165.
37. Longinos SN, Parlaktuna M. The effect of experimental conditions on methane hydrate formation by the use of single and dual impellers. *React Kinet, Mechan Catal.* 132(2):771-794.
38. Longinos SN, Parlaktuna M. Kinetic analysis of methane—Propane hydrate formation by the use of different impellers. *ASC Omega.* 6:1636-1646.
39. Longinos SN, Parlaktuna M. The effect of experimental conditions on methane (95%)—propane (5%) hydrate formation. *Energies.* 2020;13(24):6710.
40. Kvamme B, Graue A, Aspenes E, et al. Kinetics of solid hydrate formation by carbon dioxide: Phase field theory of hydrate nucleation and magnetic resonance imaging. *Phys Chem Chem Phys.* 2004;6:2327-2334.
41. Qasim M. *Microscale Modeling of Natural Gas Hydrates in Reservoirs.* Bergen, Norway: Ph.D. Thesis, University of Bergen; 2012.
42. Svandal A. *Modeling Hydrate Phase Transitions Using Mean-Field Approaches.* Bergen, Norway: Ph.D. Thesis, University of Bergen; 2006.
43. Kvamme B, Graue A, Buanes T, Kuznetsova T, Ersland G. Storage of CO<sub>2</sub> in natural gas hydrate reservoirs and the effect of hydrate as an extra sealing in cold aquifers. *Int J Greenh Gas Control.* 2007;1(2):236-246.
44. Buanes T. *Mean-Field Approaches Applied to Hydrate Phase Transition.* Bergen, Norway: Ph.D. Thesis, University of Bergen; 2006.
45. Buanes T, Kvamme B, Svandal A. Two approaches for modelling hydrate growth. *J Math Chem.* 2009;46(3):811-819.
46. Buanes T, Kvamme B, Svandal A. Computer simulation of CO<sub>2</sub> hydrate growth. *J Cryst Growth.* 2006;287(2):491-494.
47. Baig K. *Nano to Micro Scale Modeling of Hydrate Phase Transition Kinetics.* Bergen, Norway: Ph.D. Thesis, University of Bergen; 2017.
48. Baig K, Kvamme B, Kuznetsova T, Bauman J. The impact of water/hydrate film thickness on the kinetic rate of mixed hydrate formation during CO<sub>2</sub> injection into CH<sub>4</sub> hydrate. *AIChE J.* 2015;61(11):3944-3957.

**How to cite this article:** Kvamme B, Zhao J, Wei N, et al. Thermodynamics of hydrate systems using a uniform reference state. *Asia-Pac J Chem Eng.* 2021;16(6):e2706. doi:10.1002/apj.2706





Graphic design: Communication Division, UIB / Print: Skjipes Kommunikasjon AS



[uib.no](http://uib.no)

ISBN: 9788230865477 (print)  
9788230857601 (PDF)